UAB
Universitat Autònoma
de Barcelona

Ph.D. Thesis

Integration of Resonant N/MEMS for Energy Harvesting from Ambient Vibrations

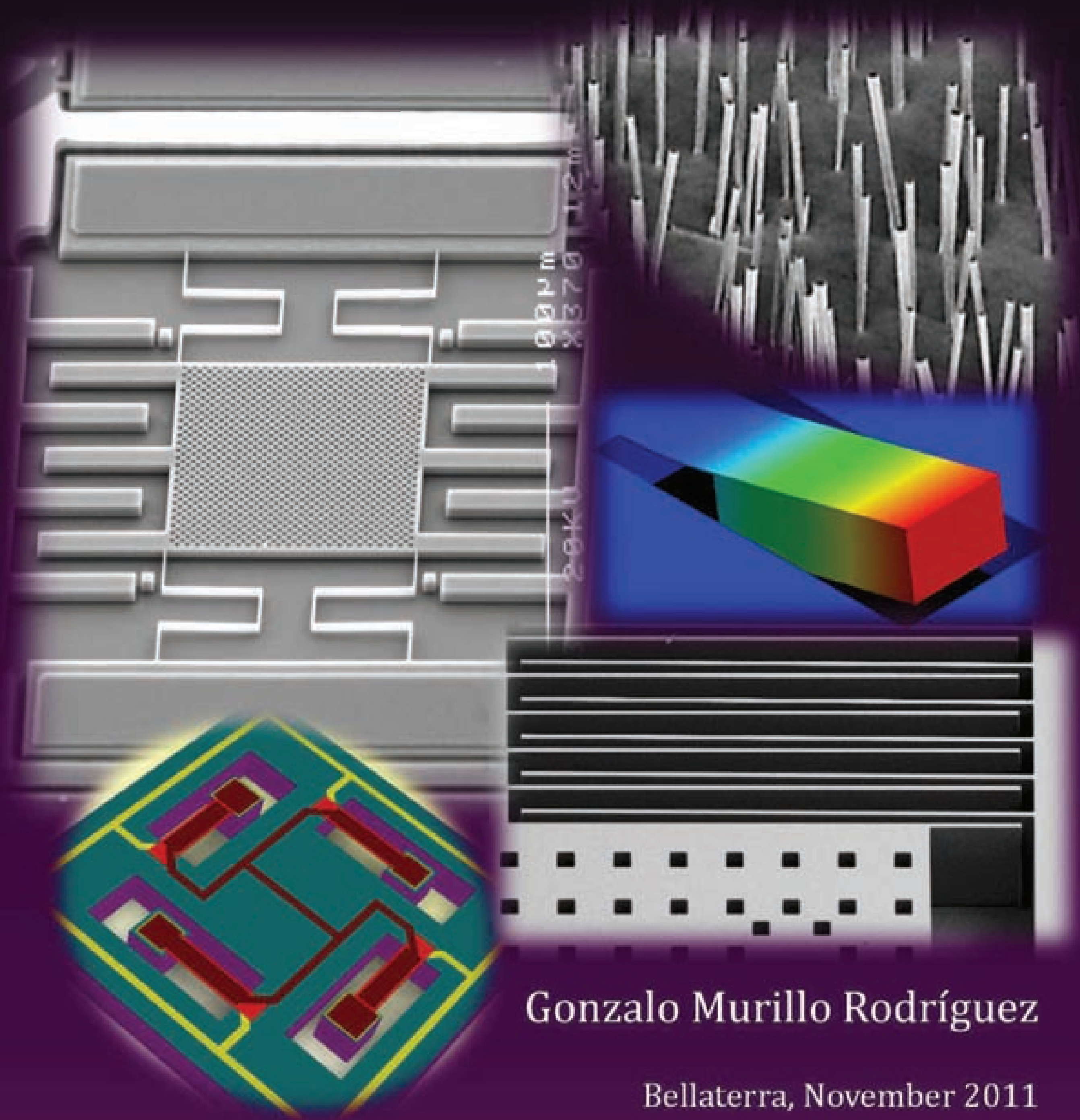

Gonzalo Murillo Rodríguez

Bellaterra, November 2011

PH.D. THESIS

INTEGRATION OF RESONANT N/MEMS FOR ENERGY HARVESTING FROM AMBIENT VIBRATIONS

Gonzalo Murillo Rodríguez

Dissertation submitted in partial fulfillment
of the requirements for the degree of
DOCTOR OF PHILOSOPHY

Bellaterra, October 2011

Major: Electronics Engineering

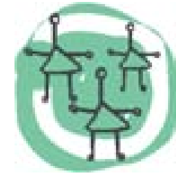

The undersigned, **Dr. Gabriel Abadal Berini**, associated professor at the Electronics Engineering Department of the *Universitat Autònoma de Barcelona*

HEREBY CERTIFY THAT

The thesis entitled "*Integration of Resonant N/MEMS for Energy Harvesting from Ambient Vibrations*" has been developed by **Gonzalo Murillo Rodríguez.**

Bellaterra, October 20, 2011

Dr. Gabriel Abadal Berini

To my mom…

You are the light that never fades away at the end of the dark corridor.

Thanks for guiding me from wherever you are.

Always alive in my memories…

ACKNOWLEDGEMENTS/AGRADECIMIENTOS

Este trabajo va dedicado a la única persona que jamás me abandona y que siempre llevo dentro de mí, mi madre, Blanca. Por desgracia, la vida nos castigó con tu ausencia y hace tiempo que no te tengo, pero cada día te encuentro en mis recuerdos. Allí siempre vivirás. Gracias por todo lo que me diste.

Quiero agradecer a toda mi familia el apoyo y cariño que siempre me han dado. Especialmente a mi padre, Rafael, mis cuatro hermanos, Blanca, Álvaro, Alejandro y Adela, a mi abuela, mi *tita* Maria Angustias y mi *tito* Julián. Gracias por haber sabido hacerme sentir arropado. Espero que siempre estemos unidos. También quiero dar las gracias a Yolanda, por haber cuidado de mi cuando he estado agobiado y bajo estrés. Esto no hubiera sido posible sin tu ayuda.

Thank you so much, Gabriel Abadal for your support and understanding. I am glad of considering you not only a boss but a friend too. I should show gratitude to the rest of members of my group: Miquel, Joan, Francesc, Eloi, Arantxa, Nuria and the rest of them for your help. And especially to Jordi, because his support has been a key point of this thesis. Thanks, my friend! Also, I want to thank to Javier Hellin his valuable help during this period.

I have to thank to some many members of the Electronics Department for these unforgettable four years. Especially to my office mates: Paris, Jose, Ferran, Gerard, Albin and Nuria. I cannot imagine a PhD without sharing my time with you all. Thank you to my "11AM coffee team": Xiomara, Vanessa and Yepes. It has been one of the best moments of every working day. I do not want to forget the rest of important people that I have met here and I can consider them my friends. Thank you guys!

During my PhD, I have traveled abroad frequently, and I have done three short stays abroad. They have been extremely helpful and useful. Not only because I have learnt a lot of things, but I have found countless wonderful people who have become my friends. Some of them are: Alberto, Stephan, Zach, Seb, Sahar, Minbaek, Calvin, Raul, Joan, Jose, Mer, Gaby, and so many more. Thank you for making me feel like at home.

Thanks to Zach Davis and the DyNEMS group (DTU) for their support during my stay at Nanotech (DTU, Denmark). Also, I want to show appreciation to Stephan Keller and the Nanotech cleanroom staff for their support on the fabrication process and training tasks.

I want to show grateful to Dr. ZL. Wang and the rest of members of his group at GeorgiaTech (Atlanta, GA, USA) for the helpful, valuable and warm welcome received. In

addition, thanks to the cleanroom staff of the Microelectronics Research Center (MiRC) at Georgia Institute of Technology for their support during the cleanroom processes and trainings.

Also, thanks to Ghislain Despesse for allowing me to use your equipment for measuring the EHiP under determined vibration conditions during my stay at MINATEC (Grenoble, France).

I want to thank to Marta Gerboles and Marta Duch for carrying out the chip post-processes to release the MEMS structures, to Jordi Marin for the help with the PCB milling tool and to Eloi Ramon and Roger Puig for their valuable support assembling both EHiP parts. Also, thanks to Jaume Esteve and Humberto Campanella for the support during our collaboration on the fabrication of the piezoelectric energy harvesters. Finally, I have to express gratitude to Jaume Verd for his help with the development of the VerilogA model.

I am sure that I am unable to remember all the people that deserve an acknowledgment, but I hope they will understand me. Thank you all!

"The only way to discover the limits of the possible is to go beyond them into the impossible."

Arthur C. Clarke, "Technology and the Future" (Clarke's second law)

English physicist & science fiction author (1917 - 2008)

SUMMARY

Nowadays, the aim of saving energy and finding new renewable sources has become a hot topic. Ambient energy sources are the best solution to obtain free energy in virtually any location. Mechanical energy sources and, in particular, vibrations are a wonderful option to recover a tiny but endless amount of energy from the environment to power low-consumption electronics circuits. N/MEMS energy harvesting devices are aimed to be the link between these two different domains. An energy scavenger can generate enough electricity to power an autonomous node of a wireless sensor network (WSN) without the need of a dedicated battery.

This thesis is focused on the study, design, fabrication and characterization of different approaches of vibration-driven energy harvesting systems at micro-scale. The transduction methods investigated to convert the mechanical energy into electricity have been the electrostatic and piezoelectric. The first one was used to monolithically integrate an energy scavenger into a commercial CMOS technology. Then, two different MEMS technologies for fabricating an electrostatic and a piezoelectric energy harvesting system were utilized. These systems took advantage of a novel concept, first defined in this thesis, called "*Energy Harvesting in Package*" that relies on the use of the whole die as inertial mass of the resonator utilized to recover the mechanical energy. The advantage of this concept is the significant increase of the extracted power density in comparison to the conventional approach. As a result of these fabrication processes, several prototypes of the converter part of different energy harvesting systems were developed and characterized showing promising expectations.

In the last part of this thesis, a shift toward nano-scale energy scavenging devices is done. It is focused on the use of piezoelectric ZnO nanowires to generate electricity from motion. This cutting-edge field has been explored and several prototypes were fabricated to prove the combination of microscopic resonant elements with ZnO nanowires.

RESUMEN (SPANISH)

En la actualidad, el propósito de ahorrar energía y encontrar nuevas fuentes de energía renovables se ha convertido en un tema candente. Las fuentes de energía ambiental son la mejor solución para obtener energía gratis en prácticamente cualquier lugar. Fuentes de energía mecánica y, en particular, las vibraciones son una magnifica opción para recuperar una cantidad pequeña, pero interminable, de energía del ambiente para alimentar circuitos electrónicos de bajo consumo. Los dispositivos de recolección de energía nano- y micro-electromecánicos (*N/MEMS*) pretenden ser el vínculo entre esos dos diferentes dominios. Un recolector de energía (*energy scavenger*) puede producir suficiente electricidad para alimentar un nodo autónomo de una red de sensores inalámbricos (*WSN*), sin la necesidad de una batería dedicada.

Esta tesis se centra en el estudio, diseño, fabricación y caracterización de diferentes tipos de sistemas de recolección de energía a micro-escala. Los métodos de transducción investigados para convertir la energía mecánica en electricidad han sido el electrostático y el piezoeléctrico. El primero de ellos fue utilizado para integrar, en un mismo chip, un recolector de energía en una tecnología CMOS comercial. Después, se utilizaron dos diferentes tecnologías *MEMS* para la fabricación de un sistema electrostático y otro piezoeléctrico. Estos sistemas se han aprovechado de un concepto novedoso, definido por primera vez en esta tesis, llamado "*Energy Harvester in Package*". Este se basa en el uso del propio chip como masa inercial del resonador utilizado para recuperar la energía mecánica. La ventaja de este concepto es el aumento significativo de la densidad de potencia extraída en comparación con los diseños convencionales. Como resultado de estos procesos de fabricación, varios prototipos de diferentes sistemas de recolección de energía fueron fabricados y caracterizados, mostrando prometedoras expectativas.

En la última parte de esta tesis, se realiza una extrapolación hacia dispositivos de recolección de energía a escala nanométrica. Esta se centra en el uso de nanohilos piezoeléctricos de ZnO para generar electricidad como consecuencia de movimientos. Esta innovadora área de investigación ha sido explorada y varios prototipos fueron fabricados para probar la combinación de elementos microscópicos resonantes y nanohilos piezoeléctricos de ZnO.

CONTENTS

ACKNOWLEDGEMENTS/AGRADECIMIENTOS ..... *III*

SUMMARY ..... *V*

RESUMEN (SPANISH) ..... *I*

1. **INTRODUCTION** **3**

1.1 MOTIVATION 3

1.2 STATE OF THE ART 13

1.3 EMPLACEMENT OF THIS THESIS 16

1.4 CHAPTER OUTLINE 18

REFERENCES 20

2. **FUNDAMENTAL THEORY AND MODELING** **23**

2.1 VIBRATION-BASED ENERGY SCAVENGING 23

2.2 MODEL OF AN ELECTROSTATIC CONVERTER 32

2.3 MODEL OF A PIEZOELECTRIC CONVERTER 48

2.4 CONCLUSIONS 56

REFERENCES 57

3. **MONOLITHIC INTEGRATION OF MICRO-SIZED ENERGY SCAVENGING SYSTEMS** **59**

3.1 MONOLITHIC FABRICATION OF MEMS AND CMOS INTEGRATION 59

3.2 A PARADIGM SHIFT IN VIBRATION ENERGY SCAVENGING: THE ENERGY-HARVESTER-ON-CHIP 61

3.3 DESIGN OF AN ELECTROSTATIC ENERGY SCAVENGER 63

3.4 FABRICATION PROCESS OF THE EHIP 68

3.5 SIMULATION RESULTS OF THE PROTOTYPE 70

3.6 MECHANICAL CHARACTERIZATION 77

3.7 CONCLUSIONS AND FUTURE APPLICATIONS 87

REFERENCES 89

4. **HETEROGENEOUS INTEGRATION OF ENERGY SCAVENGING SYSTEMS** **91**

4.1 HETEROGENEOUS INTEGRATION OF A SYSTEMS IN PACKAGE 91

4.2 A PARADIGM SHIFT: ENERGY HARVESTER IN A PACKAGE 93

4.3 MICRO-SIZED ELECTROSTATIC ENERGY SCAVENGER WITH HETEROGENEOUS INTEGRATION 95

4.4 HETEROGENEOUS INTEGRATION OF PIEZOELECTRIC ENERGY HARVESTERS 108

4.5 ANOTHER HETEROGENEOUS SOLUTION: MICROPOWER GENERATION FOR AUTONOMOUS NODES IN SMART-GRID CABLES 118

4.6 CONCLUSIONS 126

REFERENCES 128

5. **SUBMICRON-SCALE ENERGY SCAVENGING BASED ON ZNO NANOWIRES** **129**

5.1 INTRODUCTION 129

5.2 ZINC-OXIDE PROPERTIES 130

5.3 NANOWIRE GROWTH METHODS 131

5.4 FUNDAMENTALS OF NANO-PIEZOGENERATORS 135

5.5 VIBRATION-DRIVEN ENERGY HARVESTER BASED ON ZNO FINEWIRE (FW) 136

5.6 HETEROGENEOUS INTEGRATION OF MEMS ENERGY SCAVENGERS BASED ON ZNO-NW 139

5.7 CONCLUSIONS 145

REFERENCES 147

6. **CONCLUSIONS AND FUTURE APPLICATIONS** **148**

APPENDIX A. **MAIN CONTRIBUTIONS OF THE AUTHOR** **151**

APPENDIX B. **DESIGNED LAYOUTS** **157**

ABBREVIATIONS AND ACRONYMS 161

CHAPTER 1

INTRODUCTION

This chapter introduces the well-known problem of energy consumption that is being the main cause of the current crisis lived in the entire world. The aim of producing new green energies is being powerfully promoted. Saving energy at all levels is the first measure that can be taken to overcome this critical issue. Energy harvesting is a concept that pursues the recovering of the residual energy of the environment. Mechanical energy is being produced by a huge variety of sources around us and consequently wasted. Vibrations are one of these unused sources of tiny but endless energy. This energy can be extracted by using N/MEMS devices and used to supply low-power electronics system to lead to the obtaining of autonomous wireless sensor networks (WSN). These self-powered systems can help to monitor countless events and increase the energy saving of the global system.

1.1 Motivation

1.1.1 Energy crisis

Every day, humans are using tons of watts to carry out their daily-life habits. The fuel used to move the car, the electricity that allows switching a light at night or the gas that is burnt to heat up the rooms of a house are examples of energy sources that are needed every second in any place of the world. All these energy sources are derived from fossil fuel that was formed by decomposition of buried dead organisms millions of years ago. The U.S. Energy Information Administration [1] estimated in 2007 that energy sources consisted of petroleum 36.0%, coal 27.4%, and natural gas 23.0% amount to an 86.4% share for fossil fuels in primary energy consumption in the world . Non-fossil sources included hydroelectric 6.3%, nuclear 8.5% and others (geothermal, solar, tide, wind, wood, waste) amounting to 0.9 percent.

Fossil fuels are non-renewable resources because they take millions of years to form, and reserves are being depleted much faster than they can be created. Moreover, the use of fossil fuels raises environmental concerns. The burning of fossil fuels produces a net increase of 10.65 billion tons of atmospheric carbon dioxide per year. Carbon dioxide is one of the greenhouse gases that enhances radiative forcing and contributes to global warming which is one of the major adverse effects for the Earth's health. A global movement toward the

generation of renewable energy is therefore under way to help meet increased energy needs and mitigate possible environmental issues.

During the five-years from the end of 2004 through 2009, worldwide renewable energy capacity grew at rates of 10–60 percent annually for many technologies. Renewable energy comes from natural resources such as sunlight, wind, rain, tides, and geothermal heat, which are renewable (naturally replenished). About 16% of global final energy consumption comes from renewables, with 10% coming from traditional biomass, which is mainly used for heating, and 3.4% from hydroelectricity. New renewables (small hydro, modern biomass, wind, solar, geothermal, and biofuels) accounted for another 2.8% and are growing very rapidly.

1.1.2 Electronic circuits and battery issues

Nowadays, it is difficult to imagine a world without electronic circuits around us. There is a countless amount of integrated circuits that people use in their daily life, even without realizing about that. Some examples are the circuitry contained in a cell phone, the cutting-edge processor of a computer, the small ID chip hidden in a credit card or the control unit of a pacemaker. The invention of the bipolar transistor in 1947 was the first step toward modern electronics. Since then, seeking smaller and more powerful smart devices has been a worldwide topic of interest. The miniaturization of electronic systems reached unthinkable limits several decades ago. On 1965 Gordon Moore, Fairchild Semiconductor's Director of R&D, published a magazine article [2] in *Electronics* where predicted that the number of components per chip would double every 12 months. This prediction has been fulfilling since its birth for all the different types of microelectronic circuits and became the renowned Moore's Law. The same rule can be applied to different benchmarks such as, disk capacity, CPU speed, RAM size or wireless transfer speed, with the generalized Moore's Law [3, 4].

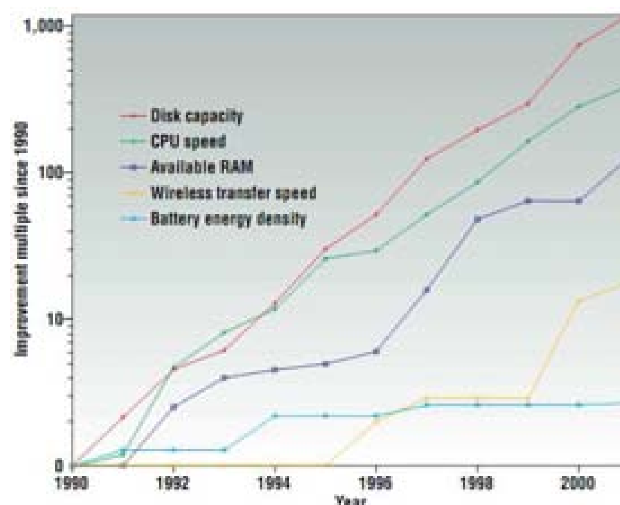

Figure 1.1. Improvement of different electronic systems [3].

It is well-kwon that batteries have not been able to follow the scaling down of other microelectronics parts, which fulfill the before-said law. It can be clearly observed a saturation of the improvement of the battery energy density in Figure 1.1, in contrast to the

constant positive slope of the rest of parameters. Energy density has only increased by approximately by 3x in the past decade.

1.1.3 New trend toward low-power electronics

In the last years, a huge interest for reducing the power composition of the electronic circuits has arrived to researchers and companies. The power consumption of different common portable devices are shown in Figure 1.2, where it can be appreciated the scaling down on power consumption for them. Figure 1.3 gives us an idea about the days of use of some types of batteries supplying a continuous power of only 100 µW, which perfectly illustrated the finite lifetime of a battery.

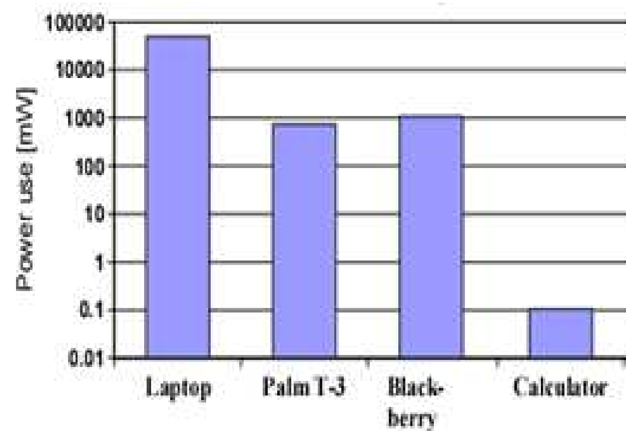

Figure 1.2. Power consumption of several portable devices [5].

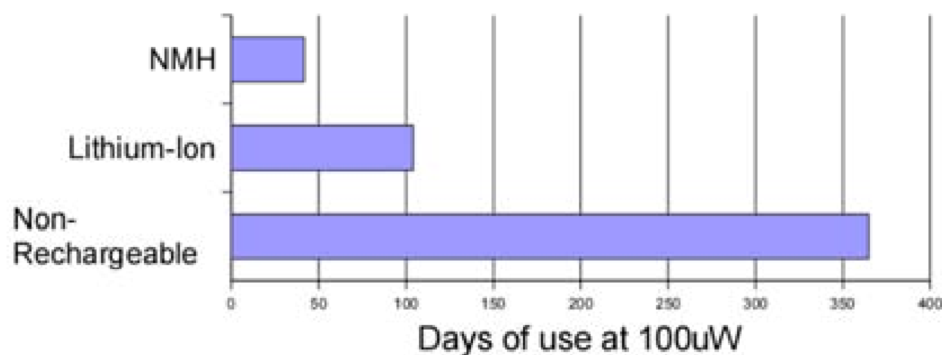

Figure 1.3. Lifetime of different batteries of 1 cm^3 for a continuous use of 100 µW [5].

1.1.4 The concepts of zero-power and energy harvesting

Therefore, this new tendency toward tiny, portable, wireless and inexpensive systems is not compatible with a battery with finite amount of energy, macroscopic size and difficult recharge or replacement. The research about new devices that extract useful electrical energy from the residual ambient energy has increased in the last few years. This is the basic idea of the energy harvesting concept [6], which can exploit different energy source types.

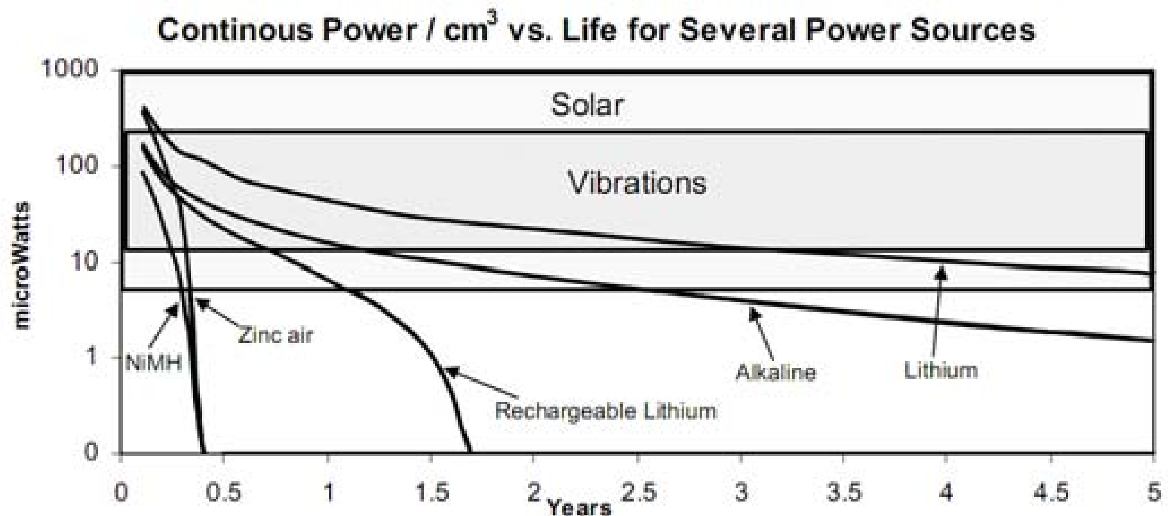

Figure 1.4. Lifetime of several power supply methods [5].

Figure 1.5. Common uses of photovoltaic cells.

There are numerous energy sources (Figure 1.4) and transduction methods to convert that energy into useful electricity. They can provide an unlimited power level, against the limited battery lifetime. Some of the most exploited energy sources are the solar (Figure 1.5), the thermoelectric or electromagnetic. An estimation of the power that these sources can offer is presented in [6]. Especially attractive are the use of ambient vibrations as energy sources because they are available over a large number of different places and by using a resonant device this harmonic motion can be scavenged (Table 1.1).

Several authors have measured the spectrum of these environmental vibrations (Figure 1.6) in different conditions and numerous locations [7, 8]. They measured the ambient vibration spectrum from different natural, industrial and residential locations.

A summary of the acceleration amplitude and frequency values of the maximum peaks of several measured spectrums are shown in Table 1.2 . It can be seen in Figure 1.6, two of the analyzed spectrums, where different acceleration peaks can be observed. Also, the power density is concentrated at low frequency. It can be inferred that all the maximum peaks have a frequency value lower than 500 Hz and an acceleration value ranging from 0.01 to 10 m/s^2.

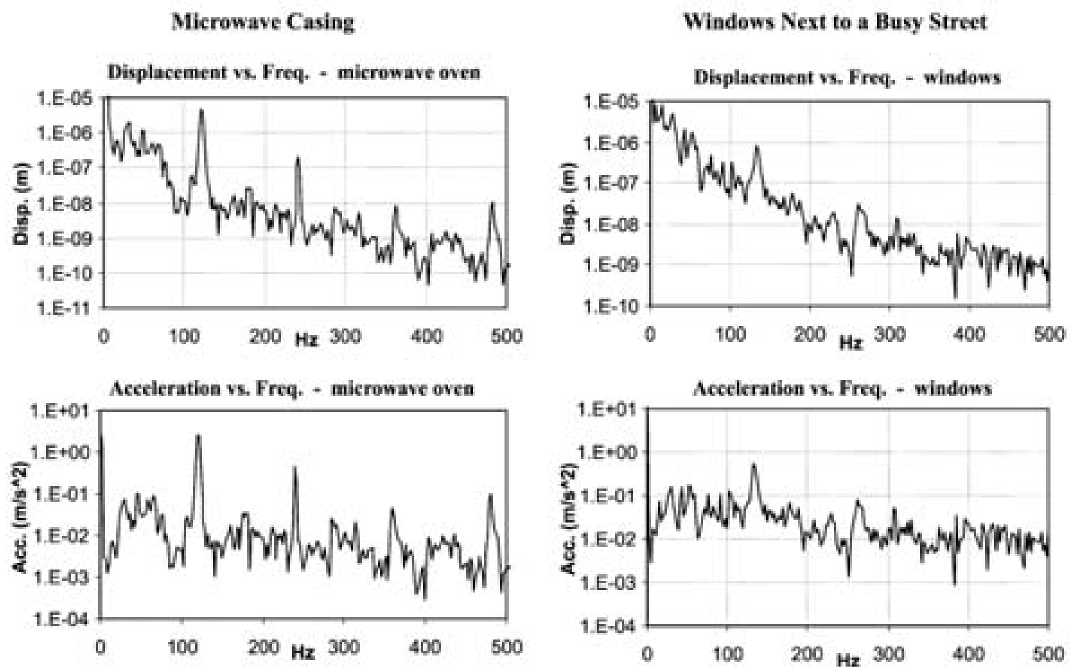

Figure 1.6. Acceleration spectrum on a microwave casing and a windows next to a bus street [9].

		Power Density ($\mu W/cm^3$) 1 Year lifetime	Power Density ($\mu W/cm^3$) 10 Year lifetime
Scavenged Power Sources	Solar (Outdoors)	15,000 - direct sun 150 - cloudy day	15,000 - direct sun 150 - cloudy day
	Solar (Indoors)	6 - office desk	6 - office desk
	Vibrations	200	200
	Acoustic Noise	0.003 @ 75 Db 0.96 @ 100 Db	0.003 @ 75 Db 0.96 @ 100 Db
	Daily Temp. Variation	10	10
	Temperature Gradient	15 @ 10 °C gradient	15 @ 10 °C gradient
	Shoe Inserts	330	330
Energy reservoirs	Batteries (non-recharg. Lithium)	45	3.5
	Batteries (rechargeable Lithium)	7	0
	Hydrocarbon fuel (micro heat engine)	333	33
	Fuel Cells (methanol)	280	28
	Nuclear Isotopes (uranium)	$6x10^6$	$6x10^5$

Table 1.1. Summary of power densities for different electric energy storage/generation methods [5].

Table 1.2. Acceleration (m/s²) magnitude and frequency of fundamental vibration mode for various sources [9].

Vibration source	A (m/s^2)	F_{peak}
Car engine compartment	12	200
Base of 3-axis machine tool	10	70
Blender casing	6.4	121
Clothes dryer	3.5	121
Person nervously tapping their heel	3	1
Car instrument panel	3	13
Door frame just after door closes	3	125
Small microwave oven	2.5	121
HVAC vents in office building	0.2–1.5	60
Windows next to a busy road	0.7	100
CD on notebook computer	0.6	75
Second story floor of busy office	0.2	100

1.1.5 Background to self-powered devices

It was Abraham-Louis Perrelet who invented a self-winding mechanism in 1770 for pocket watches (Figure 1.7). After that, a self-winding mechanism for wristwatches was created by a watch repairer named John Harwood in 1923.

Figure 1.7. Self-winding pocket watch and self-powered wireless remotes.

In 1956 Robert Adler developed "Zenith Space Command", a wireless remote (Figure 1.7) that was self-powered by the fact of pressing the buttons. When the user pushed a button on the remote control, it struck a tuned aluminum rod that resonated at an ultra-sonic frequency. The TV decoded this sound pulse and changed channels appropriately. A modern

version of this idea has been develop by Philips and Arveni [10]. In this case, the piezoelectric effect is the responsible of generating the needed energy when the buttons are pressed.

In our daily life, it can be seen are already using numerous devices that convert mechanical energy into useful electricity such as: the dynamos of bike, shake-charged flash lights, the car alternator, hydroelectric stations, etc. The most of them are using an electromagnetic transduction to convert the energy, but when we go down in dimension, the manufacturing and assembling of coils and magnets become really difficult.

1.1.6 Convergence toward a real application: Wireless Sensor Network

Combined with the boom of wireless communications, the integration of miniature smart devices with sensing capabilities and wireless features is becoming a research hot topic. By adding a large number of wireless sensor nodes, an intelligent environment known as a wireless sensor network (WSN), can be created. Although centimeter-scale smart devices are already around us, the rising challenge is to reduce their sizes in order to locate this type of device virtually everywhere. However, the miniaturization of the node, and consequently of the energy storage element, has a direct impact on the node lifetime. This limits the feasibility of this device because of the difficulty in recharging or replacing large numbers of devices and due, at times, to their unreachable locations. In order to overcome this difficulty, the concept of energy harvesting was created [2]. It claims the use of energy found at the immediate environment to power the WSN node. Figure 1.8 shows some examples of WSN that can be created in several environments such us a house, a bridge, a car, animals or a forest. In all these places it is possible to find a residual energy source to power the WSN nodes. These energy sources can have a thermal, light or mechanical nature. As commented before, mechanical vibrations [3-4] are particularly interesting because of the important power density and the nearly universal spatial and temporal availability.

Figure 1.8. Examples of Wireless Sensor Networks and ambient energy sources to power certain applications. (Created by Reiko Kusumoto)

In the near future, hundreds of wireless sensor nodes spread all around the environment and even our body will be continuously receiving and sending information, measuring data and working together to make more complex calculations. The main difficulty to make this vision real is the way of powering all these tiny devices. The charge or replacement of batteries is not feasible when there are a large number of nodes or they are implanted in a human body. The notion of energy scavenging has received a huge attention during the last years because of the need of finding an autonomous way of power supplying this type of ultralow-power integrated systems. There are a huge variety of sources of mechanical energy such as, human motion, wind, machinery motions or vibrations. Among all these choices, vibrations are a good solution to be scavenged, due to its virtually full-time availability in a huge number of locations [7, 8], e.g. a microwave, a fan, a washing machine, a building, a car or acoustic waves. Several authors have fabricated some approaches to convert vibrations into electricity using the three typical transductions: electromagnetic [11], piezoelectric [12-15] and electrostatic [16-18]. The main drawback of these devices is the difficulty of fabricating a MEMS device with a resonance frequency in the range of the common ambient vibrations (normally < 500 Hz). Some other authors have tried to overcome this difficulty with the use of a non-linear oscillator instead of a resonant linear oscillator [19, 20]. However, the approaches presented in this thesis are based on a linear spring-mass system that takes advantage of a novel concepts described in the following sections that allow reducing the resonance frequency and improving the energy density of the energy harvesters.

1.1.7 Guardian Angels project

Inside if the Seventh Framework Programme of the European Union (EU) several projects related to energy harvesting are being developed (Table 1.3). Guardian Angels is an ambitious project that is part of the FET Flagships initiatives that have been recently launched. Future and Emerging Technologies (FET) is the EU incubator in information technologies. Its mission is to promote high risk research, offset by potential breakthrough with high technological or societal impact.

Figure 1.9. Current values of power considered for computation, sensing, communication and energy harvesting and the expected goal values pursued by Guardian Angels UE project.

Table 1.3. Research projects of the Framework Programmes 6 and 7 related to Energy Harvesting.

Acronym	Project	Framework Programme	Funding (million €)
NEXTEC	Next Generation Nano-engineered Thermoelectric Converters - from concept to industrial validation	FP7	3.93
GUARDIAN ANGELS	Guardian Angels for a Smarter Life	FP7	1.4
THERMOMAG	Nanostructured energy-harvesting thermoelectrics based on Mg2Si	FP7	3.99
MESOLIGHT	Mesoscopic Junctions for Light Energy Harvesting and Conversion	FP7	2.05
PLASMHACAT	Plasmonics-based Energy Harvesting for Catalysis	FP7	1.5
WI-HEALTH	A wireless network with autonomously powered and active long range acoustic nodes for total structural health monitoring of bridges	FP7	1.18
WIBRATE	Wireless, Self-Powered Vibration Monitoring and Control for Complex Industrial Systems	FP7	2.85
WINTUR	In-situ wireless monitoring of on- and offshore WINd TURbine blades using energy harvesting technology	FP7	1.1
POWERAMP	Clean Energy Production through Roadway Surface Power Harvesting Systems for Increased Safety in the Transportation Sector	FP7	1.09
NEXTEC	Next Generation Nano-engineered Thermoelectric Converters - from concept to industrial validation	FP7	3.93
THERMOMAG	Nanostructured energy-harvesting thermoelectrics based on Mg2Si	FP7	3.99
MESOLIGHT	Mesoscopic Junctions for Light Energy Harvesting and Conversion	FP7	2.05
ZEROPOWER	Coordinating Research Efforts Toward Zero-Power	FP7	0.55
NANOPOWER	Nanoscale energy management for powering ICT devices	FP7	2.63
GREENERBUILDINGS	An ubiquitous embedded systems framework for energy-aware buildings using activity and context knowledge	FP7	1.85
TIBUCON	Self-powered Wireless Sensor Network for HVAC System Energy Improvement - Toward Integral Building Connectivity	FP7	1.59
SMART-EC	Heterogeneous integration of autonomous smart films based on electrochromic transistors	FP7	5.1
SINAPS	Semiconducting Nanowire Platform for Autonomous Sensors	FP7	2.37
GREEN SILICON	Generate Renewable Energy Efficiently using Nanofabricated Silicon	FP7	1.66
GENESI	Green sEnsor NEtworks for Structural monItoring	FP7	2
NANO-TEC	Nano-engineered high performance Thermoelectric Energy Conversion devices	FP7	1.23
ADVICE	Autonomous Damage Detection and Vibration Control Systems	FP6	1.76
VIBES	Vibration energy scavenging	FP6	2.6

Leading the charge, the FET Flagships are large-scale and science-driven initiatives that aim to achieve a visionary goal. The scale of ambition is over 10 years of coordinated effort, and a budget of up to one billion €. At this stage, 6 Pilot Actions are funded for a 12-month period started in May 2011. In the second half of 2012 two of the Pilots will be selected and launched as full FET Flagship Initiatives in 2013. It is formed by numerous industrial partners such as IBM, Infineon, Intel, Siemens or STMicroelectronics and other important European institutional partners.

Providing Information and Communication Technologies to assist people in all sorts of complex situations is the long term goal of the Flagship Initiative, Guardian Angels. These Guardian Angels will be like personal assistants and are envisioned as intelligent (thinking), autonomous systems (or even systems-of-systems) featuring sensing, computation, and communication, and delivering features and characteristics that go well beyond human capabilities. It is intended that these will provide assistance from infancy right through to old age. A key feature of these Guardian Angels will be their zero power requirements (Figure 1.9) as they will scavenge for energy. Foreseen are individual health support tools, local monitoring of ambient conditions for dangers, and emotional applications. Research will address scientific challenges such as energy-efficient computing and communication; low-power sensing, bio-inspired energy scavenging, and zero-power human-machine interfaces.

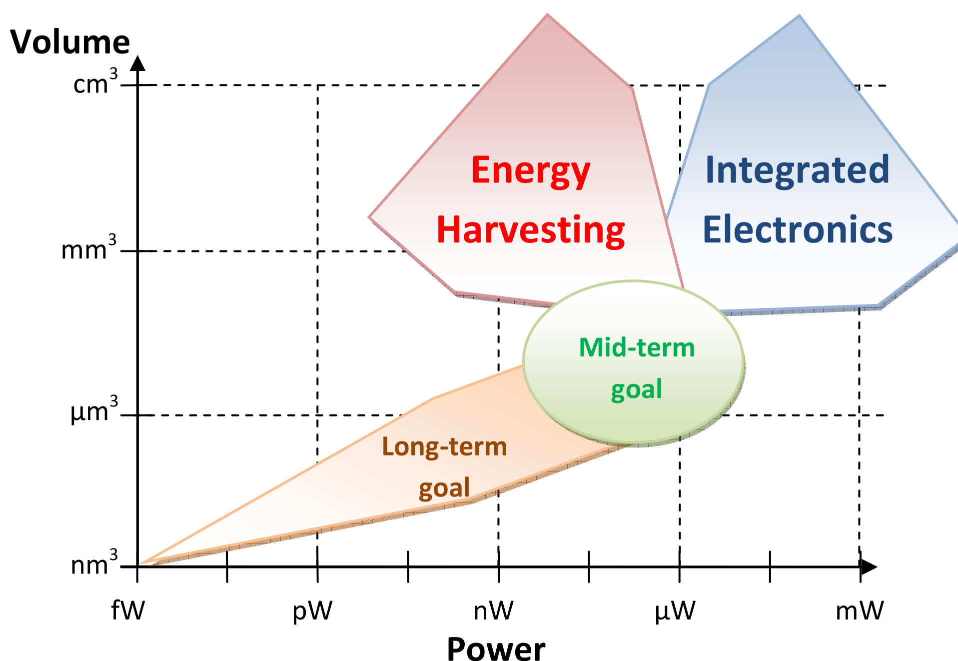

Figure 1.10. Graph that shows the convergence of energy harvesting devices and integrated circuits that is pursued by Guardian Angels project in a mid and long-term in terms of volume and power composition of both device families.

This project pursues a convergence between energy harvesting devices and integrated circuits in terms of volume and power composition. Figure 1.10 shows the volume and power consumption/generation of both device families. Currently, energy harvesters sizing less than 10 mm^3 are able to generate some hundreds of µW. Meanwhile, ultra-low-power integrated circuits can operate with a power below 1 mW with a size smaller than 1 mm^3.

1.2 State of the art

There is an increasing volume of research showing energy scavenging devices at different scales. The number of publications per year has been increased more than ten times in the last two decades as shown in Figure 1.11.

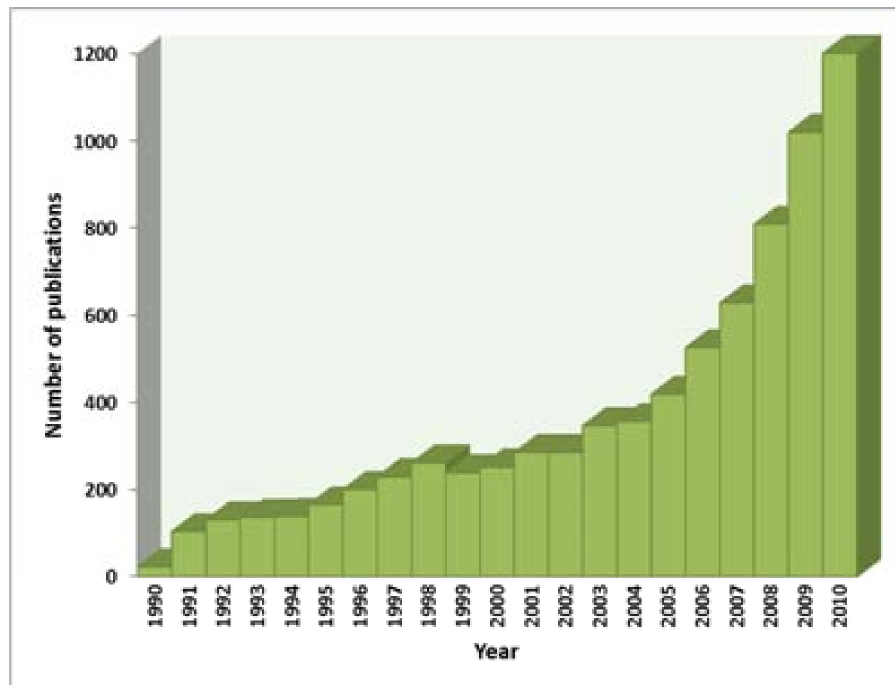

Figure 1.11. Number of publications about energy harvesting appeared in the last years

Depending on their transduction methods, it is possible to find piezoelectric, electromagnetic, electrostatic types [5-7]. The piezoelectric transduction is especially attractive because of its immediate alternate current output when the piezoelectric material is mechanically stressed. Previous literature shows everything from off-the-shelf mesoscale devices [8-11] to functional microscale prototype [5, 12-13] and generators based on nanowires (NWs) [14-17]. While the microscale devices normally consist of a spring-mass system that converts vibrations into electricity using the system's resonance frequency, most of NW-based generators are formed by arrays of NWs placed between two electrodes and are bent by the direct effect of the excitation force.

Starting from one of the numerous collections of energy scavenging devices that exist in the literature, a state-of-the-art study has been performed [21] and reported in Table 1.4, Table 1.5 and Table 1.6 concerning piezoelectric, electrostatic and electromagnetic transductions respectively.

Table 1.4. Summary of piezoelectric converters

First author/ References	Center	Year	Power (μW)	Frequency (Hz)	Acceleration (m/s²)	Mass (mg)	Volume (mm³)
White [22]	Southampton University (UK)	2001	2.1	80.1	2.3 [a]	800	125
Kymissis [23]	MIT (USA)	1998	1300	0.9	-	-	16000
Shenk [24]	MIT (USA)	2001	8400	0.9	-	-	25000
Roundy [9]	Berkeley University (USA)	2003	375	120	2.5	8500 [a]	1000
Sodano [25]	Virginia Poly (USA)	2004	11.9	30	-	9520	1947
Elfrink [12]	IMEC	2010	17	353	6.4	-	24.5[a]
Murillo [This thesis]	Universidad Autónoma de Barcelona (Spain)	2011	0.2	515	0.64	2.6	1.575

[a]estimated value

Table 1.5. Summary of electromagnetic converter

First author/ References	Center	Year	Power (μW)	Frequency (Hz)	Acceleration (m/s²)	Mass (g)	Volume (mm³)
Shearwood [26, 27]	TIMA Lab. (France)	1997	0.3	4400	382	0.0023	5.4
Serre [28]	Universidad de Barcelona (Spain)	2007	0.04	360	-	-	600-700
Beeby [29]	Southampton University (UK)	2001	530	322	-	-	240
Tudor [30]	Southampton University (UK)	2004	180	322	2.7	-	840
Perpetum company [31]	Southampton (UK)	-	4000	100	0.4	50	30000
Serre [32]	Universidad de Barcelona (Spain)	2008	50	300	-	-	1800
Beeby [33]	Southampton University (UK)	2005	0.5	9500	1.92	0.028	-
Wen [34]	Hong Kong University (China)	2001	830	110	95.5	-	1000

Table 1.6. Summary of electrostatic converters

First author/ References	Center	Year	Power (µW)	Frequency (Hz)	Acceleration (m/s²)	Mass (mg)	Volume (mm³)
Tashiro [35]	Terumo Corp (Japan)	2002	36	6	1	780000	-
Mitcheson [36]	Imperial College (UK)	2003	3.7	30	50	100	750
Roundy [5]	Berkeley University (USA)	2003	110[a]	120	2.25	-	1000
Despesse [37]	MINATEC (France)	2005	1052	50	8.8	104000	1800
Murillo [this thesis]	Universidad Autónoma de Barcelona (Spain)	2011	0.98[a]	200	0.7	19.85	7.86
Murillo [this thesis]	Universidad Autónoma de Barcelona (Spain)	2011	11[a]	287	10	26.74	12.96
[a]estimated value							

The typical extracted power is in the microwatt range, and the size goes from the micro-scale to the macroscopic scale, being the mesoscopic converter the most common size. The piezoelectric converter leads the compilation with respect to the maximum value of power density. Whereas the smallest size has been achieved for the electrostatic transduction

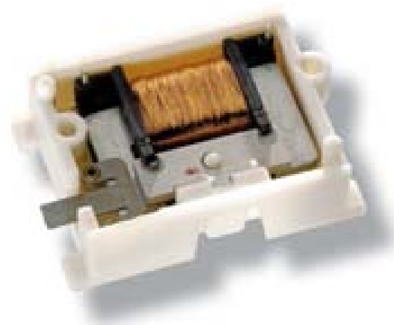

Figure 1.12. Enocean® ECO 100 – Electro-dynamic energy converter

In Table 1.7, a comparison of the most popular wireless technologies is reported, including its own ultra-low-power protocol that was created to market battery-less transmitters.

There are numerous telecommunication and electronics companies that are focusing their attention on this type of devices. For instance, based on ultra-low power technology developed by Texas Instruments has been created AdaptativEnergy [38], a new company full dedicated to energy harvesting. Moreover, Enocean [39], a spin-off from Siemens, is using a combination of miniature energy scavenging modules (Figure 1.12) together with ultra-low power RF technology to create low-cost self-powered wireless sensors. They pursue the automation of residential and industrial buildings to convert them into green and smart buildings. In fact, a consortium [40] formed by numerous companies that has the aim of

joining forces to develop related standards to spread this technology reducing fabrication and developing costs.

Table 1.7. Main off-the-shelf wireless technologies nowadays [39].

	EnOcean	Z-Wave or KNX-RF	ZigBee (802.15.4)	ZigBee (802.15.4)	Bluetooth (802.15.1)	WLAN (802.11)
Frequency (MHz)	868	868	868	2400	2400	2400
Data rate (kbyte/s)	125	9.6 / 20	20	250	720	11.000-54.000
Minimum telegram length (ms)	0.6	20	30	4	0.7	–
Energy need (incl. startup)	extremly low	low	low	low	medium	high
Basic load level of frequency band	low	low	low	high	high	high
Risk of data collision	very low	medium	medium	low	very low	high
Batteryless radio transmitter	yes	no	no	no	no	no
Life cycle costs	very good	good	good	good	good	not so good
Optimal solution for following purpose	maintenance-free batteryless wireless sensor systems	battery-powered wireless sensor systems	battery-powered wireless sensor systems	battery-powered wireless sensor systems	computer networking with printers and PDAs	computer networking (Web, e-mail, video)

According to this Alliance, the advantages of utilizing self-powered wireless microsystems are

- Energy and time saving.
- Flexibility for the applications.
- Free-maintenance devices.
- Green technology.
- Reduction of fire risks and inductive magnetic field.
- Installation simplification and costless.

Biomedical systems [35, 41] or body motion energy harnessing are also promising applications that are attracting a huge attention [42, 43].

Important international conferences in MEMS, such as Tranducers, Eurosensors, MEMS, MNE or IEDM are requesting works related to energy harvesting. Also, some conferences mainly focus of this fields are gaining attention and the best example is PowerMEMS.

1.3 Emplacement of this thesis

This thesis was carried out thanks to a fellowship from the Ministry of Spanish, to pursue a PhD held by the author during the realization of this work. The thesis was part of the project

called MEMSPORT, supported by the same Ministry. This project, which lasted from 2007 to 2010, had the aim of developing monolithic and heterogeneous CMOS-MEMS elements that allow the portability and autonomy of an overall integrated system with high performance and functionality.

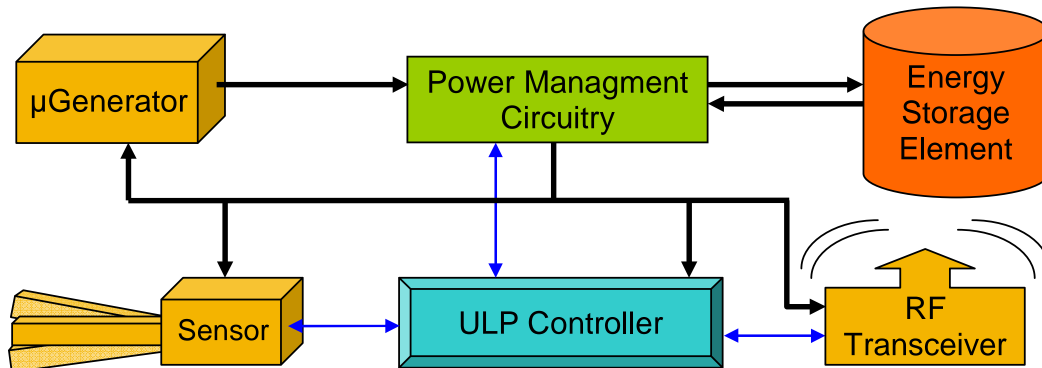

Figure 1.13. Block diagram of the autonomous integrated system pursued by MEMSPORT.

From the generic block diagram shown in Figure 1.13 can be distinguished the different functional parts that conform the autonomous MEMS-based integrated system pursued by MEMSPORT. It consists of a transduction block, a power management and conditioning circuitry, an RF transceiver to enable the wireless communication, an ultra-low-power control unit and an energy storing element such as a supercapacitor or rechargeable battery.

A well-known definition for this kind of system even if they are not autonomous is wireless sensor network (WSN) node. They are employed today in many different applications areas, ranging from health and lifestyle to automotive, smart building, machine maintenance or active RFID tags.

The project had two clear research lines. The first one relied on the development of MEMS RF resonators and the associated CMOS circuitry working as key components of the signal treatment, reception and transmission subsystem. On the other hand, the design and fabrication of resonant transducer to harvest power from ambient vibrations was explored with the aim of supplying energy for the global system.

The author of this thesis belongs to ECAS group and NANERG subgroup at the *Universidad Autónoma de Barcelona*. As observed in Figure 1.14, ECAS group has been working on MEMS and their integration into commercial CMOS technologies for more than ten years. This thesis started with MEMSPORT and has been continued with the support of OPACMEMS. This new project relies on the use of optical nanoantennae to convert light energy into heat and then by means of its associated thermal vibration it can actuate an N/MEMS resonator and finally, the mechanical energy has to be harvested using a piezoelectric element. This transition from micro and mesoscale to nanoscale at the end of the author's PhD period was translated into 6-months stay at Georgia Technology Institute, where the author was working in the successful research group of Prof. Zhong Lin Wang. Stating there, he could learn to grow ZnO nanowires, fabricate nanogenerators and measure them.

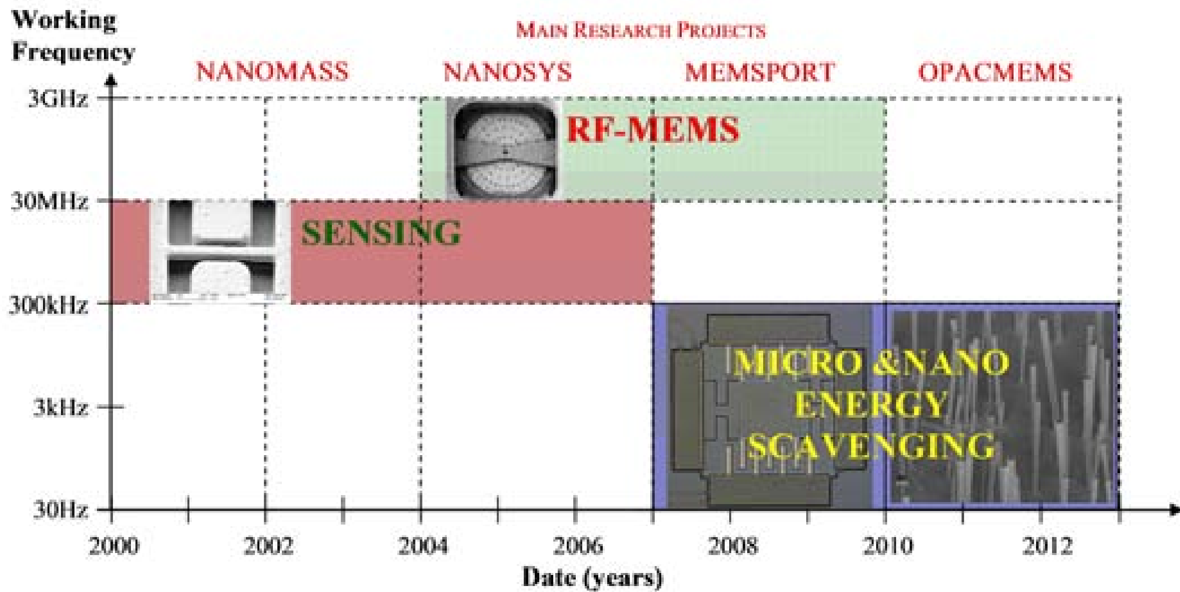

Figure 1.14. Schedule of the main projects of ECAS and NANERG groups.

The group is member of an important knowledge transfer network [44] on energy harvesting. The network works to define new research challenges and help catalyze collaborative research proposals. It tries to ensure better and broader dissemination on the current and future capabilities of energy harvesting technologies to all potential users in both industry and academia.

1.4 Chapter Outline

Despite of this preliminary chapter that introduces the motivations, state-of-the-art and framework of this PhD, this dissertation has been divided into five chapters more and two appendixes.

Chapter 2: Fundamentals theory and modeling

It is describe the main fundamentals about vibration-driven energy harvesting and the modeling of the piezoelectric and electrostatic devices.

Chapter 3: Monolithic integration of micro-sized energy scavenging systems

The fabrication and characterization of a prototype of energy harvesting system integrated in a CMOS chip is described here. It is based on the “Energy Harvester on Chip” concept, first defined here.

Chapter 4: Heterogeneous integration of energy scavenging systems

Two different transductions, piezoelectric and electrostatic, are used to fabricate several devices that can be heterogeneously integrated with an auxiliary chip to create an autonomous WSN node. This combination is the origin of the novel concept called “Energy Harvester in Package”.

Chapter 5: Submicron-scale energy scavenging based on ZnO nanowires

A shift toward nanoscale devices is performed in this chapter. Some prototypes using piezoelectric ZnO nanowires are fabricated and characterized here. Also, a fabrication process to integrate a micro-scale resonant device with ZnO nanowires is proposed here.

Chapter 6: Conclusions and future applications.

The main conclusions resulting from this thesis are collected in this chapter.

References

[1] *U.S. EIA International Energy Statistics website*. Available: http://www.eia.gov/cfapps/ipdbproject/IEDIndex3.cfm

[2] G. E. Moore, "Cramming more components onto integrated circuits (Reprinted from Electronics, pg 114-117, April 19, 1965)," *Proceedings of the Ieee,* vol. 86, pp. 82-85, 1998.

[3] T. E. Starner, "Powerful change part 1: batteries and possible alternatives for the mobile market," *Pervasive Computing, IEEE,* vol. 2, pp. 86-88, 2003.

[4] T. Starner, "Thick clients for personal wireless devices," *Computer,* vol. 35, pp. 133-135, 2002.

[5] S. Roundy, P. K. Wright, and J. M. Rabaey, "Energy Scavenging for Wireless Sensor Networks: With Special Focus on Vibrations," Springer, 2004.

[6] S. Roundy, D. Steingart, L. Frechette, P. Wright, and J. Rabaey, "Power Sources for Wireless Sensor Networks," *Berlin, Germany,* pp. 1-17, 2004.

[7] S. Roundy, "On the Effectiveness of Vibration-based Energy Harvesting," *Journal of Intelligent Material Systems and Structures,* vol. 16, pp. 809-823, 2005.

[8] G. Despesse, J. J. Chaillout, T. Jager, J. M. Léger, A. Vassilev, S. Basrour, and B. Charlot, "High damping electrostatic system for vibration energy scavenging," presented at the Proceedings of the 2005 joint conference on Smart objects and ambient intelligence: innovative context-aware services: usages and technologies, Grenoble, France, 2005.

[9] S. Roundy, P. K. Wright, and J. Rabaey, "A study of low level vibrations as a power source for wireless sensor nodes," *Computer Communications,* vol. 26, pp. 1131-1144, 2003.

[10] *Arveni website*. Available: http://www.arveni.fr/eng_home.php

[11] R. Amirtharajah and A. P. Chandrakasan, "Self-powered signal processing using vibration-based power generation," *Solid-State Circuits, IEEE Journal of,* vol. 33, pp. 687-695, 1998.

[12] R. Elfrink and et al., "Vacuum-packaged piezoelectric vibration energy harvesters: damping contributions and autonomy for a wireless sensor system," *Journal of Micromechanics and Microengineering,* vol. 20, p. 104001, 2010.

[13] M. Ferrari, V. Ferrari, D. Marioli, and A. Taroni, "Modeling, fabrication and performance measurements of a piezoelectric energy converter for power harvesting in autonomous microsystems," *IEEE Transactions on Instrumentation and Measurement,* vol. 55, 2006.

[14] G. Murillo, G. Abadal, F. Torres, J. L. Lopez, J. Giner, H. Campanella, A. Uranga, J. Esteve, and N. Barniol, "Design of piezoelectric scavengers using FBAR technology," in *8th International PowerMEMS Workshop*, Sendai, Japan, 2008.

[15] M. Marzencki, Y. Ammar, and S. Basrour, "Integrated power harvesting system including a MEMS generator and a power management circuit," *Sensors and Actuators A: Physical,* vol. 145-146, pp. 363-370.

[16] P. D. Mitcheson, P. Miao, B. H. Stark, E. M. Yeatman, A. S. Holmes, and T. C. Green, "MEMS electrostatic micropower generator for low frequency operation," *Sensors and Actuators A: Physical,* vol. 115, pp. 523-529, 2004.

[17] F. Peano and T. Tambosso, "Design and optimization of a MEMS electret-based capacitive energy scavenger," *Microelectromechanical Systems, Journal of,* vol. 14, pp. 429-435, 2005.

[18] T. Sterken, P. Fiorini, K. Baert, R. Puers, and G. Borghs, "An electret-based electrostatic microgenerator," in *TRANSDUCERS, Solid-State Sensors, Actuators and Microsystems, 12th International Conference on*, 2003, pp. 1291-1294.

[19] F. Cottone, H. Vocca, and L. Gammaitoni, "Nonlinear Energy Harvesting," *Physical Review Letters,* vol. 102, 2009.

[20] L. Gammaitoni, I. Neri, and H. Vocca, "Nonlinear oscillators for vibration energy harvesting," *Applied Physics Letters,* vol. 94, 2009.
[21] S. P. Beeby, M. J. Tudor, and N. M. White, "Energy harvesting vibration sources for microsystems applications," *Meas. Sci. Technol,* vol. 17, pp. 175–195, 2006.
[22] N. M. White, P. Glynne-Jones, and S. P. Beeby, "A novel thick-film piezoelectric micro-generator," *Smart Materials & Structures,* vol. 10, pp. 850-852, 2001.
[23] J. Kymissis, C. Kendall, J. Paradiso, and N. Gershenfeld, "Parasitic power harvesting in shoes," *Second International Symposium on Wearable Computers - Digest of Papers,* pp. 132-139, 1998.
[24] N. S. Shenck and J. A. Paradiso, "Energy scavenging with shoe-mounted piezoelectrics," *Ieee Micro,* vol. 21, pp. 30-42, 2001.
[25] H. A. Sodano, G. Park, and D. J. Inman, "Estimation of electric charge output for piezoelectric energy harvesting," *Strain,* vol. 40, pp. 49-58, 2004.
[26] C. B. Williams, C. Shearwood, M. A. Harradine, P. H. Mellor, T. S. Birch, and R. B. Yates, "Development of an electromagnetic micro-generator," *Iee Proceedings-Circuits Devices and Systems,* vol. 148, pp. 337-342, 2001.
[27] C. Shearwood and R. B. Yates, "Development of an electromagnetic micro-generator," *Electronics Letters,* vol. 33, pp. 1883-1884, 1997.
[28] C. Serre, A. Pérez-Rodríguez, N. Fondevilla, J. Morante, J. Montserrat, and J. Esteve, "Vibrational energy scavenging with Si technology electromagnetic inertial microgenerators," *Microsystem Technologies,* vol. 13, pp. 1655-1661, 2007.
[29] M. El-hami, R. Glynne-Jones, N. M. White, M. Hill, S. Beeby, E. James, A. D. Brown, and J. N. Ross, "Design and fabrication of a new vibration-based electromechanical power generator," *Sensors and Actuators a-Physical,* vol. 92, pp. 335-342, 2001.
[30] P. Glynne-Jones, M. J. Tudor, S. P. Beeby, and N. M. White, "An electromagnetic, vibration-powered generator for intelligent sensor systems," *Sensors and Actuators a-Physical,* vol. 110, pp. 344-349, 2004.
[31] *Perpetuum website*. Available: http://www.perpetuum.com/
[32] C. Serre, A. Perez-Rodriguez, N. Fondevilla, E. Martincic, S. Martinez, J. R. Morante, J. Montserrat, and J. Esteve, "Design and implementation of mechanical resonators for optimized inertial electromagnetic microgenerators," *Microsystem Technologies-Micro-and Nanosystems-Information Storage and Processing Systems,* vol. 14, pp. 653-658, 2008.
[33] S. P. Beeby, M. J. Tudor, E. Koukharenko, N. M. White, T. O'Donnell, C. Saha, S. Kulkarni, and S. Roy, "Micro machined silicon generator for harvesting power from vibrations," *Proc. Transducers 2005 (Seoul, Korea,* pp. 780–3, 2005.
[34] N. N. H. Ching, H. Y. Wong, W. J. Li, P. H. W. Leong, and Z. Y. Wen, "A laser-micromachined vibrational to electrical power transducer for wireless sensing systems," *Transducers '01: Eurosensors Xv, Digest of Technical Papers, Vols 1 and 2,* pp. 38-41, 2001.
[35] R. Tashiro, N. Kabei, K. Katayama, E. Tsuboi, and K. Tsuchiya, "Development of an electrostatic generator for a cardiac pacemaker that harnesses the ventricular wall motion," *Journal of Artificial Organs,* vol. 5, pp. 239-245, 2002.
[36] P. Mitcheson, B. Stark, P. Miao, E. Yeatman, A. Holmes, and T. Green, "Analysis and optimisation of MEMS electrostatic on-chip power supply for self-powering of slow-moving sensors," 2003, pp. 492-495.
[37] G. Despesse, T. Jager, J. J. Chaillout, J. M. Leger, and S. Basrour, "Design and fabrication of a new system for vibration energy harvesting," in *Research in Microelectronics and Electronics, 2005 PhD*, 2005, pp. 225-228 vol.1.
[38] *AdaptativEnergy website*. Available: www.adaptativenergy.com
[39] *EnOcean website*. Available: www.enocean.com/en/
[40] *Enocean Alliance website*. Available: www.enocean-alliance.org/en/

[41] P. Miao, P. D. Mitcheson, A. S. Holmes, E. M. Yeatman, T. C. Green, and B. H. Stark, "Mems inertial power generators for biomedical applications," *Microsystem Technologies,* vol. 12, pp. 1079-1083, 2006.
[42] G. Z. Yang, "Body Sensor Networks," in *Body Sensor Networks*, ed: Springer, 2006, pp. 187-217.
[43] T. von Buren, "Body-Worn Inertial Electromagnetic Micro-Generators," SWISS FEDERAL INSTITUTE OF TECHNOLOGY ZURICH, 2006.
[44] Energy Harvesting Network [Online]. Available: http://eh-network.org/

CHAPTER 2

FUNDAMENTAL THEORY AND MODELING

This chapter presents the working principles of the vibration-driven energy harvesting (VEH) concept and the mathematical development that allows obtaining the electromechanical behavior of this type of devices. The three available transduction methods to convert mechanical energy into electricity are briefly introduced here. Deeper theoretical models based on the piezoelectric and electrostatic transductions have been developed in this chapter too.

2.1 Vibration-based Energy Scavenging

The concept of energy harvesting and the different ways to convert energy coming from ambient sources has been already introduced in the last chapter. Everything around us is moving. That is the reason why mechanical energy is virtually available everywhere and all the time. Therefore, one of the most promising energy sources present in our environment are due to motion. This thesis has been focused on a specific type of motion: vibrations.

2.1.1 Motion equation

The aim of a vibration-driven energy harvester (VEH) is to convert the mechanical energy from environmental vibrations to electrical energy which can be used to power electronic circuits. As it is shown in Figure 2.1, it is partly needed the stored energy to control the transduction mechanism and the electronics to manage the extracted power.

Therefore, the typical diagram of a vibration-driven energy harvester is an inertial frame which is excited by an external acceleration and coupled to a mass through a linear spring with a specific stiffness. Moreover, there is a transduction force actuating against the movement that will be responsible for the energy harvesting process.

Figure 2.1 shows the mechanical model of an energy scavenging system, with a movable element which is designed to get in resonance with an external vibration, increasing the mechanical energy of the system. This energy is converted into electrical energy by means of a transduction method, and it is subsequently stored.

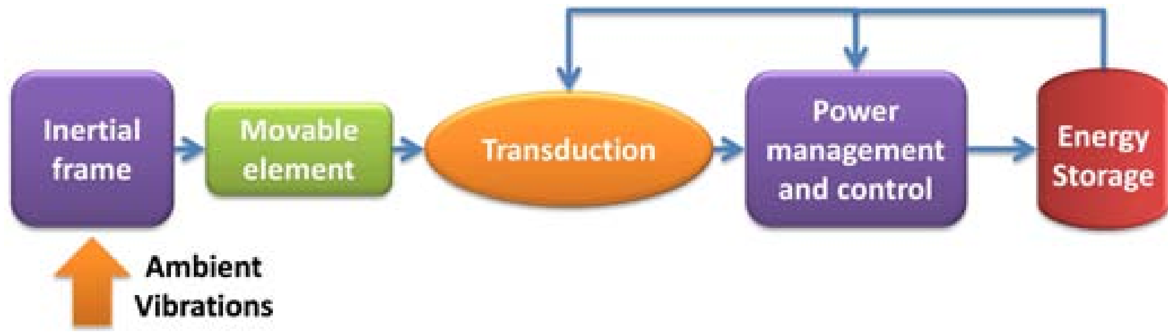

Figure 2.1. Block diagram of an energy scavenging system with active transduction control.

In Figure 2.2, it can be seen all the forces that act over the mass, *m*. The motion equation of this system is:

$$m\ddot{r} = f_{trans} + f_{damp} + f_{mec} = m(\ddot{e} + \ddot{z}), \tag{2.1}$$

where f_{mec} represents the mechanical force due to the spring, f_{trans} is the transduction force and f_{damp} is damping force. The real position of the mass, *r*, is the position of the frame, *e*, in addition to the relative position of the mass with respect to the frame, *z*.

$$r(t) = e(t) + z(t). \tag{2.2}$$

The ambient vibrations can be modeled by a harmonic acceleration of frequency, ω, and amplitude, A_{acc}:

$$\ddot{e}(t) = A_{acc}\cos(\omega t). \tag{2.3}$$

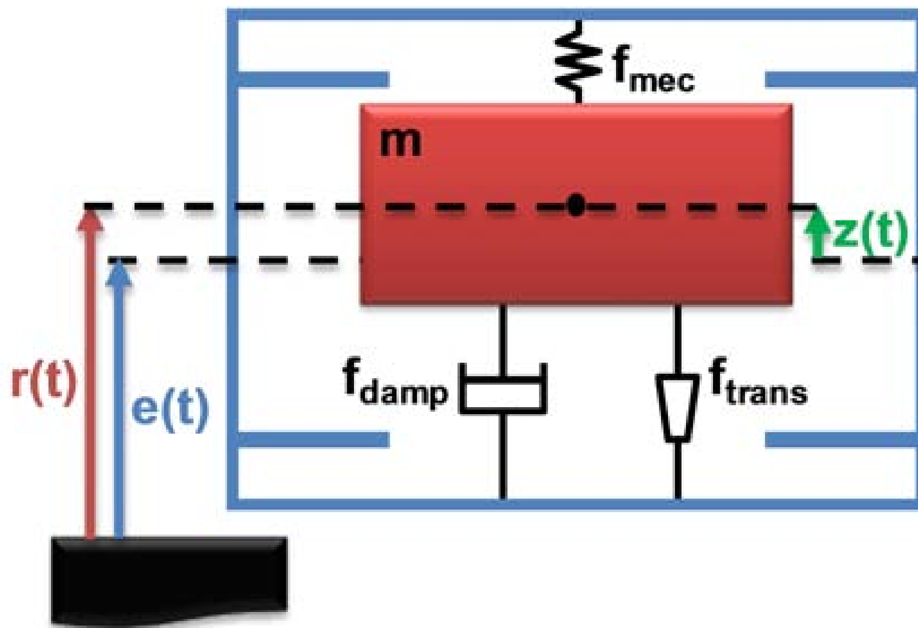

Figure 2.2. Model of a generic vibration-based energy scavenger.

➢ Damping Force

The damping force is the force that appears against the movement of the mass due to energy lost mechanisms. The typical damping force in a harmonic movement system is:

$$f_{damp} = -b\dot{z} = -2m\beta\dot{z}, \tag{2.4}$$

where *b* is the damping coefficient and β is the damping factor [1]. The quality factor is the ratio between the total energy stored in the system and the energy lost per cycle:

$$Q_f = 2\pi \frac{U_{total}}{\Delta U_{lost}}. \tag{2.5}$$

The damping factor is related with the quality factor and the resonant frequency ω_R by:

$$Q_f = \frac{\omega_R}{2\beta} = \frac{m\omega_R}{b}. \tag{2.6}$$

Thus the damping coefficient, *b*, can be estimated, by using a typical quality factor for MEMS in air, around 10^2.

Damping is one of the most important factors to take into account on the performance of MEMS structures. It relay in the energy loss mechanisms that appear during the structure operation, such as air damping, clamping loss through the anchors, surface losses, material losses and thermoelastic dissipation (TED). These mechanisms can be included in a global mechanical damping. Another important contribution is the electrical damping. It is due to the energy harvesting process and related to the conversion of kinetic energy of the moving mass into electricity. Moreover, it can be estimated as the power consumed in the resistive load. The power consumed in the mechanical domain is equal to the removed from the mechanical system.

Other authors have used analytical expressions to calculate the damping force by means of fluidic forces between the surfaces of the elements and the air [2], but these damping can be less important than other effects such as acoustic anchor losses, thermo-elastic damping and the internal losses [3]. In the cases presented in this thesis, a quality factor around 100 for a MEMS structure resonating at hundreds of Hz in air was demonstrated during the characterization of the developed systems, as it will be shown in the correspondent sections. This quality factor was calculated from frequency response measurements of the fabricated prototype, which will be presented in the following chapter, in accordance with the equation:

$$Q_f = \frac{f_R}{BW_{-3dB}}, \tag{2.7}$$

where f_R is the resonant frequency and BW_{-3dB} is the bandwidth of the frequency response curve, calculated as the interval between the frequencies before and after the resonant peak that corresponds with a magnitude equal to the peak magnitude minus 3dB.

This force represents an energy lost from the system. Therefore, it will limit the final power that the system is able to extract, and it is important to reduce these losses as much as possible. In order to avoid the damping due to the friction with the air molecules, a vacuum package can be used [4]. A novel vacuum wafer-level packaging for MEMS devices was developed during a short stay that the author did in the first year of his PhD. The fabrication

process was carried at Technical University of Denmark. Although the details of the procedure are out of the scope of this thesis, more exhaustive information can be found in [5].

➢ Mechanical Force

The mechanical force can be modeled by an elastic force resulting from a suspension which is built to hold the mass and allow its movement in a specific direction. It can be linearly approximated to:

$$f_{mec}(z) = -kz(t), \tag{2.8}$$

where k is the effective stiffness of the suspension.

The linear dependence of this force with the displacement, also called Hooke's law, can be used for a wide number of spring models such as cantilevers, bridges, serpentines, helical springs, etc. However, the spring stops obeying this law for large amplitudes, when the spring starts showing a nonlinear behavior. For energy harvesting purposes, the condition of small vibration amplitude is normally fulfilled. However, some authors take advantage of non-linear springs to obtain a wider bandwidth where the system can extract energy [6-8]. This approach is especially useful when there is not a well-defined or stable harmonic in the vibration acceleration spectrum or it is a noise [9].

➢ Transduction Force

This force, f_{trans}, is extremely important for the behavior of the system and it is the responsible to convert part of the system mechanical energy into useful electrical energy. Its expression highly depends on the type of transduction and the nature of the dominant physical effect. The most widely used methods for a mechanical-electrical conversion are the electromagnetic, piezoelectric and capacitive. They will receive a special attention and models for the last two cases will be described in next sections.

Therefore, (2.1) can be rewritten as:

$$m\ddot{z}(t) + b\dot{z}(t) + kz(t) - f_{trans} = -mA_{acc}\cos(\omega t), \tag{2.9}$$

where f_{trans} is the above-mentioned force due to the transduction, ω and A_{acc} are the frequency and the acceleration amplitude of the ambient vibrations respectively.

The importance of the mass value is clear, it is essential to use the largest available mass in order to amplify the work that the external acceleration will do to increase the energy of the system. Although the transduction force, which is the force that will actually carry out the work to be stored, must be coupled correctly with the inertial force.

Normally, the transduction force could be approximated to a damping which is added to the mechanical damping, thus the mechanical system can be studied like a typical damped spring-mass system. Therefore:

$$\omega_0 = \sqrt{\frac{k}{m}} \tag{2.10}$$

where ω_0 is the natural resonant frequency of the undamped structure.

For typical quality factors the resonant frequency of the damped system, ω_R, is almost identical to ω_0:

$$\omega_R = \sqrt{\omega_0^2 - 2\beta^2} = \omega_0^2 \sqrt{1 - \frac{1}{2Q^2}} \tag{2.11}$$

Thus, it can be obtained the next expression from (2.9):

$$\ddot{z}(t) + 2\beta \dot{z}(t) + \omega^2 z(t) - \frac{f_{trans}}{m} = -A_{acc} \cos(\omega t) \tag{2.12}$$

In that way, the movement equation is defined only by the vibration features, the mass, the damping factor and the transduction force, which has a crucial impact on the system dynamics. Although the correct procedure is to solve the complete motion equation, as a first approach, the transduction force could be approximated to an electrostatic damping.

2.1.2 Transduction methods overview

The transduction mechanism transforms the mechanical energy that moves the inertial mass into electrical energy that is accumulated in a storage capacitor. There are three transduction mechanisms commonly used to convert the mechanical energy into electricity: electromagnetic or inductive, electrostatic or capacitive and piezoelectric. In this section, a brief explanation about the fundamental principles of every method, as well as a comparison among these transductions methods will be presented. Depending on the transduction mechanism chosen and the conversion cycle used, the transduction force included in (2.12) will have a different expression. In following sections a special focus will be done for the piezoelectric and capacitive transductions because they are used in this thesis work to fabricate the energy scavenging devices.

2.1.2.1 Electromagnetic or inductive transduction

This conversion is based on the movement of a metal, typically a coil that plays the role of inductance in a magnetic field. This field is usually created by a permanent magnet placed in the system. In Figure 2.3 is shown a typical inductive generator that was presented in [10]. The device is formed by a mass connected to a rigid housing through a spring. As the housing is vibrated, the mass moves relative to the housing and the energy is stored in the mass-spring system. On the other hand, there is a wire coil attached to the mass, and it moves through the field generated by the permanent magnet as the mass vibrates.

The voltage on the coil, ε, also called induced electromagnetic force, can be calculated from the Faraday's Law given by

$$\varepsilon = -\frac{d\Phi_B}{dt} \tag{2.13}$$

where Φ_B is the magnetic flux.

In the simple case of a perpendicular magnetic field with a wire coil moving inside of it [2], the maximum open circuit voltage across that coil is

$$V_{OC} = NBl\frac{dy}{dt} \tag{2.14}$$

where N is the number of turns of the coil, B is the strength of the magnetic field, l is the length of one coil and y is the distance that the coil moves through the magnetic field

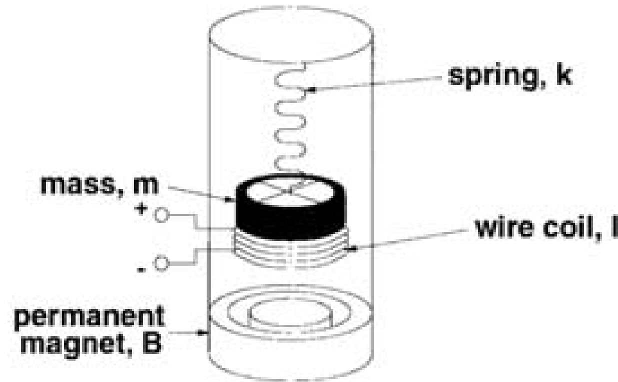

Figure 2.3. Schematic of an electromagnetic energy harvester [10].

There are several advantages of using this transducer. First, there is no need to use an initial voltage source to get the process of electromagnetic conversion started. Second, the parts of these devices do not have to get in contact during its operation, thus the mechanical damping is reduced in this type of converters. In contrast, the need of having a coil and a magnet introduces a high difficulty on the fabrication process, and makes particularly hard to integrate this kind of devices.

2.1.2.2 Electrostatic or capacitive transduction

The typical device used for this kind of transducer is a variable capacitor which changes its capacitance value due to a relative displacement between its plates. A capacitor is formed by two metallic plates, electrically independent, separated by a dielectric, so if a voltage source is connected between them, a charge accumulation will take place. In fact, these charges will be stored in the capacitor if the voltage source is removed. The relationship between charge, Q, voltage, V, and capacitance, C, is given by

$$Q = CV \tag{2.15}$$

Thus the energy stored in a capacitor can be expressed as

$$U = \frac{1}{2}QV = \frac{1}{2}CV^2 = \frac{1}{2}\frac{Q^2}{C}. \tag{2.16}$$

From this expression, it can be observed that the internal energy of the capacitor, U, can be increased if there is a change of the capacitance even if the charge or the voltage keep constant.

The electrostatic force as a function of the position is given by

$$F_{elec} = -\left(\frac{\partial U}{\partial x}\right). \tag{2.17}$$

Therefore, this transduction force will take part in the dynamic of the whole system as described by (2.12).

- **Constant-charge case**

A parallel-plate capacitor, storing a charge Q, is disconnected from its battery, and the plate separation is increased due to an external force that moves one plate while the other is kept static. With the additional plate separation, the final stored energy has increased [11]. This energy increase is due to the external agent that made a positive work which is directly converted to electrostatic energy into the capacitor. Therefore, the external force is acting against the electrostatic force given by (2.17), in order to separate the capacitor plates. Ideally, the capacitor should be completely discharged before their plates start approaching, in order to avoid the decrease of its internal energy. A more detailed explanation of this case will be included in section 2.2.

- **Constant-voltage case**

If the same cycle is repeated but keeping the capacitor connected to a battery while the plate separation is increased, the capacitor energy decreases [11]. That is due to charge reduction in the capacitor. However, the external agent is doing a positive work to separate the capacitor plates. To account for the energy discrepancy, the interaction capacitor-battery has to be studied. As the plates are separated, the decrease in capacitance needs a partial discharging of the capacitor through the battery. The released charge goes through the battery in the opposite direction. If it is a rechargeable battery, the electricity is stored inside as chemical energy. Otherwise, the generated power is dissipated as heat by the internal resistance of the battery. The battery has to be disconnected from the capacitor, when the plates are getting closer. Otherwise, the battery will be discharged to approach the parallel plates.

2.1.2.3 Piezoelectric transduction

Piezoelectricity is a property that is exhibited by some materials, called piezoelectric materials. The word piezoelectricity means electricity resulting from pressure. It is derived from the Greek *piezo* or *piezein* (*πιέζειν*), which means to squeeze or press, and *electric* or *electron* (*ήλεκτρον*), which stands for amber, an ancient source of electric charge.

The piezoelectric effect occurs when the charge balance within the crystal lattice of a material is disturbed. When there is no applied stress on the material, the positive and negative charges are evenly distributed so there is no potential difference. Basically, when a piezoelectric material is mechanically strained, the lattice is changed slightly and the charge imbalance creates a potential difference (Figure 2.4), often as high as several thousand volts. If two metallic electrodes are placed at every side of the piezoelectric material and a load resistor is connected, the created voltage difference can displace the movable electric charges from the wire through the resistor. However, the electric current generated across the load is particularly low.

The piezoelectric effect is understood as the linear electromechanical interaction between the mechanical and the electrical state in crystalline materials with no inversion symmetry. The piezoelectric effect is a reversible process in that materials exhibiting the direct piezoelectric effect (the internal generation of electrical charge resulting from an applied

mechanical force) also exhibit the reverse piezoelectric effect (the internal generation of a mechanical force resulting from an applied electrical field).

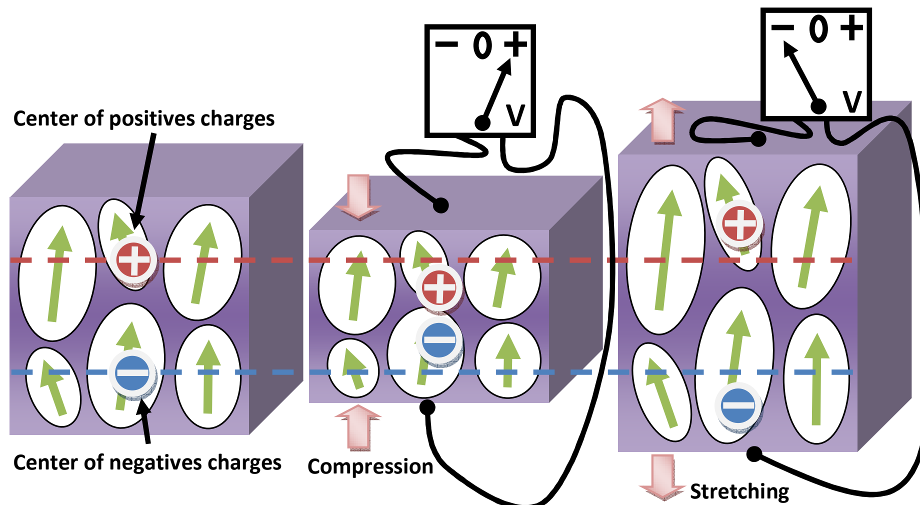

Figure 2.4. Piezoelectric effect

The first demonstration of the direct piezoelectric effect was in 1880 by the brothers Pierre Curie and Jacques Curie. They predict and demonstrated the direct effect using quartz and Rochelle salt. The Curies, however, did not predict the converse piezoelectric effect. The converse effect was mathematically deduced from fundamental thermodynamic principles by Gabriel Lippmann in 1881. The Curies immediately confirmed the existence of the converse effect, and noted that both effects usually coexist in a piezoelectric material.

For the next few decades, piezoelectricity remained something of a laboratory curiosity. More work was done to explore and define the crystal structures that exhibited piezoelectricity. This culminated in 1910 with the publication of Woldemar Voigt [12], which described the 20 natural crystal classes capable of piezoelectricity, and rigorously defined the piezoelectric constants using tensor analysis.

The first practical application for piezoelectric devices was sonar, first developed during World War I. In France in 1917, Paul Langevin and his coworkers developed an ultrasonic submarine detector. The detector consisted of a transducer, made of thin quartz crystals carefully glued between two steel plates, and a hydrophone to detect the returned echo. By emitting a high-frequency chirp from the transducer, and measuring the amount of time it takes to hear an echo from the sound waves bouncing off an object, one can calculate the distance to that object.

Piezoelectricity is found in useful applications such as the production and detection of sound, generation of high voltages, electronic frequency generation, microbalances, and ultrafine focusing of optical assemblies. It is also the basis of a number of scientific instrumental techniques with atomic resolution, the scanning probe microscopes such as STM, AFM, MTA, SNOM, etc.

The use of piezoelectricity in sonar, and the success of that project, created intense development interest in piezoelectric devices. Over the next few decades, new piezoelectric materials and new applications for those materials were explored and developed.

Among the most common types of piezoelectric materials, it can be found Lead Zirconate/Titanates (PZTs), which are solid solutions of lead zirconate and lead titanate. These manufactured ceramics have a much important piezoelectric behavior than the material found in nature. In order to manufacture these components, multiple steps have to be carried out. The first step involves the mixture of all the raw materials at 800/1000 ºC, a perovskite powder is formed and mixed with a binding agent. When cooled at a desired shape, the PZT unit cells (Figure 2.5) take on a tetragonal structure with a mechanical and electrical asymmetry [13].

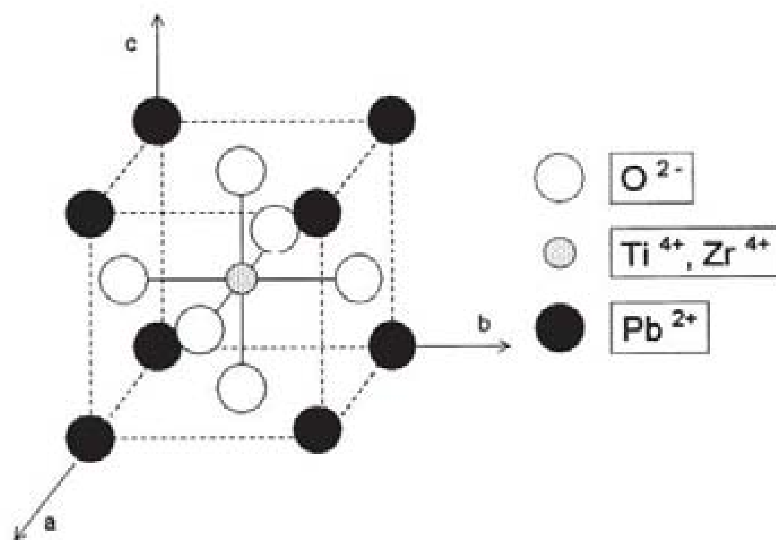

Figure 2.5. Typical PZT unit cell [13].

The process called poling is necessary for this kind of ceramic materials to take on piezoelectric properties. Before poling, all the crystals within the material are randomly oriented and it does not present piezoelectric properties. Poling consists in heating the material over the Curie temperature that allows the molecules to move more freely. In that point, a large electric field is applied causing the crystals inside the material to align themselves in the same direction. This effect is permanent and continues after eliminating the electric field and the material goes back to ambient temperature.

Poling process is only relevant for polycrystalline ferroelectric materials. A piezoelectric but not ferroelectric polycrystalline material, e.g. quartz or AlN, with randomly oriented grains cannot be poled. It can only exhibit macroscopic piezoelectric properties if the growth orientation of the different grains is well controlled. Strong efforts have been done in order to integrate piezoelectric materials in the form of thick or thin films into silicon wafer base batch processes. Non-ferroelectric and piezoelectric materials such as AlN or ZnO are relatively easy to integrate into a conventional IC process flow. In contrast, PZT type materials which require high temperature processing find strong difficulties to be integrated with standard silicon technology.

2.2 Model of an electrostatic converter

The electrostatic transduction is based on the increase of the internal energy stored into a variable capacitor by means of the work made by an external force against the electrostatic force to take the capacitor plates apart. For a VEH, the external force is produce by the effect of an alternate acceleration, coming from an ambient vibration, over an inertial mass. In fact, the relative plate motion is increased by the resonance effect of the system.

Although, all kind of variable capacitors can be used, it is considered the simplest case of a parallel plate capacitor, in order to explain the fundamental principle of its operation. We suppose that one capacitor plate is fixed and the other one is moving with a harmonic motion. In that way, the capacitor is oscillating between a minimum and maximum capacitance positions (i.e. when the distance between plates is maximum and minimum respectively).

The internal energy of a capacitor is given by:

$$U = \frac{1}{2}QV = \frac{1}{2}CV^2 = \frac{1}{2}\frac{Q^2}{C}. \tag{2.18}$$

where Q, V and C are the charge, voltage and capacitance respectively. It can be appreciated that a change in the capacitance is translated into a change in the stored energy. Therefore, an increase or decrease of the internal energy can be produced even if the voltage and charge of the capacitor are held constant.

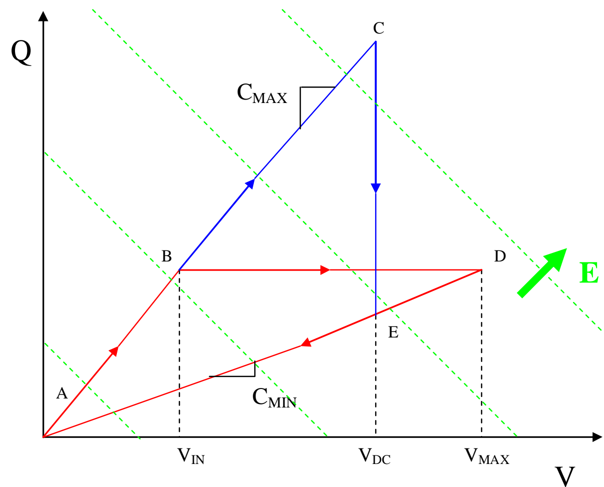

Figure 2.6. Q-V graph with the typical operation modes of an electrostatic converter.

In order to increase the internal capacitor energy, two ideal modes of operation can be typically identified and they are shown in Figure 2.6: the constant-charge (ABDA) and the constant-voltage (ACEA) cycles. For constant-charge cycle, when the capacitor goes from the maximum to minimum capacitance positions:

$$Q = C_{max}V_{in} = C_{min}V_{max}. \tag{2.19}$$

And the electrostatic force as a function of the position is given by:

$$F = -\left(\frac{\partial U}{\partial x}\right). \tag{2.20}$$

Therefore, when the capacitance of the energy scavenger changes from the maximum value, C_{max}, with a voltage V_{in} to the minimum value, C_{min}, since the charge must held constant, the voltage increases to V_{max}:

$$V_{\max} = \frac{C_{\max}}{C_{\min}} V_{in}. \tag{2.21}$$

Also the energy increases in this transition, by an amount which is given by:

$$\Delta U_{Q=cte} = U\left(C_{\min}\right) - U\left(C_{\max}\right) \tag{2.22}$$

and operating, it is obtained,

$$\Delta U_{Q=cte} = \frac{1}{2} V_{in}^2 \frac{C_{\max}}{C_{\min}} \left(C_{\max} - C_{\min}\right) = \frac{1}{2} V_{in}^2 r_C \Delta C, \tag{2.23}$$

where r_c and ΔC are the ratio and difference between the maximum and minimum capacitance values.

For a voltage constant cycle, the expression for the energy gain per transition is:

$$\Delta U_{V=cte} = \frac{1}{2}\left(C_{\max} - C_{\min}\right) V_{DC}^2 = \frac{1}{2} \Delta C V_{in}^2, \tag{2.24}$$

Then, the external inertial force, which works against the electrostatic force, drives the capacitor to its minimum capacitance position, so that energy from the mechanical work done by the external force is harvested [14].

The basic circuit to implement the charge-discharge cycle is shown in Figure 2.7. There, it can be seen the simplest circuit to model the generator, where C_V is the vibration-driven variable capacitor, V_{in} is an ideal voltage source that provides the initial charges to the variable capacitor, C_{sto} is a capacitor to store the energy extracted and finally two ideal switches to synchronize the cycle stages. We have to highlight the fact that the model of Figure 2.7 is only a block diagram that allows us to cover the different parts of the complete ideal operation cycle.

In order to implement the initial voltage, there are several approaches to be used: a capacitor which is precharged before using the device by first time, an electret which has quasi-permanent electric charges [15-17] or, in the case of supplying only a critical subsystem with the scavenger, it could use the main system voltage source as initial voltage. When the scavenger starts working, it will be able to use the C_{sto} like initial charge source. Although circuitry design is out of the scope of this thesis, there are a variety of research works about different approaches to create power management circuitry for energy harvesters [18-20]. The switches, which are typically electronically controlled, could be fabricated using MEMS technology. The use of mechanically actuated switches [21, 22] can avoid this electronic circuitry and therefore, its power consumption.

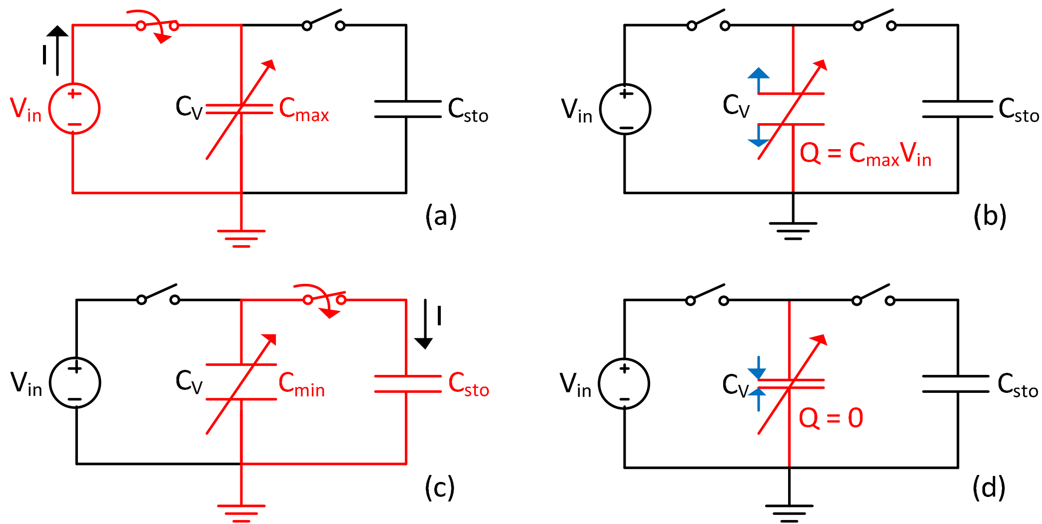

Figure 2.7. Basic conversion circuit for an electrostatic converter and different stages of the charge-constant cycle: initial charge of the variable capacitor at maximum capacitance value (a), separation of the capacitor plates (b), transfer of the charge within the variable capacitor to the storage capacitor (c) and approaching of the capacitor plates to get the initial cycle position of maximum capacitance (d).

The main problem to process the output power for these constant-charge electrostatic microgenerators is that they work with reduced amounts of charge at high voltage. Moreover, the variable MEMS capacitance has normally a parasitic capacitance in parallel which is not negligible in the minimum capacitance position and has a direct effect over the extracted power. Therefore, we must keep it as low as the technology allows us.

When an electrostatic transduction configuration and a defined cycle are kept constant, we could calculate the maximum energy that the device is able to extract if the movable part goes from the position of maximum capacitance up to the position for minimum capacitance, but it only would happen if the mechanical part was perfectly coupled and the external force, due to the environmental vibration, was enough to reach these positions.

Since the electric force is dependent on the capacitance internal energy, the value of the increased energy and the electrical effect in the movement are strongly coupled. Hence, it is necessary to know the dynamic behavior of the movable part when the whole system is working, whereupon the complete movement equation must be solved to know the real energy amount that is being extracted per cycle and the power that the system is able to provide. Then, a coupled electromechanical simulation together with consideration of the circuitry effect is necessary to report real values of expected harvested power.

2.2.1 Comb-drive capacitor

In order to obtain a capacitance value as large as possible, a comb structure is proposed. This structure is well known as part of capacitive sensors and actuators. The aim of reaching a large capacitance is widely reported, and it will be explained in the following sections.

Figure 2.8 shows a comb drive, where the bottom electrode can move along the three directions of space and the top electrode is anchored. The plane XY is the substrate plane, t_f is the beam thickness, L_f and w_f are the finger length and width, d_f is the gap between fingers of the different drivers and L_p is the adjacent fingers overlapping length. All these parameters are defined by the layout and the design rules of the technology used to fabricate this device.

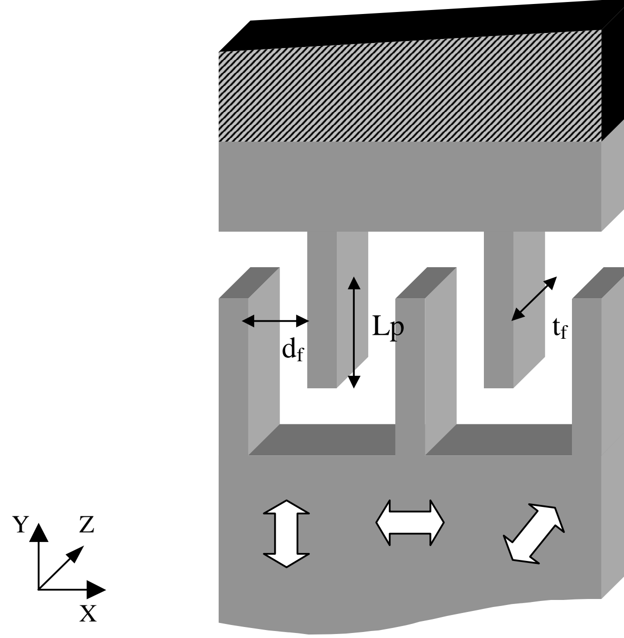

Figure 2.8. Comb-drive with a mobile part (bottom) and the static part (top). The mobile part can move along the three directions of the space.

This structure of transduction keeps moving the movable part along the three directions. Depending on this direction, the transduction is called:

- X direction: In-plane gap closing (IPGC) transduction.
- Y direction: In-plane overlap varying (IPOV) transduction.
- Z direction: Out-of-plane gap closing (OPGC) transduction.

For each transduction, there is an expression for the capacitance, the electric force and the energy gain per cycle that depends on the displacement in the corresponding direction of the movable part. Considering the parallel plate capacitance approximation between the parallel faces of the beams and avoiding the fringing field effects, it is calculated the capacitance between the movable and static parts. With the calculated capacitance value, it can be obtained the electric force magnitude, f_e, deriving of the expression of the energy stored in the capacitor, U. These expressions depend on the moved distance, z.

A. IPGC comb-driver transduction:

$$C(z) = N_g \varepsilon L_p t_f \frac{d_f}{d_f^{\,2} - z^2} \tag{2.25}$$

$$U(z) = \frac{1}{2}\frac{Q^2}{C} = Q^2 \frac{d_f^{\,2} - z^2}{2N_g \varepsilon L_p t_f d_f} \tag{2.26}$$

$$f_e(z) = -\left(\frac{\partial U}{\partial z}\right) = \frac{Q^2 z}{N_g \varepsilon L_p t_f d_f} \tag{2.27}$$

B. IPOV comb-driver transduction:

$$C(z) = \frac{N_g \varepsilon t_f \left(L_p + z\right)}{d_f} \tag{2.28}$$

$$U(z) = \frac{1}{2}\frac{Q^2}{C} = Q^2 \frac{d_f}{2N_g \varepsilon t_f \left(L_p + z\right)} \tag{2.29}$$

$$f_e(z) = -\left(\frac{\partial U}{\partial z}\right) = \frac{Q^2 d_f}{2N_g \varepsilon t_f \left(L_p + z\right)^2} \tag{2.30}$$

C. OPGC comb-driver transduction:

$$C(z) = \frac{N_g \varepsilon L_p \left(t_f - |z|\right)}{d_f} \tag{2.31}$$

$$U(z) = \frac{1}{2}\frac{Q^2}{C} = Q^2 \frac{d_f}{2N_g \varepsilon L_p \left(t_f - |z|\right)} \tag{2.32}$$

$$f_e(z) = -\left(\frac{\partial U}{\partial z}\right) = \frac{-|z|}{z}\frac{Q^2 d_f}{N_g \varepsilon L_p \left(t_f - |z|\right)^2} \tag{2.33}$$

where Q is the initial constant charge inside the capacitor given by (2.19), N_g is the number of gaps between adjacent fingers of both driver. It is important to note that the electrostatic force is proportional to the relative displacement of the mass and, therefore, it acts like a mechanical spring that operates in the opposite direction to the mechanical force, i.e. f_e has opposite sign to f_{mec}.

We have to take into account that the electric force for this chosen transduction type is treated like a negative mechanical force because it has the same effect as a negative non-linear spring in the motion equation (2.9).

Finally, the power generated by the scavenger is the product of the extracted energy per capacitance cycle by the cycle numbers in a period, and by the frequency, f:

$$Power = n_{cycles} \Delta U_{cycle} f \tag{2.34}$$

In Table 2.1, a comparative between the different comb-driver transductions is shown. Moreover, taking into account some typical values that could define an arbitrary traditional energy scavenger, a estimation of the numeric values of the extracted power for each type of transduction has been calculated (see Figure 2.9), where V_{in} = 5 V, d_{stop} = 0.6 µm, t_f = 5.87 µm, w_f = 10 µm, d_f = 25 µm, f = 100 Hz, L_p = 80 µm, L_f = 100 µm, L_m = 2 mm, and therefore, N_g = 56. Note that d_{stop} is the minimum gap that two opposite fingers can be approached. This distance can be controlled with the pattern of several stoppers that limit the motion amplitude of the inertial mass.

From the results shown in Table 2.1, we can conclude that the most suitable transduction type seems to be the IPGC, because it can be obtained more power and, in addition, this transduction type improves the stability of the system against the other two types [23].

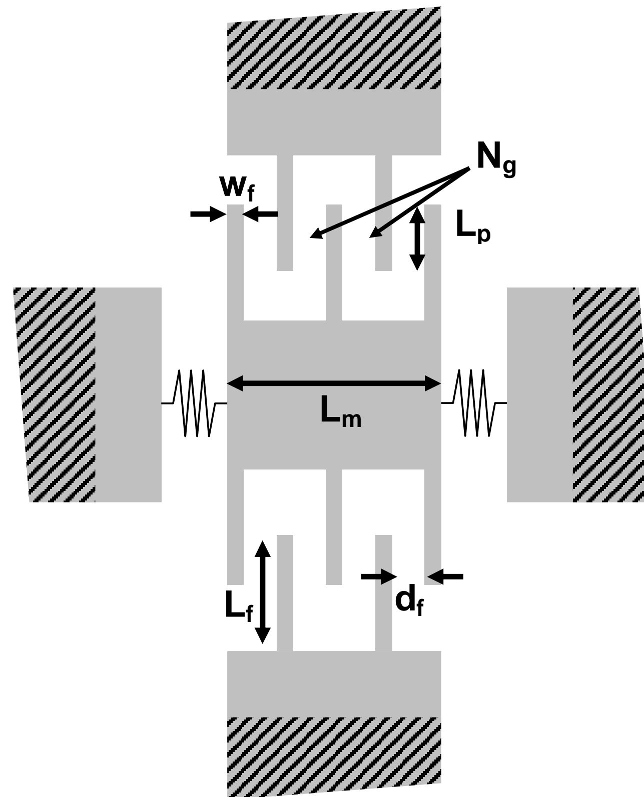

Figure 2.9. Most important dimensions of a typical energy scavenging device.

2.2.2 MATLAB model of the electrostatic converter

By using the expressions from Table 2.1, several MATLAB® code models have been developed to solve the motion equation coupled to the transduction operation and obtain the plots of capacitance versus time for these different transductions as shown in Figure 2.10. With these plots, we can know the number of cycles, from maximum to minimum capacitance value, inside each period of the relative sinusoidal displacement between both comb-driver electrodes.

2.2.2.1 Typical IPGC electrostatic converter at constant-charge cycle.

In this section, it is considered a typical vibration energy harvester, as presented in Figure 2.9, with similar parameters to the mm-scale electrostatic converters that can be found in the literature. Some numerical simulations of this arbitrary device have been performed in order to estimate its mechanical behavior. The design parameters utilized for this device are shown in Table 2.2 and they have been selected accomplishing the features of the technology MEMSOI from Tronics [24] and some typical dimensions for an energy-harvesting device.

Table 2.1. Comparative among the different comb-driver transductions

	IN-PLANE GAP CLOSING (IPGC)	IN-PLANE OVERLAP VARYING (IPOV)	OUT-PLANE OVERLAP VARYING (OPOV)
C_{max}	$\frac{N_g \varepsilon L_p t_f d_f}{2d_f d_{stop} - d_{stop}^2}$	$\frac{N_g \varepsilon \left(L_f - d_{stop}\right) t_f}{d_f}$	$\frac{N_g \varepsilon L_p t_f}{d_f}$
C_{min}	$\frac{N_g \varepsilon L_p t_f}{d_f}$	$\frac{N_g \varepsilon d_{stop} t_f}{d_f}$	$\frac{N_g \varepsilon L_p t_{stop}}{d_f}$
ΔC	$N_g \varepsilon L_p t_f \left[\frac{d_f}{2d_f d_{stop} - d_{stop}^2} - \frac{1}{d_f}\right]$	$\frac{N_g \varepsilon \left(L_f - 2d_{stop}\right) t_f}{d_f}$	$\frac{N_g \varepsilon L_p \left(t_f - t_{stop}\right)}{d_f}$
r_C	$\frac{d_f^2}{2d_f d_{stop} - d_{stop}^2}$	$\frac{L_f}{d_{stop}} - 1$	$\frac{t_f}{t_{stop}}$
ΔU_{cycle}	$N_g \varepsilon L_p t_f \left[\frac{d_f}{2d_f d_{stop} - d_{stop}^2} - \frac{1}{d_f}\right] \frac{d_f^2}{2d_f d_{stop} - d_{stop}^2}$	$\frac{N_g \varepsilon t_f V_{in}^2}{d_f}\left(L_f - 2d_{stop}\right)\left(\frac{L_f}{d_{stop}} - 1\right)$	$\frac{N_g \varepsilon L_p t_f V_{in}^2}{d_f t_{stop}}\left(t_f - t_{stop}\right)$
Power	$n_{cycles} f N_g \varepsilon L_p t_f \left[\frac{d_f}{2d_f d_{stop} - d_{stop}^2} - \frac{1}{d_f}\right] \frac{d_f^2}{2d_f d_{stop} - d_{stop}^2}$	$n_{cycles} f \frac{N_g \varepsilon t_f V_{in}^2}{d_f}\left(L_f - 2d_{stop}\right)\left(\frac{L_f}{d_{stop}} - 1\right)$	$n_{cycles} f \frac{N_g \varepsilon L_p t_f V_{in}^2}{d_f t_{stop}}\left(t_f - t_{stop}\right)$
	19.72 nW	**26.66 pW**	**408.84 pW**

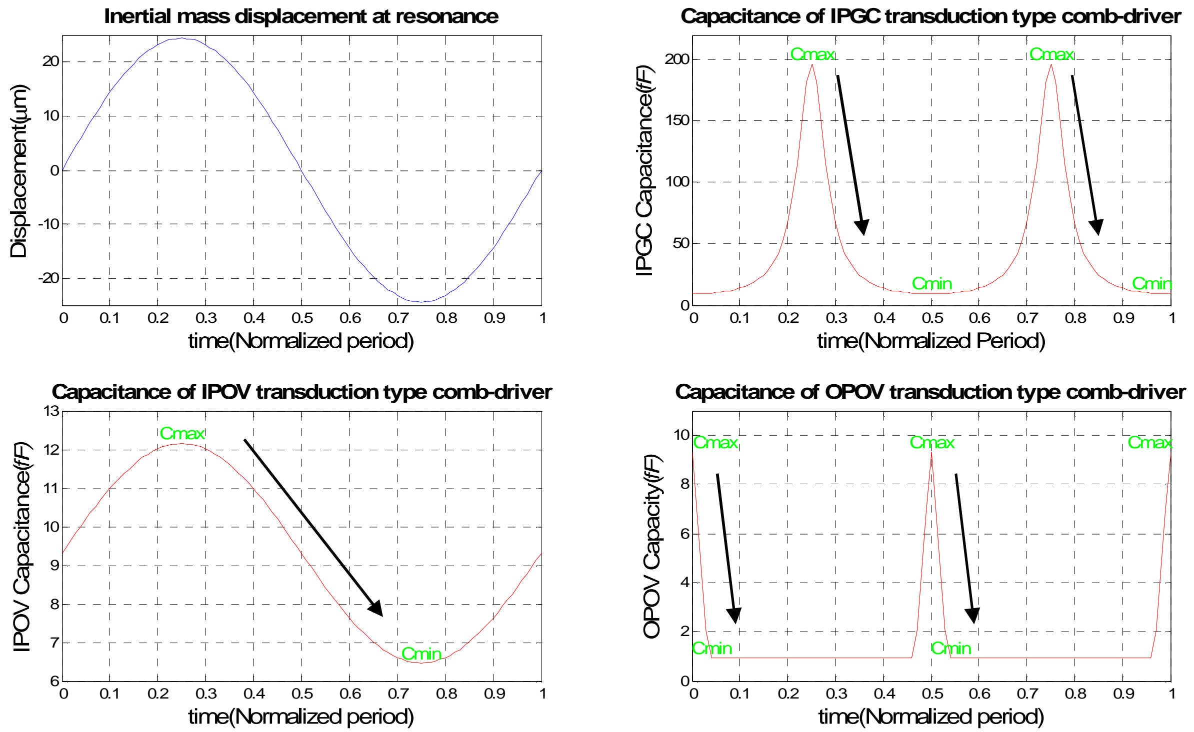

Figure 2.10. Comparative of single comb-driver capacitance values among different transductions for a sinusoidal displacement, and the arrows which indicate the energy increasing cycles.

The charge will be set to zero when the mass position crosses the x-axis, i.e. relative displacement equal to 0 and minimum capacitance position. These two steps are slightly far from the real operation of an energy harvester working together with a control and power management circuitries. First, the instantly charge and discharge of a capacitor is impossible because of the inherent parasitic resistance of the charge circuit, but because of the low system resonant frequency and the low capacitance value to be charged, it can be considered instantaneous as first approximation. On the other hand, the fact of completely extracting the charge of the vibration-driven variable capacitor (C_V) at zero position is performed to avoid that the electrostatic force acts against the motion when the system goes from minimum to maximum capacitance position, because if it is not completely removed, the transduction force works as a damping mechanism, decreasing the internal energy of C_V, instead of increasing it. Although in a real situation leaves a small amount of charge in the capacitor can be used to monitor the maximum and minimum capacitance position without affecting to the system dynamic. This operation mode leads to the maximum limit of extracted power that can be processed by this transducer performing a charge-constant cycle.

Figure 2.11 shows the relative amplitude of the inertial mass, i.e. the movable fingers respect to the fixed fingers and its velocity when the system is excited by a harmonic ambient vibration. As it can be observed, the amplitude reaches a stable value after 0.1 s, i.e. approximately 20 periods for a frequency of 200 Hz. That is due to the relative high expected quality factor of this device and it means a reproducible behavior during practically all the operation time.

Table 2.2. Parameters used for the MATLAB model of a vibration-driven electrostatic energy scavenger.

Parameters	Value	Units	Description
Lp	40	µm	Overlap between two adjacent parallel fingers
df	10	µm	Initial distance or gap between opposite fingers
Ng	150	µm	Number of gaps by comb-driver
tf	60	µm	Finger thickness
dstop	1	µm	Distance from stopper to finger contact
Qf	50	µm	Mechanical quality factor
fres	200	Hz	Frequency of resonance
area	10	mm³	Whole chip area
dens	2.5e3	Kg/m²	Substrate density (silicon)
m	12.75	mg	Scavenger mass
Vin	5	V	Initial voltage of input capacitor
Acc	0.8	m/s²	Input vibration acceleration magnitude

Taking into account that the maximum allowed traveling distance of the comb driver is 9 µm, i.e. d_f - d_{stop} from Table 2.2, and the movement amplitude at the steady state is 8.73 µm, we can say the simulation perfectly accomplishes the design requirement, without touching the physical stoppers placed to avoid the contact between two adjacent fingers of opposite comb-drivers.

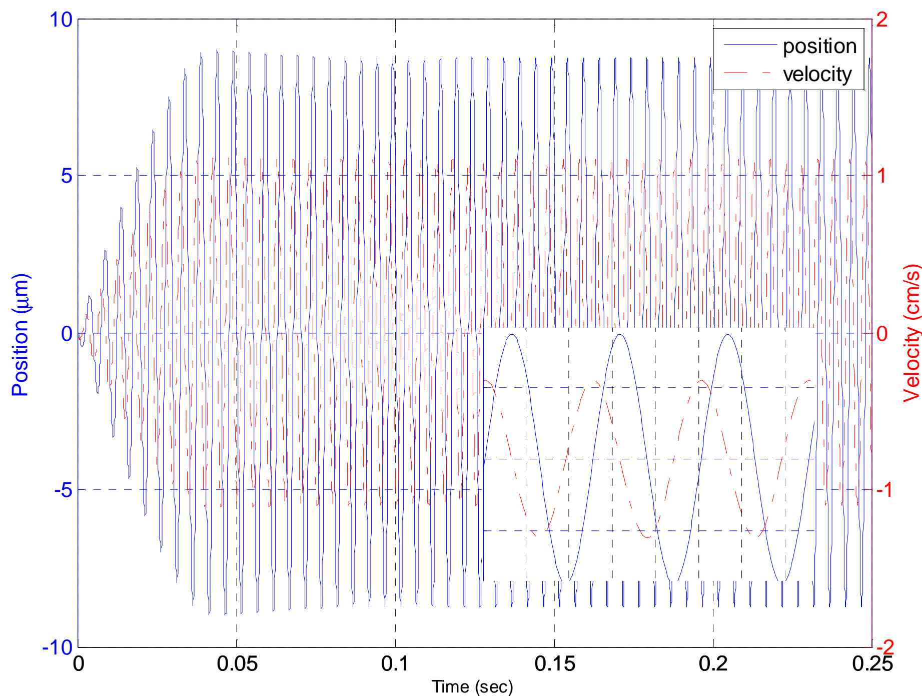

Figure 2.11. Relative position and velocity of the inertial mass of the energy scavenger. Inset: Detail of the steady state.

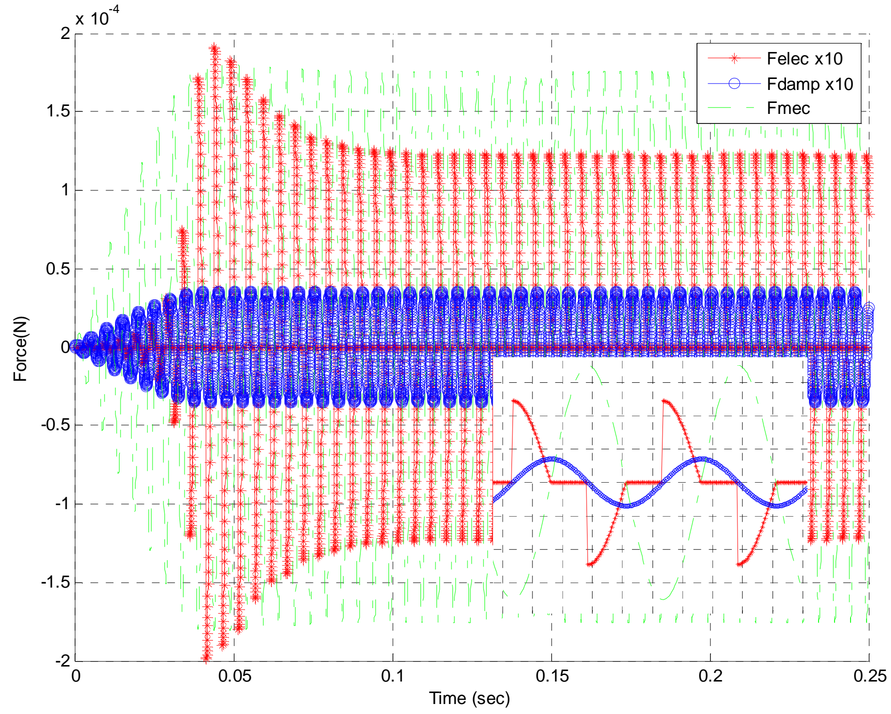

Figure 2.12. Graph of electrostatic, damping and mechanical force actuating on the system. Inset: Detail of the steady state.

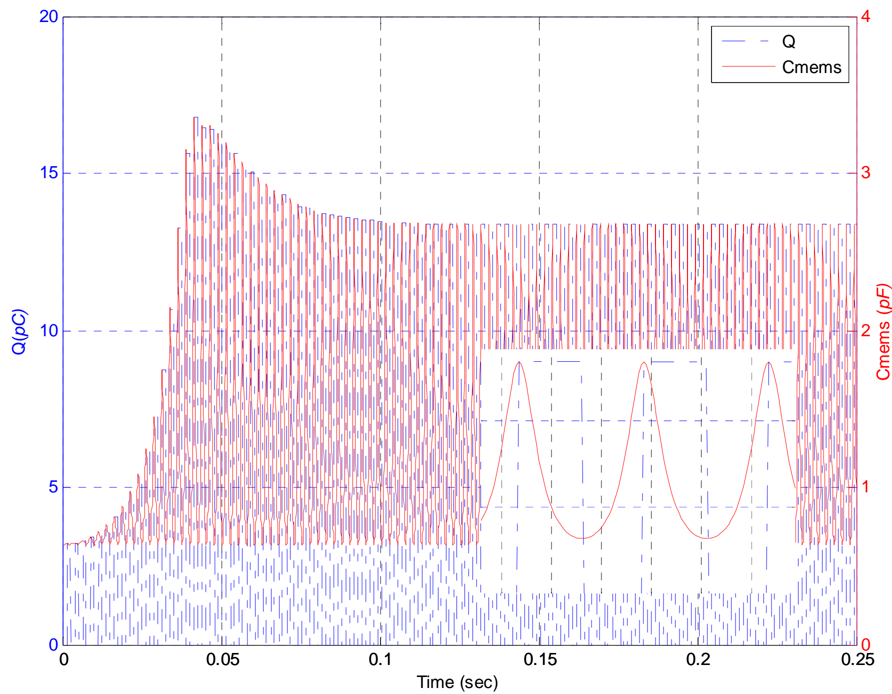

Figure 2.13. Graph of charge and capacitance values reached by the vibration-driven variable capacitor. Inset: Detail of the steady state.

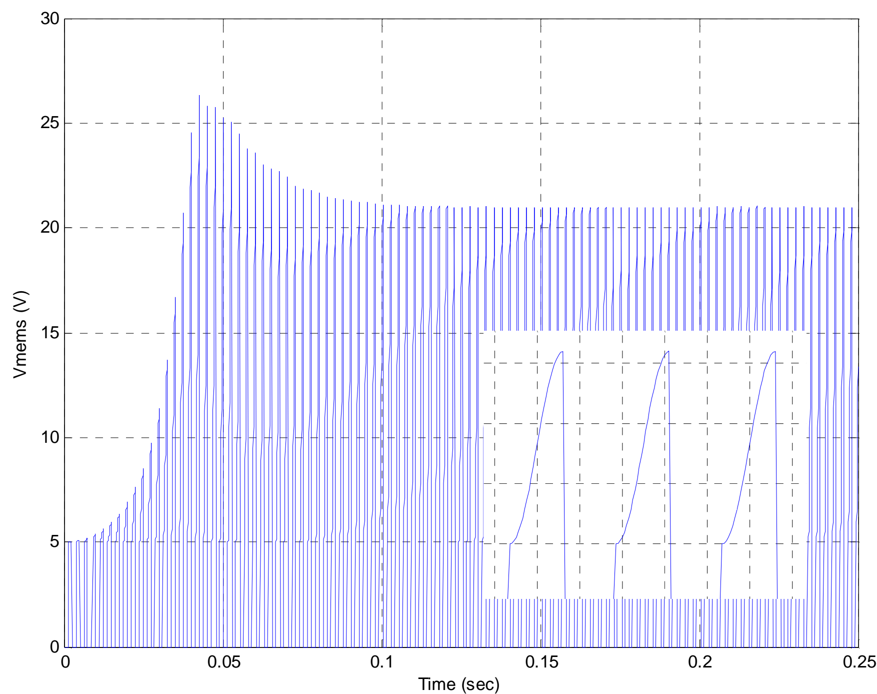

Figure 2.14. Voltage over the vibration-driven variable capacitor. Inset: Detail of the steady state.

In Figure 2.12, all the forces actuating over the inertial mass are represented, except the inertial force due to the mass motion. It can be seen the characteristic shape of the electrostatic force, which is activated only for the decreasing semicycles, for a constant-charge mode operation. Note that the damping and electrostatic force are one order of magnitude lower than the elastic force due to the spring. That allows a steady-state with constant amplitude and transducing energy from the system at the same time.

Figure 2.13 shows the charge within the capacitor and its capacitance value. It can be noted that the charge reaches the value $C_{max}V_{in}$ at maximum capacitance position and zero at minimum value. These two values are 2.7 pF and 0.6 pF for the maximum and minimum capacitance respectively. Using these quantities in (2.23) and (2.34), an ideal extracted power to be reached with this configuration of 17 µW can be obtained, which means an increase of 43 nJ every transition from C_{max} to C_{min}. Also from Figure 2.14, it can be appreciated that the voltage over the variable capacitor goes from the initial 5 V to 21 V during the maximum-to-minimum capacitance increase.

2.2.3 VERILOGA model of the electrostatic converter

This section introduces a model for an electrostatic converter that has been developed in the language VerilogA. The model has been used to simulate the operation of the same electrostatic converter that was described in the last section and simulated with a MATLAB code. A comparison between the results that provide both simulation approaches will be presented.

VerilogA is a standard language to model analog circuits, and it is considered as subset of the language VerilogAMS that is a single language covering both analog and digital design. Modeling with this language is a powerful way to solve mathematical expressions, such as time-dependent differential equations, and translate the solutions to voltage and current output signals of this model. The main advantage of this language is the direct integration of its models in the commercial software environment Virtuoso, from Cadence. Virtuoso platform contains tools for designing full-custom integrated circuits, used mainly for analog, mixed-signal, RF, standard-cell and memory designs. The SPICE-class circuit simulator included in Virtuoso is called Spectre. It provides the basic SPICE analyses and component models, and it can introduce behavioral modeling with the support of the VerilogA language.

When a model is created using VerilogA language in Cadence Virtuoso, it is treated as a regular electric component. The model in the electrical simulation tool is considered as a black box, where we can define an arbitrary electrical input and outputs or pins that will have a specific value of voltage and current for each moment. Also initial parameters can be defined before simulating the whole circuit by means of the regular properties menu.

The electromechanical model of the electrostatic converter is governed by the differential motion equation whose solution is the relative position of the mass attached to the movable capacitor electrode. When the energy scavenger has to be physically implemented, the co-design of an appropriate control and management circuit is mandatory, and the charge-discharge scheme of the scavenger capacitance will vary from the ideal cycles that have been presented above. Therefore a mixed electromechanical simulation of the whole system, transducer and circuitry, is essential to be able to design the whole system.

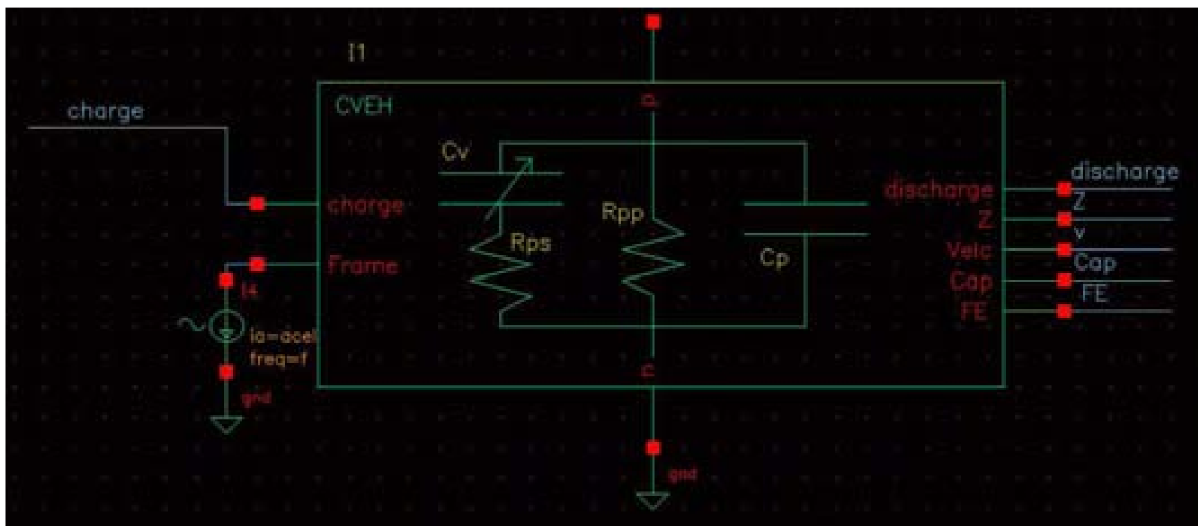

Figure 2.15. Symbol of the vibration-driven variable capacitor (VDVC) in Spectre simulator.

The modeled element, which is electrically passive, has the same behavior than a typical capacitor with the particularity of changing its total capacitance value when the element is mechanically excited.

The model symbol (Figure 2.15) has the same appearance than a typical CADENCE instance. But it has additional parameters corresponding to the configurable variables

included in the VerilogA code. In our case, we can externally set a list of 15 parameters that will determine the behavior of the system. In Table 2.3 are listed the description and default value of all the model editable parameters, that are an extended version of the values used in Table 2.2

The model is represented as a 2-port element, where the current between its ports is described by:

$$I_{pn} = I_{Cv} + I_{Rpp} + I_{Cp} = I_{Cv} + \frac{V_{pn}}{R_{pp}} + C_p \frac{d}{dt} V_{pn} \quad (2.35)$$

Where both the voltage between its terminals, V_{pn}, and the internal global capacitance of the energy harvester, C_v, are dependent of time. I_{Cv} can be calculated by numerically solving this equation system:

$$I_{Cv} = \frac{d}{dt}(C_V V_C) \quad (2.36)$$

$$V_C = V_{pn} - R_{ps} I_{Cv} \quad (2.37)$$

Therefore, in order to obtain the current through this branch, the following differential equation (2.38) together with (2.35) have to be numerically solved:

$$\frac{d}{dt}(C_v V_{pn}) - R_{ps} \frac{d}{dt}(C_v I_{Cv}) - I_{Cv} = 0 \quad (2.38)$$

The variable capacitance value is modeled for an in-plane gap closing transduction as (2.25), taking into account that there is a comb drive at each side of the inertial mass,

$$C_V(z) = 2 N_{cell} N_g \varepsilon L_p t_f \frac{d_f}{d_f^{\,2} - z^2} \quad (2.39)$$

The electrostatic force generated against the inertial movement is expressed as (2.27). This transduction force should be introduced into the motion equation (2.12) and this expression has to be solved at real time inside of the VerilogA module.

Table 2.3. Default configurable parameters of the model properties.

Parameters	Value	Units	Description
Lp	40	μm	Overlap between two adjacent parallel fingers
df	10	μm	Initial distance or gap between opposite fingers
Ng	150	μm	Number of gaps by comb-driver
Nc	2	μm	Number of comb drives by shuttle (typ. 2)
tf	60	μm	Finger's thickness
dstop	1	μm	Distance from stopper to finger contact
Qf	50	μm	Mechanical quality factor
fres	200	Hz	Frequency of resonance
M	12.75	mg	Scavenger's mass
Initialpos	0	μm	Initial position of the inertial mass
alpha	0		Fringing field factor
Cp	0	F	Parallel parasitic capacitance
Rps	10	Ω	Series parasitic resistance
Rpp	10	GΩ	Parallel parasitic resistance
zero_value	1e-6		Tolerance value for considering zero.

The element is able to provide two control signals to be used to know the instants of maximum and minimum capacitance. Also it can be found several outputs that can be used to monitor the capacitance value, the displacement and the velocity of the inertial mass. The external acceleration is applied to the element as a voltage signal through the pin called *frame*.

2.2.3.1 Ideal circuit implementation

Figure 2.16 shows a circuit formed by the VerilogA model as key element connected to an input capacitor, which has to be initially pre-charged and provides the initial voltage to the vibration-driven variable capacitor (C_V), and an output capacitor in order to collect the charge after the energy is increased. The connection is done through two ideal voltage-controlled switches modeled into VerilogA language. These switches are driven by two control signals generated by the pins of the model called *charge* and *discharge*. Each one produces a pulse when the maximum and minimum capacitance positions are reached respectively. These pins can be used for test purposes, but a method for detecting these exact moments has to be developed for obtaining a full-functional device. There are four additional monitoring signals called *Z*, *Velc*, *Cap* and *FE* that provide immediate values of position, velocity, capacitance and electrostatic force presented in the energy harvester respectively.

Also, it can be noticed a load resistor connected to the output capacitor that emulates the possible load circuit powered by this energy harvesting system. In order to model the parasitic resistance when charging and discharging C_V, two resistors have been included. Finally, an AC voltage source emulates the input ambient acceleration, taking into account that 1 V is considered as 1 m/s^2.

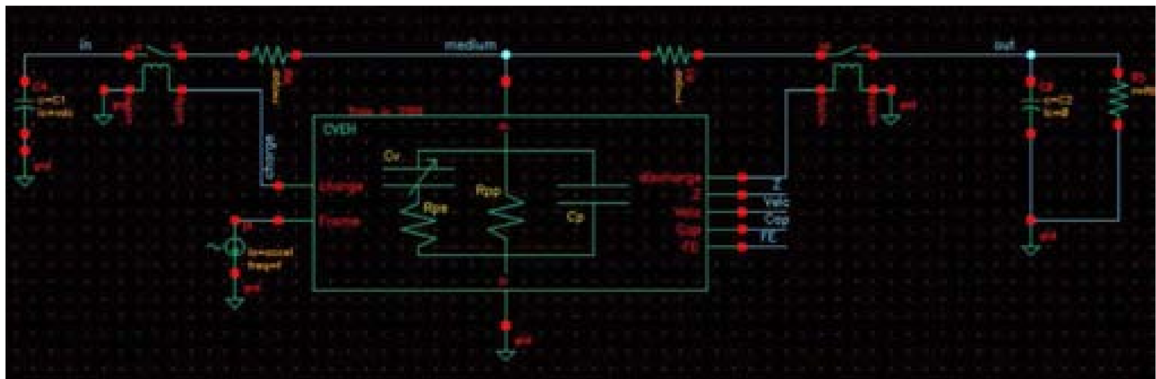

Figure 2.16. Schematic of VerilogA model in Spectre simulator.

This configuration is not a functional circuitry to extract the energy from the system, because there is a charge transfer from the initial capacitor to the output capacitor through C_V as long as the output capacitor do not reaches its maximum charge capacity. When the output capacitor is filled, its voltage will saturate to the maximum value. However, this configuration is useful to consider the suitable component values that maximize the extracted energy for each input acceleration and energy harvester configuration. The operation of this schematic allows an ideal operation similar to the Matlab model presented in the last section.

In Figure 2.17, it can be seen that the influence of the parallel resistance is imperative. When the resistance value drops below 1 GΩ, the output voltage goes down quickly. The reason is that the charge amount contained into the variable capacitor is minuscule, so any leakage mechanism is translate into a considerable capacitor discharge. In Figures 15-19 the amplitude, capacitance and voltage of the vibration-driven variable capacitance are shown in addition to the voltage over the output load capacitor. All these plots can be easly generated, demonstrating that this model can be a really powerful tool to simulte the real behaivor of the energy-scavenging transducer that accounts for the influenece and the effect of the power management circuitry.

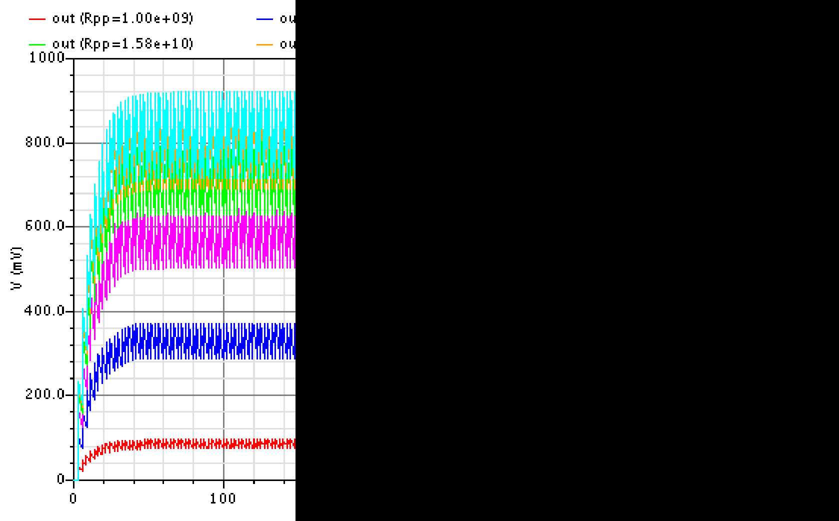

Figure 2.17. Voltage over the output capacitor for different parallel parasitic resistance.

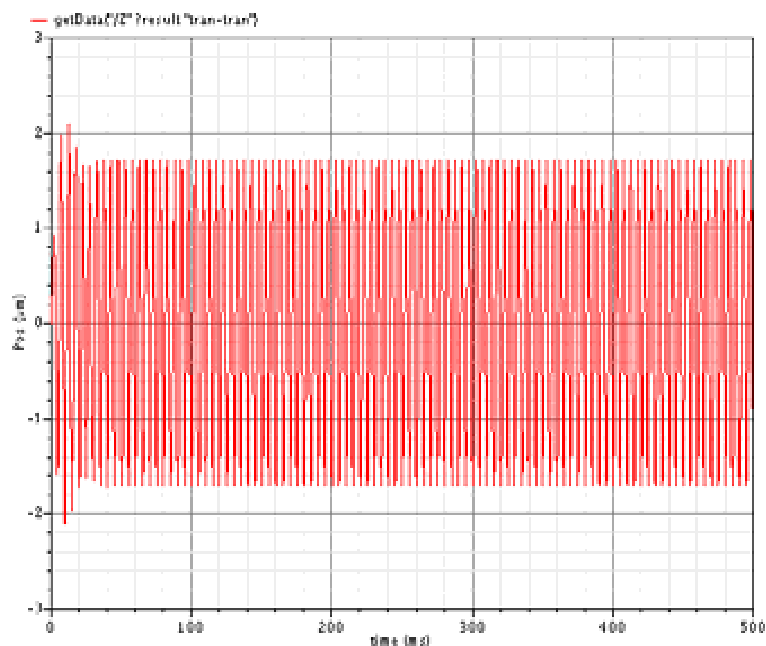

Figure 2.18. Amplitude of the mass motion at resonance.

From Figure 2.18 to Figure 2.21 the amplitude, capacitance and voltage of the vibration-driven variable capacitance are shown in addition to the voltage over the output load capacitor.

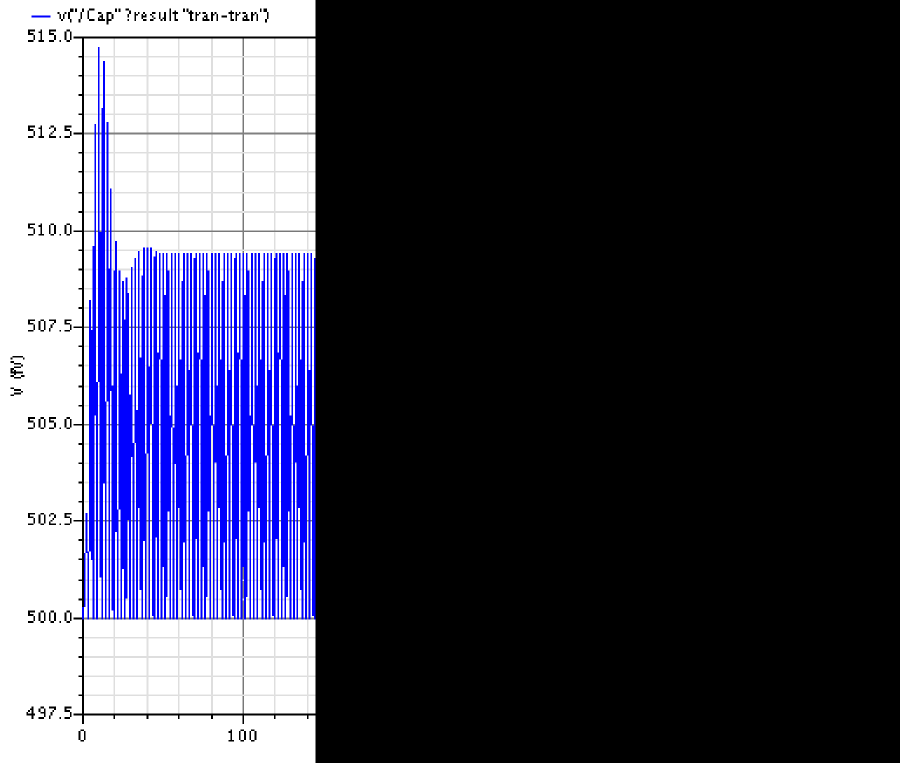

Figure 2.19. Capacitance of the vibration-driven variable capacitor at resonance.

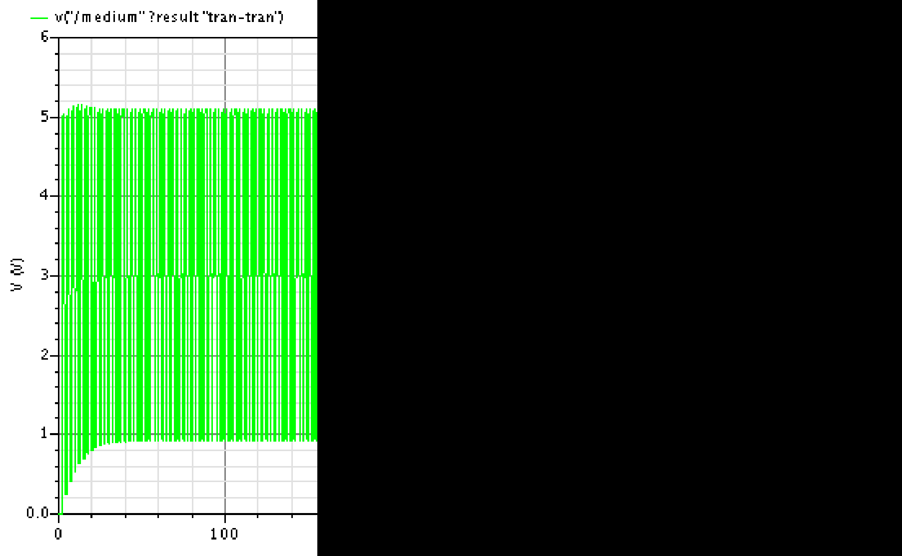

Figure 2.20. Voltage over the vibration-driven variable capacitor at resonance.

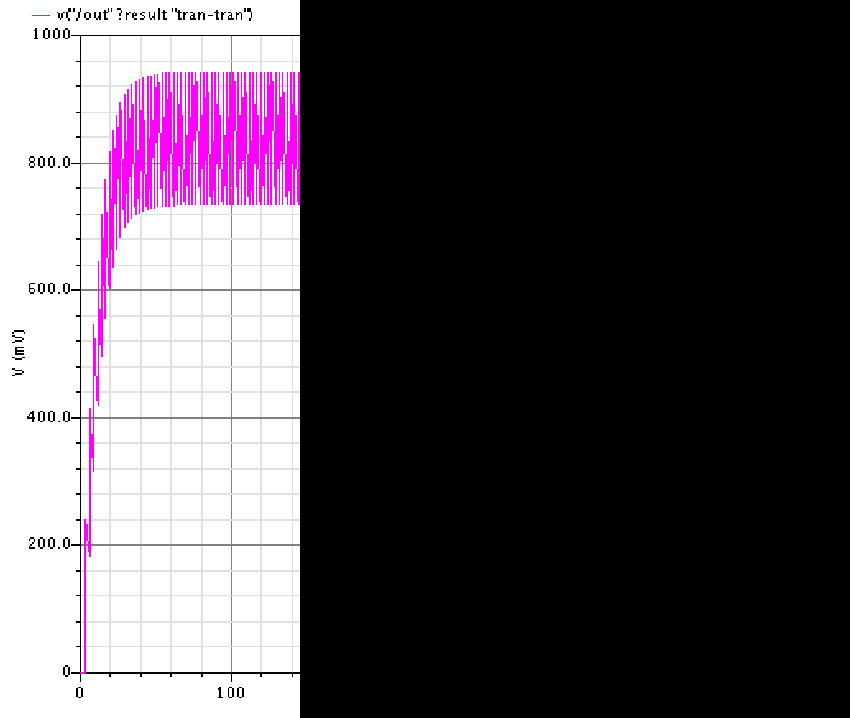

Figure 2.21. Voltage over the output capacitor at resonance.

2.3 Model of a piezoelectric converter

A generic piezoelectric converter formed by a cantilever covered by a piezoelectric layer and a tip mass at its end. In this section, the coupled piezoelectric-elastic properties of this device are modeled. Finally, is has been calculated an analytical expression of the generated power when the energy scavenger is driven by a harmonic vibration.

2.3.1 Constitutive Relations

The constitutive equations of linear piezoelectricity can be derived from classical mechanics and thermodynamics. The steps to derive the classical constitutive equations are detailed described in [25] and [26]. By definition, piezoelectric materials exhibit elastic, dielectric and coupled elastic-dielectric phenomena, so it is necessary to discuss the classical continuum approach for each phenomenon. The classical elastic continuum is described by the well-known relations between stresses and strains in a solid.

Under small field conditions, the constitutive relations for a piezoelectric material are [13, 27]:

$$\begin{bmatrix} \vec{D} \\ \vec{\delta} \end{bmatrix} = \begin{bmatrix} \vec{\varepsilon}^{\sigma} & \vec{d} \\ \vec{d} & \vec{s}^{E} \end{bmatrix} \begin{bmatrix} \vec{E} \\ \vec{\sigma} \end{bmatrix} \tag{2.40}$$

Where the vector D (3x1), is the electric displacement (C/m^2), δ is the mechanical strain vector (6x1) (dimensionless), E is the applied electric field vector (3x1) (V/m) and σ is the

stress vector (6x1). The piezoelectric constants are dielectric permittivity ε^{σ} of size (3x3), the piezoelectric coefficient d (3x6) and the compliance vector, s^E, of size (6x6).

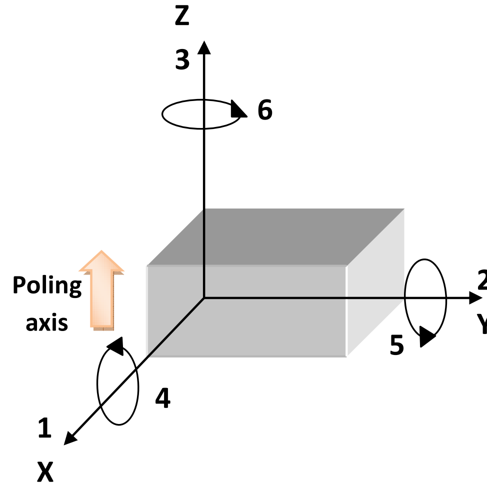

Figure 2.22. Axis convention and directions of the deformation.

The superscripts σ and E indicate the quantity is measured at constant stress or constant electric field respectively. As can be seen in Figure 2.22, the poling direction is denoted at the 3-axis and is along the thickness of the piezoelectric sheet. On the other hand, the 1-axis and 2-axis are in plane of that sheet.

For general purposes, a piezoelectric material can be used in two modes that are the 33 mode, which means that both the voltage and stress act in the 3-axis direction, and the 31 mode, meaning that the voltage acts in the 3-axis and the mechanical stress or strain in the 1-axis direction.

The 31-mode is specially used for bimorphs or when having a thin piezoelectric layer over another thicker beam, because the bending of the compound element in the 3-axis direction develops a large strain in the 1-axis direction. Although the electrical/mechanical coupling for 31 mode is lower than for 33 mode, this configuration makes the system much more compliant, obtaining a larger strain with smaller input forces. Also the resonant frequency is lower as the beam is less stiff.

In order to compare the throughput of different piezoelectric materials as power generator, several properties have to be taken into account. First the piezoelectric strain coefficient, d, relates strain to electric field. Then the coupling coefficient, k_{m-e}, is an index to evaluate the ability of certain material to convert mechanical energy to electrical energy and vice versa. It can be expressed as:

$$\kappa_{m-e} = \sqrt{\frac{Y}{\varepsilon}} d \tag{2.41}$$

The dielectric constant, ε, and the Young's modulus, Y, have a notable importance in the conversion behavior of the material. The impedance of a piezoelectric generator is used to have a high value that results in higher voltage and lower current power. Increasing the value of the dielectric constant, this impedance can be reduced. The elastic modulus is related to

the stiffness of the bender and the resonant frequency of the system. A larger bending can be obtained for the same force with a lower Young's modulus value. Finally, the tensile strength, which is the maximum stress that a material can withstand while being stretched, is desired to be as high as possible.

The piezoelectric coefficients experimentally measured are reported in [3]. The main expressions and theoretical analysis about piezoelectricity is developed in Chapter 2. The piezoelectric constants can be expressed in voltage-to-stress (d). The piezoelectric constant d is defined as the electric polarization induced on a material per unit mechanical stress applied to it. Alternatively, it is the mechanical strain experienced by the material per unit electric field applied to it. The first subscript refers to the direction of polarization at zero-electric field (E = 0), or to the applied field strength. The second one refers to the direction of the applied stress, or to the direction of the induced strain, respectively.

Two relevant components of the d-constant are:

d33 [m/V]: is the induced polarization per applied unit stress, both in the Z-axis ("3"). Alternatively it is the induced strain per unit electric field applied in the same direction.

d31 [m/V]: is the induced polarization in direction 3 per unit stress applied in direction 1. Alternatively it is the strain induced in direction 1 per unit electric field applied in direction 3.

The values of d_{33} and d_{31} are 2.85 and 1.12 pm/V, whose magnitudes are roughly equal to a half the value of previously reported epitaxial AlN films. With these values, we can expect a voltage signal enough to extract the energy, when this signal is regulated and conditioned.

2.3.2 Resonance frequency of a composite beam with an attached tip mass

The typical structure used in MEMS to create a piezoelectric energy scavenger is a composite beam layer with an attached tip mass. The composite beam is normally formed by a thin piezoelectric layer and another thicker passive layer (typically silicon) that plays the role of structural layer.

On the other hand, the resonance frequency of a spring-mass system is expressed as follows:

$$f_r = \frac{1}{2\pi}\sqrt{\frac{k_{eff}}{m_{eff}}} \tag{2.42}$$

In piezoelectric energy scavenging, an extended mass is commonly attached to the end of a cantilever. This mass cannot be considered as a concentrated mass, and its size has to be taken into account. Therefore, effective parameters for stiffness and mass considering the tip mass have to be used.

Therefore, the stiffness of the structure is highly dependent on the passive part. In order to calculate the value of the stiffness for a composite beam, a new magnitude has to be introduced. It is the neutral axis, which is defined as a sheet into the beam that experiences no strain when it is bend [28, 29].

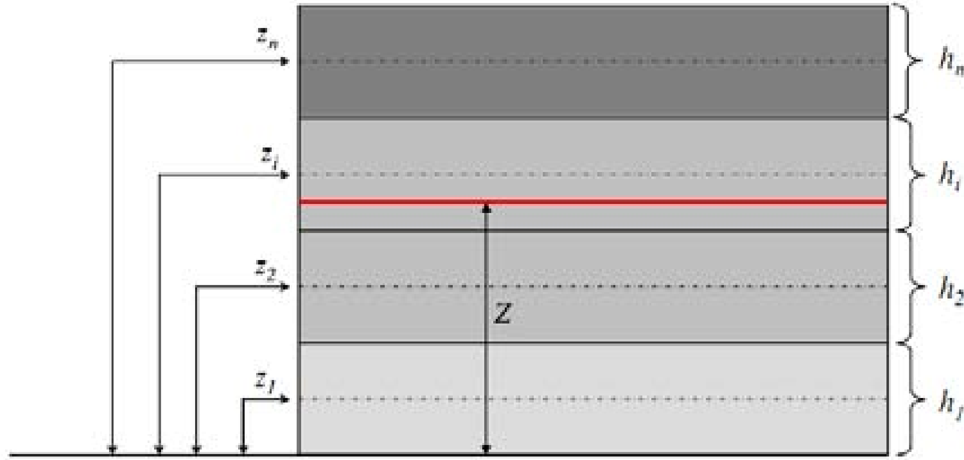

Figure 2.23. Multilayered beam structure where Z is the modulus-weighted neutral axis, z_i is the height of the centroid layer i and h_i is the thickness of the layer i [29].

For composite beams as shown in Figure 2.23 the neutral axis is a parallel sheet at a certain distance *Z* from the beam bottom. This value is related to the distance from the beam bottom to the centroid of each layer, z_i, the thickness of each layer, h_i, and the Young's modulus of the material that compound every layer, Y_i:

$$Z = \frac{\sum_{i=1}^{n} z_i Y_i h_i}{\sum_{i=1}^{n} Y_i h_i} \tag{2.43}$$

It is easy to calculate the height of the centroid of the layer *i*, by means of:

$$z_i = \left(\sum_{j=1}^{i} h_j\right) - \frac{h_j}{2} \tag{2.44}$$

Once the neutral axis is known, the stiffness k of the beam can be determined. The second moment of the area of a rectangular cross section layer *i* is given by,

$$I_i = \frac{w_i h_i^3}{12} \tag{2.45}$$

where w_i is the beam width. The parallel axis or Huygens-Steiner theorem [30] allows calculating the second moment of area of a cross section that is not bending about an axis that crosses its centroid, but of which bending axis is parallel to that centroid axis. It is the case for each of the composite layer which makes up the composite cantilever beam. Therefore, the second moment of the area needs to be adjusted for each material layer as follows:

$$I_{iP} = \frac{w_i h_i^3}{12} + A_i \left(z_i - Z\right)^2 \tag{2.46}$$

where A_i is the cross section area of the layer *i*. The stiffness of a cantilever beam (without any tip mass) can be calculated with:

$$k = \frac{3YI}{l^3} \tag{2.47}$$

Where *l* is the beam length. In order to obtain the total equivalent stiffness k_T, the contribution of each layer has to be taken into account:

$$k_T = \frac{3}{l^3} \sum_{i=1}^{n} Y_i I_{iP} \tag{2.48}$$

Substituting the corresponding expressions, it can be obtained:

$$k_T = \frac{3}{l^3}\left[\sum_{i=1}^{n} Y_i \left(\frac{w_i h_i^3}{12} + l h_i \left(\left(\sum_{j=1}^{i} h_j\right) - \frac{h_j}{2} - Z\right)^2\right)\right] \tag{2.49}$$

For a composite beam as shown in Figure 2.24 with a mass with a total length l_m attached to its end, a modified expression for the effective total stiffness can be used [31]:

$$\left(k_T\right)_{eff} = \frac{3}{l^3}\left[\sum_{i=1}^{n} Y_i \left(\frac{w_i h_i^3}{12} + l h_i \left(\left(\sum_{j=1}^{i} h_j\right) - \frac{h_j}{2} - Z\right)^2\right)\right] \times \left(1 + \frac{3l}{4l_m}\right)^{-1} \tag{2.50}$$

In the same way, an effective mass, m_{eff}, can be approximated by [31]:

$$m_{eff} = m\left(\frac{4}{3}\right)\left(\frac{l_m}{l_b}\right) \tag{2.51}$$

2.3.3 Strain and stress of the structure

In order to calculate the strain that appears in a simple cantilever beam (without tip mass), an elemental section, dx, of the beam between two vertical lines in an unbent beam has to be considered. If the beam is bent, the elemental section dx is deformed along a curve with a radius of curvature R. For small deformations and a section of the horizontal layer at the neutral axis plane, $\tan\theta \approx \theta$, we can consider that $dx = R\,d\theta$. However, at a certain distance of the neutral axis, the material is stretched or compressed in the x-direction due to the total bending. Therefore the elongation of this elemental section is expressed as [32]:

$$\Delta(dx) = \left(R + \frac{h_b}{2}\right)d\theta - R d\theta = \frac{h_b}{2} d\theta \tag{2.52}$$

The strain produced by this relative elongation of the material is:

$$\delta_l = \frac{\Delta(dx)}{(dx)} = \frac{\frac{1}{2} h_b d\theta}{R d\theta} = \frac{h_b}{2R} \tag{2.53}$$

This expression uses the assumption that the material does not suffer an initial residual stress.

When the beam presents an attached tip mass with a length l_m, the strain distribution over the beam has to be formulated in another way (Figure 2.24). It is assumed that a force, $F = m\,Q_{mec}\,a_0$, is applied to the middle of the mass, when a base acceleration a_0 is presented. A bending moment at any point x along the beam can be calculated as:

$$M(x) = m Q_{mec} a_0 \left(l_b - x\right) \tag{2.54}$$

This moment results in a varying radius of curvature. The torque, which is only acting at the beam-mass connection, leads to a constant radius of curvature and it is defined as:

$$T = m Q_{mec} a_0 \left(\frac{l_m}{2}\right) \tag{2.55}$$

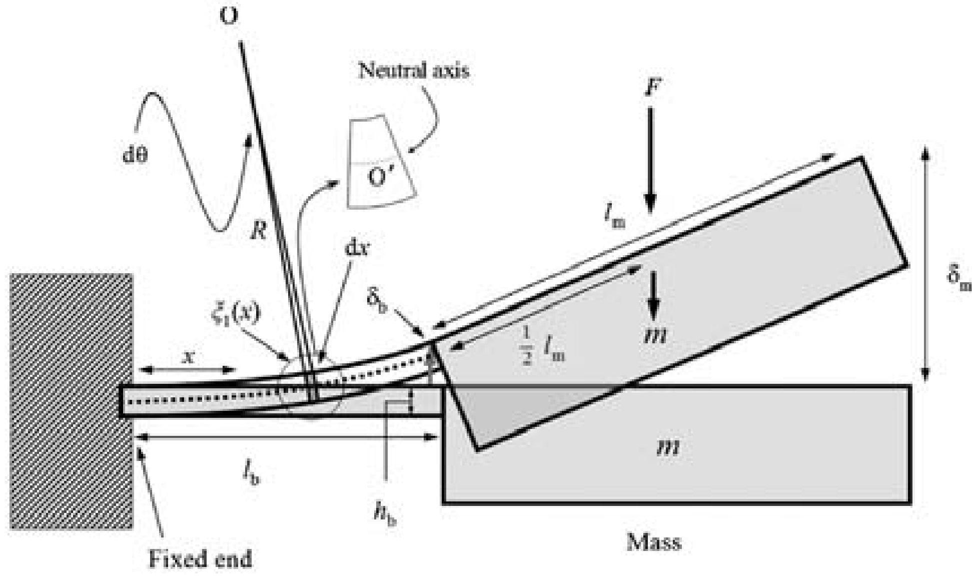

Figure 2.24. Cantilever beam of length l_b and height h_b under stress with an attached tip mass m with length l_m [29].

Then, the beam curvature, κ, that can be estimated as:

$$\kappa(x) = \frac{d^2 z(x)}{dx^2} = \frac{1}{R} \tag{2.56}$$

where R is the resulting curvature radius and z is the vertical bending at the position x on the beam.

The beam curvature is related to the applied moment acting on the beam. Therefore, by applying the superposition principle, the motion equation of an n-layer composite beam can be found:

$$mQ_{mec}a_0\left(l_b - x\right) + mQ_{mec}a_0\left(\frac{l_m}{2}\right) = \sum_{i=1}^{n} Y_i I_i \frac{d^2 z(x)}{dx^2} \text{ ,} \tag{2.57}$$

By isolating the curvature radius, it can be obtained the following compact expression:

$$\frac{d^2 z(x)}{dx^2} = \frac{mQ_{mec}a_0}{\sum_{i=1}^{n} Y_i I_i}\left(l_b + \frac{l_m}{2} - x\right) \tag{2.58}$$

Then, by integrating twice, the bending beam profile formula can be found:

$$z(x) = \frac{mQ_{mec}a_0}{\sum_{i=1}^{n} Y_i I_i}\left(\frac{1}{4}l_m + \frac{1}{2}l_b - \frac{1}{6}x\right)x^2 \tag{2.59}$$

Substituting x = l_b, the deflection at the end of the beam is given by,

$$z_b = z(z = l_b) = \frac{mQ_{mec}a_0}{12\sum_{i=1}^{n} Y_i I_i} l_b^2\left(3l_m + 4l_b\right) \tag{2.60}$$

Finally, by using the expressions from (2.58) and (2.54), the strain distribution for the beam is obtained:

$$\sigma_l = \frac{mQ_{mec}a_0}{\sum_{i=1}^{n} Y_i I_i}\left(l_b + \frac{l_m}{2} - x\right)\frac{h_b}{2} \tag{2.61}$$

At a certain input acceleration value, a_0, the following term can be evaluated when the beam reaches certain vertical deflection amplitude, z_b:

$$\frac{mQ_{mec}a_0}{\sum_{i=1}^{n} Y_i I_i} = 12\frac{z_b}{(3l_m + 4l_b)l_b^2} \quad (2.62)$$

On the other hand, assuming a constant slope at the beam-mass connection, the mass tip displacement z_m and beam displacement z_b are related by the following expression:

$$z_m = \frac{4l_b^2 + 9l_b l_m + 6l_m^2}{l_b(4l_b + 3l_m)} z_b \quad (2.63)$$

Thus the final strain distribution function along the beam length in terms of the mass tip displacement is given by:

$$\delta_l = \frac{3h_b}{l_b}\frac{2l_b + l_m - 2x}{4l_b^2 + 9l_b l_m + 6l_m^2} z_m \quad (2.64)$$

2.3.4 Optimal load and power estimation

Most existing modeling approaches [33] assume the vibration amplitude of the energy harvester to be independent of the connected circuit. However, the vibration amplitude is importantly influenced by the connected circuit. It is needed to include the piezoelectric coupling in the mechanical equation, to predict the variation of the resonance frequency with the load resistance. A vibration-driven piezoelectric energy harvester with no connected external load is normally modeled either as a current source in parallel with the piezoelectric capacitance, C_P, or as a voltage source in series with C_P [34]. These modeling representations are based on the piezoelectric constitutive equation presented in (2.40) :

$$\delta_1 = s_{11}^E\sigma_1 + s_{12}^E\sigma_2 + s_{13}^E\sigma_3 + d_{31}E_3 \quad (2.65)$$

$$\delta_2 = s_{12}^E\sigma_1 + s_{11}^E\sigma_2 + s_{13}^E\sigma_3 + d_{31}E_3 \quad (2.66)$$

$$\delta_3 = s_{13}^E(\sigma_1 + \sigma_2) + s_{33}^E\sigma_3 + d_{31}E_3 \quad (2.67)$$

$$D_3 = d_{31}(\sigma_1 + \sigma_2) + d_{33}\sigma_3 + \varepsilon_{33}^{\sigma}E_3 \quad (2.68)$$

According to these equations, the applied mechanical stresses induce an electric displacement (induced charge) on the piezoelectric surface. Analogously, an electric field applied across the electrodes in the thickness direction affects the mechanical strain too. This backward coupling has the effect of founding two limit values of the resonance frequency depending on the load resistance. Therefore, it can be found short-circuit (zero resistance) and open-circuit (infinite resistance) resonance frequencies. For these two cases, one can consider E_3 = 0 or D = 0, respectively. However, in the real operation, the energy harvester is connected to an external load. Thus, the use of these approximations means an overestimation of the generated power.

On the other hand, it is common to represent a piezoelectric element as a current source in parallel with its internal capacitance. Based on that, it has been frequently used an optimum load impedance as $R_{opt} = 1/\omega_r C_p$.

However, the approximation of using uncoupled analysis is fairly valid for low coupling systems such as MEMS devices [31]. It was experimentally observed [29] that the mass displacement at the maximum power point is reduced as the load resistance approaches the overall impedance of the circuit. The load resistance reduces the motion amplitude at the short-circuit resonance frequency up to a load value (optimum load) and enlarges the motion amplitude at the open circuit resonance frequency. It has been repeatedly observed that the experimental optimum load resistance at maximum power point nicely matches with the internal impedance of the piezoelectric film.

Referring to the piezoelectric constitutive equations (2.65)-(2.68), for the calculation of the short-circuit current, it is assumed that $E = 0$ in (2.68). Since the film is free to move in the z-direction, the magnitude of the stress component σ_3 can be set to 0. In the mechanical-to-electrical mode, the charges generated and fed through the external circuit at ($E_3 = 0$) can be estimated as:

$$D_3 = d_{31}(\sigma_1 + \sigma_2) \tag{2.69}$$

Mathematically manipulating (2.66) and (2.67), the electric displacement can be set in terms of strains as:

$$D_3 = \left(\frac{d_{31}}{s_{11}^E + s_{12}^E}\right)(\delta_1 + \delta_2) = e_{31}(\delta_1 + \delta_2) \tag{2.70}$$

As the piezoelectric layer is much thinner than the beam thickness, it can be assumed that the strains δ_1 and δ_2 are constant along the thickness of the film, and their values are identical to the surface strains of the beam. The transversal strain δ_2 is related to the longitudinal one δ_1 by Poisson's ratio υ_b of the beam which is made of Si in our case, were $\upsilon_b = \delta_2/\delta_1$. The electrical displacement becomes:

$$D_3 = e_{31}(1 - \upsilon_b)\delta_1(x) \tag{2.71}$$

Where $\delta_i(x)$ is the strain distribution function of the beam and is given by (2.64). Because of the charge difference on the electrode surfaces a current is force to flow to the external circuit, the amplitude of the short-circuit current is that of the charge times the angular frequency:

$$i_{sc} = \omega_{sc} D_3 w_{te} dx \tag{2.72}$$

This current is due to the charge generated on the rectangular segment ($w_{te}dx$) of the top electrode. Assuming that the piezoelectric layer as well as the top electrode extends over the whole beam, the total short-circuit current (I_{sc}) can be obtained after taking the integral over the whole beam length:

$$I_{sc} = 2\pi w_{te} f_r e_{31}(1 - \upsilon_b)\int_0^{l_b} \delta_1(x)dx \tag{2.73}$$

For the calculation of the voltage source, a similar approach is used when $D_3 = 0$ in (2.68). The voltage across the piezoelectric electrodes is given by:

$$V_{oc} = \frac{-e_{31}}{\varepsilon_0 \varepsilon_{33}^T}\left(\frac{t_p}{l_b}\right)(1 - \upsilon_b)\int_0^{l_b} \delta_1(x)dx \tag{2.74}$$

where t_p is the piezoelectric layer thickness. It is obvious that the above calculations for current or voltage are valid only in the case of $E_3 = 0$ or $D_3 = 0$, respectively.

The typical characteristics of a MEMS piezoelectric energy harvester allows the use of a resonance frequency (ω_r), where $\omega_r \approx \omega_{sc} \approx \omega_{oc}$. The current I_1 through the load is given by,

$$I_l = \frac{V_{oc}}{Z_p + Z_l} \tag{2.75}$$

where Z_p and Z_l are the complex impedance of the piezoelectric capacitor and connected load, respectively. The average power delivered to the load is,

$$P_{rms} = \frac{1}{2} I_l^2 Z_l = \frac{1}{2} \frac{V_{oc}^2}{\left(Z_p + Z_l\right)} Z_l \tag{2.76}$$

For maximum power transfer, the load impedance Z_l must be equal to the complex conjugate of the piezoelectric impedance.

In a situation in which the load is purely real, the maximum average power occurs when:

$$R_{l,opt} = \left|Z_p\right| = \frac{1}{\omega_r C_p} \tag{2.77}$$

Based on the Thevenin-Norton source transformation theorem, the piezoelectric internal impedance is also determined as,

$$\left|Z_p\right| = \frac{V_{oc}}{I_{sc}} \tag{2.78}$$

Using (2.77) and (2.78) in (2.76), it can be conclude that:

$$P_{rms} = \frac{1}{2}\left(\frac{V_{oc}}{2}\right)^2 \left|Z_p\right|^{-1} = \frac{1}{2}\left(\frac{I_{sc}}{2}\right)^2 \left|Z_p\right| \tag{2.79}$$

From this expression it can be inferred that,

$$I_{l,opt} = \frac{I_{sc}}{2} \quad \text{and} \quad V_{l,opt} = \frac{V_{oc}}{2} \tag{2.80}$$

Therefore, an extended form of the maximum average power consumed in the load can be written as:

$$P_{rms} = \frac{9\pi}{4} f_r \frac{e_{31}^2 \left(1-\upsilon_b\right)^2}{\varepsilon_{33}^T} \frac{l_{te} w_{te} t_p h_b^2}{l_b} \left(\frac{l_b + l_m}{4l_b^2 + 9 l_b l_m + 6 l_m^2}\right)^2 z_m^2 \tag{2.81}$$

2.4 Conclusions

The fundamental theory about vibration-driven energy scavengers have been described in this chapter. An overall description of the main blocks that form this system was firstly presented. Detailed model for electrostatic and piezoelectric converters have been developed too. Numerical implementations in several modeling languages have been carried out for both models. The main goal of this chapter is the achievement of expressions to calculate the theoretical power that can be extracted with both transductions.

References

[1] J. Marion, *Classical dynamics of particles and systems*, 2nd edition ed. New York: Academic Press, 1970.

[2] S. Roundy, P. K. Wright, and J. M. Rabaey, "Energy Scavenging for Wireless Sensor Networks: With Special Focus on Vibrations," Springer, 2004.

[3] J. Brotz, "Damping in CMOS-MEMS Resonators," *Masters Project Report in ECE. Carnegie Mellon University,* 2004.

[4] R. Elfrink and et al., "Vacuum-packaged piezoelectric vibration energy harvesters: damping contributions and autonomy for a wireless sensor system," *Journal of Micromechanics and Microengineering,* vol. 20, p. 104001, 2010.

[5] G. Murillo, Z. J. Davis, S. Keller, G. Abadal, J. Agusti, A. Cagliani, N. Noeth, A. Boisen, and N. Barniol, "Novel SU-8 based vacuum wafer-level packaging for MEMS devices," *Microelectronic Engineering,* vol. 87, pp. 1173-1176, 2010.

[6] F. Cottone, H. Vocca, and L. Gammaitoni, "Nonlinear Energy Harvesting," *Physical Review Letters,* vol. 102, 2009.

[7] L. Gammaitoni, I. Neri, and H. Vocca, "Nonlinear oscillators for vibration energy harvesting," *Applied Physics Letters,* vol. 94, 2009.

[8] M. Ferrari, V. Ferrari, M. Guizzetti, B. Andò, S. Baglio, and C. Trigona, "Improved Energy Harvesting from Wideband Vibrations by Nonlinear Piezoelectric Converters," *Procedia Chemistry,* vol. 1, pp. 1203-1206, 2009.

[9] L. Gammaitoni, I. Neri, and H. Vocca, "Noise powered nonlinear energy harvesting," *International Conference on Applications in Nonlinear Dynamics (Icand 2010),* vol. 1339, pp. 151-157, 2010.

[10] R. Amirtharajah and A. P. Chandrakasan, "Self-powered signal processing using vibration-based power generation," *Solid-State Circuits, IEEE Journal of,* vol. 33, pp. 687-695, 1998.

[11] N. R. Greene, "Energy Flow for a Variable-Gap Capacitor," *The Physics Teacher,* vol. 43, p. 340, 2005.

[12] W. Voigt, *Lehrbuch der kristallphysik*: BG Teubner, 1910.

[13] J. Sirohi and I. Chopra, "Fundamental behavior of piezoceramic sheet actuators," *Journal of Intelligent Material Systems and Structures,* vol. 11, pp. 47-61, 2000.

[14] S. Meninger, J. O. Mur-Miranda, R. Amirtharajah, A. Chandrakasan, and J. H. Lang, "Vibration-to-electric energy conversion," *Very Large Scale Integration (VLSI) Systems, IEEE Transactions on,* vol. 9, pp. 64-76, 2001.

[15] F. Peano and T. Tambosso, "Design and optimization of a MEMS electret-based capacitive energy scavenger," *Microelectromechanical Systems, Journal of,* vol. 14, pp. 429-435, 2005.

[16] T. Sterken, P. Fiorini, K. Baert, R. Puers, and G. Borghs, "An electret-based electrostatic microgenerator," in *TRANSDUCERS, Solid-State Sensors, Actuators and Microsystems, 12th International Conference on*, 2003, pp. 1291-1294.

[17] W. H. Hsieh, H. Tseng-Yang, and T. Yu-Chong, "A micromachined thin-film Teflon electret microphone," in *Solid State Sensors and Actuators, 1997. TRANSDUCERS '97 Chicago., 1997 International Conference on*, 1997, pp. 425-428 vol.1.

[18] E. O. Torres and G. A. Rincon-Mora, "Electrostatic Energy Harvester and Li-Ion Charger Circuit for Micro-Scale Applications," in *Circuits and Systems, 2006. MWSCAS '06. 49th IEEE International Midwest Symposium on*, 2006, pp. 65-69.

[19] P. D. Mitcheson, E. M. Yeatman, and T. C. Green, "Power processing circuits for MEMS inertial energy scavengers," *Arxiv preprint arXiv:0711.3311,* 2007.

[20] P. D. Mitcheson, T. C. Green, and E. M. Yeatman, "Power processing circuits for electromagnetic, electrostatic and piezoelectric inertial energy scavengers," *Microsystem Technologies,* vol. 13, pp. 1629-1635, 2007.

[21] E. M. Yeatman, "Applications of MEMS in power sources and circuits," *Journal of Micromechanics and Microengineering,* vol. 17, pp. S184-S188, 2007.

[22] P. D. Mitcheson, P. Miao, B. H. Stark, E. M. Yeatman, A. S. Holmes, and T. C. Green, "MEMS electrostatic micropower generator for low frequency operation," *Sensors and Actuators A: Physical,* vol. 115, pp. 523-529, 2004.

[23] G. Despesse, J. J. Chaillout, T. Jager, J. M. Léger, A. Vassilev, S. Basrour, and B. Charlot, "High damping electrostatic system for vibration energy scavenging," presented at the Proceedings of the 2005 joint conference on Smart objects and ambient intelligence: innovative context-aware services: usages and technologies, Grenoble, France, 2005.

[24] *MEMSOI technology - Tronics*. Available: http://www.tronicsgroup.com/mems-foundry/memsoi-mpw-run-europractice

[25] W. P. Mason, "Piezoelectric crystals and their application to ultrasonics," 1950.

[26] W. G. Cady, *Piezoelectricity*: McGraw-Hill, 1946.

[27] A. Meitzler, H. Tiersten, A. Warner, D. Berlincourt, G. Couqin, and F. Welsh III, "IEEE Standard on Piezoelectricity," *IEEE, New York,* 1988.

[28] T. Eggborn, "Analytical models to predict power harvesting with piezoelectric materials," Virginia Polytechnic Institute and State University, 2003.

[29] T. M. Kamel and et al., "Modeling and characterization of MEMS-based piezoelectric harvesting devices," *Journal of Micromechanics and Microengineering,* vol. 20, p. 105023, 2010.

[30] L. D. Landau and E. M. Lifshit s "Mechanics," 3rd ed: Pergamon Press, 1976.

[31] M. Renaud, "Piezoelectric energy harvesters for wireless sensor networks," PhD, Katholieke Universiteit, Leuven, Belgium, 2009.

[32] M. H. Bao, *Analysis and design principles of MEMS devices*: Elsevier Science, 2005.

[33] A. Erturk and D. J. Inman, "Issues in mathematical modeling of piezoelectric energy harvesters," *Smart Materials & Structures,* vol. 17, 2008.

[34] G. K. Ottman, H. F. Hofmann, A. C. Bhatt, and G. A. Lesieutre, "Adaptive piezoelectric energy harvesting circuit for wireless remote power supply," *Ieee Transactions on Power Electronics,* vol. 17, pp. 669-676, 2002.

CHAPTER 3

MONOLITHIC INTEGRATION OF MICRO-SIZED ENERGY SCAVENGING SYSTEMS

In this chapter, a commercial CMOS technology is used to integrate a proof-of-concept prototype of an electrostatic energy harvester. It is introduced the concept called Energy Harvester on Chip (EHoC) that relies on the use of the whole chip as inertial mass of the vibration-driven resonator and the total chip area to define the comb drives that develop the transduction. The design, simulations, fabrication and electromechanical characterizations are compiled here. The feasibility of fabricating large movable electromechanical structures (hundreds of microns) with a standard CMOS technology has been demonstrated too. The results derived from the simulations and measurements show the improvement in the energy density with the application of the EHoC concept, reaching a maximum expected value of 5.78 µW/cm³.

3.1 Monolithic fabrication of MEMS and CMOS integration

Nowadays, MEMS technology is well-established and widely spread around a huge number of industries. It can be found numerous devices using MEMS in our daily life. MEMS can be found as part of numerous systems and having different functions, such as oscillators, mixers, and filters for modern RF devices, accelerometers, gyroscopes, pressure or mass sensors for sensing applications, and energy harvesters for power supplying at micro-scale. A growing number of MEMS foundries are fabricating microsystems to be integrated in electronic devices. However, this integration used to be a heterogeneous combination between an entirely MEMS element and an electronic circuit fabricated with CMOS technology.

On the other hand, MEMS technology is trying to improve its integration with the current leader technology in electronics circuits, i.e. the CMOS technology. Hence, the possibility of making MEMS with a standard CMOS technology is especially tempting.

The author's group has been working in the design of MEMS for mass sensing and RF applications using a commercial CMOS technology for more than a decade [1-9]. Several commercial CMOS technologies have been used to fabricate MEMS elements in the heart of the standard IC (integrated circuit). In the framework project supporting this thesis and

called MEMSPORT, the CMOS technology AMS-C35, from *austriamicrosystems* foundry, was accessed via Europractice using the Multi-Project Wafer (MPW) service and it consists of four metal and two polisilicon layers, as shown in Figure 3.1. These two layers have been utilized our group to pattern MEMS structures, such as cantilevers, clamped-clamped beams or tuning forks. They are designed to resonate at RF frequencies to develop oscillators, mass sensors, filters, mixers, and other RF elements. The goals of this approach are the miniaturization of the devices compared to traditional approaches and, even more importantly, the monolithic integration in a commercial CMOS technology. This last point is crucial to reduce the value of the parasitic elements (inductance, resistance and capacitance) related to a typical bonding process that critically decrease the performance of the whole system.

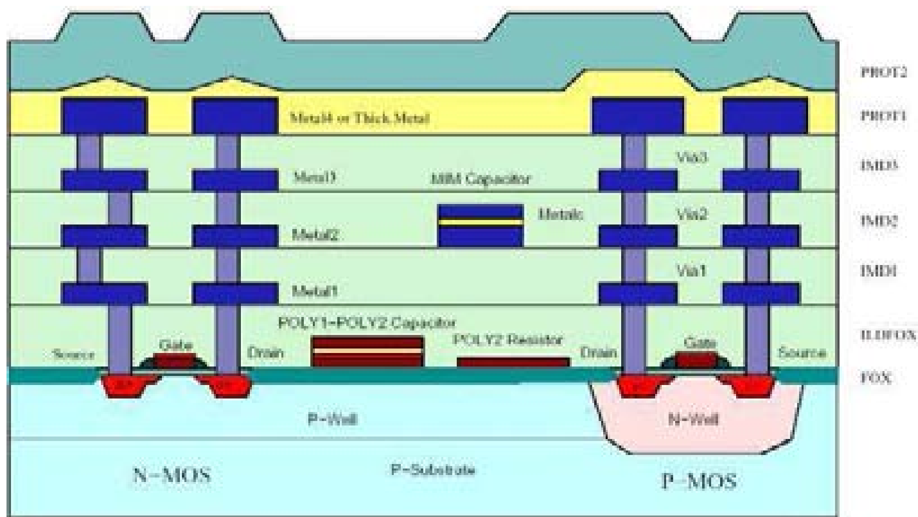

Figure 3.1. Cross-section view of the 4M2P CMOS technology

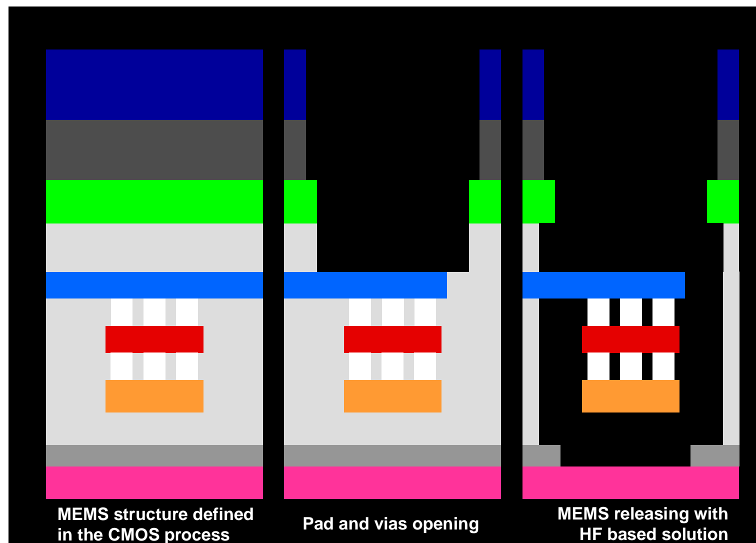

Figure 3.2. Releasing post-process without mask.

The most important information for the design of MEMS structures with this type of technology is shown in Table 3.1. With these design rules and the thickness of each layer, and together with the properties of the layers materials, we can design the MEMS structures to be fabricated with this technology.

Table 3.1. Design rules and thicknesses of the structural layers

Chip physical features	
Area	10.91 mm^2
Thickness	720 µm
Volume	7.86 mm^3
Mass	19.85 mg

Layer	Minimum width (µm)	Minimum spacing (µm)	Typical thickness (nm)
Metal4	0.6	0.5	925
IMD3	n.a.[a]	n.a.	1000
Metal3	0.6	0.5	640
IMD2	n.a.	n.a.	1000
Metal2	0.6	0.5	640
IMD1	n.a.	n.a.	1000
Metal1	0.5	0.45	665
ILDFOX	n.a.	n.a.	645
FOX	n.a.	n.a.	290

[a] n.a. means non applicable.

In order to exploit the back-end layers to make MEMS structures, the four metal layers are used as like structural layers, and the oxide layers as sacrificial layers. The vias between metal layers are used to increase the thickness of the metal layers, i.e. by means of joining few layers with a matrix of vias at minimum spacing, i. e. 0.45 µm. For this approach the four layers are connected through an array of vias to achieve the thicker compound layer possible with this technology. This vias have fixed dimensions of 0.5 µm x 0.5 µm, and with a minimum metal enclosure of 0.2 µm. A similar use of this technique is described in several works [10, 11].

The next step, when the CMOS chip, with MEMS structures embedded, has been designed and manufactured in the foundry, is releasing the movable structures. This is achieved by following a wet-etching post-process with an HF-based solution. In this way, we can remove the sacrificial oxide layers, so that the structures are released as it is shown in Figure 3.2.

However, a drawback of using CMOS technology to develop scavengers is the low mass available with these layers. Therefore, it is actually necessary to deposit an additional dense material on the top or another type of external mass.

3.2 A Paradigm Shift in Vibration Energy Scavenging: Energy Harvester on Chip

In the state of the art [12], it can be seen several energy scavenging devices whose basic concept is a mass coupled by a suspension to a frame, which is anchored to a vibrant environment. The system is designed to get at resonance with the environmental vibrations. Then, part of this mechanical energy is turned into electrical energy using some transduction methods (electrostatic, piezoelectric or electromagnetic). These devices used to be based on a millimetric inertial mass with comb drivers in both sides. In this section, we present two novel ideas to improve the performance of this type of microgenerators.

First idea: The concept of micro energy scavenging cells

A traditional energy harvester consists of a single rectangular millimetric inertial mass with a comb drive to each side. The idea proposed here is the use of several miniature energy harvesters, called "energy scavenging cells", covering the entire surface in order to increase the overall capacitance value (see Figure 3.3). The main effect is the enhancement of the transduction force for the same initial voltage and a resulting increase in the extracted power value. A daily-life analogy is the comparison between dissolving sugar cubes or powder. Because of the larger exposed area of the second case, it will be dissolved sooner. In the case presented here, the capacitance and consequently the electrostatic force depend on the capacitor area.

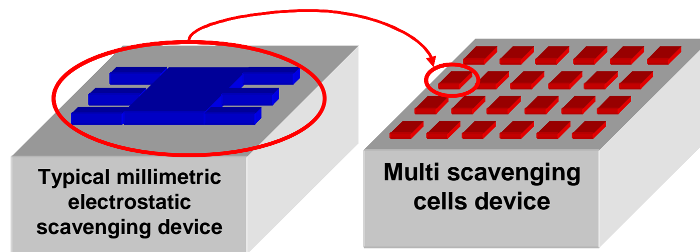

Figure 3.3. The evolution to the multi microcells array concept.

Second idea: The whole chip as inertial mass

The inertial mass has a direct impact on the extracted power, because the available mechanical energy of the resonator increases with a larger mass value. In order to increase the value of the inertial mass, this idea proposes to move the whole chip mass instead of moving the millimetric microfabricated mass (Figure 3.4(a)). Figure 3.4(b) shows how the chip is anchored to the vibrant environment from the suspended element instead of anchoring it by the substrate. Therefore, in this last case, the springs play the same role but the whole chip is transformed into the new inertial mass. Moreover, this inertial mass does not have to be fabricated because it is inherent to the dicing process and it does not waste the active area of the chip to be patterned.

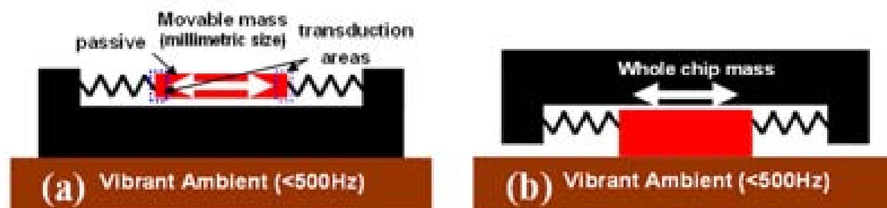

Figure 3.4. Typical vibration-based scavenger structure (a) and sketch showing the new idea included in the EHoC concept (b).

The convergence of these two new ideas leads to the concept of Energy Harvester-on-Chip (EHoC) shown in Figure 3.5. It can be defined as a chip only dedicated to scavenge energy from the environmental vibrations. Therefore, the chip mass, the equivalent whole spring constant of all the suspensions, and the total variable capacitance are the global main design parameters. The support substrate, which provides physical support and outside electrical connection, could be another chip that is powered by the EHoC.

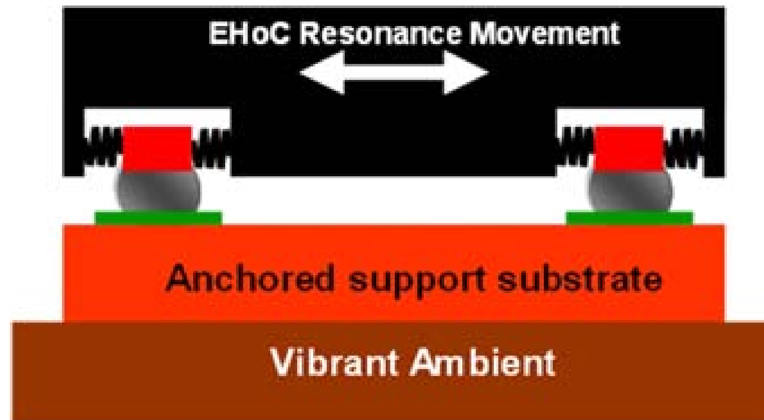

Figure 3.5. New concept: the energy Harvester-on-Chip.

Moreover, since we fabricate the chip in a commercial CMOS technology, we can reuse the same chip, already used to contain all the low-power circuits, sensors and transceiver, to make MEMS elements that are able to extract useful energy from the environmental vibrations.

3.3 Design of an electrostatic energy scavenger

A prototype to prove the EHoC concept was designed and fabricated. This concept was briefly presented in [13-15]. In Figure 3.6, the whole chip layout and the detail of a cell layout are shown. It is basically a suspended plate, with the typical dimensions of a pad, with fingers at both sides in a comb-type configuration. It is suspended by four U-type suspensions as shown in the inset of Figure 3.6.

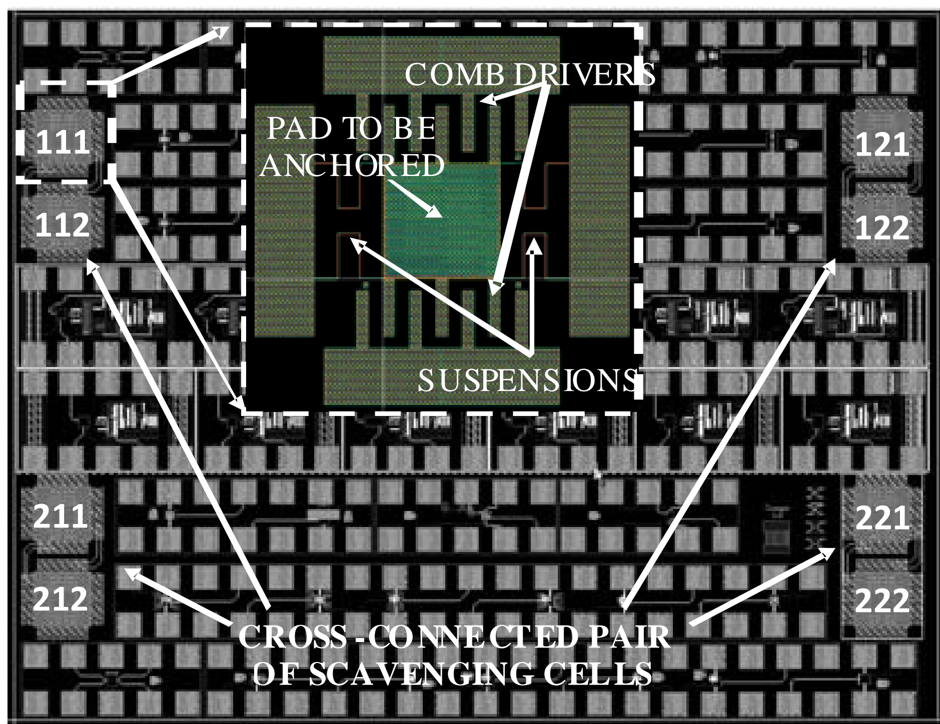

Figure 3.6. Layout of the fabricated chip with numbered cells. Inset: Layout of a single scavenging cell.

3.3.1 Suspension design

Since we are using the whole chip as inertial mass, it is needed to estimate its volume:

$$V_{chip} \approx A_{chip} t_{sub} \tag{3.1}$$

where A_{chip} is the chip area and t_{sub} is the substrate thickness.

Therefore,

$$m_{chip} \approx V_{chip} \rho_{Si} = t_{chip} A_{chip} \rho_{Si} \tag{3.2}$$

where V_{chip}, m_{chip} and ρ_{Si} are the volume and mass of the chip and the silicon density respectively.

In order to calculate the volume of a single energy scavenging cell, we have to take into account the squared pad area and the addition of all the fingers forming the cell:

$$V_{cell} \approx \left(A_{pad} + \frac{Ng}{2} w_f l_f \right) t_f \tag{3.3}$$

where A_{pad} is the pad area, and l_f, t_f, w_f are the finger length, thickness and width respectively.

Therefore,

$$m_{cell} \approx V_{cell} \rho_{Al} = \left(A_{pad} + \frac{Ng}{2} w_f l_f \right) t_f \rho_{Al} \tag{3.4}$$

where ρ_{Al} is the aluminum density.

The first design of the several suspensions of our system was calculate for a target resonant frequency of 100 Hz. It was an arbitrary value of frequency bellow 500 Hz which could correspond to the peak value of an acceleration spectrum available in our environment. However, the initial suspension modeling was not accurate enough and the resonant frequency of the resulting fabricated device is closer to 200 Hz. As it will be shown in the following sections, the simulated and measured values support this data. Therefore, in this section we are presenting a theoretical analysis more than the design process, where another mathematical expression to model the suspensions had to be found.

In Figure 3.7, it can be seen the layout of the designed suspension, with the most important dimensions indicated. The rest of important values needed to calculate the value of the suspension stiffness are shown in Table 3.2.

So from this new modeling start point, if we would like to suspend the whole chip mass with a single spring, its stiffness should be the next one to obtain a resonant frequency around 200Hz:

$$k_{chip} = \omega^2 m_{chip} = (2\pi \cdot 200Hz)^2 \cdot 19.85 \cdot 10^{-6}\,Kg = 31.35\, {}^{N}\!/_{m} \tag{3.5}$$

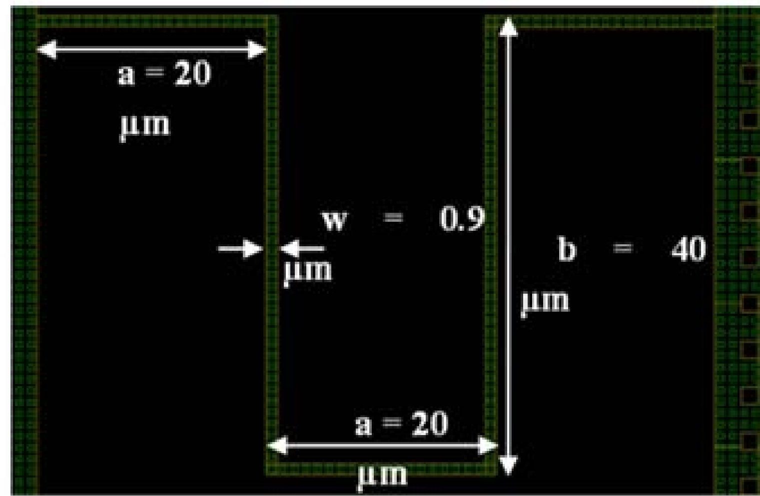

Figure 3.7. U-type suspension dimensions.

The suspensions for this mass can be designed with several shapes, but it is needed to take into account that the microsuspensions must allow the movement of the mass mostly in one direction, with a resonant frequency near the external vibrations, but minimizing the movement in both perpendicular directions.

Therefore, since we have several single cells, each one with its suspension, and taking into account the series and parallel spring constant conversion simplification, it can be calculated the required stiffness for each single suspension.

Table 3.2. Design layout dimensions

Parameters	Value	Units	Description
w_f	10	µm	Finger width
L_p	40	µm	Overlapped length between two adjacent fingers
L_f	50	µm	Finger length
t_f	5.87	µm	Finger thickness
N_g	6		Number of gaps in a cell side
d_f	12.5	µm	Initial distance between two fingers
a	20	µm	Length of span-meander beam
b	40	µm	Length of U-shape suspensions
w_s	0.9	µm	Suspension width
d_{stop}	0.2	µm	Minimum allowed distance between two adjacent fingers (physical stop).
t_{sub}	720	µm	Chip substrate thickness
A_{cell}	100 x 100	µm^2	Single scavenging cell area
E_{Al}	$7.7 \cdot 10^{10}$	Pa	Young's modulus of Aluminum
ρ_{Al}	2300	kg/m^3	Density of aluminum
ρ_{Si}	2500	kg/m^3	Density of silicon

If N_{cell} is the number of cells in the chip, the equivalent spring constant for each cell, k_{cell}, will be:

$$k_{cell} = \frac{k_{chip}}{N_{cell}} \tag{3.6}$$

In the same way, to calculate the spring constant, k_{susp}, of each of the suspensions, N_{susp}, forming the cell flexures it can be used:

$$k_{susp} = \frac{k_{cell}}{N_{susp}} = \frac{k_{chip}}{N_{susp} N_{cell}} \tag{3.7}$$

In order to achieve this behavior, it is needed to use microsuspensions such as the U-spring, serpentine or folded beam types [16-20]. In any case, microsuspensions can be modeled through their equivalent effective stiffness, which can be defined in the three-directions of the space, depending on each design.

As shown in Table 3.3, several mathematical expressions modeling this kind of suspension have been extracted from the literature [16-20] to try to reproduce its real behavior.

From Table 3.3, it is clear that the model called "serpentine II" is the one that gets a resonant frequency closer to the simulated value of 200 Hz that will be shown in the next section. Moreover, the resonant frequency of the energy scavenging cell is almost identical to the value that will be simulated and measured. Another important issue to take into account, when choosing a scavenger configuration, is the maximum deflection that the structure will reach. There are the static deflection due to the gravity and the dynamic deflection due to the resonance effect.

Table 3.3. Comparison among different suspension models for lateral in-plane motion

Suspension model	Expression of suspension stiffness $\left(\text{with } I = t_f w_s^3/12\right)$	k_{susp} (N/m)	k_{cell} (N/m)	Freq cell (Hz)	Freq chip (Hz)
Equivalent beam	$\frac{E}{4} t_f \left[\frac{w_s}{2b}\right]^3$	0.12	0.49	12.52	70.83
U-type [16]	$\frac{3EI}{2a^3 + 3a^2 b}$	1.29	12.01	2.73E+08	229.26
Serpentine I [17]	$\frac{E}{n} t_f \left[\frac{w_s}{b}\right]^3$	3.00	5.15	4.16E+04	352.03
Serpentine II [18, 19]	$\frac{12EI\left[n(a+b)-b\right]}{b^2(n-1)\left[(3a^2+4ab+b^2)n+3a^2-b^2\right]}$	0.92	3.69	2.31E+04	194.16

The out-of-plane stiffness of this suspension can be calculated as [19]:

$$k_z \approx \frac{48GJ}{a^2\left(\left(GJ / EI_{x,a}\right)a + b\right)n^3} \tag{3.8}$$

where G is the torsion (or shear) modulus of elasticity, and J is the torsion constant. The torsion modulus is related to Young's modulus and Poisson's ratio, υ, by:

$$G = \frac{E}{2(1+\nu)} \tag{3.9}$$

The torsion constant is a geometrical property of a beam's cross-section which is involved in the relationship between angle of twist and applied torque along the axis of the bar, for a homogeneous linear-elastic bar. Its value can be approximated to [21]:

$$J \approx t_f w_f^3 \left(\frac{1}{3} - 0.21 \frac{w_f}{t_f} \left(1 - \frac{w_f^4}{12 t_f^{\,4}} \right) \right) \tag{3.10}$$

From (3.8), (3.9) and (3.10), a value of 1.01 N/m can be calculated for the out-of-plane stiffness.

It can be estimated the out-of-plane static deflection as,

$$z_{Static} = \frac{m_{chip} g}{k_{Z-axis}} = \frac{g}{\omega_{Z-axis}^2}, \tag{3.11}$$

where m is the scavenger mass, $k_{Z\text{-}axis}$ is the effective stiffness of the whole chip in the z-axis, $\omega_{Z\text{-axis}}$ is the equivalent resonant frequency in the same direction, and g is the gravity acceleration, 9.81m/s^2. This means a static displacement of 6 µm due to the chip mass. On the other hand, the maximum dynamic deflection at steady-state can be approximated to,

$$z_{Dynamic} = Q_f \frac{m A_{acc}}{K_{mov}} = \frac{Q_f A_{acc}}{\omega^2}, \tag{3.12}$$

where Q_f is the effective quality factor of the scavenger, m is the scavenger mass, K_{mov} is the stiffness in the movement direction and A_{acc} is the amplitude of the environmental vibration acceleration.

For a typical low-magnitude environmental acceleration, ω = 2π·200 Hz and A_{cc} = 0.8 m/s^2. Also it is estimated a typical quality factor of $Q_f \approx 50$, but taking into account the equivalent electrostatic damping, it is taken a final value of $Q_f \approx 25$, which is extracted from whole motion equation solution. Hence, the typical dynamic displacement for these vibrations is around 12.5 µm.

On the other hand, it can be estimated the maximum length of the fingers, if it is considered that the resonant frequency of the fingers should be one order of magnitude higher than the frequency of the oscillations. It can be found a maximum length of about 100 µm.

3.3.2 Electrical connection among energy scavenging cells

Several different electrical connections among energy scavenging cells are possible. This connection depends on the number and distribution of the cells. The important thing here is that the only points which will be electrically and mechanically connected with the outside are the central suspended plate of each cell. Thus, the minimum number to obtain the two outputs correspond to the two electrodes of the total capacitance is two, and both cells have to be cross-connected as Figure 3.8(a) shows.

With the same concept, it can be grouped several cells in 1-D (Figure 3.8(b)) or 2-D arrays (Figure 3.8(c)). Nevertheless, in order to have a large number of cells, it can be connected the cells with a more suitable layout as it is shown in Figure 3.8(d). In this case, it is connected all the central parts and the anchored electrodes and finally using a cross-connected pair of cells, the external connection for these electrodes is provided. Although, since the effective stiffness of the suspensions of every single cell is inversely related to the number of cells, the most numerous, the stiffest, and therefore the largest suspensions. This problem could be solved

by removing the most of the suspensions and creating an array of interconnected cells, similar to a thin comb-type shuttle.

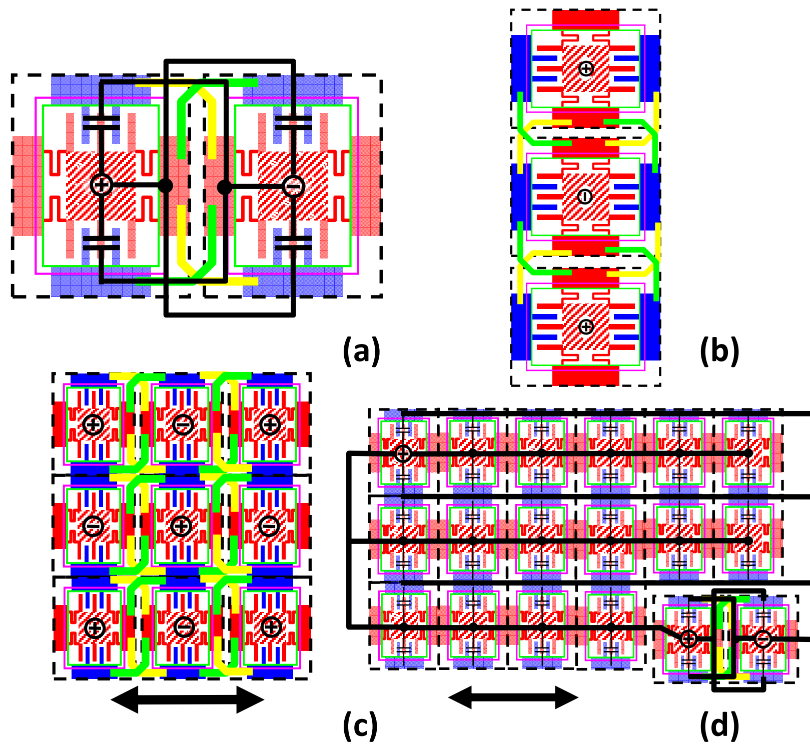

Figure 3.8. Cross-connected pair of energy scavenging cells (a), array (b) and matrix (c) of energy scavenging cells electrically connected, and parallel electrical connection among scavenging cells (d)

3.4 Fabrication process of the EHoC

It can be divided the fabrication process of this type of device in three different parts to obtain a functional vibration-based microgenerator.

3.4.1 First step: Chip fabrication

In this step, the chip was fabricated using a 0.35 μm CMOS technology, which has four metal layers and two polysilicon layers. It has been taken advantage from standard CMOS technologies in order to create functional MEMS structures [3, 6, 8, 9, 22] during the last decade. In this case, the metal layers are used like structural layers, and the oxide layers as sacrificial layers. Therefore, when the structures are fabricated in the commercial foundry, a wet-etching post-process with a buffered HF-based solution is performed in order to release the movable structures (see Figure 3.9).

A total of 30 chips with a size of 3610 x 2850 m^2 were received from the foundry. The chip layout is shown in Appendix B, where it can be observed that the layout contains numerous designs of RF MEMS resonators and oscillators, in addition to the four cross-connected pair of energy scavenging cells.

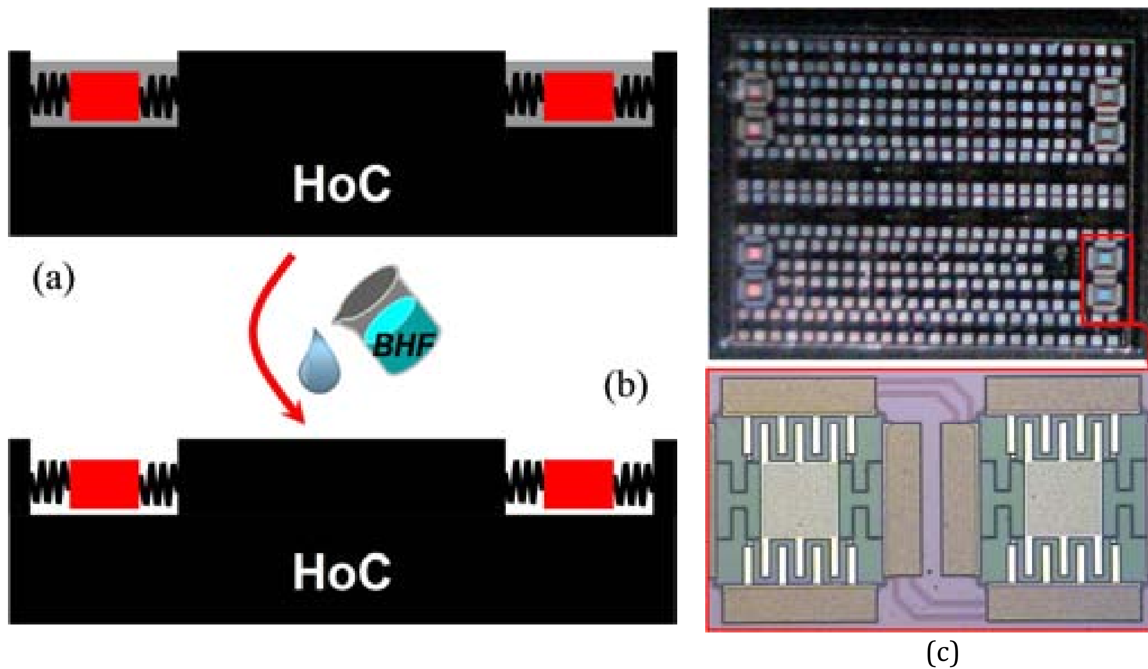

Figure 3.9. Chip fabrication process steps: In-foundry standard CMOS fabrication process (a) and out-foundry maskless BHF etching to release the movable structures (b). Optical image of the chip (c) and detail of two energy scavenging cells (Inset).

However, a drawback of using CMOS technology to develop scavengers is the low mass available with these layers, therefore actually it is necessary to deposit an additional dense material on the top [23] or another type of external mass [24]. Nevertheless, the use of the novel concept of harvester-on-chip can solve this problem.

3.4.2 Second step: Substrate fabrication and bonding balls deposition

This step describes how the support substrate has been fabricated. The substrate could be another electronic chip that will be supplied by the microgenerator or a dedicated substrate fabricated to match the resonant frequency with the environmental acceleration spectrum peak. In this work a PCB substrate has been used, which is the least complicated and expensive fabrication technology to define the electrical connections which allow us to perform a preliminary electrical characterization.

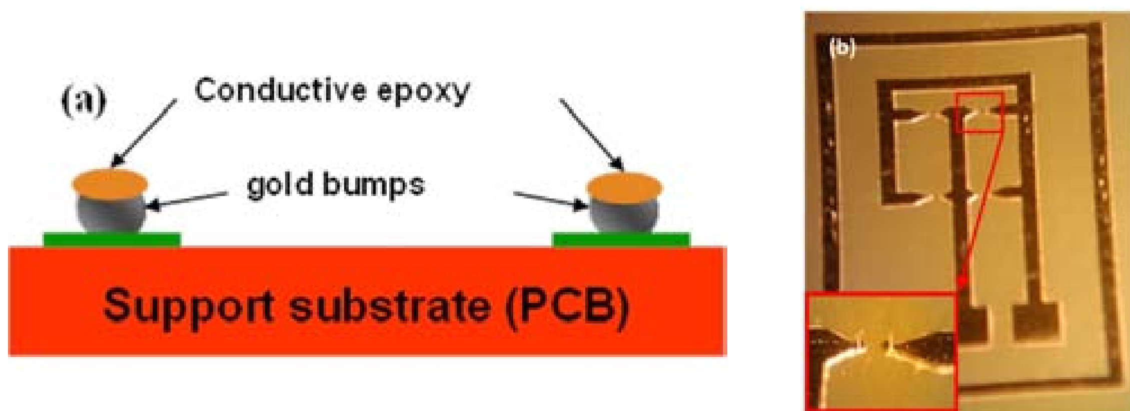

Figure 3.10. Sketch (a) and optical image (b) of the PCB substrate with bonding balls to perform the pseudo-flip-chip bonding. Inset: detail of gold ball bumps placed into the pads.

When the tracks and the pads were patterned in the copper layer that was gold-coated by electrodeposition, a gold ball bumps were placed on top of these pads. The inset of the Figure 3.10(b) shows the shape of a ball bumps that were created by the wire bonder. In order to flatten the peak of the ball bump and create a flat, it can be used a coining process consisting of the application of force that “smashes” the peak into a smooth flat surface [25]. It was carried out with the help of a glass slide and the chuck of a probe station, Suss Microtech MS8, which has micrometric control of the height. Afterwards, it was manually applied a tiny dot of conductive epoxy to the top of each gold stud.

Therefore the dot of epoxy will provide the “glue” to hold the two surfaces together and complete the electrical path (Figure 3.10(a)). The material used in this step was the two-part silver-loaded conductive epoxy Chemtronics CW2400, which cures at room temperature.

Together, the solder material and the metallic contact, have to form an elevation, which will be the separation between the support substrate and the EHoC. After this step both parts, substrate and chip, will be ready to be assembled.

3.4.3 Third step: EHoC assembling

As Figure 3.11 shows, the assembling between the EHoC and the support substrate has to be performed. This procedure is extremely delicate, because the cell suspensions are fragile and the bonding forces could break these ones. A technique similar to a flip-chip bonding was developed to align and assemble the both parts.

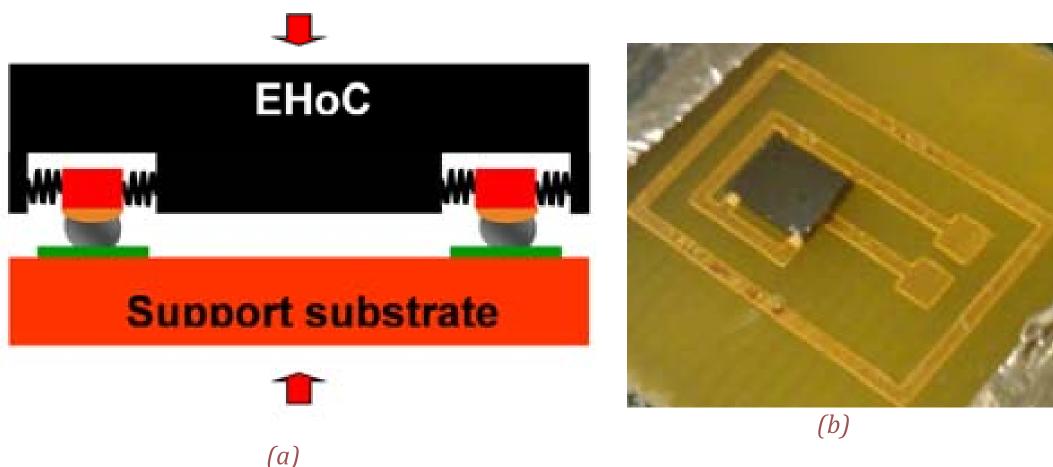

(b)

(a)

Figure 3.11. Sketch (a) and optical image (b) of the EHoC assembling process with a support substrate.

The alignment between the chip and the PCB was carried out with a component alignment system (ERSA PL 550) which allows us to precisely place the EHoC over the PCB substrate, and match the epoxy-coated PCB bumps with the chip pads.

3.5 Simulation results of the prototype

Here, it is presented the simulations of this specific design developed by means of an FEM tool and numerical calculations. These results are extremely useful to prove the feasibility of the designed device.

FEM simulations

Several FEM simulations have been performed using COVENTOR® software [26]. In the whole chip modal simulation shown in Figure 3.12, it can be seen that the resonant frequency of 285 Hz is higher than the required frequency of 200 Hz, which has been used as a design specification. The use of maximum allowed mesh, because of the problem of having a huge device with tiny elements, is still not enough to obtain an accurate result. However, the resonance frequency calculated from the simulation of a single cell (Figure 3.13) gives us a value of stiffness in accordance to the theoretical value calculated in the last section and collected in Table 3.4.

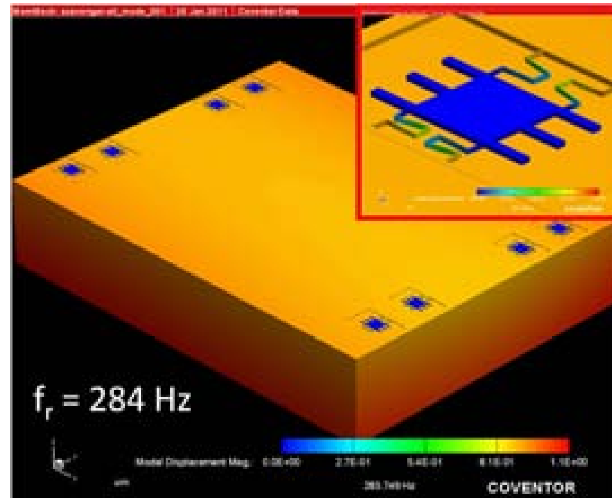

Figure 3.12. Modal simulation of the whole chip (Resonance frequency at 284 Hz).
Inset: Deflected single cell suspensions.

Simulation of suspensions behavior, such as the dynamic response at resonance or the static response to see the vertical deflection due to the chip and the single anchoring plate weight, are really useful to perform the first device operation validation.

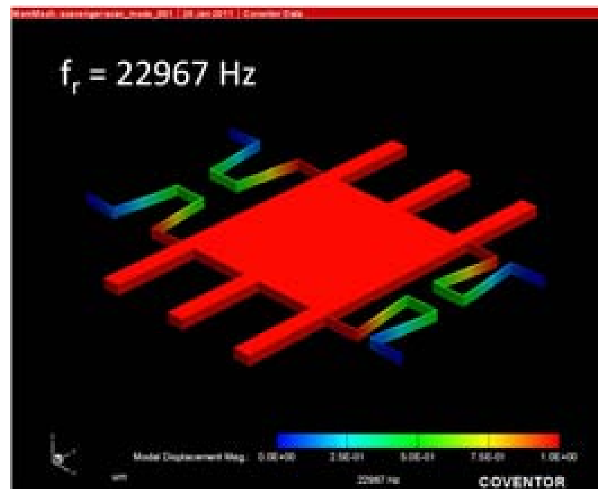

Figure 3.13. Modal simulation of a single cell (Resonance frequency at 22.97 kHz).

Also, the harmonic response allows us to know the real expected displacement amplitude for a specific harmonic excitation. With the design rules from the theoretical expressions of the last sections and using these simulation tools, the proof of concept prototype was

designed. This chip has four pairs of electrically cross-connected scavenging cell pair, distributed near the four corners.

In order to achieve a flexible spring in the surface chip plane, but the hardest spring possible in the perpendicular direction, four U-type suspensions were designed and validated by means of simulations. If the suspension is not hard enough along this direction, the suspended mass could collapse with the substrate due to gravity and the capillary forces which appear in the typical drying step because of the creation of a gas-liquid interface.

In order to demonstrate the validity of the approximation for spring association used in (3.6) and (3.7), four modal simulations with the cell mass suspended by different number of flexures have been performed. From the value of the resonant frequency and the effective mass, it can be calculated the effective stiffness of the cell and consequently the one for each suspension. It can be seen that the equivalent stiffness values of every suspension are very similar, verifying the use of this approximation here. The last row in the Table 3.4, try to point out the behavior difference between an identical U-type suspension without the span beams that connect the U-shape to the cell and the anchor and the case with this additional beams. This simulation can explain the resulting values showed in the Table 3.4 of the theoretical expression of the U-type suspension.

Table 3.4. Suspension simulation report

Simulation type	Frequency (Hz)	Effective mass (kg)	k_{cell} (N/m)	k_{susp} (N/m)
4 suspensions	2.30E+04	1.76E-10	3.671	0.918
3 suspensions	1.99E+04	1.76E-10	2.757	0.919
2 suspensions	1.63E+04	1.75E-10	1.840	0.920
1 suspensios	1.16E+04	1.74E-10	0.920	0.920
U-type	1.59E+04	1.76E-10	1.747	1.747

Real structure versus Simplified model simulations

Because of the nature of the technology used to build the energy scavenger, a homogeneous layer of metal cannot be obtained to create the micromachined structures. Instead, a multilayered stack of metals joined by vias can be achieved. The fact of having this special constitution changes the mechanical behavior of the fabricated structures with respect to the expected one of the same structures made of a single thick layer. The I-shape is expected to increase the vertical component of the inertial moment of the beam and consequently the elastic constant of the beam is expected to increase too. That means an increment of the robustness and vertical-motion resonant frequency. In order to compare the behavior of a real multi-layer suspension fabricated with CMOS technology working as a spring with an equivalent ideal monolayer beam, several simulation have been carried out.

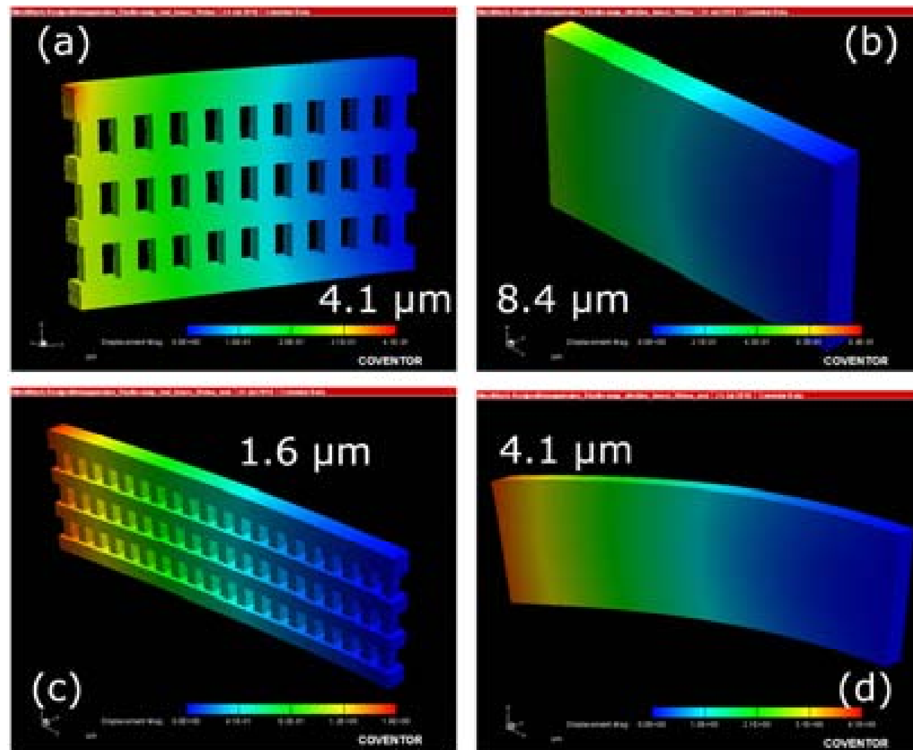

Figure 3.14. Comparison between the vertical deflection of the real multilayered structure (a and c) and a single-layer model (b and d) for two different cantilever lengths where acting a 1 μN vertical force over the free end.

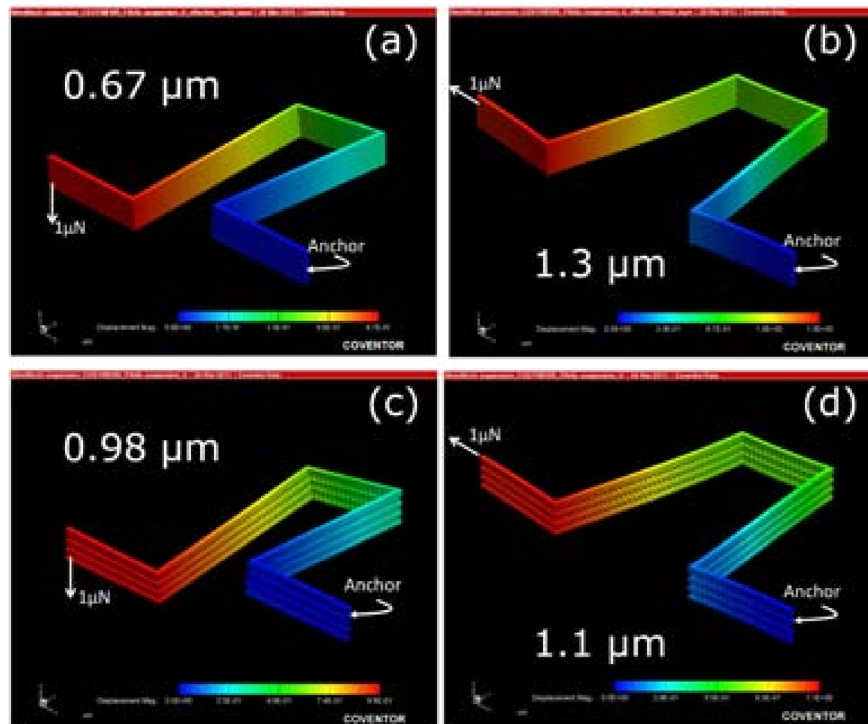

Figure 3.15. Simulation of the deflection suffered by a single-layer model (a and b) and the real multilayered structure (c and d) of an U-type suspension when acting an out-of-plane and in-plane force (1 μN) at the free end of the suspension.

From Figure 3.14, it can be observed that the stiffness of the cantilever is incremented for the real structure. The next step is to prove this fact in the U-type suspensions used to hold

the inertial mass (or anchoring pad) of the energy scavenging cells (or EHoC). After simulating the whole suspension (Figure 3.15), it is demonstrated that the rigidity improvement is true for the in–plane movement, but it does not work for the out-of-plane deflection, which is the opposite of the optimum effect. From these simulations, the effective elastic constant of the U-type suspensions can be calculated and they are shown in Table 3.5.

Table 3.5. Simulated effective elastic constant

Stiffness (N/m)	In-plane	Out-of-plane
Simplified suspension	0.751	1.493
Real suspension	0.966	1.017
Stiffness agreement	78%	68%
Resonant frequency agreement	88%	83%

3.5.1 MATLAB electromechanical simulation of the charge-constant cycle.

The MATLAB® code described in Chapter 2 has been utilized to solve the differential motion equation (11) for this designed chip and the supposed environmental vibration. Several plots can be generated from the complete motion equation solution, and they are very useful to know the expected behavior that the system will have in operation.

In Figure 3.16 (a), it can be seen the increase of the amplitude due to the effect of the resonance, and how the system reaches the stationary state with an expected resonant maximum displacement of 11.6 µm, which is close to the maximum possible amplitude of 12.3 µm, corresponding to the comb-drive finger distance. Also, the velocity of the system is represented in the same plot. The Figure 3.16(b) shows the different forces actuating in the system. It is interesting to see the shape of the non-lineal electrostatic force and its damping effect on the movement. Note that the damping and electrostatic forces are more than one order of magnitude lower than the mechanical force due to the equivalent spring constant of the suspension. That is the reason why the solution shape is very similar to a typical damped spring-mass system.

The charge and capacitance values against the time are shown in Figure 3.17(a), where it can be appreciated that the charge is forced to be zero when the minimum capacitance is reached. The voltage in the variable capacitor (Figure 3.17(b)) goes from the initial voltage to almost 31 V, because of the ideal constant-charge cycle that is performed. Also, it can be seen that there are two peaks by period for this transduction type. From our experience, this voltage can be supported by MEMS fabricated with the metal layers of this technology.

Taking into account the theoretical expressions, the final chip design and the last results of solving the complete motion equation, it can be obtained the expected features of the fabricated prototype and the extrapolation to a full EHoC with scavenging cells into the whole chip surface (see Table 3.6). The power density values are especially interesting, which are comparable to the state-of-the-art values, taking into account that a CMOS technology is being used. Against this point, it will be needed conversion electronics, and that parasitic capacitances and other non-ideal factors are going to decrease this expected extracted power.

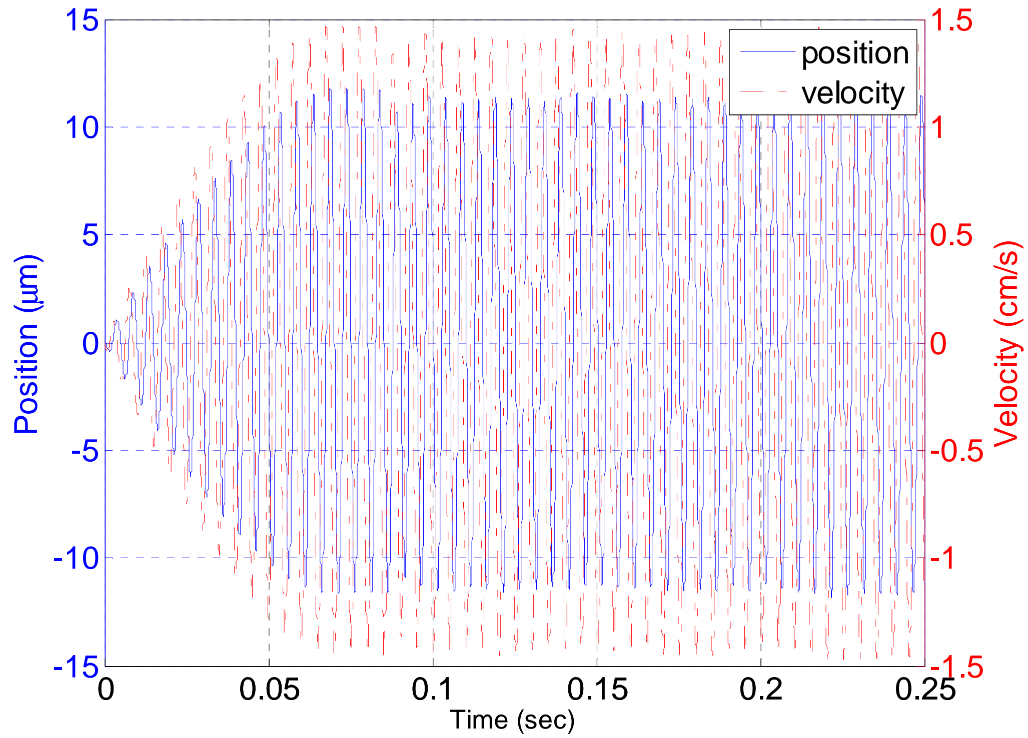

(a)

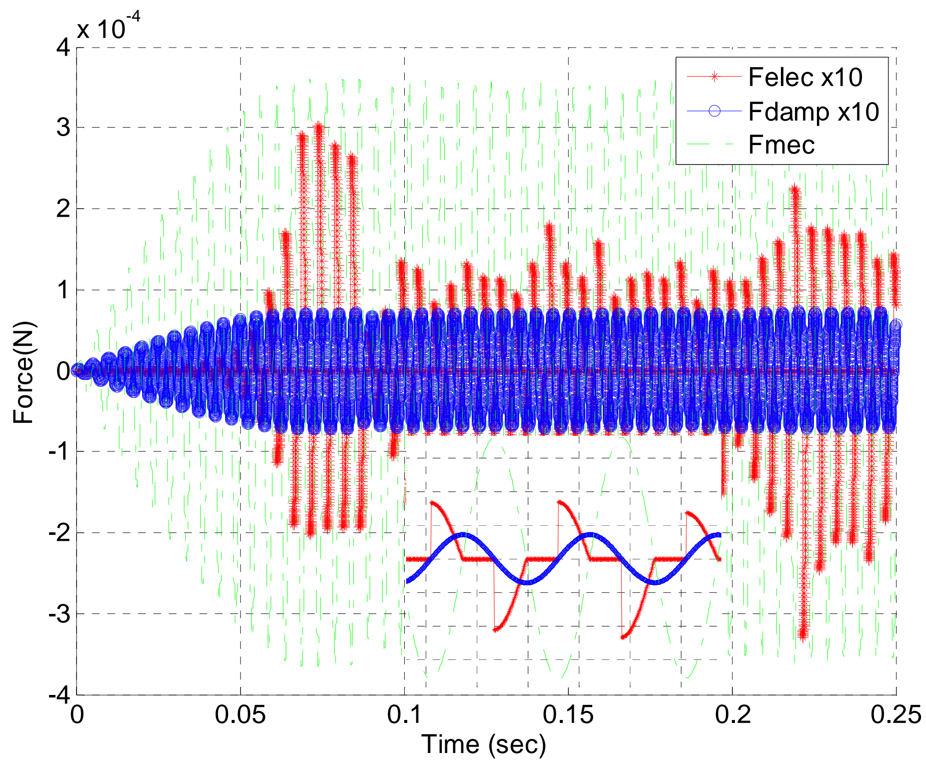

(b)

Figure 3.16. Displacement and velocity (a) and forces (b) for the complete system, when an ambient acceleration is actuating on it (acceleration = 0.7 m/s²).

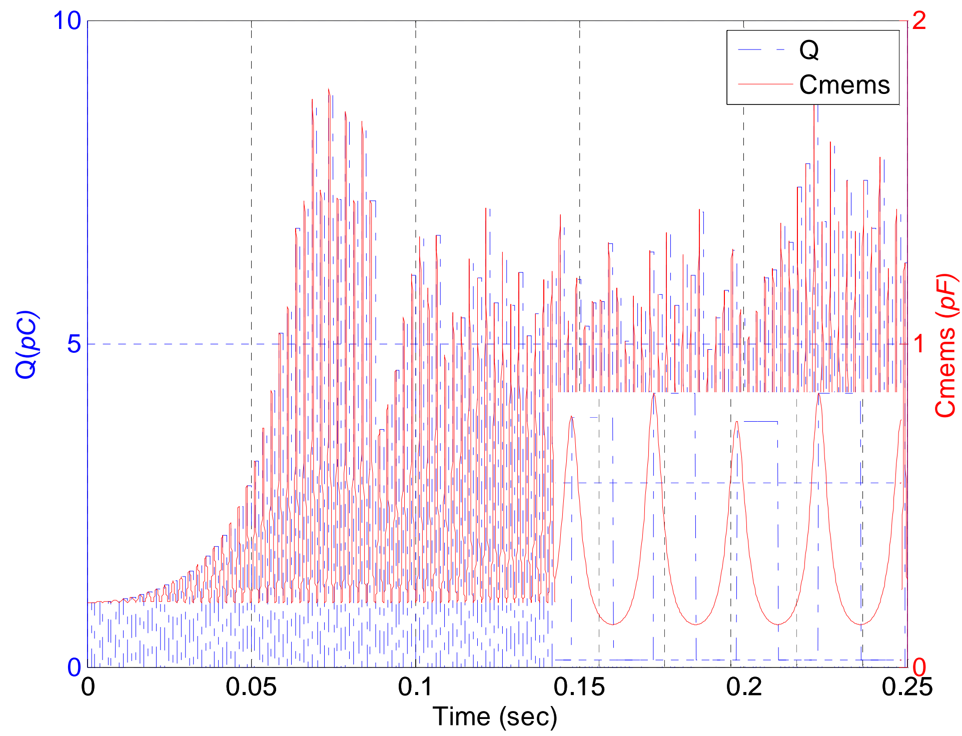

(a)

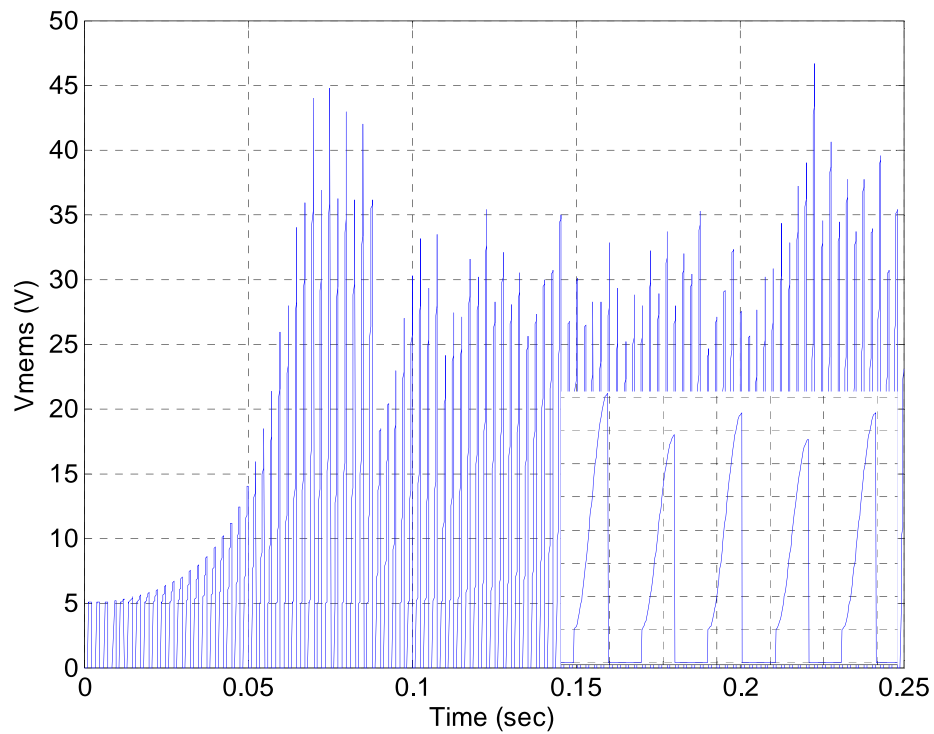

(b)

Figure 3.17. Charge together with total capacitance (a) in the energy scavenger (100 scavenging cells) and voltage (b) across it.

In case of fabricating a conventional non-HoC scavenger, i.e. two comb-drivers and one single large mass, by using this CMOS technology, the inertial mass must be made of the metal layers stack. This means that it will be necessary an area of around 800 mm^2 in order to have the same mass, and multiplying by the chip thickness, it is obtained 320 mm^3. Moreover, there is an additional drawback, which is the capacitance reduction due to the loss of part of the transduction area, only dedicated to form the inertial mass. Therefore, in this case, the extracted power will be similar to one row of cells, i.e. around 280 cells for the calculated chip size, and the extracted power will be around 170 nW. If it is calculated the final power density for this device, it is obtained around 530 nW/cm^3. From this simple estimation and taking into account that they are maximum ideal power values in both cases, it can be seen that with the application of the EHoC concept, instead of using the classical approach, it can be increased more than 10 times the extracted energy density (up to 200 times if the resonance motion is maximum).

Table 3.6. Expected EHoC electrical features extracted from simulated results

N_{cell}	8 (prototype)[a]	100 (full EHoC)[a]	100 (full EHoC)[b]
C_{max}	117 fF	1.46 pF	6.40 pF
C_{min}	16 fF	200 fF	200 fF
V_{max}	36 V	36 V	157 V
ΔU_{per}	27 pJ	113.57 pJ	2.44 nJ
Power	3.63 nW	45.43 nW	0.98 µW
Power Density	0.46 µW/cm^3	5.78 µW/cm^3	110 µW/cm^3
$V_{initial}$	5V		

[a] Simulated values for a resonant motion amplitude of 11.6 µm, which is extracted from the stationary solution of the complete motion equation for an environmental vibration of 0.7 m/s^2 to 200Hz.

[b] Maximum values when resonant motion amplitude is 12.3 µm, which is the maximum allowed by the sttopers.

3.6 Mechanical characterization

Some measurements have been carried out to determine the mechanical behavior of this device. Visual inspection was the first characterization to be performed. The resonance motion of the scavenging cells was excited and its amplitude was measured with an ad-hoc experimental setup.

3.6.1 Optical and Electron Microscope inspection

The first characterization performed was the optical inspection, resulted in images of Figure 3.18. This first inspection allows determining which cells result collapsed after the last releasing step, due to the capillary forces during the drying step.

In Figure 3.18, it can be clearly seen that the energy scavenging cells are collapsed to the substrate, because the difference between the heights of the fingers is the same than the distance between the cell bottom and the substrate, i.e. around 1.2 µm (Figure 3.19(a)).

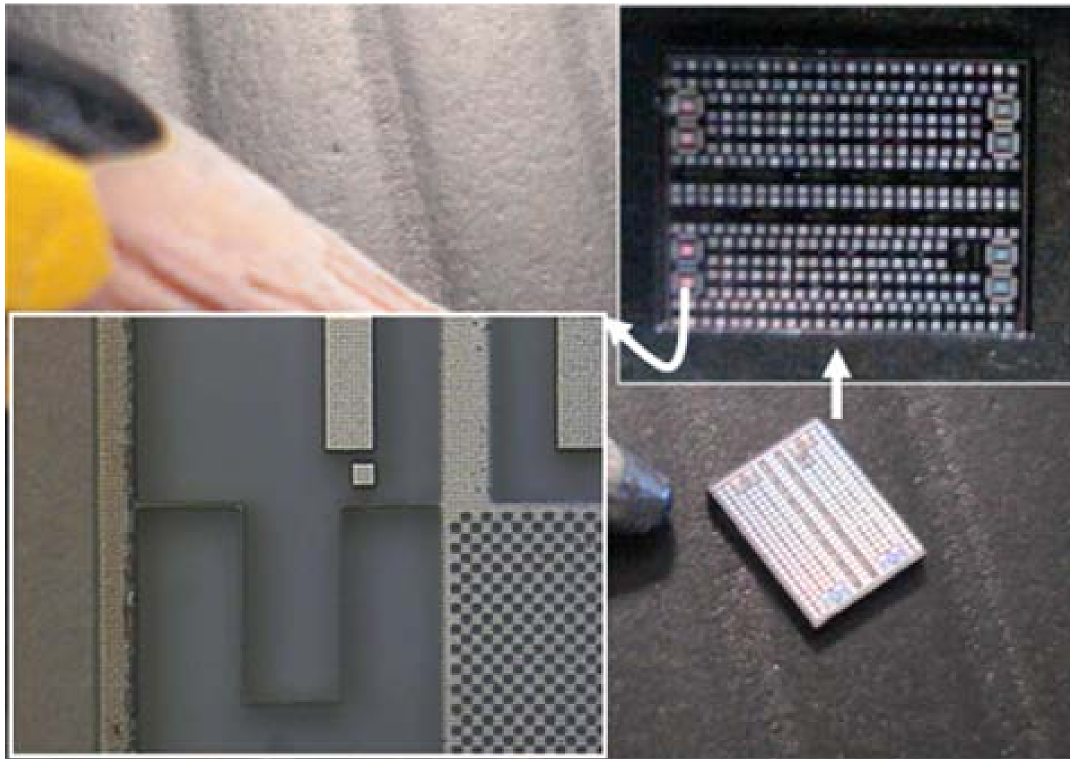

Figure 3.18. Optical image of a fabricated chip. Inset: Detail of clear focus difference between the anchored driver and the inertial mass adhered to the bottom.

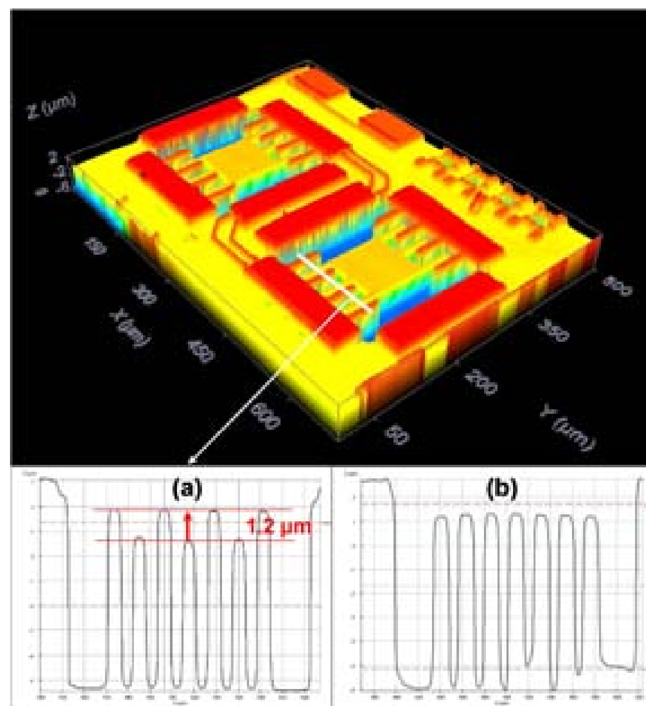

Figure 3.19. 3-D profile of a pair of scavenging cells with cross section detail in fingers: collapsed (a), and non-collapsed (b) structures.

Afterwards, several chips were processed with a critical point drier (CPD), in order to avoid these forces. The 3-D profiles (Figure 3.19(b)) of a pair of scavenging cells show that the cells are not collapsed after this process.

From the SEM images shown in Figure 3.20, it can be seen that all the sacrificial oxide is removed and the structure is release. It can be achieved due to the presence of holes in every scavenging cell. They allow the penetration of the HF under the scavenging cells to etch the sacrificial silicon oxide. It can be also seen in the inset details that the aluminum of the metallic layer has been partly etched, because of the long BHF solution etching time.

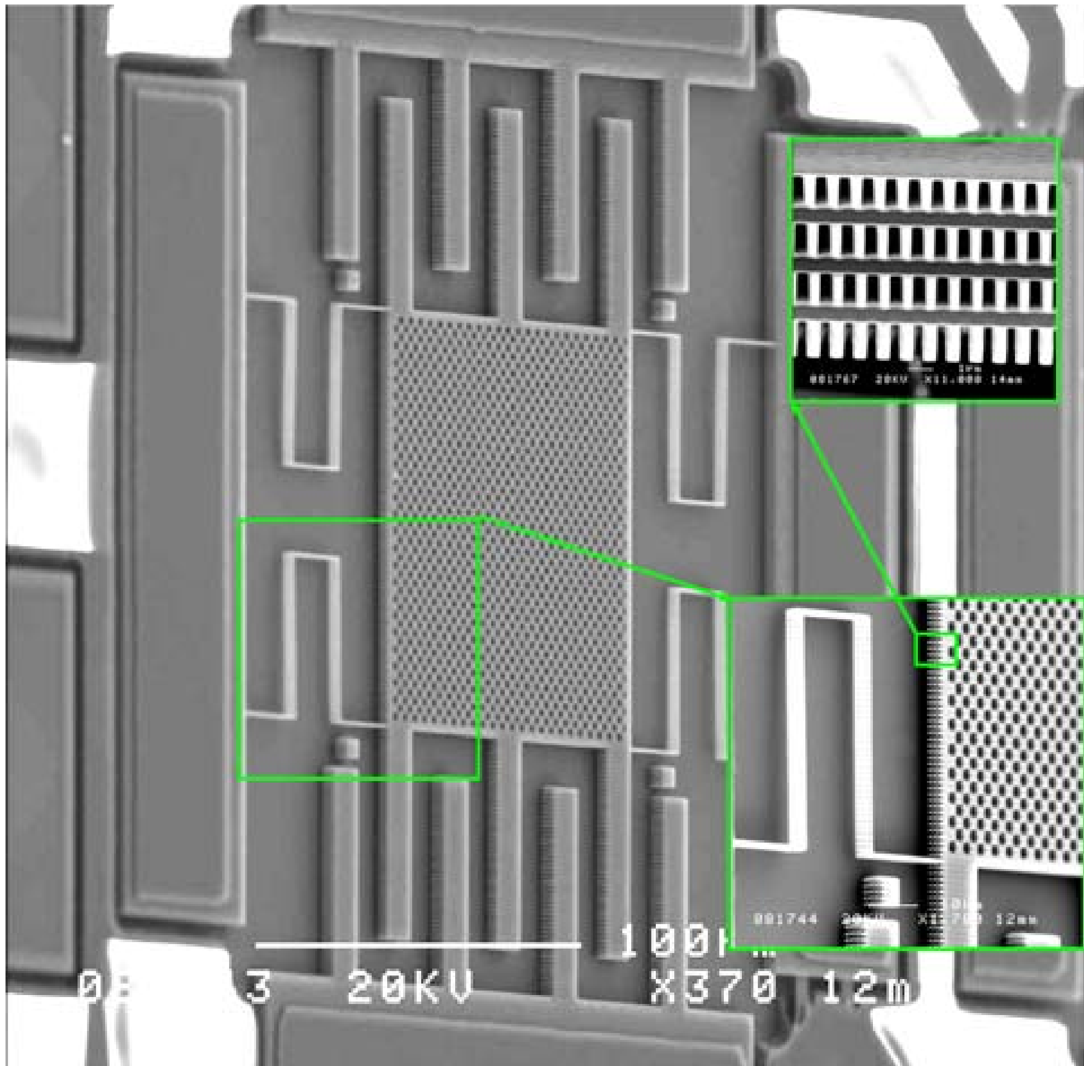

Figure 3.20. SEM images of a scavenging cell. Inset: detail of suspensions and layer stack.

3.6.2 Measurement of the resonance frequency of the energy scavenging cells

After the releasing of the structures and before the flip-chip process, the first step was measuring the resonant frequency of the energy scavenging cells, one by one. In order to perform this characterization, the measurement optical system shown in Figure 3.21 was setting up.

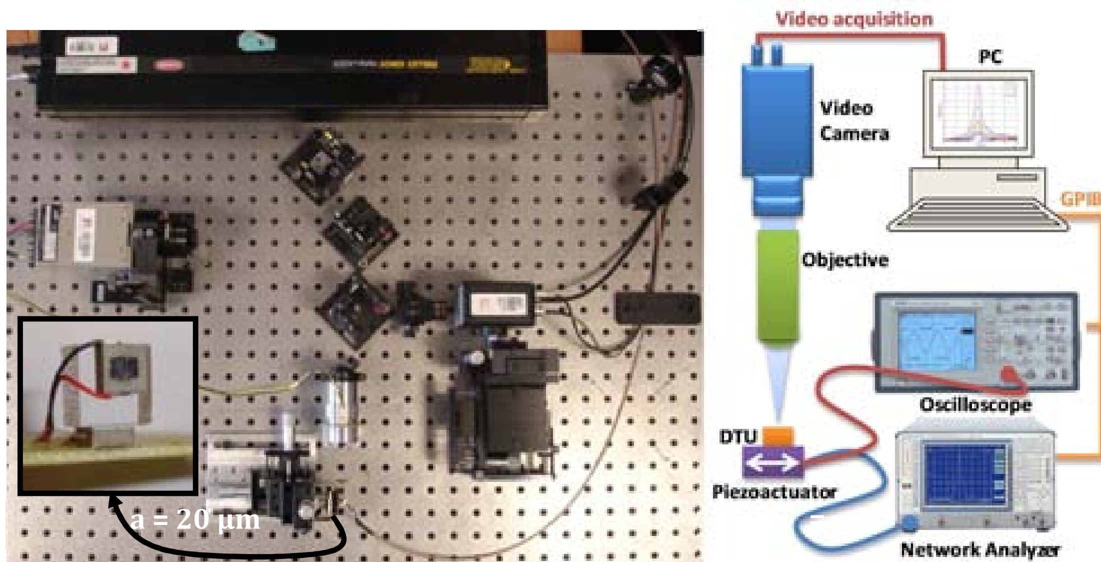

Figure 3.21. Picture (a) and diagram (b) of the optical setup to measure the resonance frequency of the energy scavenging cells. Inset: biaxial piezoactuator to mount the chip and move it along two different directions of space.

The working principle of this characterization system is pretty simple. On one hand, the piezoactuator is excited by the network analyzer while an oscilloscope is measuring the peak-peak voltage over the actuator. Both instruments are controlled by the MATLAB program running on the PC and connected through GPIB. On the other hand, in order to capture the resonant motion of the movable structures, a video camera with a large focal distance objective is used. The image is processed by the PC, which is able to detect and quantify the motion amplitude. Then, a frequency sweep can be carried out to different input acceleration values. In Figure 3.22, it is shown the optical image captured by the camera when the input frequency does not match with the resonant frequency of the cell (a) and the case of the cell at resonance (b).

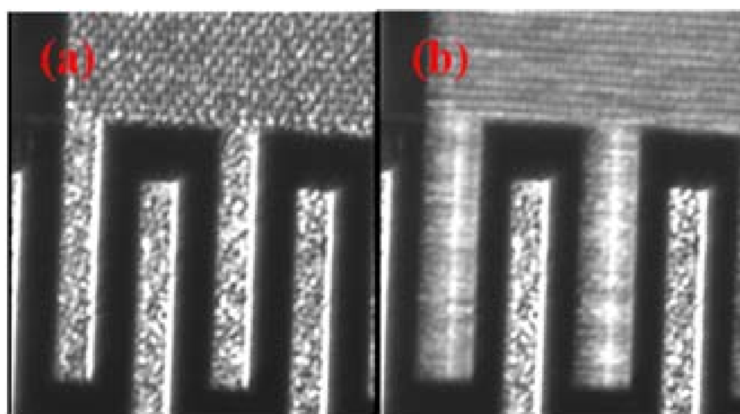

Figure 3.22. Optical image representing an energy scavenging cell out of (a) and at resonance (b).

The code MATLAB is capable to generate graphs as shown in Figure 3.23 or Figure 3.24. A frequency sweep has been performed for four different actuation voltage values. In order to calculate the acceleration associated to each input peak-peak voltage, the specifications of the

piezoactuator have to be used. The biaxial piezoactuation module is formed by two identical piezoelectric actuators, PL055.30 from PI, which has a nominal displacement of 2.2 μm at 100V.

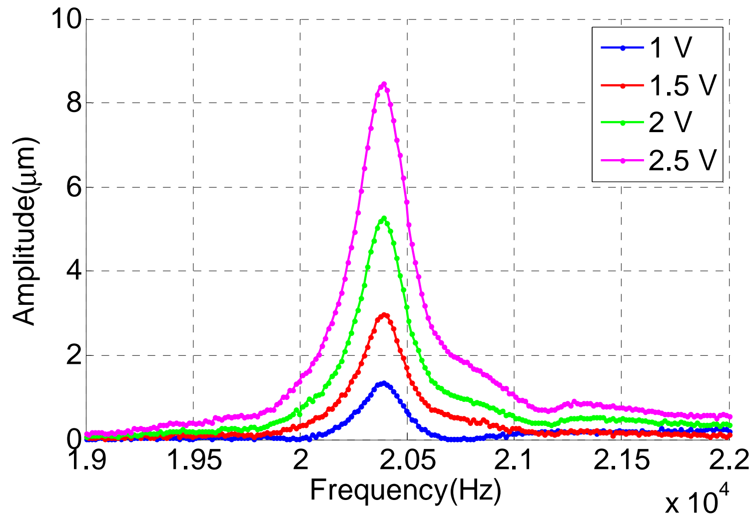

Figure 3.23. Graph resulting from a frequency sweep of the input acceleration that actuates over the cell number 222 of the chip B6 to excite the resonant motion for different peak-peak voltage values.

Table 3.7. Measurements of the resonant peaks of the energy-scavenging cells of B6.

Cell name	Peak-peak Voltage (V)	Input acceleration (m/s²)	Resonant frequency (kHz)	Maximum amplitude (μm)	Q_{factor}
111	1	355	20.21	0.49	158
	1.5	532	20.21	1.30	115
	2	709	20.21	2.84	107
	2.5	887	20.21	5.38	97
112	1	360	20.37	0.67	137
	1.5	542	20.39	1.46	126
	2	721	20.37	3.29	101
	2.5	901	20.37	5.20	95
212	1	343	19.86	0.81	104
	1.5	514	19.87	1.86	80
	2	686	19.87	2.90	87
	2.5	860	19.90	4.83	88
221	1	371	20.66	1.61	81
	1.5	555	20.64	2.98	82
	2	740	20.64	4.42	75
	2.5	927	20.66	6.87	70
222	1	361	20.39	1.36	136
	1.5	542	20.39	2.98	126
	2	722	20.39	5.28	118
	2.5	903	20.39	8.47	101

Therefore, approximating the hysteresis cycle of the actuator to a lineal behavior, it can be easily calculated the nominal displacement for every voltage value. Since the actuator is excited by a harmonic signal, the final motion amplitude can be modeled by a harmonic function multiplied by the peak-peak amplitude. Deriving twice the actuator amplitude function, the module of the acceleration can be extracted.

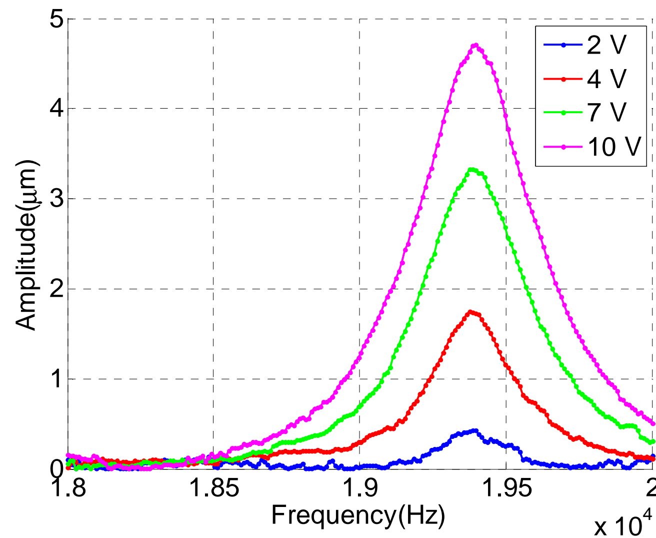

Figure 3.24. Graph resulting from a frequency sweep of the input acceleration that actuates over the cell number 221 of the chip B7 to excite the resonant motion for different peak-peak voltage values.

Table 3.8. Measurements of the resonant peaks of the energy-scavenging cells of B7.

Cell name	Peak-peak voltage (V)	Input acceleration (m/s^2)	Resonant frequency (kHz)	Maximum amplitude (µm)	Q_{factor}
111	2	623	19.87	0.29	14
	4	1150	19.08	0.70	105
	7	2008	19.06	1.99	86
	10	2871	19.07	3.31	74
112	2	554	18.73	0.22	33
	4	1186	19.38	1.47	88
	7	2076	19.38	3.19	73
	10	2969	19.39	4.88	68
121	2	600	19.49	0.34	149
	4	1200	19.49	1.35	86
	7	2102	19.50	2.75	70
	10	3005	19.51	3.11	48
121	2	555	18.75	0.16	149
	4	1114	18.78	0.77	94
	7	1953	18.80	1.95	80
	10	2791	18.80	3.12	70
211	2	613	19.70	0.14	219
	4	1083	18.52	0.64	95
	7	1896	18.52	1.60	77
	10	2711	18.53	2.67	70
212	2	594	19.39	0.43	104
	4	1186	19.38	1.74	80
	7	2078	19.39	3.33	87
	10	2972	19.40	4.71	88
221	2	617	19.76	0.24	79
	4	1153	19.11	1.42	90
	7	2018	19.11	3.03	65
	10	2883	19.11	4.63	65
222	2	657	18.93	0.37	64
	4	1313	18.92	1.03	85
	7	2298	18.91	2.40	73
	10	3283	18.92	3.51	64

The result of the characterization of all the energy-scavenging cells of the first chip is shown in Table 3.7, where only five cells were successfully characterized. The rest of cells had broken suspensions and the resonant motion was impossible to be reached. The mean value of the resonant frequency is 20.30 kHz and the quality factor is 104 in air. These values agree with the simulated results, verifying the approximations used in previous sections.

In case of chip B7 (Table 3.8), all the scavenging cells were successfully released and a mean value of 19.3 kHz was measured for the resonance frequency of the scavenging cells.

3.6.3 AFM measurement of the equivalent out-of-plane stiffness of a single cell

The effective elastic constant of a single cell can be obtained by performing measurement with an atomic force microscope (AFM) [27, 28]. Therefore, a home-made AFM-like setup has been developed over a vibration-isolated optical table. The system (Figure 3.25) consists of a commercial AFM cantilever (k = 0.2 N/m), a laser (λ = 432 nm) and a four-quadrant photodiode detector, operating in a two-segment mode. The deflection of the reflected laser beam on the backside of the AFM cantilever is detected by the photodetector in a differential mode. This deflection can be translated to force acting over the cantilever through the elastic constant.

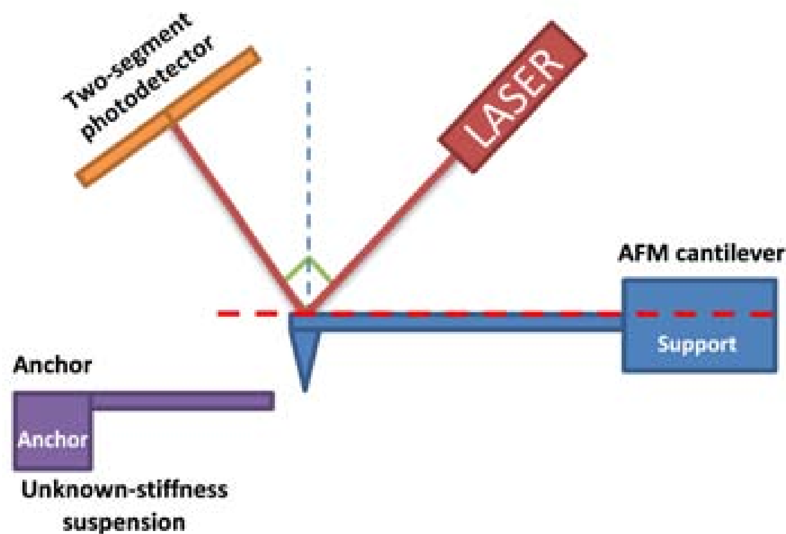

Figure 3.25. AFM-based stiffness measurement setup..

Measurement system calibration

In order to carry out the stiffness measurement, the system has to be calibrated by performing an approaching curve on a hard surface, such as the suspension anchor (Figure 3.26). The AFM beam and the chip to be tested are placed in two three-axis micrometer stage in order to accurately control the relative position of the AFM tip and the suspended cell. The AFM cantilever is mounted over a piezoelectric stage that allows precisely controlling the final tip approach. The piezoelectric stage is controlled via GPIB by a computer that captures the voltage from the photodetector for each tip vertical position.

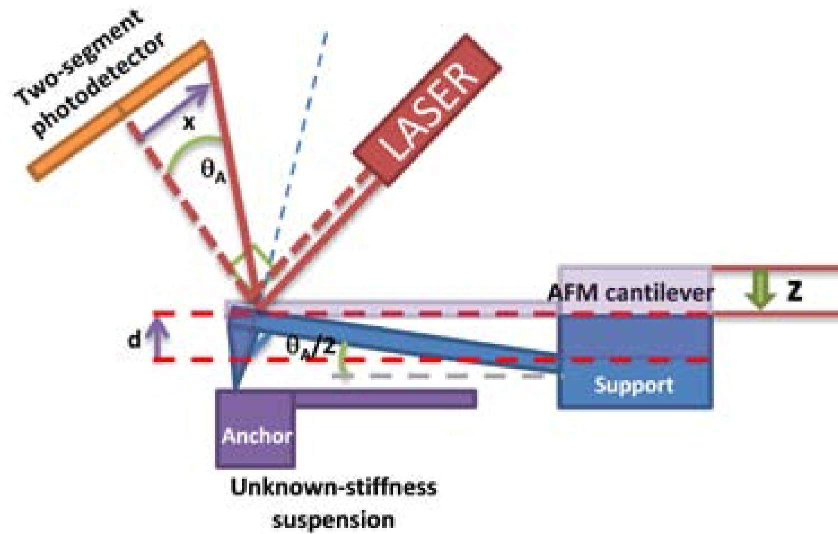

Figure 3.26. Calibration of the AFM-based stiffness measurement system.

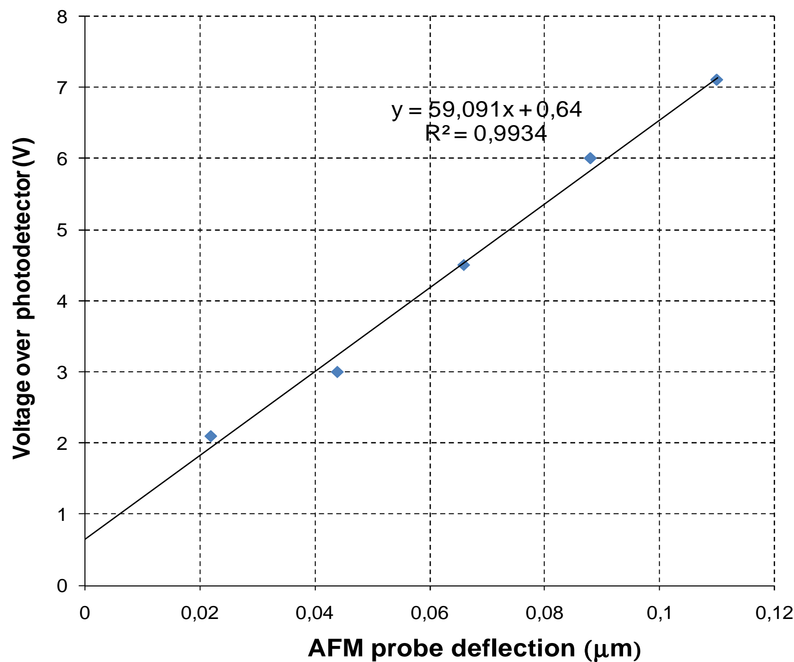

Figure 3.27. Calibration approach curve over a hard surface (5.9 V/μm) .

In that way, it has been achieved a lineal relationship between the AFM probe tip deflection and the voltage generated over the photodetector. As it is shown in Figure 3.27, for small deflection a lineal behavior can be considered and a conversion factor of 590 mV/nm is found.

Test of the method

The next step is to place the AFM tip over the suspension to be measured. In a preliminary test, a commercial cantilever with known elastic constant (2.2 N/m) is used. In that case, when the AFM support is moved toward the test cantilever, both cantilevers suffer a deflection related to the serial combination of these two springs (Figure 3.28).

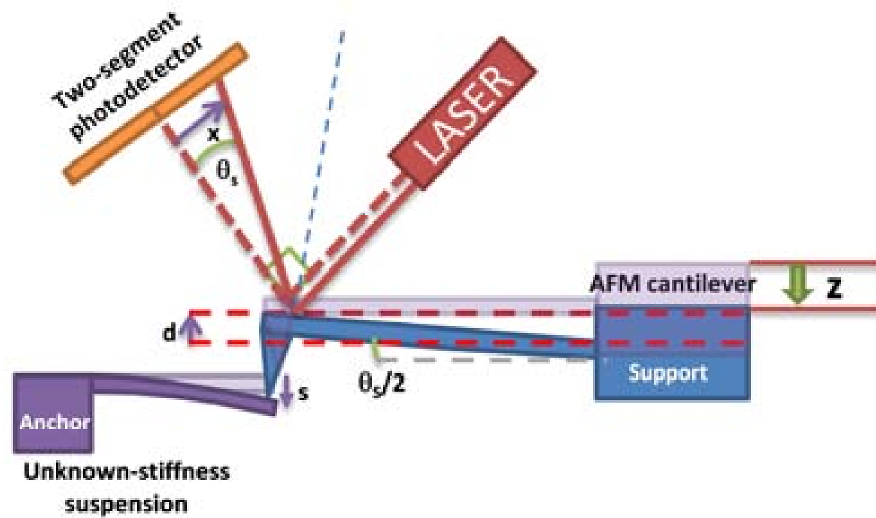

Figure 3.28. AFM-based stiffness measurement procedure.

The force between AFM probe and cantilever sample can be expressed as:

$$F = k_b s = k_{AFM} d \tag{3.13}$$

where k_b and k_{AFM} are the beam and AFM probe elastic constants, s is the deflection of the cantilever sample and d is the deflection of the AFM probe tip. Because the displacement of the AFM support is the sum of the beam and probe deflection, z = s + d, (3.13) can be rewritten as:

$$F = k_{eff} z = \frac{k_b k_{AFM}}{k_b + k_{AFM}} z = k_{AFM} d \tag{3.14}$$

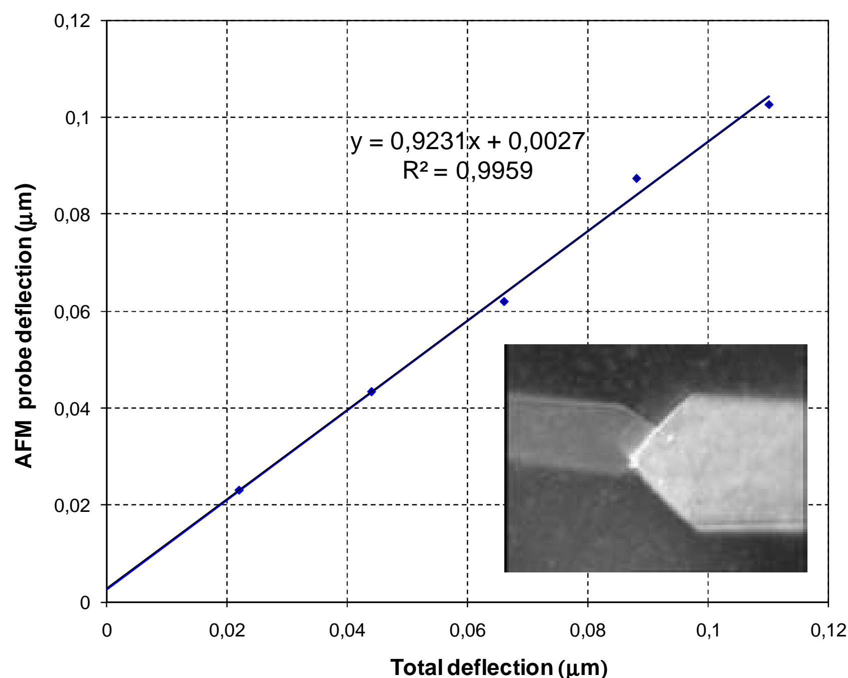

Figure 3.29. Approach curves for the test cantilever over the tip of the test cantilever.

Therefore, the slope of the curve deflection versus z displacement obtained with the AFM gives:

$$slope = \frac{k_{eff}}{k_{AFM}} = \frac{k_b}{k_b + k_{AFM}} \tag{3.15}$$

And the stiffness of the sample cantilever can be calculated as:

$$k_b = \frac{k_{AFM}\, slope}{1 - slope} \tag{3.16}$$

In Figure 3.29, the aproach curve for the sample beam is shown and its spring constant of 2.40 N/m can be calculated from the slope of its lineal regresion curve. This value is quite similar to the expected value of 2.2 N/m, thefore the validity of this procedure has been demonstrated.

Measurement on a scavenging cell

In Figure 3.30 (calibration over a fixed part of the chip) and Figure 3.31 (meassurement over the scavenging cell), the results of the aproaching curves in one of the energy-scavenging cells are presented. From them and (3.16) an equivalent spring constant of 2.89 N/m has been obtained. Taking into account that the cell is suspended by four suspensions, the spring constant of a single suspension is 0.72 N/m. This value is quite close to the theoretical value of 1.01 N/m, but the fabricated suspension seem to be more flexible than the expected along the z-axis, which is an important drawback.

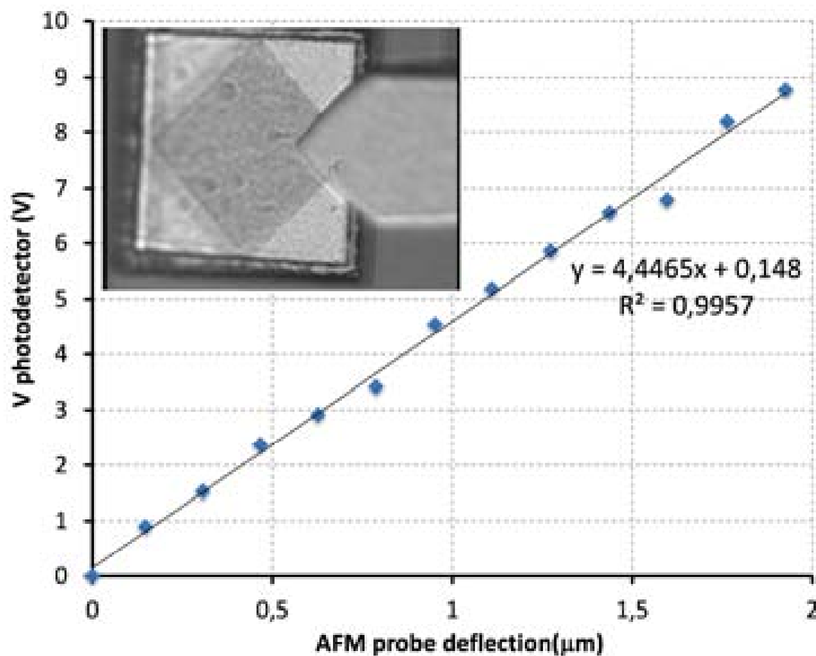

Figure 3.30. Approach curve over the anchor of a suspension (4.5 V/µm).

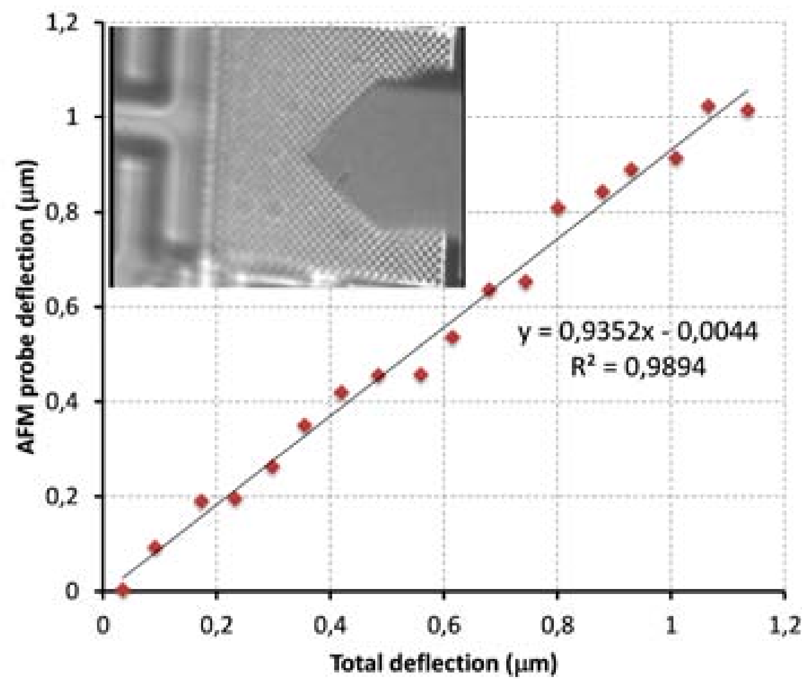

Figure 3.31. Approach curve over the center of the suspended cell.

3.6.4 Post-assemble characterization

Several attempts of assembling the test PCB with the CMOS chips were performed. Unfortunately, even the process (consisting of PCB preparation, PCB-chip alignment and placement procedure) seemed to be successful, the final result was not functional. It was impossible to demonstrate the resonance motion of the whole assembled system. The damage of the suspensions due to the long etching time with the BHF solution could be a decisive factor to take into account in the success of this process. This damage was mainly produced by the practically full etch of the aluminum layer, leaving only the TiN layers interconnected through vias as supporting structure.

3.7 Conclusions and future applications

This chapter reports the detailed theoretical analysis and electromechanical modeling of the concept called energy harvester-on-chip. A complete theoretical study of this type of devices has been developed, and the electromechanical behavior has been simulated by means of FEM tools and a MATLAB® code which solves the complete differential equations system. Using these analyses, a proof of concept prototype was designed and fabricated with a standard CMOS technology. As conclusion of using this type of technology to fabricate this device, we can say that the metallic layers stack thickness is too thin to build a robust enough device. Therefore, the use of a specific MEMS technology with a thicker layer to fabricate the capacitive electrodes and the suspensions would improve the mechanical stability and increase the capacitance values. However, the possibility of successfully fabricate large MEMS structure with a standard CMOS technology have been demonstrated.

For a 100-cell prototype and from the simulation results, a maximum power about 45.43 nW is expected for a low-level environmental vibration, with a very low-level acceleration of 0.7 m/s^2 and a peak-frequency of 200 Hz. Therefore, for a whole energy harvesting chip, a

theoretical power density about 5.78 μW/cm³, which is comparable with the state-of-art values. Enhancing the resonant motion amplitude up to its maximum, i.e. 12.3 μm limited by the stoppers, this value could be increased up to a limit value of 110 μW/cm³. The most relevant conclusion is that comparing these ideal power values with the values calculated for a conventional scavenger designed for a similar resonance frequency and fabricated with the same fabrication technology, the density power is increased in more than one order of magnitude, only by applying the new concept of EHoC.

Although this technology seems not to be the more suitable to develop this kind of devices, it could be interesting to explore in that direction, taking advantage of the ideas presented in this chapter. There are several additional applications that could deserve a further extensive research work:

Micro energy scavenging cell array for broad-bandwidth ambient vibrations.

We have seen that due to the tolerance in the fabrication and realease processes, the resonance frequency of the cells do not have the same value. As shown in Figure 3.32 when we put together the frequency responses of the cells of this prototype, we get an overall wider frequency response. This effect can be used to create an integrated broad bandwith microgenerator.

Energy harvesting from sonic or ultrasonic waves

The resonance frequencies of these energy-scavenging cells are in the range of the sound or ultrasound. Thus, using several energy scavenging cells integrated in a chip, it is possible to harvest the energy of this sort of pressure waves, to be used in noisy environment or to monitor animals that produce sonic or ultrasonic waves such as birds, mammals, bats, etc.

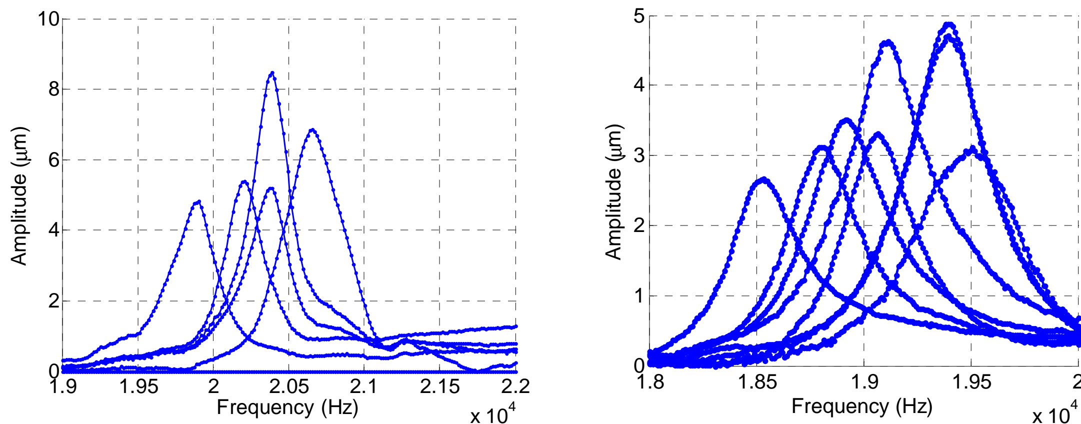

Figure 3.32. Graphs of superimposed frequency responses of all the chip cells for mean value of the input acceleration of 8.96 m/s² (2.5 V).

Electrostatic energy harvester with integrated build-in battery/capacitor.

With another CMOS technology that allows breaking their design rules to fabricate MEMS structures and with a thicker overall thickness of metals, the auxiliary substrate could be formed by a tiny battery or supercapacitor. In that case, the whole system is a fully functional energy harvester. If we are able to fabricate the supercapacitor in the same CMOS chip, the chip could operate with a passive supporting substrate.

References

[1] G. Abadal, Z. J. Davis, B. Helbo, X. Borrise, R. Ruiz, A. Boisen, F. Campabadal, J. Esteve, E. Figueras, and F. Perez-Murano, "Electromechanical model of a resonating nano-cantilever-based sensor for high-resolution and high-sensitivity mass detection," in *Nanotechnology* vol. 12, ed, 2001, pp. 100-104.

[2] G. Abadal, Z. J. Davis, B. Helbo, X. Borrise, R. Ruiz, A. Boisen, F. Campabadal, J. Esteve, E. Figueras, F. Perez-Murano, and N. Barniol, "Electromechanical model of a resonating nano-cantilever-based sensor for high-resolution and high-sensitivity mass detection," *Nanotechnology,* vol. 12, pp. 100-104, 2001.

[3] G. Abadal, G. Murillo, J. Teva, J. L. Lopez, A. Uranga, J. Verd, F. Torres, J. Esteve, F. Perez-Murano, and N. Barniol, "Micromechanical Hz to MHz frequency up-converter integrated in a standard CMOS-0.35um technology for energy scavenging applications " in *33rd Micro- and Nano-Engineering*, Copenhague, Denmark, 2007.

[4] J. L. Lopez, J. Verd, J. Teva, G. Murillo, J. Giner, F. Torres, A. Uranga, G. Abadal, and N. Barniol, "Integration of RF-MEMS resonators on submicrometric commercial CMOS technologies," *Journal of Micromechanics and Microengineering,* vol. 19, p. 015002, 2009.

[5] E. Marigo, J. L. Lopez, G. Murillo, F. Torres, J. Giner, A. Uranga, G. Abadal, J. Esteve, and N. Barniol, "Zero-level packaging of MEMS in standard CMOS technology," *Journal of Micromechanics and Microengineering,* vol. 20, pp. -, 2010.

[6] J. Teva Meroño, "Integration of CMOS-MEMS resonators for radiofrequency applications in the VHF and UHF bands," *http://www.tesisenxarxa.net/TDX-1102107-092623/*.

[7] J. Arcamone, M. Sansa, J. Verd, A. Uranga, G. Abadal, N. Barniol, M. van den Boogaart, J. Brugger, and F. Perez-Murano, "Nanomechanical Mass Sensor for Spatially Resolved Ultrasensitive Monitoring of Deposition Rates in Stencil Lithography," *Small,* vol. 5, pp. 176-180, 2009.

[8] J. Verd, A. Uranga, G. Abadal, J. Teva, F. Perez-Murano, and N. Barniol, "High-sensitivity capacitive sensing interfacing circuit for monolithic CMOS M/NEMS resonators," *Electronics Letters,* vol. 43, 2007.

[9] J. Verd, A. Uranga, G. Abadal, J. Teva, F. Torres, F. Pérez-Murano, J. Fraxedas, J. Esteve, and N. Barniol, "Monolithic mass sensor fabricated using a conventional technology with attogram resolution in air conditions," *Applied Physics Letters,* vol. 91, p. 013501, 2007.

[10] H. Xie and G. K. Fedder, "Vertical comb-finger capacitive actuation and sensing for CMOS-MEMS," *Sensors and Actuators A: Physical,* vol. 95, pp. 212-221, 2002.

[11] J. C. Chiou, Y. J. Lin, and L. J. Shieh, "Out-of-plane CMOS-MEMS Resonator with Electrostatic Driving and Piezoresistive Sensing," in *Sixth IEEE Conference on Nanotechnology, 2006. IEEE-NANO 2006.* , 2006, pp. 929-932.

[12] S. P. Beeby, M. J. Tudor, and N. M. White, "Energy harvesting vibration sources for microsystems applications," *Meas. Sci. Technol,* vol. 17, pp. 175–195, 2006.

[13] G. Murillo, G. Abadal, F. Torres, J. L. Lopez, J. Giner, A. Uranga, and N. Barniol, "Harvester-on-Chip: Design and fabrication of a proof of concept prototype " in *8th International PowerMEMS Workshop*, Sendai, Japan, 2008.

[14] G. Murillo, G. Abadal, F. Torres, J. L. Lopez, J. Giner, A. Uranga, and N. Barniol, "Harvester-on-Chip: Design of a proof of concept prototype " in *34th Micro- and Nano-Engineering (MNE)*, Athens, Greece, 2008.

[15] G. Murillo, G. Abadal, F. Torres, J. L. Lopez, J. Giner, A. Uranga, and N. Barniol, "Harvester-on-chip: Design of a proof of concept prototype," *Microelectronic Engineering,* vol. 86, pp. 1183-1186, 2009.

[16] N. Lobontiu and E. Garcia, "Microsuspensions," in *Mechanics of Microelectromechanical Systems*, ed: Springer, 2004, pp. 131-182.

[17] J. Tsay, L. Su, and C. Sung, "Design of a linear micro-feeding system featuring bistable mechanisms," *Journal of Micromechanics and Microengineering,* vol. 15, p. 63, 2005.
[18] H. Luo, G. Zhang, L. R. Carley, and G. K. Fedder, "A post-CMOS micromachined lateral accelerometer," *Journal of Microelectromechanical Systems,* vol. 11, pp. 188-195, 2002.
[19] G. K. Fedder, "Simulation of Microelectromechanical Systems," University of California, 1994.
[20] G. Barillaro, A. Molfese, A. Nannini, and F. Pieri, "Analysis, simulation and relative performances of two kinds of serpentine springs," *Journal of Micromechanics and Microengineering,* vol. 15, pp. 736-746, 2005.
[21] W. C. Young and R. G. Budynas, "Roark's formulas for stress and strain," 2002.
[22] G. Murillo, G. Abadal, F. Torres, J. L. Lopez, J. Giner, A. Uranga, and N. Barniol, "On the Monolithic Integration of CMOS-MEMS Energy Scavengers " in *23rd Conference on Design of Circuits and Integrated Systems (DCIS)*, Grenoble, France, 2008.
[23] S. Roundy, P. K. Wright, and J. M. Rabaey, "Energy Scavenging for Wireless Sensor Networks: With Special Focus on Vibrations," Springer, 2004.
[24] Y. Chiu, C. T. Kuo, and Y. S. Chu, "MEMS design and fabrication of an electrostatic vibration-to-electricity energy converter," *Microsystem Technologies,* vol. 13, pp. 1663-1669, 2007.
[25] J. Jordan, "Gold stud bump in flip-chip applications," *Twenty Seventh Annual Ieee/Cpmt/Semi International Electronics Manufacturing Technology Symposium,* pp. 110-114, 2002.
[26] *Coventor website*. Available: www.coventor.com
[27] C. Serre, P. Gorostiza, A. Perez-Rodriguez, F. Sanz, and J. R. Morante, "Measurement of micromechanical properties of polysilicon microstructures with an atomic force microscope," *Sensors and Actuators a-Physical,* vol. 67, pp. 215-219, 1998.
[28] C. Serre, A. Perez-Rodriguez, J. R. Morante, P. Gorostiza, and J. Esteve, "Determination of micromechanical properties of thin films by beam bending measurements with an atomic force microscope," *Sensors and Actuators a-Physical,* vol. 74, pp. 134-138, 1999.

CHAPTER 4

HETEROGENEOUS INTEGRATION OF ENERGY SCAVENGING SYSTEMS

This chapter presents the different approaches used to develop energy scavenging systems by heterogeneous integration. First, the design and characterization of an electrostatic converter consisting of a fully-dedicated core die and PCB substrate for test purpose. The core die has been fabricated by using a SOI-based MEMS technology which allows us to fix the issues found in the first CMOS prototype. An FBAR-based piezoelectric technology has been used to fabricate a wide range of microscale converter prototypes. The design, fabrication and electromechanical characterization are also reported in detail. Finally, an alternative to the ambient vibrations as mechanical energy input source is proposed. It is based on the integration of a permanent magnet attached to the inertial mass of the converter that is actuated by the magnetic field generated by a current-carrying wire of a residential or industrial power grid with a frequency of 50/60 Hz.

4.1 Heterogeneous integration of a Systems in Package

As it was stated in the previous chapter, a monolithic integration of the whole autonomous system would be the ideal solution that leads to the real autonomous sensor node concept. Since the current leader technology to implement circuitry still is CMOS, a homogeneous integration of each element in the same technology would simplify the fabrication process and the production cost could be reduced. However, frequently this homogeneous integration cannot be performed and the heterogeneous integration of several fabrication technologies is the only solution.

Heterogeneous integration designates technologies that can be integrated on one platform device. Or it can designate materials that are not compatible and cannot be manufactured on the same substrate, at least not in a cost-effective manner. In microelectronics and microsystems, such multi-technology devices refer to Systems-on-Chip (SoCs) or Systems-in-Package (SiPs). SiPs are a combination of one or more wire-bonded or flip-chip dies with one or more passive components attached to a standard package, whereas SoCs aim to integrate all functionalities on the same die.

The entity forms a module that can be used as a standard component, allowing optimization of the system at a higher hierarchical level (module) and outperforming traditional systems in which the subsystem is optimized at a lower level.

SiPs, in contrast to SoCs, have the advantage that standard dies and passive components as well as standard packaging technologies are used (Figure 4.1), which provides flexibility and — at least for low and medium production volumes — a cost advantage. SoCs have a greater performance improvement potential. By integrating all functionalities on one die instead of distributing them across different chips interconnected via a wiring board, performance is enhanced owing to the shorter interconnect path (reduced signal delay and power consumption). Moreover, more massively parallel processing is possible (no large chip-to-chip communication bus).

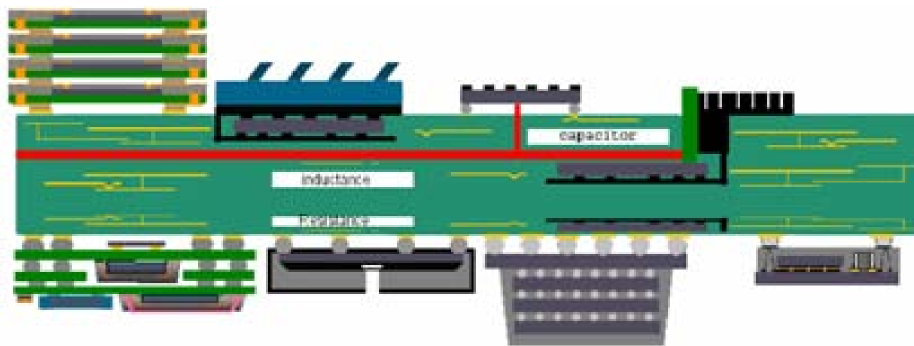

Figure 4.1.Expample of System-in-Package (SiP). Extracted from [1].

Although a greater investment is required to develop the technologies allowing this high level of integration, it leads to some cost advantage thanks to, for example, simplified packaging and smaller system form factors. Therefore, as shown in Figure 4.2, after a certain complexity level of the systems, SoCs cannot be developed without a high negative impact in the cost and time to market of the product. Current SoCs are mainly related to standard CMOS technology, in which microelectronic devices, traditionally produced separately for reasons of cost and flexibility, are merged on one die. Examples of this are embedded DRAM in ASIC, dynamic graphic processing in multicore processor chips, and processors with various peripherals.

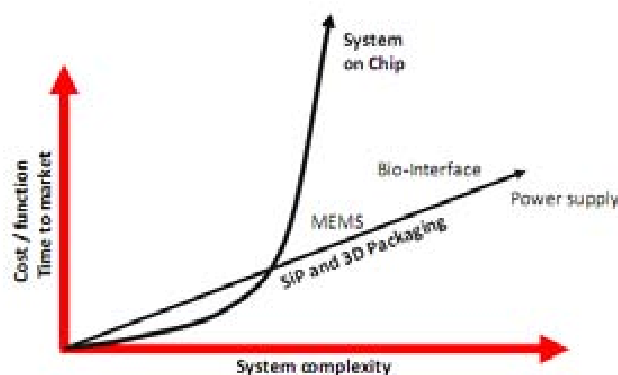

Figure 4.2. Dependence with the system complexity of the cost and time-to-market of the System-in-Packages (SiPs) and System-on-Chips (SoCs). Extracted from [2]..

SoCs that provide desirable integrated solutions are generally limited to technologies that, for most of the fabrication process, are compatible and thus require no or only minor processing changes. SoCs made by integrating heterogeneous devices require a major change in their fabrication process. Here the challenge is to merge subdevices with incompatible materials and processes to obtain the desired functionality.

Integration of MEMS and/or optoelectronic devices on CMOS is an example where considerable research and development has been done. In most cases, the problem has been solved by making a compromise on the global performance and by trying to make the technologies compatible. Even if some have achieved product status, it remains as a challenge to merge these technologies at advantageous costs and performance.

Going back to the energy harvesting concept, and the different transduction types, the only method that can be compatible with CMOS is the electrostatic one, despite of the electromagnetic and piezoelectric. However, in this chapter, a purely MEMS technology is used to fabricate the core die of an electrostatic energy harvester. In addition, a piezoelectric approach is developed and described in this chapter too. Therefore, a heterogeneous integration is necessary to assemble the corresponding whole functional systems.

4.2 A paradigm shift: Energy Harvester in a Package

The basic ideas of the concept of EHoC are the use of the whole chip as inertial mass of a damped spring-mass system, and the micromachinable area to define the transduction and anchored parts. The first EHoC prototype, which was just a proof-of-concept, was introduced in the previous chapter [3] and it was fabricated in a CMOS technology. In this case, the core dice has been fabricated by using a SOI-based MEMS technology which allows us to fix the problems found in the first prototype. In this case, the MEMS die requires a heterogeneous integration with, at least, an additional chip that should include electronic circuits and storage elements (for storage, sensing, and RF-capabilities).

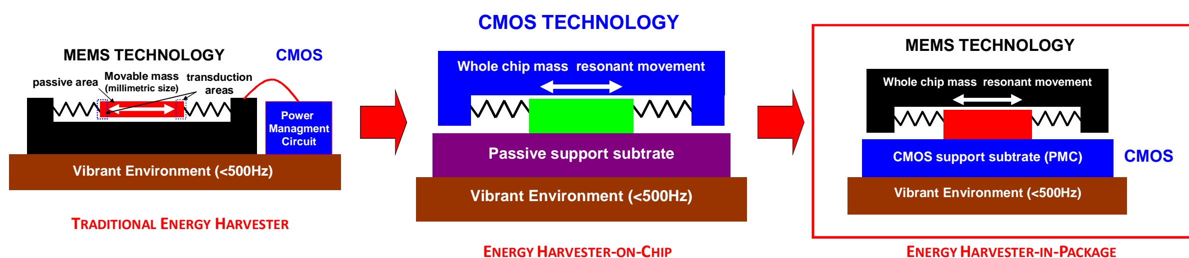

Figure 4.3. Paradigm shift in Energy Scavenging: From the traditional approach to the Energy Harvester in Package.

Thus, Figure 4.3 illustrates the evolution from the traditional energy scavenging approach to the novel concept of Energy Harvester in Package (EHiP) going through the intermediate approach of the EHoC. As commented previously, a traditional microscale energy harvester consists of an inertial mass suspended by some springs and fabricated by a MEMS technology. By using a CMOS technology for creating both the energy harvester (and other MEMS devices) and the circuitry, the concept of EHoC was developed. A paradigm shift is presented here, when the passive support substrate of the EHoC is changed by a chip containing all the

circuitry (A storage capacitor could be incorporated in the same chip too.) and the die dedicated to transduce the ambient mechanical energy into electricity is fabricated in a MEMS technology with higher performance than with a standard CMOS technology.

The concept of Energy Harvester in Package (EHiP) [1-2] becomes an excellent platform to build vibration-driven energy scavenging systems that can provide power autonomy to the nodes of a wireless sensor network (WSN). It is focused on the vertical heterogeneous integration of a MEMS die, which plays the double role of inertial mass and transduction unit, with another auxiliary chip which can include the control and power management circuitry, sensors and RF capabilities and could be fabricated with a CMOS technology. In order to obtain a functional system, an assembling process between the energy scavenging die and the support chip, similar to a flip-chip technique, has to be carried out.

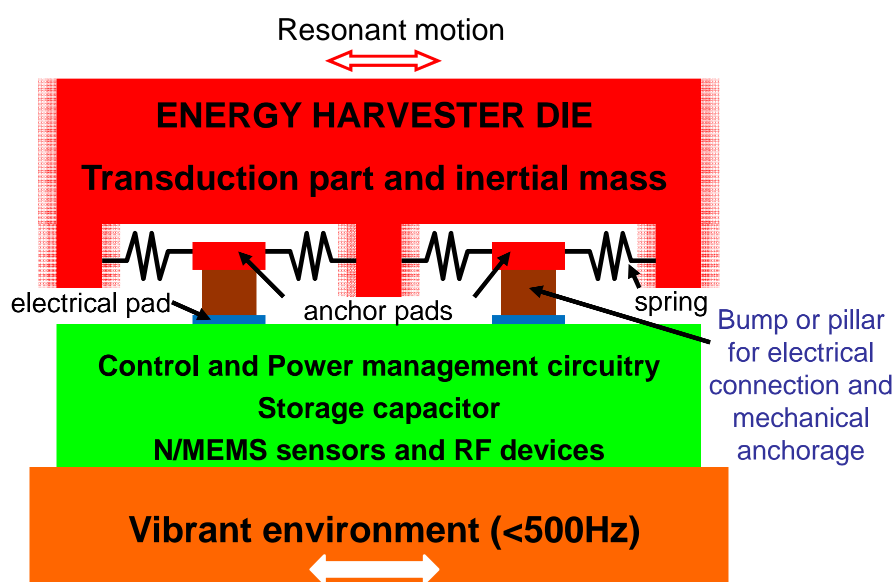

Figure 4.4. Diagram of the generic concept of Energy Harvester-in-Package (EHiP).

As depicted in Figure 4.4, the MEMS die is held from several free-standing anchor pads by conductive pillars, which can be created by solder bumps or PCB milling, placed over the connection pads of the auxiliary chip. Therefore, these pillars have the double function of mechanically supporting the MEMS chip and electrically connecting both chips. The anchor pads in the MEMS die (also referred as core die), which have the main function of providing an anchor point to perform the assembling process, are suspended by several microfabricated springs that allow the resonant motion of the whole die. The energy associated to this this resonant motion can be harvested by means of the integration of transduction elements in the core die.

EHiP concept has two main advantages, the increase of the power density, compared with the traditional approach, and the resonance tunability by adaptation of the movable die mass. In addition, it allows reaching lower frequency values because of the mass increase, enabling the matching between the device resonance frequency and the acceleration peaks of the most common vibration sources available in industrial and residential environments.

4.3 Micro-sized Electrostatic Energy Scavenger with Heterogeneous Integration

This section is focused on the design, fabrication and characterization of the MEMS core die assembled with a passive test PCB instead of the auxiliary chip shown in Figure 4.5. Therefore, there is no mention to the control and power management circuitry or the storage element in this section. Figure 4.5(b) shows a conceptual diagram of the assembled device that has been developed in this section. It is shown that the suspended anchor pads of the core die are electrostatically coupled to the chip through variable capacitors that vary their value by a relative motion between pads and die. These capacitors are implemented by comb drives and they are the key part of the electrostatic transduction used by this energy scavenger. The test PCB provides an electrical connection to the anchor pads and a mechanical anchorage to the MEMS die for allowing us to carry out a preliminary characterization. When the PCB is placed over a surface vibrating laterally at a certain frequency, the energy harvester can get into in-plane resonance.

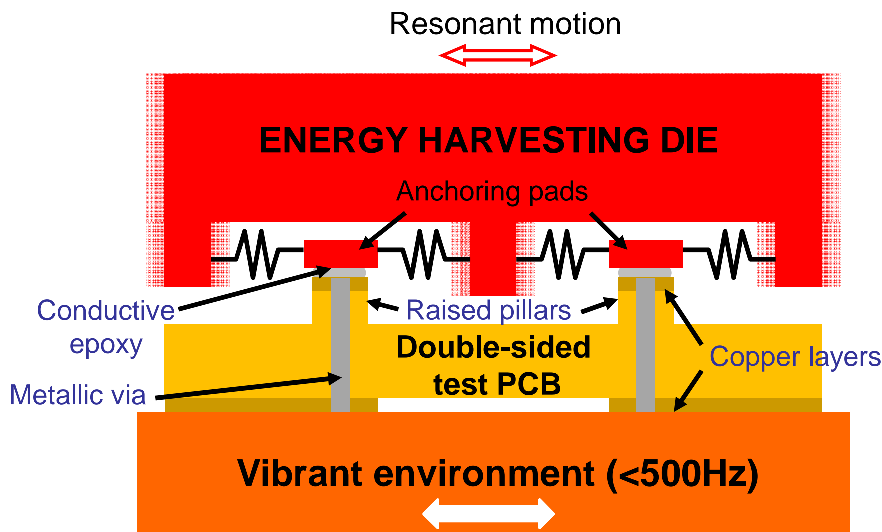

Figure 4.5. Fabricated prototype assembled with a test PCB.

4.3.1 Design of the core die of an electrostatic energy harvester

A monolithic integrated version of the EHiP concept was fabricated in a standard CMOS technology [3], demonstrating the feasibility of integrating large MEMS structures in a commercial CMOS technology. In order to improve the throughput of the CMOS prototype [1], a dedicated MEMS has been developed. The technology used to fabricate the core die was MEMSOI from Tronics® [6]. An SOI wafer is patterned and etched by DRIE that provides a 60-µm-thick silicon layer to build our comb-drive fingers and suspensions. This thickness means an improvement of the suspension robustness along the out-of-plane direction and an increase of more than one order of magnitude in the transduction density with respect to the first CMOS approach [3].

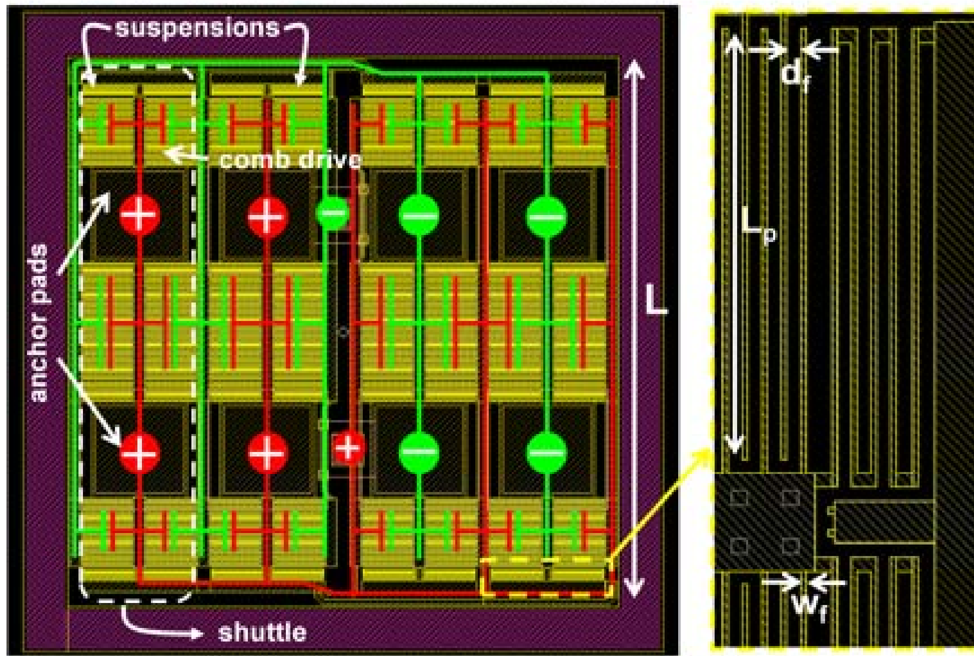

Figure 4.6. Layout of whole chip with the four electrically-connected shuttles that create an equivalent variable capacitor. Inset: Detail of the layout of a serpentine suspension, comb-driver and stopper.

From the point of view of the transduction design, this generator is enclosed into the electrostatic energy harvesters. Specifically, it uses an in-plane gap closing electrostatic transduction (IPGCT), formed by comb drivers and designed to work in the constant charge cycle [4, 5] (see Section 2.2). With this configuration, a maximum and minimum capacitance value, C_{max} and C_{min} respectively, can be reached as the inertial mass is moving. Energy increment per cycle and generated power for this type of generator are depicted by (4.1) and (4.2). In order to reach a higher value of the energy increase into the variable capacitor, ΔU, it should be increased the capacitance ratio, r_C, or the capacitance difference, ΔC, or the initial precharge voltage, V_{in}.

$$\Delta U_{Q=cte} = \frac{1}{2} V_{in}^2 \frac{C_{\max}}{C_{\min}} (C_{\max} - C_{\min}) = \frac{1}{2} V_{in}^2 r_C \Delta C \quad (4.1)$$

$$Power = n_{cycles} \Delta U_{cycle} f \quad (4.2)$$

But taking into account that with this conversion cycle (where n_{cycles} = 2) the maximum reached voltage between the capacitor plates, V_{max}, depends on this capacitance ratio, r_c, and the initial voltage, V_{in}, as well.

$$V_{\max} = r_C V_{in} \quad (4.3)$$

Since the maximum voltage is restricted by technological limitations, and the energy depends on the square of the voltage, the parameter (among these three: V_{in}, r_c and ΔC) which should not be maximized is r_c. Thus, it should be found a design with a value of its medium capacitance as large as possible and remaining the ratio with a suitable value.

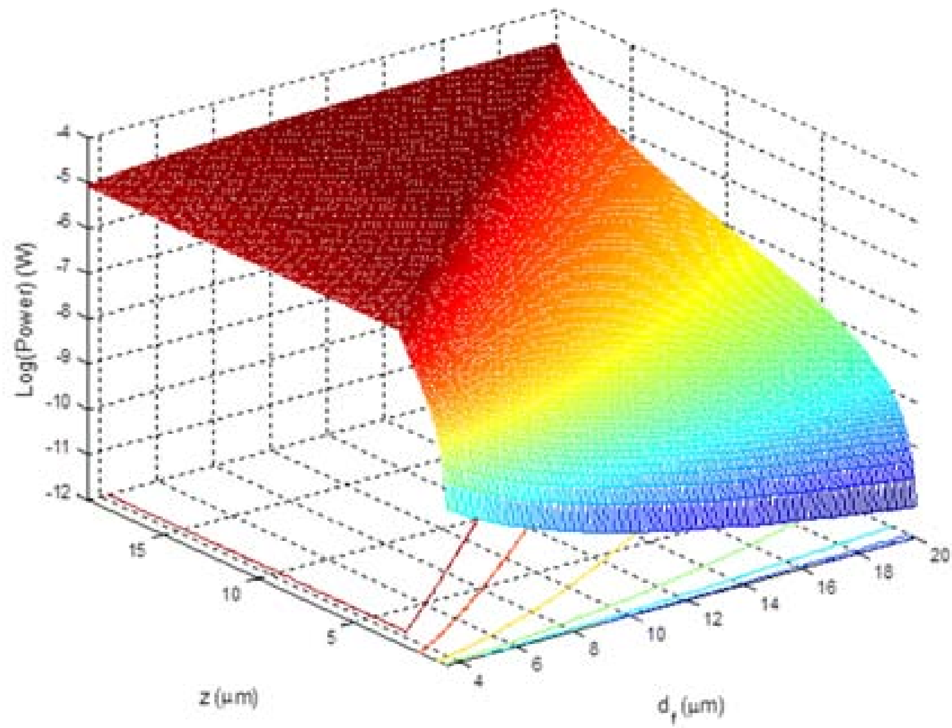

Figure 4.7. Ideal maximum reachable power depending on initial adjacent fingers distance, d_f, and moved distance, z.

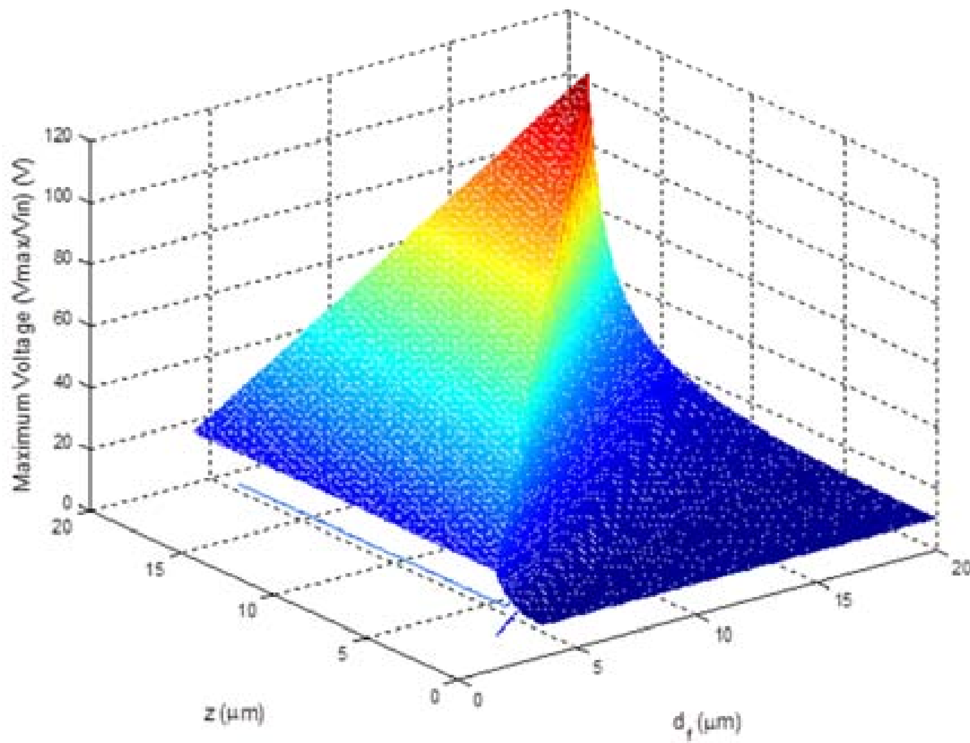

Figure 4.8. Maximum voltage depending on initial adjacent fingers distance, d_f, and moved distance, z.

In a comb drive as shown in the inset of Figure 4.6, its total length, L, is related to the finger width, w_f, the gaps number, N_g, and the initial gap between fingers, d_f, as follows:

$$N_g = \frac{L - w_f}{w_f + d_f} \underset{L \gg w_f}{\approx} \frac{L}{w_f + d_f} \tag{4.4}$$

When this relationship is introduced in the capacitance formula of the designed IPGCT scavenger [4], an analytical expression depending on the design parameters can be obtained. A study of the maximum reachable power related to the number and separation of the beams has been performed. As shown in Figure 4.7, the maximum reachable power is almost independent of the fingers motion at resonance and critically dependent on the minimum gap between adjacent fingers. However, the longer amplitude, the higher maximum voltage is obtained over the variable capacitor (see Figure 4.8). Due to the independence between resonant amplitude and throughput, the maximum allowed displacement was set to 9 µm in order to limit the maximum voltage to a moderate value of 53 V.

4.3.2 Fabrication and assembling processes of the whole EHiP

The technology used to fabricate the core die was MEMSOI from Tronics® [6]. A SOI wafer is patterned and etched by deep reactive ion etching (DRIE) that provides a 60-µm silicon layer to build the comb-drive fingers and suspensions. After the fabrication of the SOI wafer, it is bonded with a cap wafer to systematically seal the MEMS structures contained in the bottom wafer. However, the opening of several access holes in the lid can be ordered to have direct access to the MEMS structures, pads or cavities. In Figure 4.9, a cross section of this technology is shown, where it can be observed the bonding between the cap wafer, with a thickness of 300 µm, and the SOI wafer that consists of a silicon substrate with a thickness of 450 µm, a buried oxide layer of 2 µm and a device silicon layer of 60 µm as commented before.

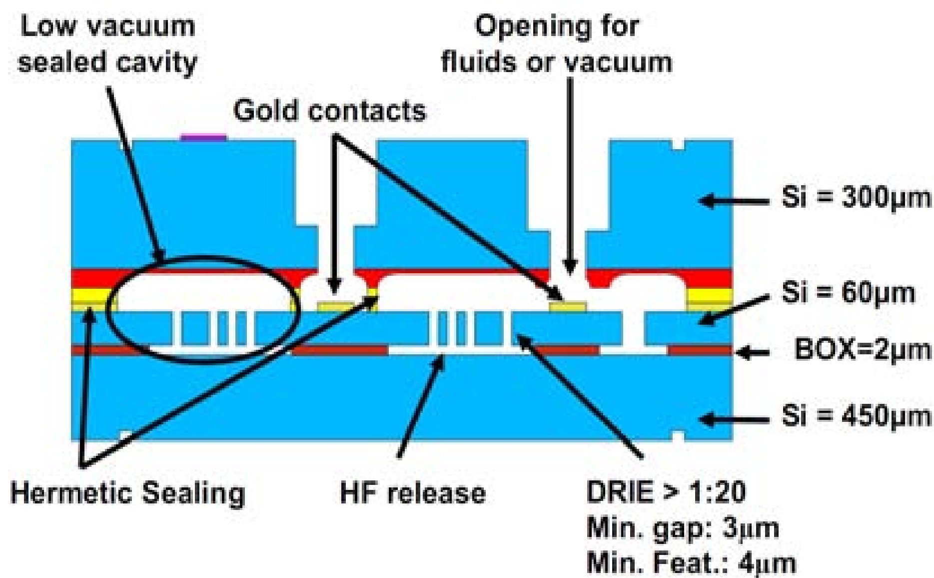

Figure 4.9. Cross section of the technology Tronics with the more important features

Figure 4.10 shows the optical image (a) and 3D model (b) of the fabricated die. Figure 4.11 shows the SEM images of the same chip before the encapsulation that were used to measure the final fabricated dimensions taking into account the underetching.

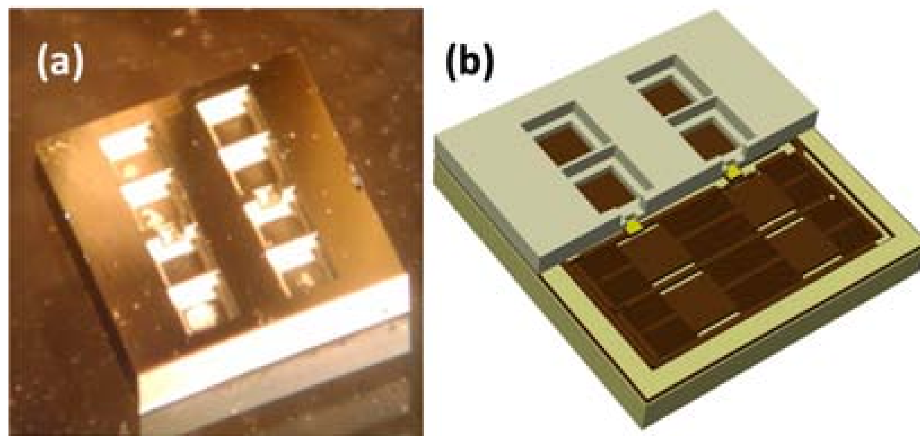

Figure 4.10. Optical image (a) and 3D model (b) of the fabricated chip.

After the reception of the chips from the foundry, an etching with HF 49% for seven minutes, i.e. SiO_2 etching of 10 µm, followed by a critical point dry was carried out to make sure the total release of the structures. Finally, a Cr/Au bilayer (20 nm/40 nm) was deposited by evaporation over the chips in order to obtain a good conductive layer on top of the movable pads and avoid the oxidation of the silicon surface. The access holes in the lid played the role of mask for that process. In our case, the cap is a serious drawback when the anchor pads have to be contacted.

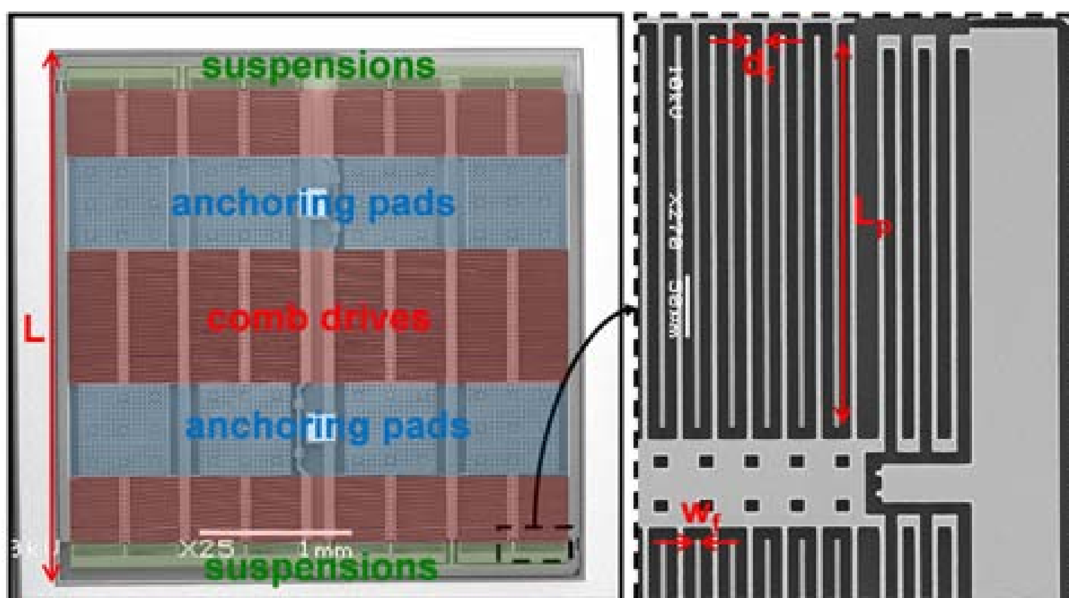

Figure 4.11. SEM image of fabricated chip before the encapsulation. Inset: detail of comb drive fingers and suspensions.

In order to perform the first test of the whole device and overcome the inconvenient of having a chip lid, a special test PCB layout was designed to allow the physical support and electrical connection. The fabrication has been carried out by using a circuit board plotter

(also called computer numerical controlled milling machine or CNC) to pattern on one side the tracks to electrically connect in parallel the different comb drivers and obtain two electrodes of the total equivalent capacitor, and on the other side, the support pillars with a metallic pad on top to be bonded to the anchor pads of the core die. These columns have been raised to allow mounting the chip on top of them and the resonance motion of the core die by means of avoiding the contact between both surfaces.

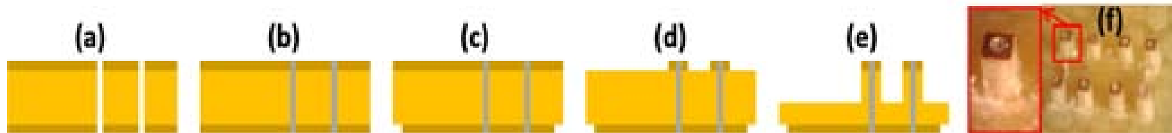

Figure 4.12. Test PCB fabrication process: vias are drilled (a) and filled up with silver paste (b), tracks (c) and pads (d) are patterned on both PCB sides, pillars are created by milling (e) and the final PCB is obtained (f). Inset: detail of one holed pillar.

The PCB fabrication consists of the following steps: eight holes corresponding to each pillar are drilled through the whole thickness of a standard double-sided PCB (Figure 4.12(a)) (with a thickness for the FR4 substrate of 16 mm and 35 μm for the copper layers), and then every hole is filled up with conductive silver paste to create an electrical via between pad and track (Figure 4.12(b)). To do that, a syringe with a thin needle that is utilized to introduce silver paste inside of every perforation and then a spatula is used to make sure that the holes are completely filled. Afterwards, two tracks are patterned on one copper side associating four holes by track (Figure 4.12(c)). These tracks have the function of providing an external connection to the VEH capacitor electrodes shown in Figure 4.6 (positive and negative poles). On the opposite PCB side, the next step (Figure 4.12(d)) is the patterning of the pads (with a size of 200 μm x 200 μm) and the milling of a layer of the intermediate dielectric with a depth of more than 300 μm around these pads (Figure 4.12(e)). The result (Figure 4.12(f)) is eight pillars with a height of more than 300 μm, which is the thickness of the chip lid, with a holed metal pad on top that is connected through conductive vias to a pair of metallic tracks patterned on the opposite PCB side.

In order to perform the assembling a two-part silver-loaded conductive epoxy, Chemtronics CW2400, that cures at room temperature, has been used. A thin layer of this epoxy was formed over a flat surface by using a spatula (Figure 4.13(a)), afterwards the fabricated PCB was placed facing down-side on a vacuum handling system (Figure 4.13(b)) to put in contact the PCB pads with the epoxy layer keeping the planarity (Figure 4.13(c)). With this last step, a thin layer of conductive epoxy can be transferred to the top of the pillars (Figure 4.13(d)). Finally, the alignment was carried out with an alignment system (ERSA PL 550) for an surface mount devices (SMDs) which allows us to accurately place the core die over the PCB substrate, and align the PCB pillars with the chip pads (Figure 4.13(e-i)). The force made when both parts are put in contact has to be reduced as much as possible to avoid the fracture of the MEMS structures. The assembled system can be dried in an oven to cure faster the epoxy (e.g. 100 ºC for 45 minutes). Figure 4.14 illustrates the final assembled EHiP with the direction of the resonance motion and a cross-section of the final system where the pillars and tracks can be appreciated.

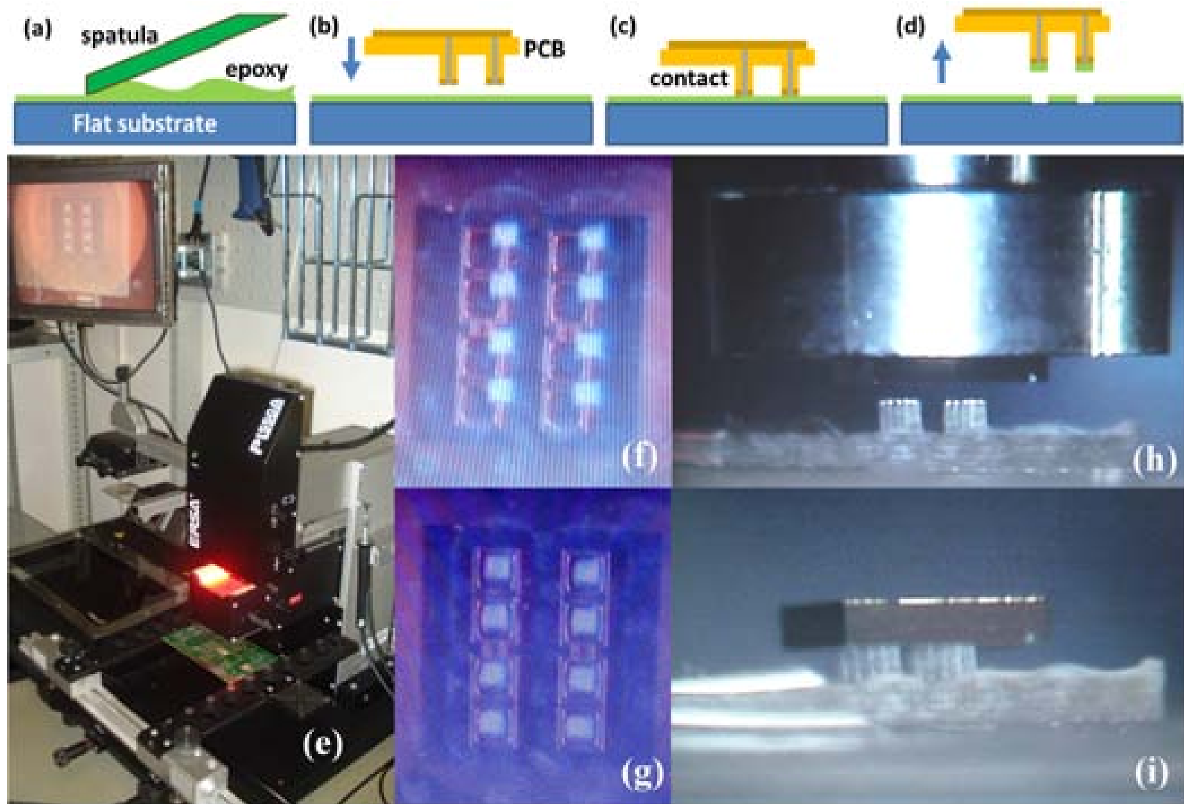

Figure 4.13. Epoxy deposition process of the test PCB(a-d), ERSA PL 550 component alignment system (e), view of PCB pillars and chip pad alignment (f and g), and lateral view of chip and PCB before (h) and after (i) contact.

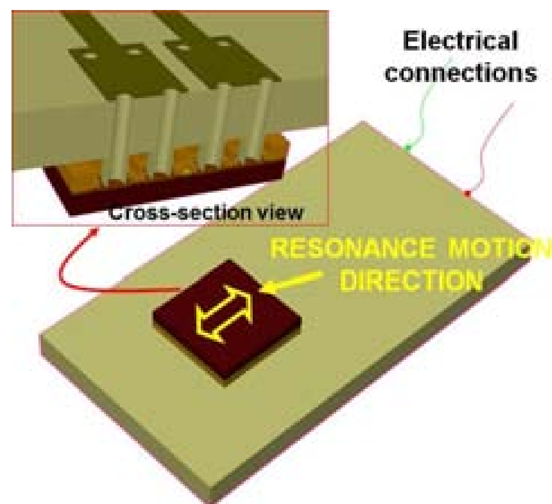

Figure 4.14. 3D image of the final assembled Energy Harvester in Package. Inset cross-section of the final system where the pillars and tracks can be appreciated.

4.3.3 Simulations and numerical calculations

The first simulation carried out was a harmonic analysis provided by ARCHITECT about the resonance frequencies of the core die when it is suspended by the anchoring points. A harmonic acceleration of was defined along the three space directions. Figure 4.15 shows the

first resonance peaks that can be found for the three directions. It can be inferred that the resonance frequency of this device for the desired in-plane motion is around 235 Hz and, more importantly, that the rest of spurious motions are located at frequencies five times higher than the designed target frequency.

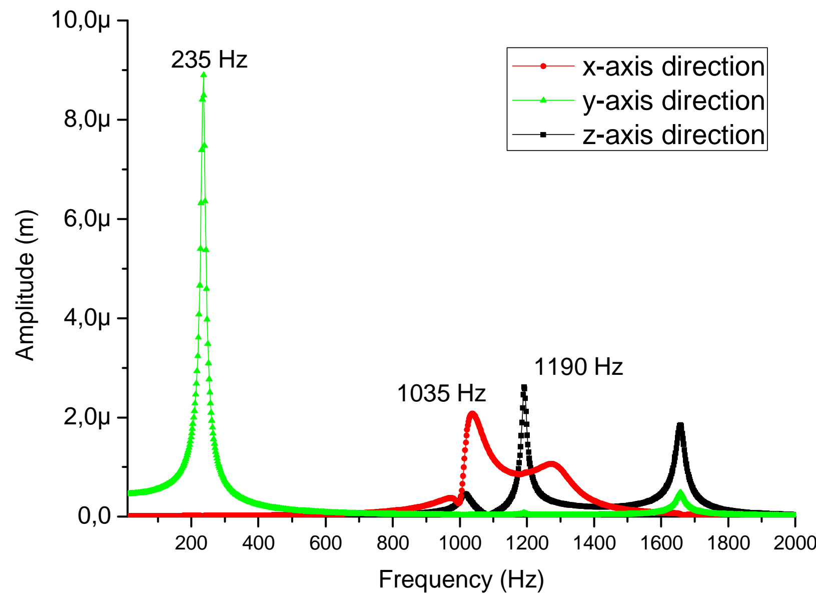

Figure 4.15. Simulated relative displacement amplitudes in the three space directions.

A FEM mechanical simulation was performed for a suspended single shuttle and the first mode of resonance was found at 1836 Hz (Figure 4.16(a)). The effective inertial mass that is being moved in this resonance mode is 0.14 mg.

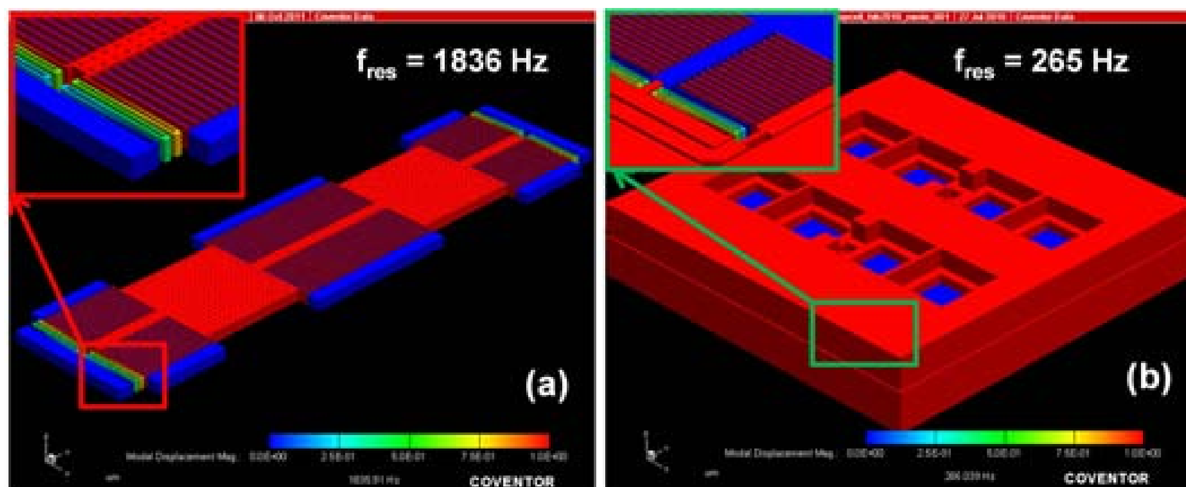

Figure 4.16. Modal FEM simulation of a single shuttle, when it is free to be moved and the die is anchored to a resonant surface (a) and the same simulation of the whole chip when it is anchored by its anchor pads (b). Insets: details of the suspension bending (the cap is set invisible).

The same modal simulation of the whole chip suspended has been performed. Figure 4.16(b) presents the first mode of resonance is located at ~265 Hz for the desired motion direction. In that case the effective inertial mass is increased to 26.74 mg. Non-desired

motions have almost five times higher resonant frequencies. A Matlab code that solves the electromechanical motion equation has been developed. The results from this program have been used to predict the electromechanical behavior of the whole system implementing a constant-charge cycle.

The same Matlab code, which was described in Chapter 2, has been used here to simulate the electromechanical behavior of the EHiP prototype. Maximum and minimum capacitance values of 90 pF and 17 pF respectively could be reached in a best-case scenario, which means a capacitance ratio of 5.2 and a capacitance difference of 73 pF. The maximum power which could be ideally obtained with this converter would be around 11 μW, i.e. 0.85 mW/cm^3, for an acceleration magnitude of ~10 m/s^2 (~1 g), an initial and final voltage of 10 V and 52 V respectively, and an effective quality factor of 50 (electrical and mechanical damping effects). A summary of the simulated results are collected in Table 4.1.

Table 4.1. Expected EHiP electrical features extracted from simulated results

	Tronics EHiP prototype[a]
$N_{shuttle}$	4
N_g	130
C_{max}	90 pF
C_{min}	17 pF
V_{max}	52 V
ΔU_{per}	19.2 nJ
Power	11 μW
Power Density	0.85 mW/cm^3
$V_{initial}$	10 V

[a] Simulated values for a resonant motion amplitude of 9 μm, which is extracted from the stationary solution of the complete motion equation for an ambient vibration of 10 m/s^2 to 287 Hz (meassured value).

4.3.4 Electromechanical characterization

Three different characterizations have been carried out to demonstrate the right operation of our approach for harvesting mechanical energy. One of them uses the constant acceleration of gravity to statically characterize the device. The second characterization involves only the MEMS die which is anchored to a piezoactuator that provides a sinusoidal acceleration to study the resonance motion of one single shuttle. Finally, the whole assembled system is placed over an electrodynamical shaker in order to get the resonance motion of the whole MEMS die and measure the motional current generated by its associated capacitance change.

Static capacitance measurements

First of all, several capacitance measurements (Table 4.2) have been performed with an impedance meter for different inclination of the assembled system to demonstrate the right operation when excited by a constant acceleration of the system. An equivalent electrical model consisting of a capacitance in parallel with a parasitic resistance has been used to characterize the EHiP. From these values, it can be inferred that the minimum capacitance of our device is ~20 pF, and also that the suspensions have the desired behavior, stiff for lateral motions and compliant along the required direction. A parallel parasitic resistance of ~540

MΩ was measured. This element is another critical factor for a right system operation. It is being used the capacitor formed by the MEMS die to store charge during the motion from minimum to maximum capacitance values, thus, leakage currents have to be avoided. Charges can flow through this parasitic resistor even if the capacitor is kept open-circuited. Then, in order to be able to keep the charge constant during that time period, the parasitic resistance value should be five times higher than the time constant of the formed RC circuit (~1.5 ms). That means a parasitic resistance value of $R_{p\min} = (0.4 f C)^{-1} = 433 M\Omega$. Therefore, the measured value is enough to keep the charge constant during the energy-harvesting operation cycle. Open-circuit is detected over the dies that have not been post-processed. The metallization and assembling steps are critical, because any metallized dust particle can partly short-circuit a comb-drive capacitor.

Table 4.2. Measurement of impedance of the EHiP for a Cp||Rp model

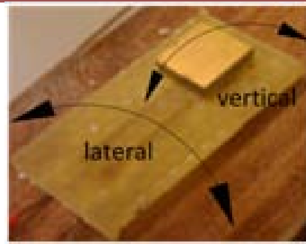

Rp = ~540 MΩ

	Vertical inclination	**Lateral inclination**
Angle	Capacitance (pF)	Capacitance (pF)
-90º	33.16	20.43
-45º	24.87	20.58
0º	20.70	20.61
45º	22.45	20.51
90º	27.80	20.25

Resonance of a single shuttle

Secondly, if the chip is anchored to a vibrating substrate, the movable pads will play the role of inertial masses and will get into resonance at a higher frequency. In order to measure this effect, a non-assembled core die was mounted on a piezoactuator that was excited by a network analyzer while an oscilloscope was measuring the peak-peak voltage over the actuator. On the other hand, in order to capture the resonant motion of the movable structure the setup described in Section 3.6.2.

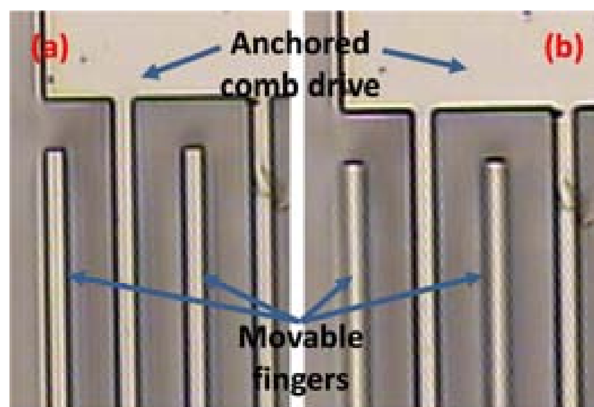

Figure 4.17. Detail of comb-drive fingers out of resonance (a) and at resonance (1420 Hz) (b) of a single shuttle motion driven by a piezoactuator.

Figure 4.18 (a) shows a resonant peak at 1420 Hz with a quality factor of ~100, that is useful to corroborate the resonance peak measurement of the assembled system. Figure 4.17 illustrates an optical image of the comb-drive finger out of resonance (a) and at resonance (b), where an in-plane resonance motion can be observed.

The difference between measured and simulated values, with a 23% of error, can indicate a mass loss of the shuttle or a decrease of the suspension stiffness due to the underetching that took place during the die fabrication. From this single shuttle resonance frequency, an expected value for the assembled die of ~207 Hz can be deduced, taking into account the different masses and number of suspensions of each case or the ratio between both simulated resonance frequencies.

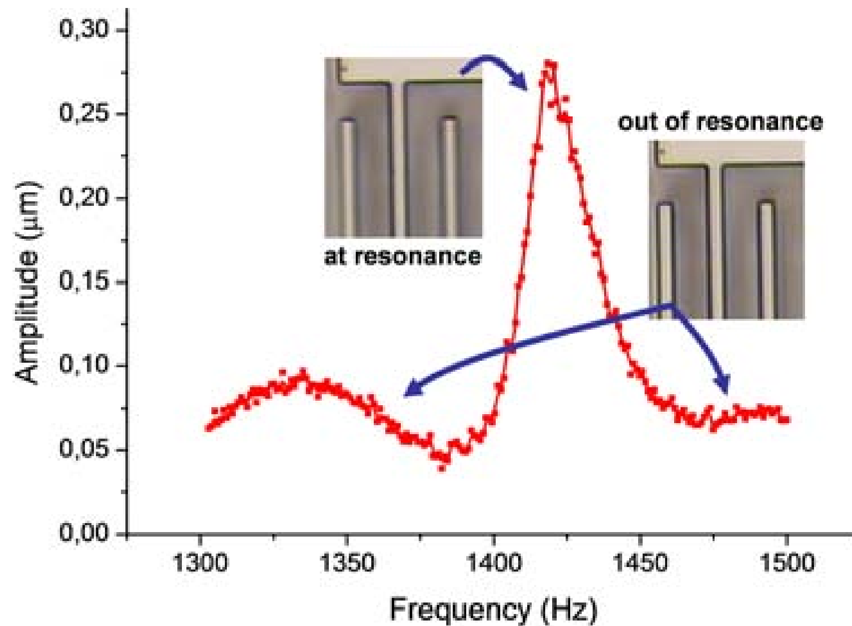

Figure 4.18. Captured resonance peak corresponding to a single shuttle motion driven by a piezoactuator (1420 Hz). Insets: optical image showing the resonance motion of the comb drive.

Resonance of the assembled Energy Harvester in Package

In order to carry out the last electromechanical characterization, one electrode of the energy scavenger is connected to a DC voltage source and the other one is connected to the input port of a network analyzer (HP8751A) that has an input resistance of 50 Ω. Thus, the motional current generated by the voltage-biased vibration-driven capacitance change will generate a voltage difference over the input resistor that can be measured (Figure 4.19(a)). The scavenger is placed over an electrodynamical shaker (V20 SignalForce from G&W) that provides the harmonic vibration (Figure 4.19(b)). The shaker is powered by the output port of the network analyzer after passing through a power amplifier (PA100E SignalForce from G&W). During the measurement, the network analyzer was measuring the power associated to motional current resulting from a frequency sweep around the resonance frequency.

The measured resonance peak (Figure 4.20) is centered at a resonance frequency of 289 Hz with a quality factor around 30 for V_{DC} = 6 V. The shown magnitude is a measurement of absolute power dissipated by the input load impedance of the port A. From the expression of the capacitance of this type of comb drive [4], the motional current could be calculated and subsequently the power delivered to the input port. This calculation could be useful to experimentally obtain the maximum capacitance reached during the experiment. From this

value, it is possible to estimate the theoretical power that could be generated with this capacitance variation.

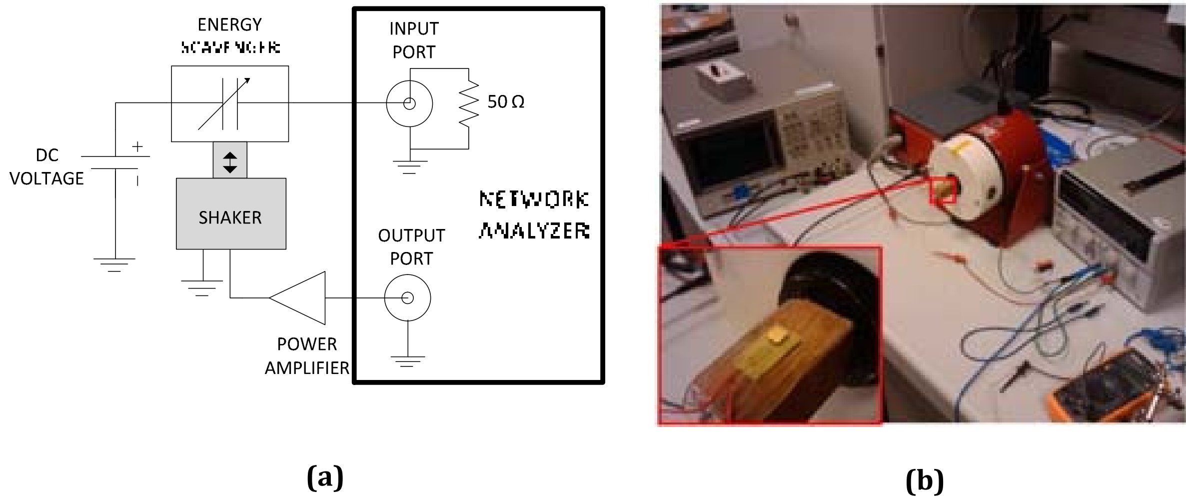

Figure 4.19. Measurement setup used to characterize the device, diagram (a) and optical picture (b). Inset: detail of the assembled system mounted on the shaker.

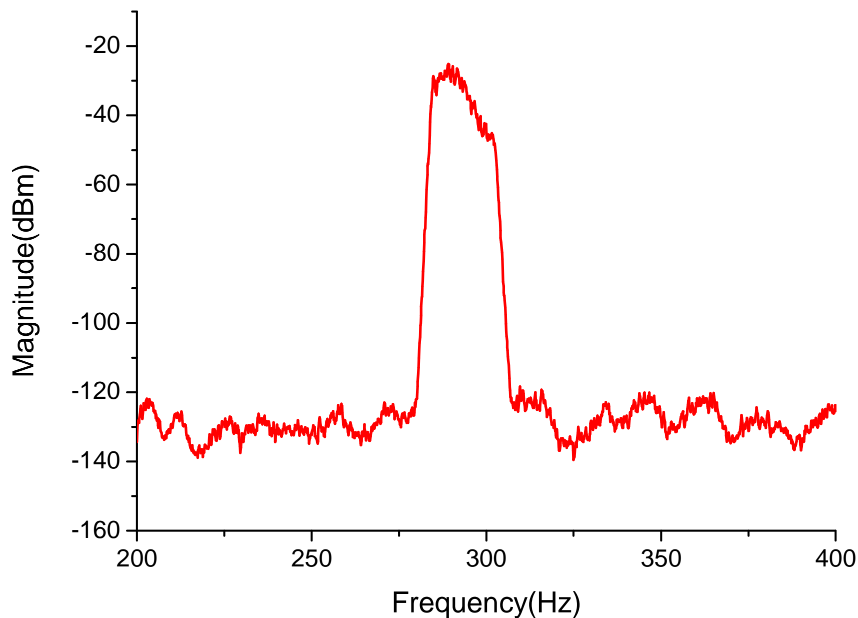

Figure 4.20. Resonance peak of the assembled EHiP system (278 Hz) driven by a shaker.

The shown magnitude is a measurement of absolute power dissipated by the input load resistance of the port A. The mathematical expression is given by:

$$Magnitude(dBm) = 10\log\left(\frac{Power_A}{1mW}\right) \qquad (4.5)$$

Where $Power_A$ is the absolute power measured at the input port of the network analyzer with an input resistance, R_i.

$$Power_A = \frac{V_{RMS\,A}^2}{R_i} = R_i I_{RMS\,A}^2 \tag{4.6}$$

The root-mean-square (RMS) of the voltage and current, V_{RMS} and I_{RMS} respectively, are calculated for a signal period, T = 2πω, from the motional current, i_{mot}, that appears whit the change of the capacitance value:

$$I_{RMS\,A} = \int_{t_0}^{t_0+T} i_{mot}^2 dt \tag{4.7}$$

This current can be calculated with the derivate of the expression of the capacitance of the comb-driver:

$$i_{mot} = V_{DC}\frac{dC(z)}{dt} = V_{DC}\frac{dC(z)}{dz}\frac{dz}{dt} \tag{4.8}$$

The expression that describes the capacitance dependence with the relative displacement of the movable plates is different for each type of transduction. In our case an in-plane gap closing (IPGC) transduction was used to implement this prototype and the capacitance value is:

$$C(z) = N_g \varepsilon L_p t_f \frac{2d_f}{{d_f}^2 - z^2} \tag{4.9}$$

Where ε is the air dielectric constant, t_f is the beam thickness, L_f and w_f are the finger length and width, d_f is the gap between fingers of the different drivers and L_p is the adjacent fingers overlapping length. On the other hand, we are supposing that the energy scavenger is driven by a harmonic ambient vibration. Therefore, at the steady-state the relative displacement of the capacitor plates will have the following harmonic nature:

$$z(t) = z_0 \sin(\omega t), \tag{4.10}$$

where z_0 and ω are the inertial mass amplitude and the angular frequency at resonance respectively.

Figure 4.21 contains the graphical representation of one period of the relative displacement of the capacitor plates (a), the capacitance value corresponding to the relative motion (b), motional current due to the capacitance variation (c) and squared value of the current to calculate the RMS value of the power consumed for the load resistance (50 Ω) of the measurement instrument.

However, the expected value of the absolute power peak should be around -76 dBm when the system reaches the maximum capacitance, i.e. when the shuttles nearly touch the stoppers. The unexpected peak of -27 dBm, shown in Figure 4.18(b), can be due to the impact of the shuttles with the stoppers. This fact could produce an additional bending of the comb-drive fingers that can get closer than the distance allowed by the stoppers (1 µm). It would mean a huge increase of the capacitance and subsequently of the motional current.

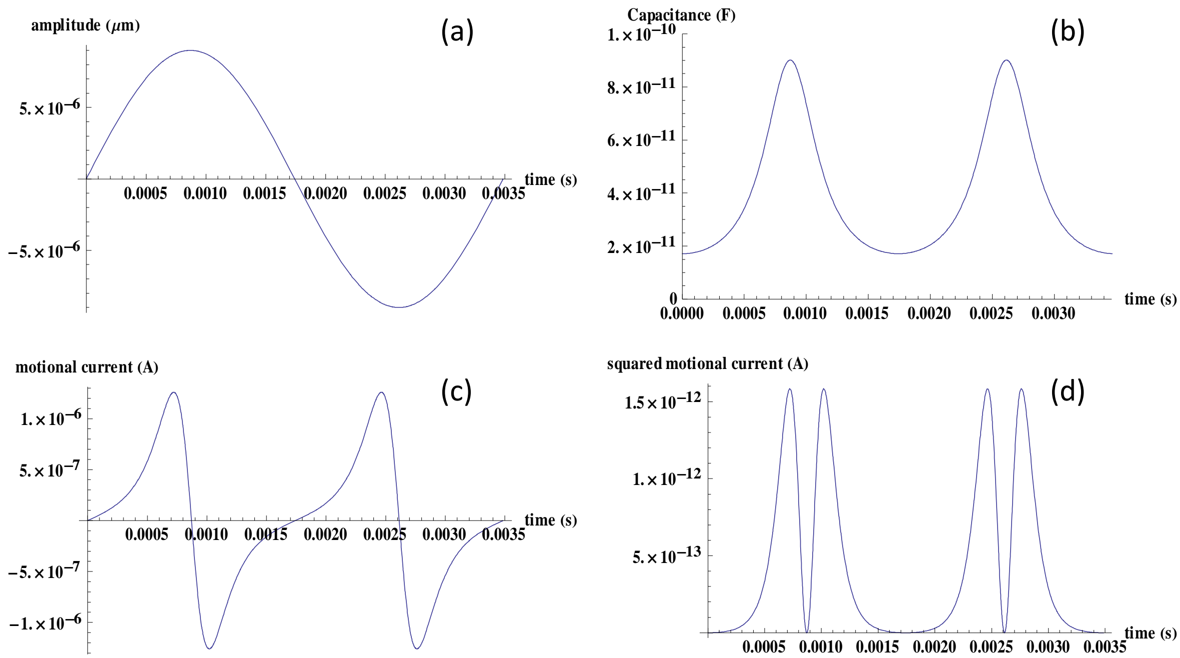

Figure 4.21. Harmonic motion (one period) of the capacitor plate (a), capacitance value corresponding to the relative displacement of the plates (b), motional current due to the capacitance variation (c) and squared value of the current (d).

Additionally, an eventually short-circuit between opposite fingers could be possible, if the shock is strong enough. These two factors could contribute to increase the power measured at resonance (Figure 4.18(b)). Therefore, this resonance peak cannot be used as an indirect measurement of the power generated by our device. However, it provides valuable information about the resonance frequency of the fabricated assembled device and proves the EHiP concept.

4.4 Heterogeneous integration of piezoelectric energy harvesters

In this section, the heterogeneous integration of an energy scavenging system is implemented by using a piezoelectric transduction. As commented in previous chapters, the concept of energy harvesting aims to extract useful energy from environmental vibrations, coupling the typical resonance frequency of the scavenger device with the vibration frequency. In this case, the mechanical energy is converted to electrical energy by means of a piezoelectric transduction [7].

The fabrication process used to develop these piezoelectric devices is based on an ad-hoc technology developed to integrate AlN-based FBAR resonators. Thus, the main goal of this technology process is the possibility of integrating, at the same time, piezoelectric energy scavengers along with FBAR resonators. An FBAR resonator can be used for wireless RF communications systems. Figure 4.23 shows the resonance peak at 2.4 GHz of an FBAR resonator fabricated with the same piezoelectric technology [8]. It could provide ZigBee connectivity to the whole system. Moreover, another FBAR resonator has been successfully characterized as a mass sensor [9]. Thus, the sensing capabilities of a WSN node could be covered with this kind of devices integrated in the same die (Figure 4.22).

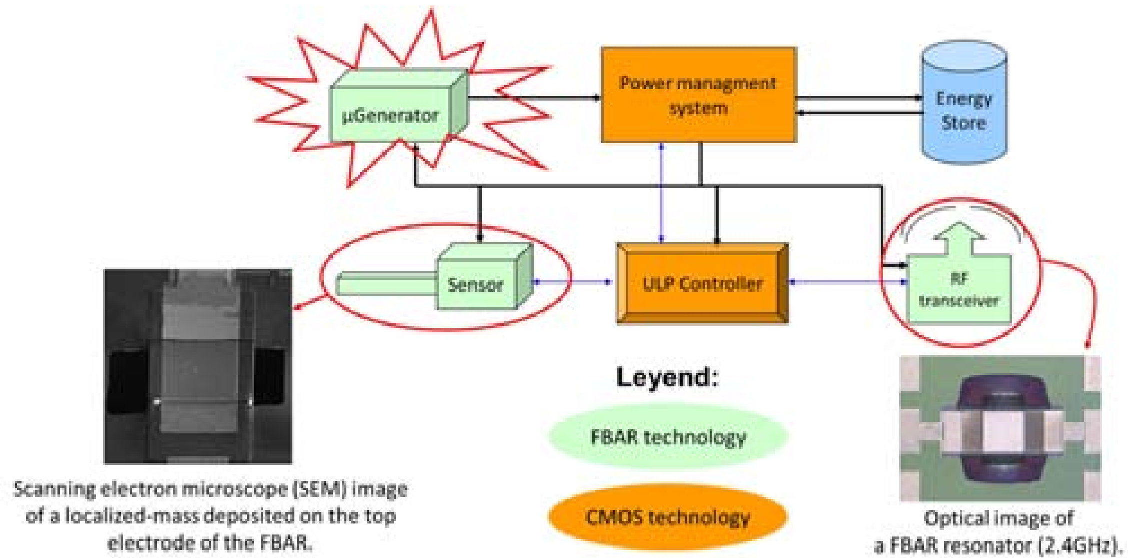

Figure 4.22. Heterogeneous integration of Wireless Sensor Node (WSN) on AlN-based FBAR technology. Insets: Images of FBAR-based mass sensor [9] and resonator [8].

Figure 4.24 illustrates a 3D model of an autonomous WSN node based on the EHiP idea, where a heterogeneous integration between the piezoelectric die and an additional chip is performed. The bottom part is a vibration-driven cantilever-shaped energy harvester fabricated with the piezoelectric technology described here. In addition, an auxiliary chip is bonded by the flip-chip technique to the inertial mass of the energy harvester, in concordance with the EHiP concept. This attached chip could contain the integrated elements usually included in a WSN node such as a transceiver, a power management circuit or the storage element. Due to the special features of this technology, an FBAR resonator, which could be used like an oscillator for the transceiver or a sensor, can be integrated on top of the same inertial mass, and connected to the auxiliary chip. Thus, a self-powered WSN node can be obtained with a reduced size (~10 mm^3) by taking advantage of this hybrid piezoelectric technology and the EHiP concept.

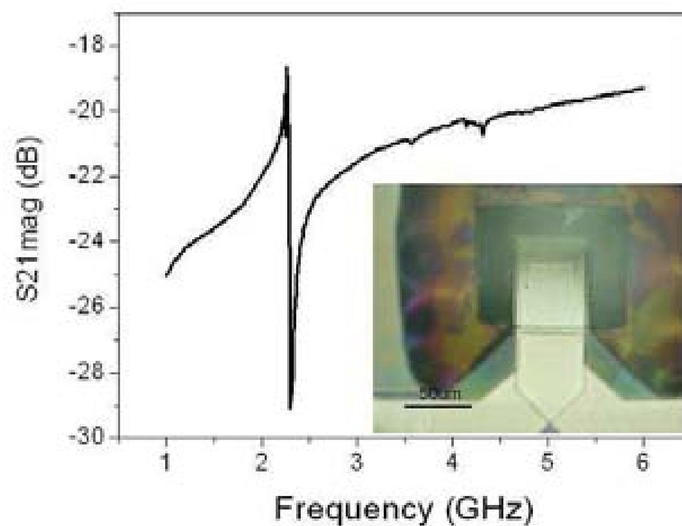

Figure 4.23. Resonant peak at 2.4 GHz of an FBAR fabricated with the same technology [8]. Inset: Optical image of the FBAR resonator.

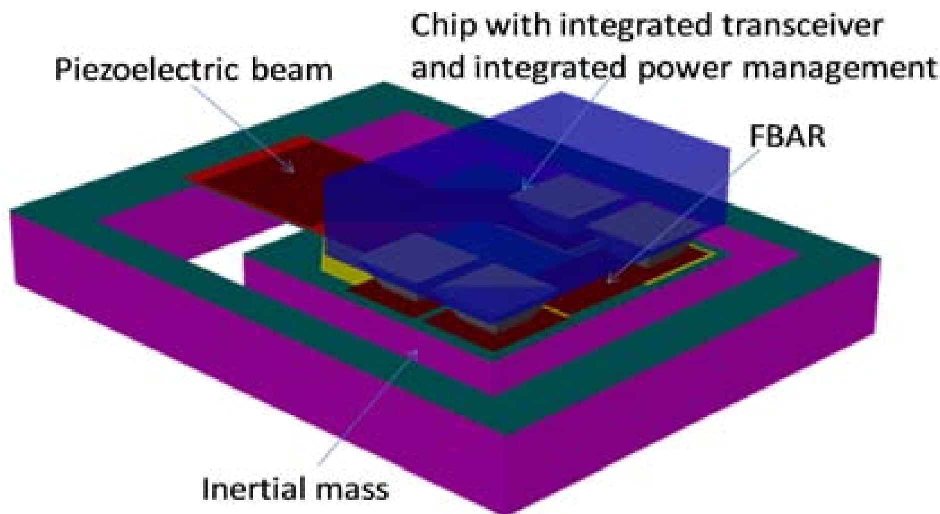

Figure 4.24. 3D model of an autonomous wireless sensor node powered by a vibration-driven energy harvester based on a piezoelectric transduction.

4.4.1 Fabrication process of the core die

As it has been pointed before, the process to fabricate piezoelectric energy micro-generators presented here is based on a technology used to deposit AlN for FBAR components recently developed [10]. Thus, the same AlN material and processes can be shared to integrate piezoelectric energy scavenger elements, along with FBAR resonators for wireless RF communications systems and mass sensors.

In Figure 4.25, it can be observed the whole manufacture process. The process begins with a 100-mm silicon BESOI wafer, p-type, (100) oriented and 510μm thick, from Si-Mat.

The thickness of the top silicon layer is 15 μm, separated by an oxide layer of 1 μm. Then, a TEOS oxide is deposited on the component side. Afterwards, DRIE_BACK mask is used to etch 1 μm of silicon on the backside. Therefore, the rest of masks can be aligned with this backside level. Then, the bottom electrode is created on the top side (mask: METAL_1), over the oxide. Lift-off technique and RF-sputtering of Ti/Pt is used to do it (30 nm Ti /150 nm Pt).

The next step is the deposition of the AlN, i.e. the piezoelectric material which is the transduction material to extract the energy and the acoustic layer of FBAR as well. With a standard photo-lithography and the AlN etching, the devices are ready for the creation of the Pt/Ti top electrode (mask: METAL_2) with similar steps than for the bottom electrode. Then, the layout of the scavenger must be patterned with the mask RIE_FRONT and the top silicon layer can be completely etched by RIE. A layer of Al/Cu is deposited by sputtering on the backside to play the role of mask for the DRIE step. Afterwards, a 2 μm thick resist is spun coated over both sides. The resist of the front side will protect the fragile devices. A DRIE step is processed to completely etch the wafer substrate (510 μm). Finally, in order to release the structures, the buried oxide of the SOI wafer can be etched with HF vapor and the resist and Al/Cu layers can be removed.

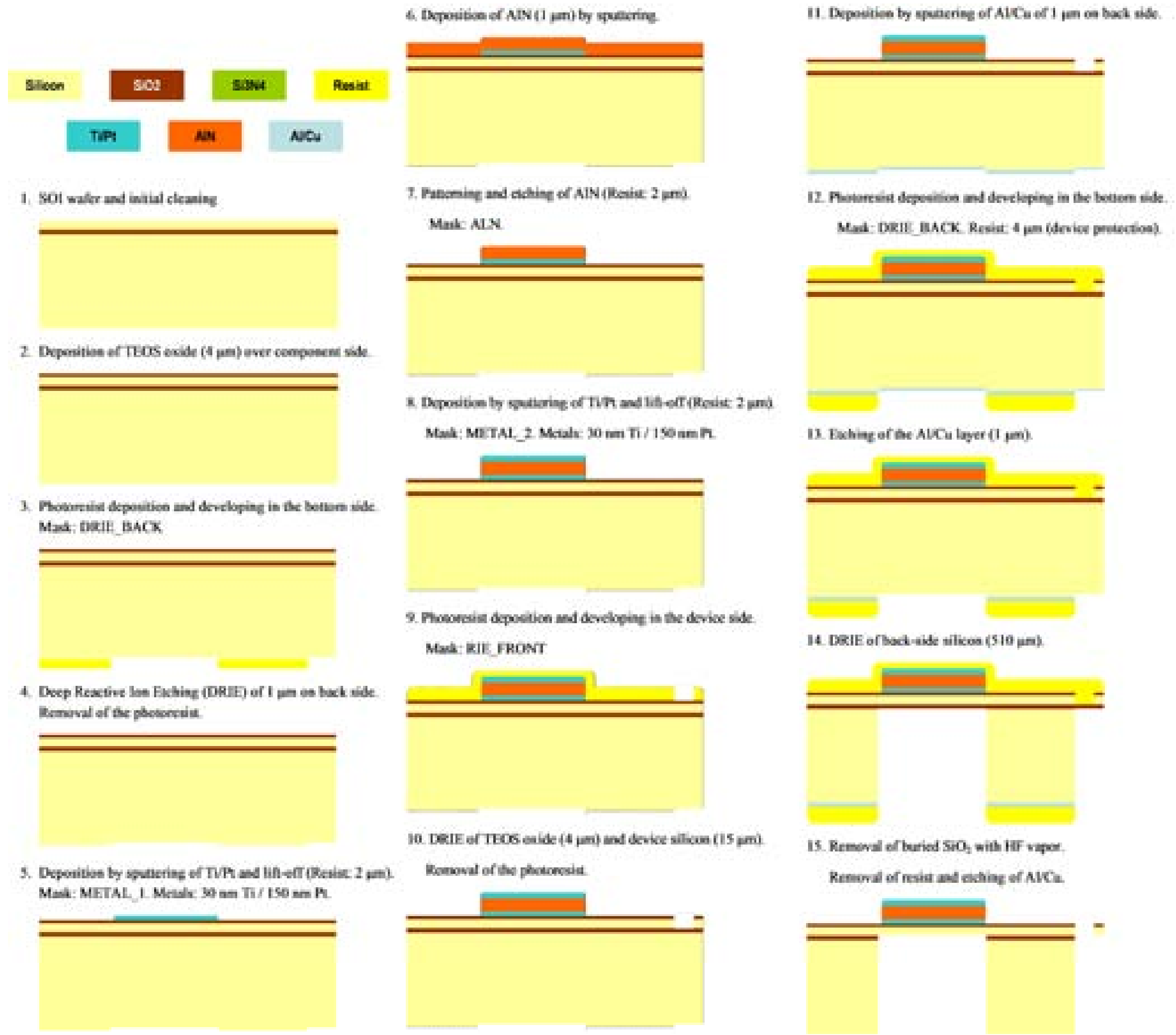

Figure 4.25. Fabrication process to make piezoelectric scavenger based on FBAR technology.

4.4.2 Energy Scavengers Design

This energy harvesting concept tries to couple the typical resonant frequency of the scavenger device, composed basically of an inertial mass and a cantilever based spring, with the environmental vibration frequency. The inertial mass movement in resonance generates torsion in the piezoelectric material, AlN, which generates a voltage signal.

In order to design a resonant element coupled with the environmental vibration, it can be used the well-kwon expression for the frequency of a mass-spring system:

$$f = \frac{\omega}{2\pi} = \frac{1}{2\pi}\sqrt{\frac{k_{ef}}{m_{ef}}} \qquad (4.11)$$

Where the effective mass of the system, m_{eff}, is approximately the inertial mass, and the effective spring constant of the compound support beam, k_{eff}, was defined in Chapter 2.

A whole wafer with several structures has been designed, fabricated and characterized in order to develop this concept. Several topologies and sizes were designed in order to explore

different applications and mechanical behaviors. Table 4.3 shows the device configurations included into the wafer layout (it can be seen in Appendix B).

Table 4.3. Summary of designed cantilever-shaped devices for several configurations of beam and mass sizes.

			Mass size (µm)										
Beam size		Length (µm)	1000	1000	1000	1000	2000	2000	2000	500	300-100	300-100	200-100
Length (µm)	Width (µm)	Width (µm)	1000	2000	3000	4000	1000	2000	4000	500	300	200	200
2000	500									X			
1000	1000		X	X	X	X	X	X	X				
1000	500								X	X			
1000	200							X					
500	500												
300-350	200-100-50										X		X
200-250	200-100-50										X		
100	200-100-50										X		X

In addition to the devices described in Table 4.3, two different resonators have been designed. The first device has a spiral-shaped beam (with a total length of 11.5 mm) that holds a central inertial mass (2 mm x 2 mm) as observed in Figure 4.26.

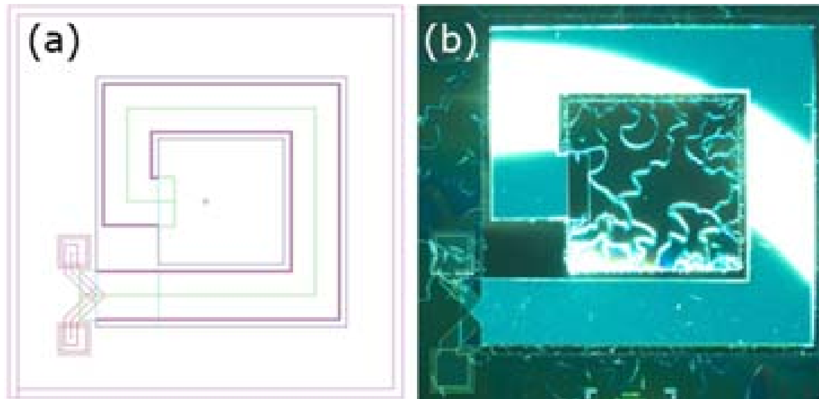

Figure 4.26. Layout (a) and optical image (b) of piezoelectric spiral-shaped energy harvester

This design pursues the decrease of the resonance frequency without the expected proportional size increase. However, it is typical for this type of design that when the inertial mass is driven at resonance, each beam segment will suffer bending with opposite signs that can partly cancel the charges generated by piezoelectric effect. One solution is to place separated electrodes for each beam section with a different bending sing and connect them with the right polarity. In the case presented here, this consideration has not been taken into account and a continuous top and bottom electrodes have been used. Although the power is

not optimized, it could be used as a proof-of-concept in order to demonstrate the resonance motion of this device.

Another special design is an EHiP core die, which can be used to be assembled with an additional chip as shown in Figure 4.27. It is based in the same concept presented in previous sections, but with an out-of-plane resonance motion direction.

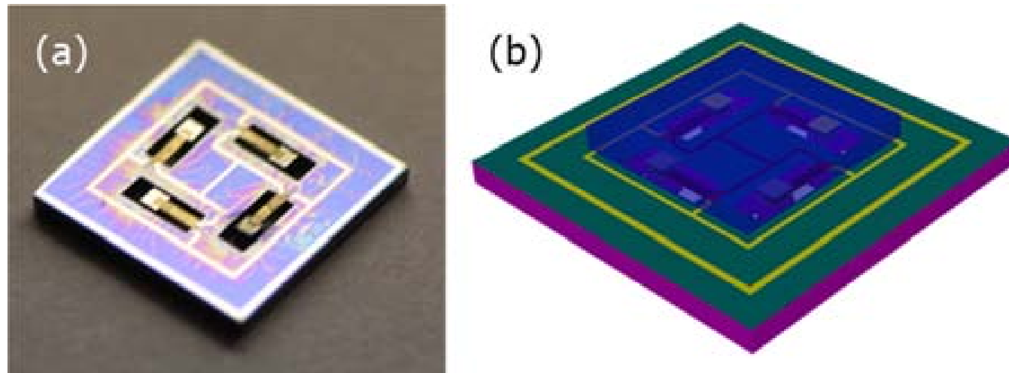

Figure 4.27. Optical image (a) and 3D model (b) of piezoelectric EHiP core die.

A collection of several fabricated devices after dicing is shown in Figure 4.28. It can be noticed the reduced size of all of them.

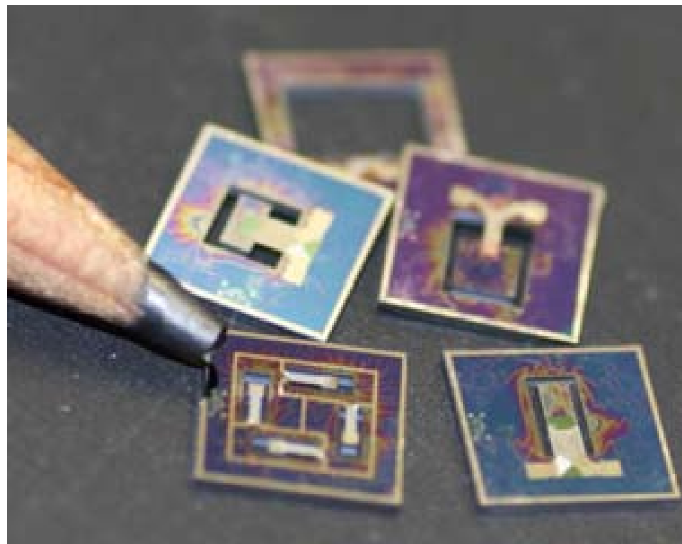

Figure 4.28. Optical image of several piezoelectric energy harvesters after dicing

4.4.3 Analysis and Mechanical Simulations

The designed structures have been analyzed by means of modal simulations using COVENTOR® software as well. Figure 4.29 contains the modal simulation for a design with L_b = 1000 µm, W_b = 1000 µm, L_m = 2000 µm and W_m = 1000 µm. The designs are pointed to maximize the mass and the power extracted. The energy scavengers have been simulated with COVENTOR software to find the resonance frequency and the expected behavior and performance. A simulation of the spiral-shaped device is shown in Figure 4.30, where can be seen the low value of resonance frequency achieved.

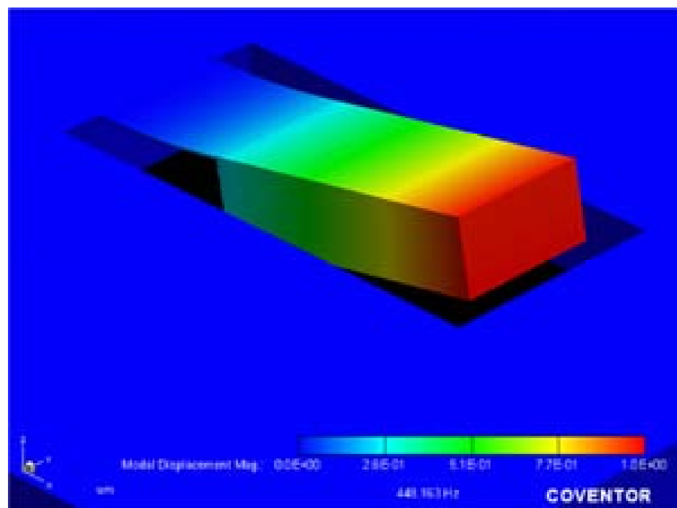

Figure 4.29. FEM simulation that shows the first mode of resonance at 448 Hz of the device with L_b = 1000 μm, W_b = 1000 μm, L_m = 2000 μm and W_m = 1000 μm.

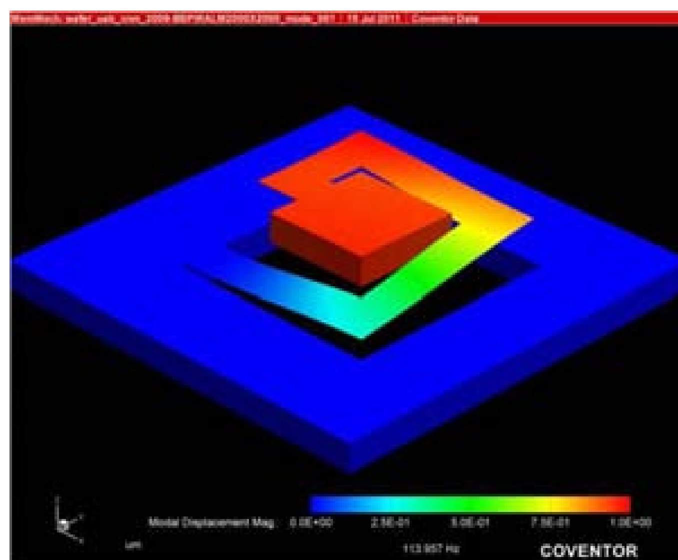

Figure 4.30. FEM simulation that shows the first mode of resonance at 114 Hz of the spiral-shaped device.

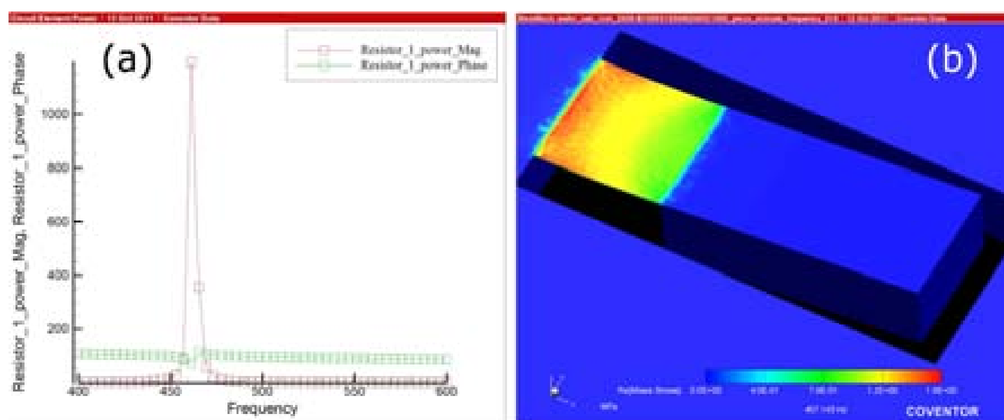

Figure 4.31. Harmonic simulation of a piezoelectric scavenger showing stress at resonance and the power over an R_L = 1.17 MΩ

The same device was simulated with COVENTOR, and an extracted power of 1 μW was obtained at a resonance frequency of 447 Hz (Figure 4.31(a)) from a 1-g harmonic acceleration and an effective quality factor of 50. The stress generated in the beam is shown in (Figure 4.31(b)) at resonance motion. It is clear that the area closer to the anchor suffers the higher value of stress and become the weakest point of the structure.

4.4.4 Electromechanical characterization

The first characterization was carried out placing the wafer on a probe station (Süss-Microtech PM-8) with a Network Analyzer (Agilent E5100A) that plays the role of both electrical excitation and read-out instrument. A frequency sweep can be generated by an S-parameter analysis, where the typical shape of a resonance peak is shown in Figure 4.32 Figure 4.32 for the S-21 parameter at different excitation power (in dBm). The characterized device is a cantilever beam without tip mass, with a beam of 2000 μm x 500 μm. These results are the first demonstration of the piezoelectric generation due to an electrically-driven resonance motion.

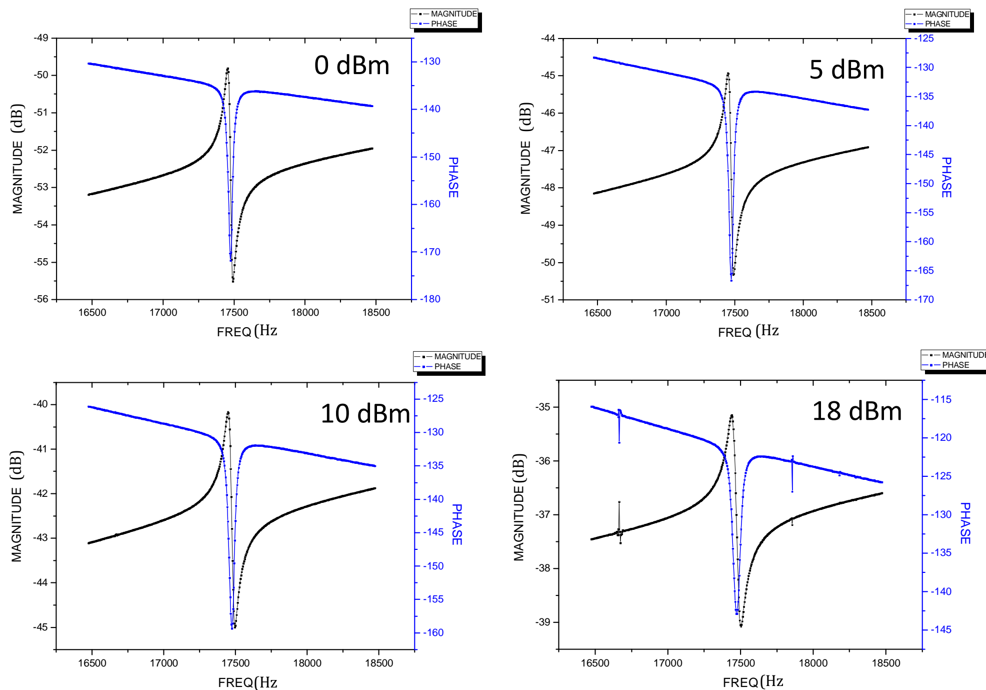

Figure 4.32. S21-parameter measurements of a piezoelectric cantilever beam resonating at 17.5 kHz for different excitation power values where magnitude is expressed in dB and frequency in Hz.

Another Network Analyzer (Stanford Research SR785) that allows capture voltage signals at low frequencies (from DC to 102.4 kHz) was used to first characterize some of the structures with tip mass. The setup used was formed by an ad-hoc wafer support that allows to the vibration motion of the cantilevers. A piezoelectric buzzer (2 cm of diameter) located to under the wafer at a distance of ~5 mm. A probe station was used to electrically connect the scavenger electrodes to the ports of the Network Analyzer. In Figure 4.33, the resonance peak of the device J8 is found at 625 Hz. A summary of some of the measured devices can be found in Table 4.4.

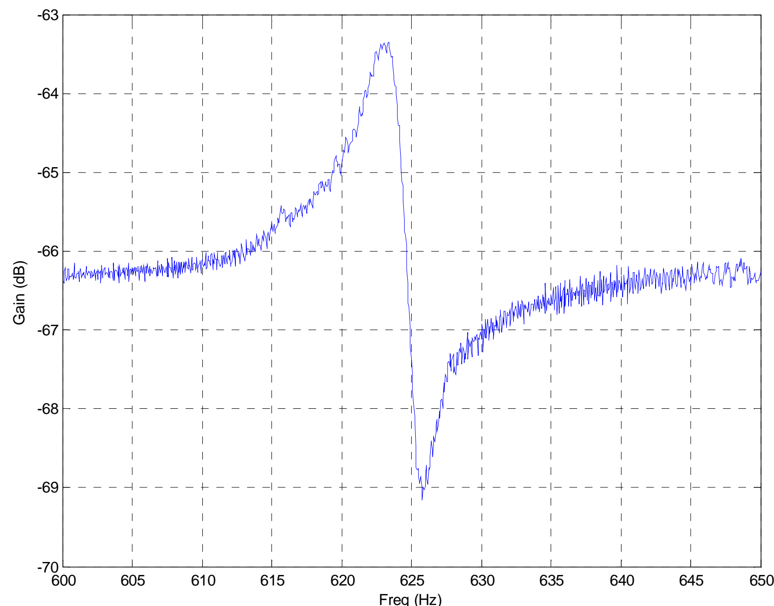

Figure 4.33. Resonance peak of device J8 measured with a Network Analyzer.

Table 4.4. Summary of several measured piezoelectric energy harvesters.

Device name	Beam length (µm)	Beam width (µm)	Mass length (µm)	Mass width (µm)	Resonance Frequency
K3	1000	500	500	500	2.17 kHz
L5	1000	1000	2000	1000	515 Hz
C5	1000	1000	1000	3000	622 Hz
J8	1000	1000	1000	3000	625 Hz
K8	1000	1000	1000	4000	530 Hz

Finally, it has been used a small speaker under the wafer under test to generate an acoustic wave (or sound) that remotely excites the inertial mass of the device placed directly over the speaker diaphragm. The measurements are performed at wafer-level in the probe station that allows connecting a probe to each electrode of the device under test. The two electrodes are connected through two coaxial cables to two different analog input ports of a data acquisition card in order to carry out a differential voltage. The data collected by this card is received into the computer running a MATLAB code that process the signals received by means of the subtraction of both signal, after this first step, the FFT of the resulting signal is calculated. A digital notch filters are used to remove the 50 Hz signal corresponding to the interferences from power lines and the DC signal too. The speaker is driven by a signal generator that is controlled by the MATLAB code too. Then, the maximum peak of the FFT is calculated (in volts) for every frequency point set into the signal generator for a certain excitation voltage. In addition, the electrodes are connected to an ad-hoc device that is controlled by the code and allows selecting eight different values of load resistors. The characterization of one of the device L5 with an excitation voltage of 8 V is reported in Figure 4.35. This voltage produces a sound of 92.6 dB that corresponds to a pressure of 0.85 Pa over the mass area. It is translated into an acceleration of ~0.64 m/s^2. Therefore, the force suffered by the mass is 1.7 µN It can be seen the optical image and the voltage generated over a load resistor of an optimum resistance value of 1.17 MΩ, for a frequency sweep (Figure 4.34).

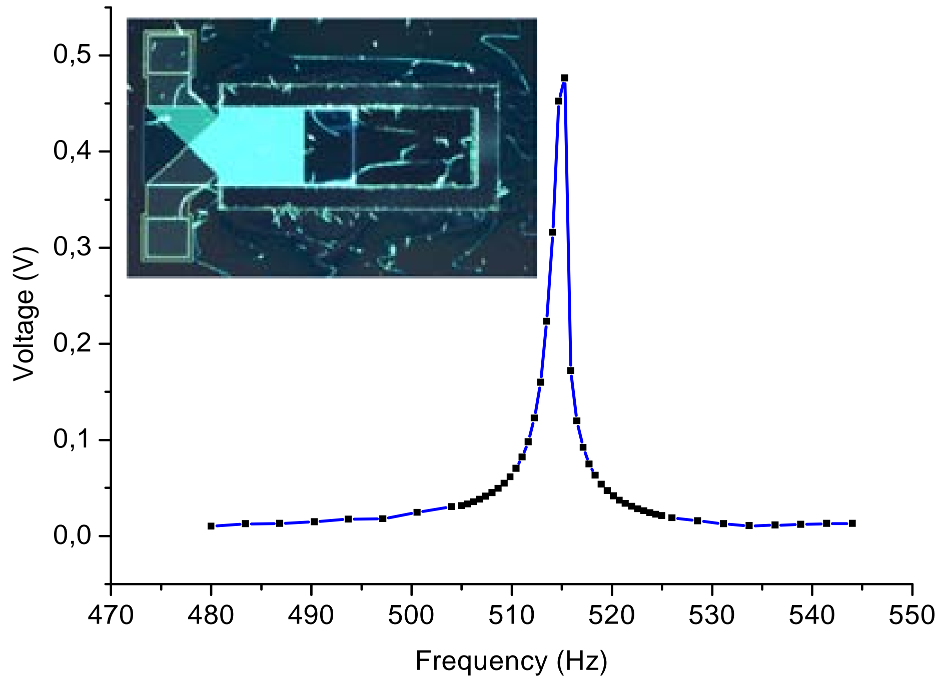

Figure 4.34. Generated voltage at resonance (515 Hz) of device L5 over a load resistor with optimal value of 1.17 MΩ. Inset: Optical image of the measured resonator.

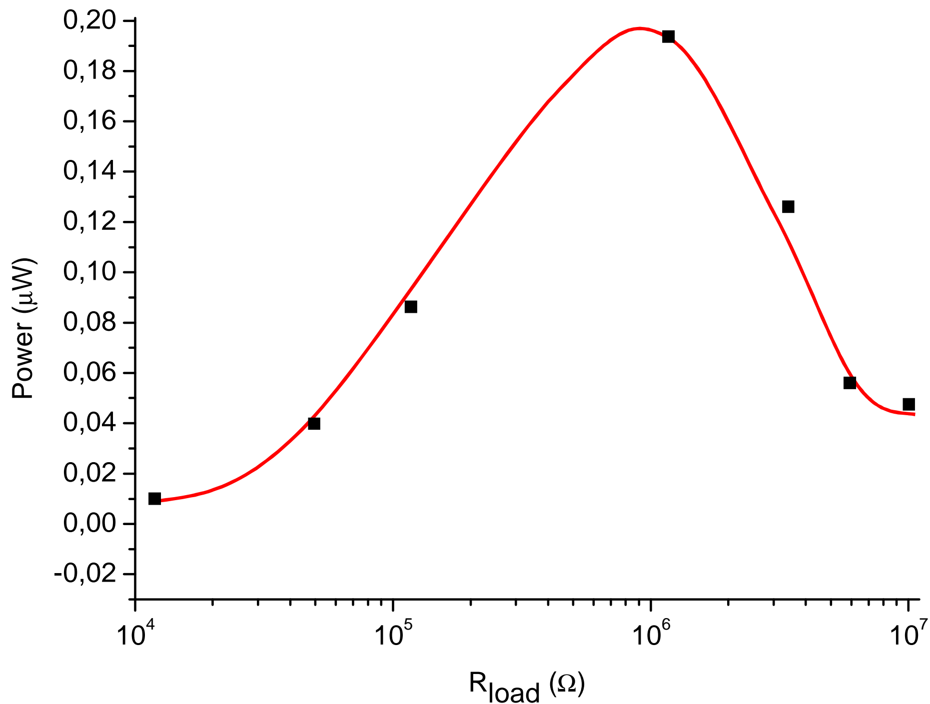

Figure 4.35. Dependence of the maximum generated power with the load resistance for the measured device.

It is clearly identifiable the resonance peak that occurs at 515 Hz with a quality factor of around 350. The different load resistors were used to find the optimal value where the

extracted power reaches a maximum value of almost 0.2 µW (Figure 4.35). That means an extracted power density value of 0.13 mW/cm^3.

One of the fabricated wafers has been diced for a further characterization of the single dice by using another speaker that emulates the function of an electrodynamical shaker. With this setup the die can be directly actuated by a vibration of larger acceleration amplitude instead of using acoustic waves over the inertial mass.

4.5 Another heterogeneous solution: Magnetically driven energy harvester

Since the weak point of the vibration-based energy scavengers is the difficulty of having availability of a constant-amplitude, frequency-stable, continuous-time ambient vibration, a new application field has to be exploited to find different ambient energy sources. In a domestic or industrial environment, the grid power is normally available and it is generating parasitic magnetic energy that could be used to cover numerous applications.

In this section, it is performed an analysis about the suitability of using the resulting force generated by a two-wire cord carrying an AC electric current over a permanent magnet. The sinusoidal magnetic force induced by the wires can be used to excite the resonant motion of a vibration-driven energy harvester tuned to the grid power frequency (50 and 60 Hz for Europe and US respectively).

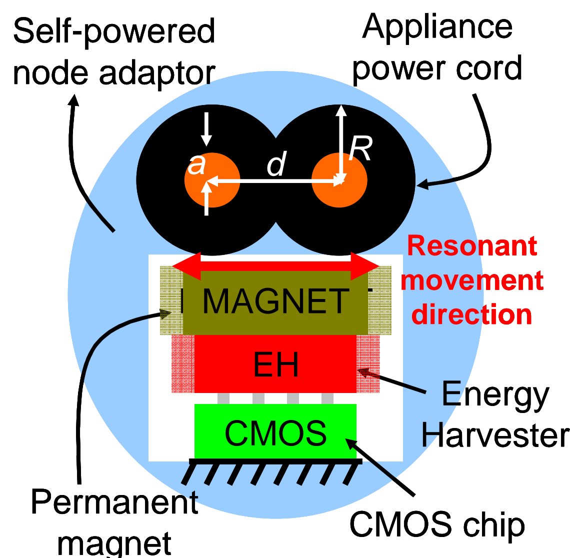

Figure 4.36. Diagram of a magnetically-actuated Energy Harvester in Package (EHiP) attached to an appliance power cord.

Therefore, this section introduces a micro-scale vibration-driven energy scavenging approach that uses a permanent magnet as part of the inertial mass with the aim of magnetically inducing an acceleration over it. Therefore, this concept can be considered as a special case of EHiP, where the role of inertial mass is played by the core die as well as the permanent magnet that is placed on top of this chip (see Figure 4.36). All these coupled elements together form an electrostatic energy harvester in package with magnetically induced resonant motion. The detailed study about the use of the magnetic field generated by

a two-wire cord has been carried out. Different numerical calculations and simulations have been performed to find the optimum design parameters and validate the main idea proposed here.

4.5.1 Configuration of the magnetically-driven EHiP

As stated before, a vibration-driven energy harvester with a well-defined resonance frequency at 50Hz is needed (European case). It is needed a device equivalent to a damped mass-spring system capable to get in resonance at the required frequency. The typical approach consists of a macroscopic piezoelectric beam with a large magnet attached to its tip. The main disadvantages of this system are the large size and the impossibility of put the device close to the wires. In order to solve this problem, the concept of energy harvester in package (EHiP) is used again.

In this case [11], the role of inertial mass is played by the core die as well as the permanent magnet that is placed on top of this chip. All these coupled elements form a micro-scale electrostatic energy harvester integrated in a package with magnetically induced resonant movement.

The electrostatic EHiP described in Section 4.3 can be used for this purpose. As COVENTOR simulations demonstrate, its resonance frequency of around 289 Hz (experimentally measured) drops to around 50 Hz by means of adding the mass of the permanent magnet (Figure 4.37).

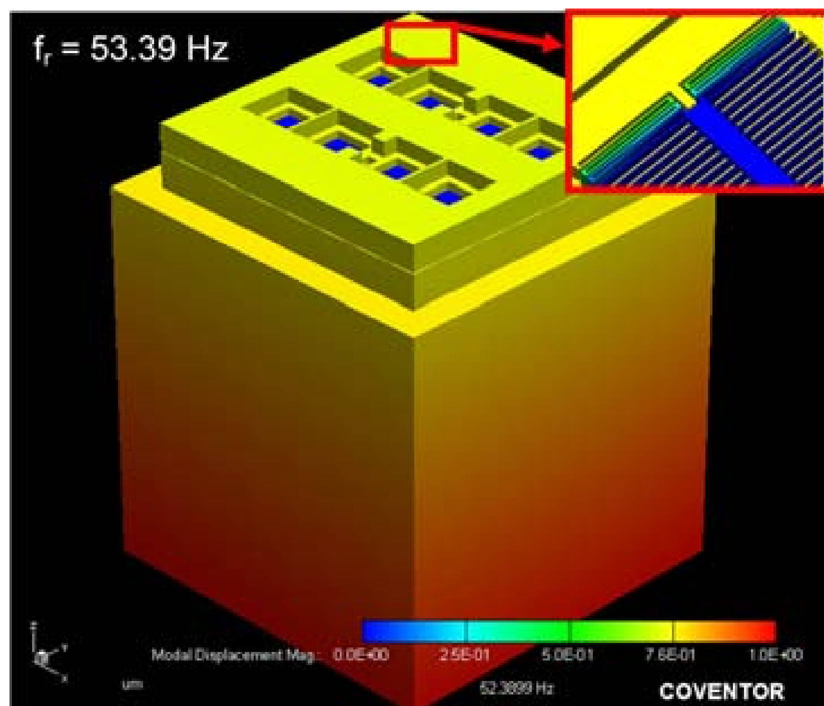

Figure 4.37. FEM modal simulation of the first resonant mode and detail of compressed suspensions. Note that the chip is anchored by the pads.

The resulting mass, taking a density of neodymium of 7.5 g/cm^3, is around 800 mg. Therefore the mass will displace around 3.9 μm due to the gravity acceleration. Since the

maximum internal distance to the substrate is 2 µm, a new design with stiffer suspensions for out-plane movements should be taken into consideration.

Due to its reduced size, this energy scavenger can be placed very close to the wires of the cord to find the point of maximum generated force over the magnet. Figure 4.36 illustrates a proposed adaptor to place the energy harvester in the desired position, and the system parameters are described in Table 4.5.

Table 4.5. Device and power cord features

Parameter		Value
Chip mass	m_{chip}	27 mg
Magnet mass	m_m	799 mg
Magnet remanence	Br	1.22 T
Length of cubic magnet side	l_m	4.85 mm
Conductor wire radius	a	0.65 mm
Distance between center of wires	d	3.6 mm
Radius of wire insulation	R	1.95 mm
Current carried by the cord	i	10 A (AC)

4.5.2 Magnetic force calculation

Theoretical fundaments

The magnetic field, $\vec{H}$, generated by a current-carried single wire is described by the Biot-Savard Law:

$$\left.\begin{aligned} r > a, \quad \vec{H} &= \frac{i}{2\pi r} u_t \times u_r \\ r < a, \quad \vec{H} &= \frac{ir}{2\pi a^2} u_t \times u_r \end{aligned}\right\} \tag{4.12}$$

Where i is the current passing through the wire, r is the radial distance from the center of the wire to the point of interest, u_l and u_r are unitary vectors pointing to the current direction and the interest point respectively.

From [3, 4], the force to a permanent magnet with magnetization, $\vec{M}$, in an external magnetic field, $\vec{H}$, can be calculated by integration of the force density, $\vec{f}$, over the magnet volume, V.

$$\vec{f} = \vec{\nabla}(\vec{M} \cdot \vec{H}) \tag{4.13}$$

Since the magnetization of the permanent magnet is constant, the longitudinal forces are given by,

$$F_{xMx} = B_r \int \frac{dH_x}{dx} dV, \quad F_{yMx} = B_r \int \frac{dH_x}{dy} dV \tag{4.14}$$

$$F_{xMy} = B_r \int \frac{dH_y}{dx} dV, \quad F_{yMy} = B_r \int \frac{dH_y}{dy} dV \tag{4.15}$$

Where the remanence of the permanent magnet, B_r, is uniform and oriented in the positive x-direction (M_x) or y-direction (M_y).

Numerical simulations

A MATLAB program has been created to numerically compute the magnetic force generated by two wires carrying an alternating current. In parallel, several COMSOL simulations have been carried out to verify the right working of the numerical calculations.

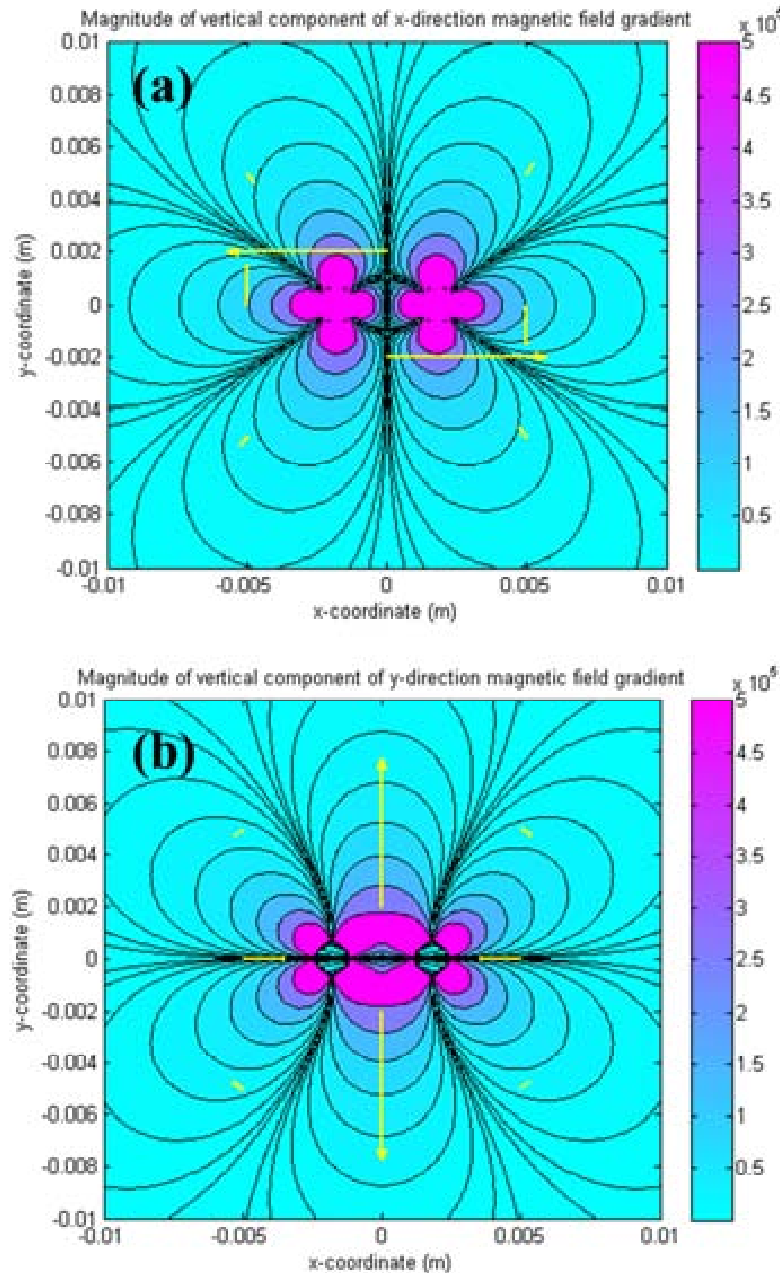

Figure 4.38. Magnitude of the vertical component of derivative of the magnetic field with respect to x (a) and y (b). Magnetic force vectors in several locations of a horizontally (a) or vertically (b) magnetized permanent magnet.

Figure 4.38 shows the two components of gradient of the magnetic field generated by the two wires of a power cord. By integration of this gradient over the volume of the desired

permanent magnet (vertically or horizontally magnetized) in several locations, the magnetic force has been calculated.

The more interesting working positions of the magnet are through the y-axis, because a force with maximum magnitude and only one direction can be obtained. For our purpose a magnet horizontally oriented is going to be used to get a lateral magnetic force.

4.5.3 Parametric analysis

In [12], Leland et al. calculated the expression (4.16) for the y-direction gradient of H_y along the y-axis line. They found the location when the gradient is maxima and they claim that the magnetic force will be maximum at this position too. But it is not completely right, because the magnetic force is proportional to the area behind the gradient surface. The magnet will enclose this maximum of gradient, but it can be numerically demonstrated that it will be centered farer from the wires, which is advantageous for this device.

$$\left.\frac{dH_y}{dy}\right|_{(x=0)} = -\frac{i2yd}{\pi(y^2+d^2)^2} \tag{4.16}$$

However, it can be used this expression (or the analogous for an x-axis oriented magnet) to calculate the force by supposing that the gradient has the same shape for the whole magnet volume.

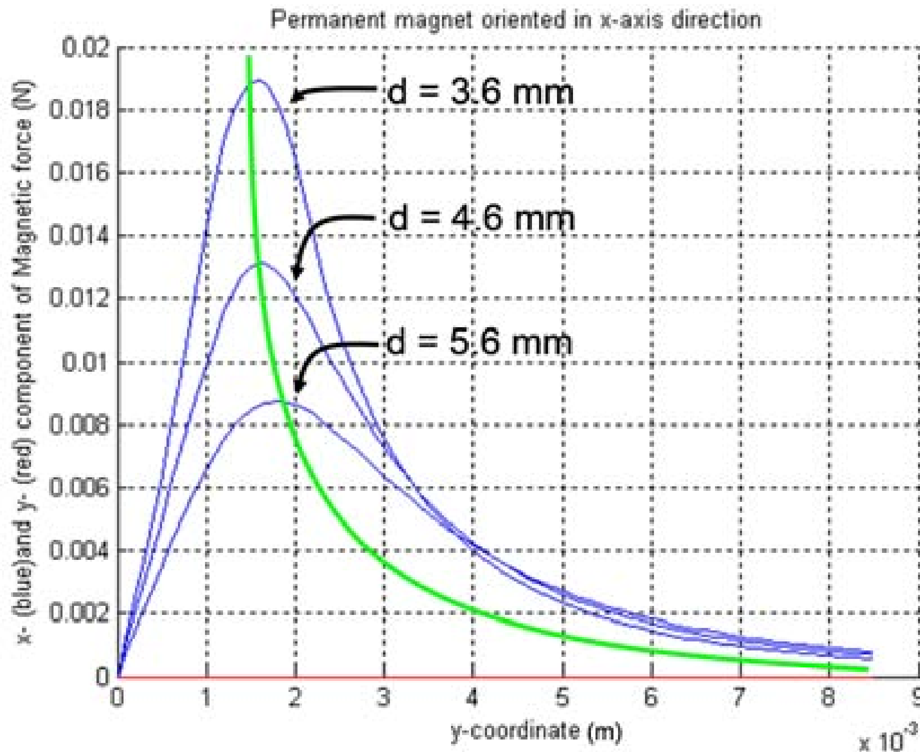

Figure 4.39. Comparison between different methods to calculate the magnetic force along the y-axis.

The comparison between this approximation, a COMSOL simulation and MATLAB numerical calculation is shown in Figure 4.39. Both numerical approaches have identical

shapes, but the approximation is not able to fit them perfectly. Nevertheless, it can be certainly useful as analytic approach the early stages of design.

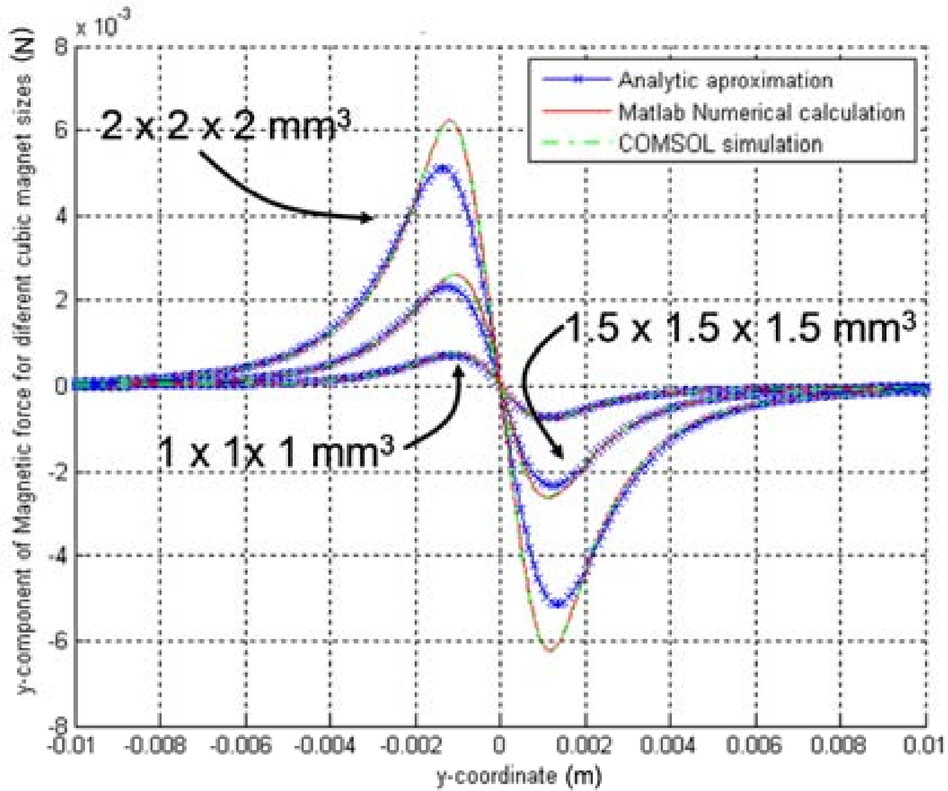

Figure 4.40. Parametric study between magnetic force and separation of the cord wires.

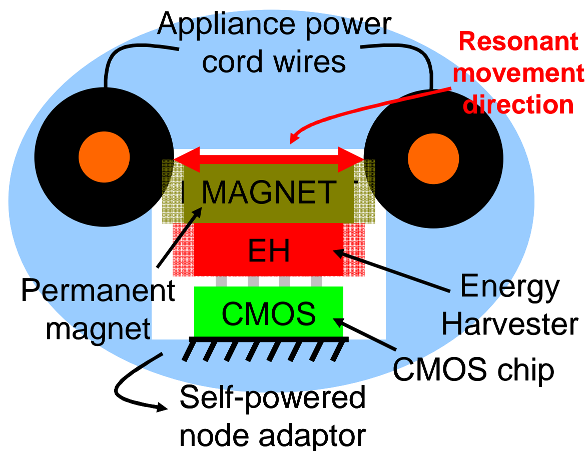

Figure 4.41 .Diagram of new possibility of attaching the energy harvester to an appliance power cord.

A parametric analysis has been made with a magnet size of 1 x 1 x 1 mm³ and changing the distance between wires. In Figure 4.40, it is observed that the larger separation of the wires, the lower force magnitude. But another interesting effect is taking place, the curve maximum

is moving away from the cord insulation layer and it is now possible to place the magnet in this maximum induced force point.

In order to take advantage of this positive effect, Figure 4.41 shows a new proposal to attach the energy harvester to the power cord.

4.5.4 EHIP prototype at cm-scale

A prototype of an EHiP has been fabricated at the cm-scale to demonstrate the feasibility of moving the device with the magnetic force generated over a magnet close to a current-carrying power cable. Figure 4.42 shows picture of the prototype, where the concept of using the own magnet as part of the inertial mass has been used. In that case, because of the size of the whole device, it is not especially interesting to apply the ideas of the EHiP, but it plays a key role as a proof of concept.

As shown in Figure 4.42, four commercial piezoelectric beams (MEAS-SPEC DT-series) that suspend a center shuttle which is supporting an attached permanent magnet. The electrodes of the piezoelectric beams are connected in parallel, in order to maximize the generated current value. A red line on the top of the permanent magnet indicates its magnetization direction. A power cable has been placed over the device in order to generate the magnetic field that will move the center shuttle.

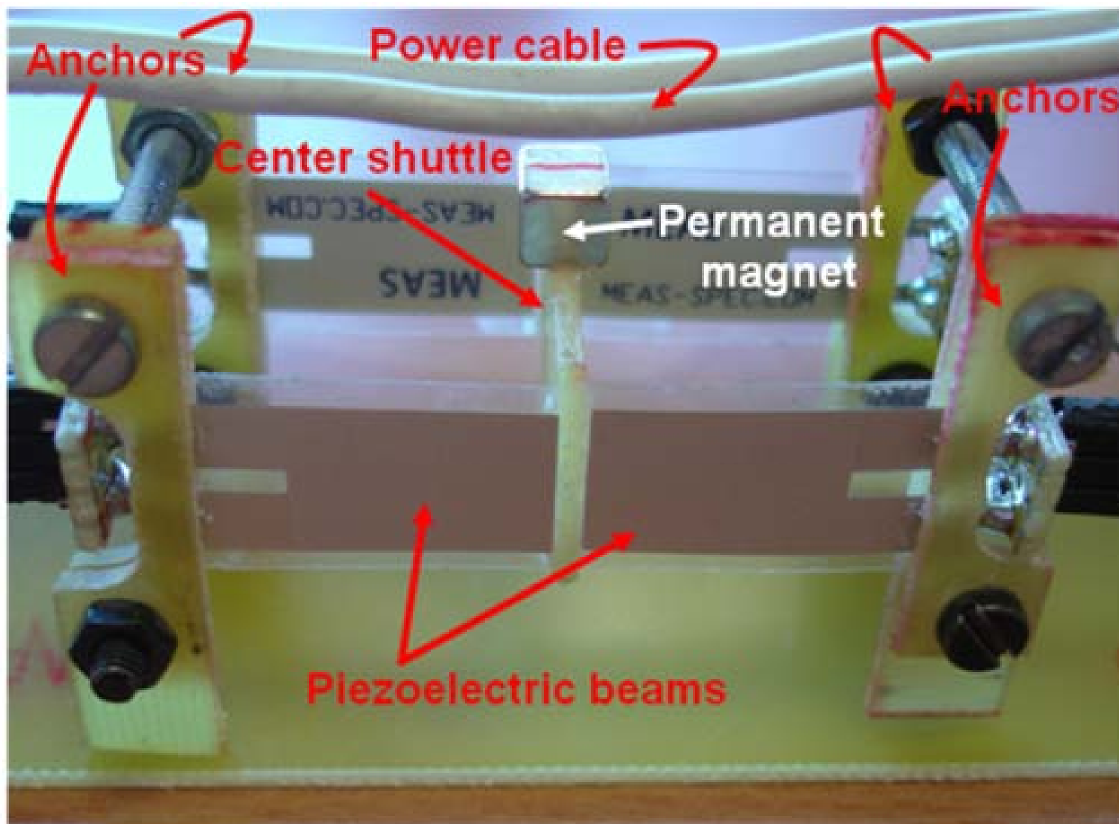

Figure 4.42. Prototype picture under the power cable.

The harvested electrical power has been characterized through the piezoelectric voltage measured with an oscilloscope (R_{in} = 1 MΩ) for four different values of the power cable

current. The power and current values used to characterize the prototype are collected in Table 4.6. Also, it is presented the RMS value of the power that is generated by this prototype over the oscilloscope input resistance.

Table 4.6. Summary of RMS current and power generated by an appliance working at difference power values at 220V @50Hz.

Appliance power (W)	RMS current (A)	RMS power (µW)
1200	5.45	0.029
2400	10.91	0.104
3600	16.36	0.220
4800	21.82	0.336

Figure 4.43 shows the voltage measured by the oscilloscope for different values of the appliance power.

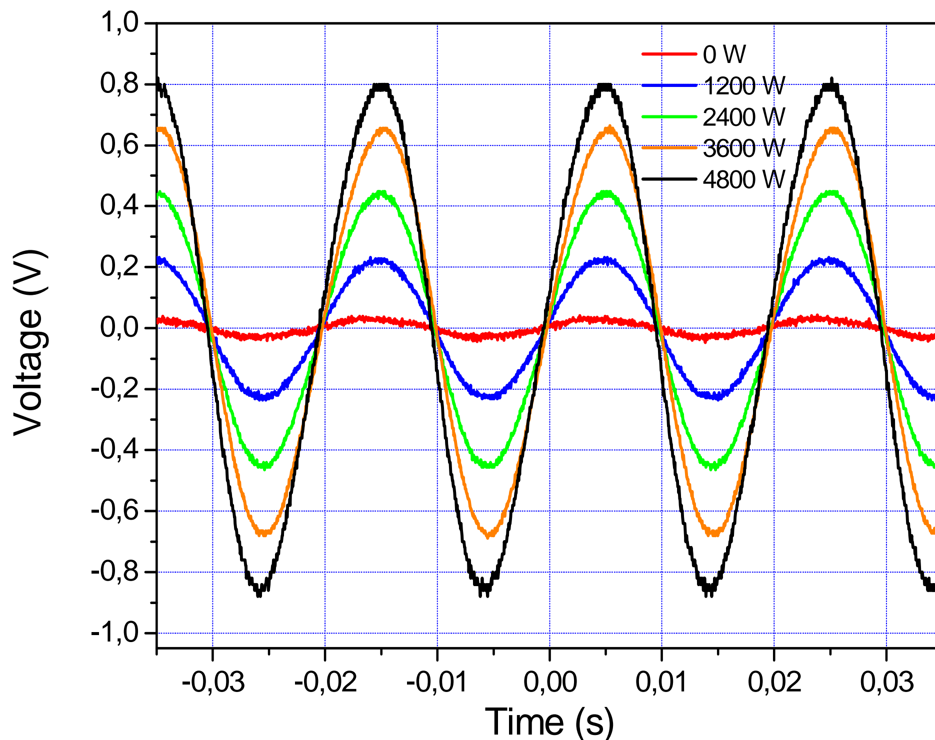

Figure 4.43. Voltage generated (over an R = 1 MΩ) by the prototype for four different values of current carried by the cable (i.e. appliance power at 220V @ 50 Hz).

In order to clearly illustrate the operation of this device, its frequency response is shown in Figure 4.44. It can be observed that the peak of resonance centered at 51 Hz when the prototype is excited by an electromagnet connected to a signal generator. The insets show an optical image of the motion of the border of the center shuttle at and out of resonance.

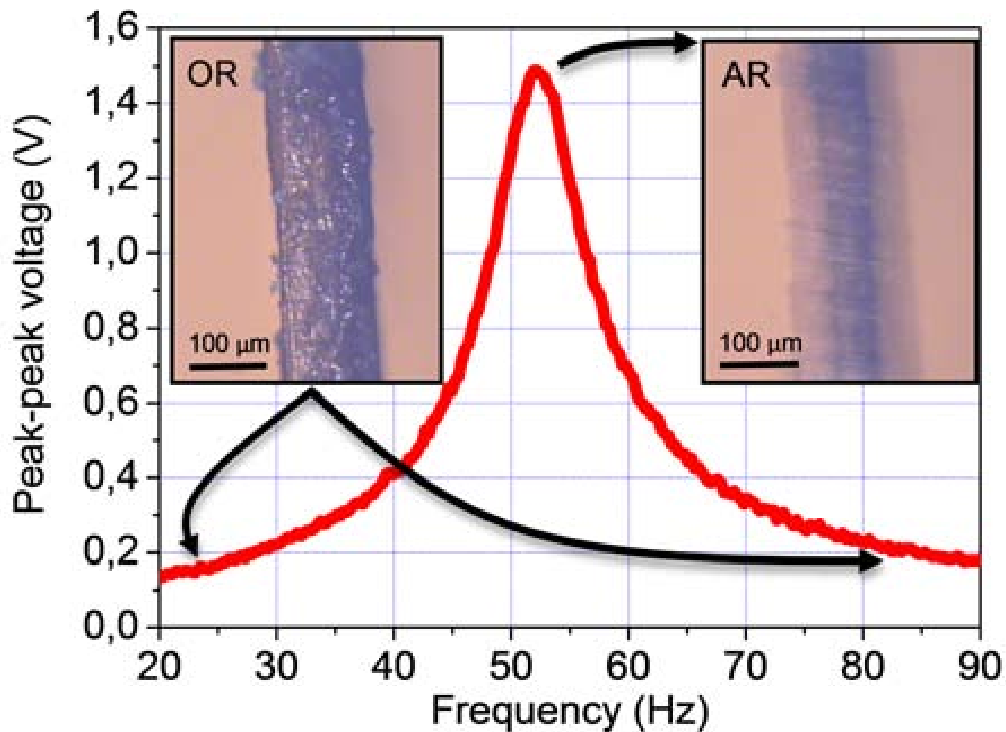

Figure 4.44. Frequency response of the prototype. Excitation source: electromagnet. Inset: Optical images of the piezoelectric beam edge at resonance (AR) and out of resonance (OR).

4.6 Conclusions

The use of a heterogeneous integration is presented as a key aspect in the proliferation of this type of devices and toward the development of real autonomous wireless sensors networks. It has been demonstrated that the use of the ideas involved in the concept of EHiP supposes an improvement in the throughput of a vibration energy converter. The design, fabrication and characterization of a fully-dedicated core die of an energy harvester in package (EHiP) with electrostatic transduction are presented in this chapter. A parametric design has been developed by using ARCHITECH® software. A SOI- based MEMS technology, which allows a robustness improvement and better performance, has been used instead of a commercial CMOS technology [4]. An ad-hoc assembling process between the energy-harvesting core die and a test PCB substrate has been successfully developed. Experimental characterizations have been carried out to demonstrate the resonance motion at 289 Hz and the correct operation of the assembled system. An expected maximum generated power of 11 µW has been calculated when the energy harvester operates at charge-constant cycle, for a best-case scenario. That means a power density of ~0.85 mW/cm^3, for an input vibration acceleration of around 1 g, an initial and final voltage of 10 V and 52 V respectively, and an effective quality factor of 50.

A manufacture process to build piezoelectric energy scavengers has been proposed, using a well-kwon process compatible with FBAR fabrication. Hence, it is possible to use the same run to fabricate energy microgenerators and FBAR devices for RF and sensing applications.

A deep theoretical study based on numerical method analysis has been performed concerning to the use of the magnetic force generated by a current-carrying cord in a permanent magnet. It has been demonstrated the advantages of using a micro-scale energy harvester to be attached to the power cord. Due to the EHiP concept presented in this chapter, a reduced size and a high extracted power density can be achieved.

In order to demonstrate these advantages, two different prototypes have been analyzed. On one hand, the micro-scale energy harvester presented in Section 4.3 is adapted with a permanent magnet to achieve a magnetically actuated resonant device tuned to 50 Hz. On the other hand, a cm-scale prototype made with commercial piezoelectric beams was fabricated and the concept was proved.

References

[1] E. H. Herbert. Heterogeneous Integration. Available: ftp://ftp.cordis.europa.eu/pub/ist/docs/eniac/sra_gre_ws_heterointegration.pdf

[2] K. Pressel. (2008, System Integration. *(Euripides Forum)*. Available: http://www.euripides2008.de/download/vortraege/Euripides%20Pressel%20ITRS%209_10_2008%20v0%20fin.pdf

[3] G. Murillo, G. Abadal, F. Torres, J. L. Lopez, J. Giner, A. Uranga, and N. Barniol, "Harvester-on-chip: Design of a proof of concept prototype," *Microelectronic Engineering,* vol. 86, pp. 1183-1186, 2009.

[4] S. Roundy, P. K. Wright, and J. M. Rabaey, "Energy Scavenging for Wireless Sensor Networks: With Special Focus on Vibrations," Springer, 2004.

[5] G. Murillo, G. Abadal, F. Torres, J. L. Lopez, J. Giner, A. Uranga, and N. Barniol, "On the Monolithic Integration of CMOS-MEMS Energy Scavengers " in *23rd Conference on Design of Circuits and Integrated Systems (DCIS)*, Grenoble, France, 2008.

[6] *MEMSOI technology - Tronics*. Available: http://www.tronicsgroup.com/mems-foundry/memsoi-mpw-run-europractice

[7] M. Marzencki, S. Basrour, and B. Charlot, "Design, modelling and optimisation of integrated piezoelectric micro power generator," 2005, pp. 545–54.

[8] H. Campanella Pineda, "Thin-film bulk acoustic wave resonators-FBAR: fabrication, heterogeneous integration with CMOS technologies and sensor applications," Universitat Autònoma de Barcelona, 2008.

[9] H. Campanella, A. Uranga, A. Romano-Rodriguez, J. Montserrat, G. Abadal, N. Barniol, and J. Esteve, "Localized-mass detection based on thin-film bulk acoustic wave resonators (FBAR): Area and mass location aspects," *Sensors and Actuators A-Physical,* vol. 142, pp. 322-328, 2008.

[10] G. Murillo, G. Abadal, F. Torres, J. L. Lopez, J. Giner, H. Campanella, A. Uranga, J. Esteve, and N. Barniol, "Novel designs of piezoelectric scavengers using FBAR technology," in *8th International PowerMEMS Workshop*, Sendai, Japan, 2008.

[11] G. Murillo, J. Agusti, G. Abadal, F. Torres, J. Giner, E. Marigó, A. Uranga, and N. Barniol, "Microscale energy harvester driven by a built-in permanent magnet for self-powered nodes in appliance power cables " in *10th International PowerMEMS Workshop*, Leuven, Belgium, 2010.

[12] E. S. Leland, P. K. Wright, and R. M. White, "A MEMS AC current sensor for residential and commercial electricity end-use monitoring," *Journal of Micromechanics and Microengineering,* vol. 19, pp. -, 2009.

CHAPTER 5

SUBMICRON-SCALE ENERGY SCAVENGING BASED ON ZNO NANOWIRES

ZnO is a promising material that has received a huge attention in the last years. The convergence of piezoelectric, semiconductor and photonic properties in a single material is one key of its successful. The other point is that it can be used to create a wide variety of nanostructures. Nanowires (NWs) have a direct application on energy harvesting. The bending of this wire generates a piezoelectric potential that can drive a current over a load resistor that leads to a mechanical-to-electrical energy conversion. The generated power can be enhanced by integrating NW arrays or by using a resonance motion that increase the mechanical energy input when the source is an ambient harmonic vibration.

5.1 Introduction

This chapter mainly presents the know-how learning by the author during the 5-month stay in the research group leading by Prof. Zhong Lin Wang at Georgia Institute of Technology (Atlanta, Georgia, USA). This research group is one of the most cited worldwide in the field of nanotechnology, reaching thousands of citations of their works. They defined the concept of nanopiezotronics in 2004 and nanopiezophototronics in 2009 and invented the first energy generator powered by piezoelectric nanowires (NWs) of ZnO.

In that stay the author learn how to grow the NWs by different process and how to implement some of their nanogenerators. In addition, several novel approaches were developed by the author, mixing the micro-scale vibration-driven energy harvesting with the nanogeneration of energy based on ZnO NWs. For this reason this chapter contains an important part that is a tutorial about the different growth methods and a compilation of the state-of-the-art in the field of energy harvesting with ZnO NWs. This part has been based on [1], where a more detailed description about this field can be found. Finally, several novel experiments and out-going projects in collaboration with this group are presented after the review part.

5.2 Zinc-oxide properties

ZnO has become a hot topic in material science over last few years. It is due to its wonderful properties, provided in Figure 5.1, that are difficult to be found in nature in one single material. It was exploited as photonic material because of its direct bandgap of 3.37 eV that can result in the generation of UV light. It is possible to grow a wide variety of nanostructures utilizing this material, and it has the dual property of being both a semiconductor and piezoelectric material. One of the most useful nanostructures that can be utilized to generate energy is the NW. The ZnO NW can grow from different substrates, even though a crystalline material with a similar lattice constant is the best choice in order to obtain aligned and high-quality NWs. Additionally, in order to catalyze the growth of the NW, a seed material, such as a gold or ZnO layer, has to be used.

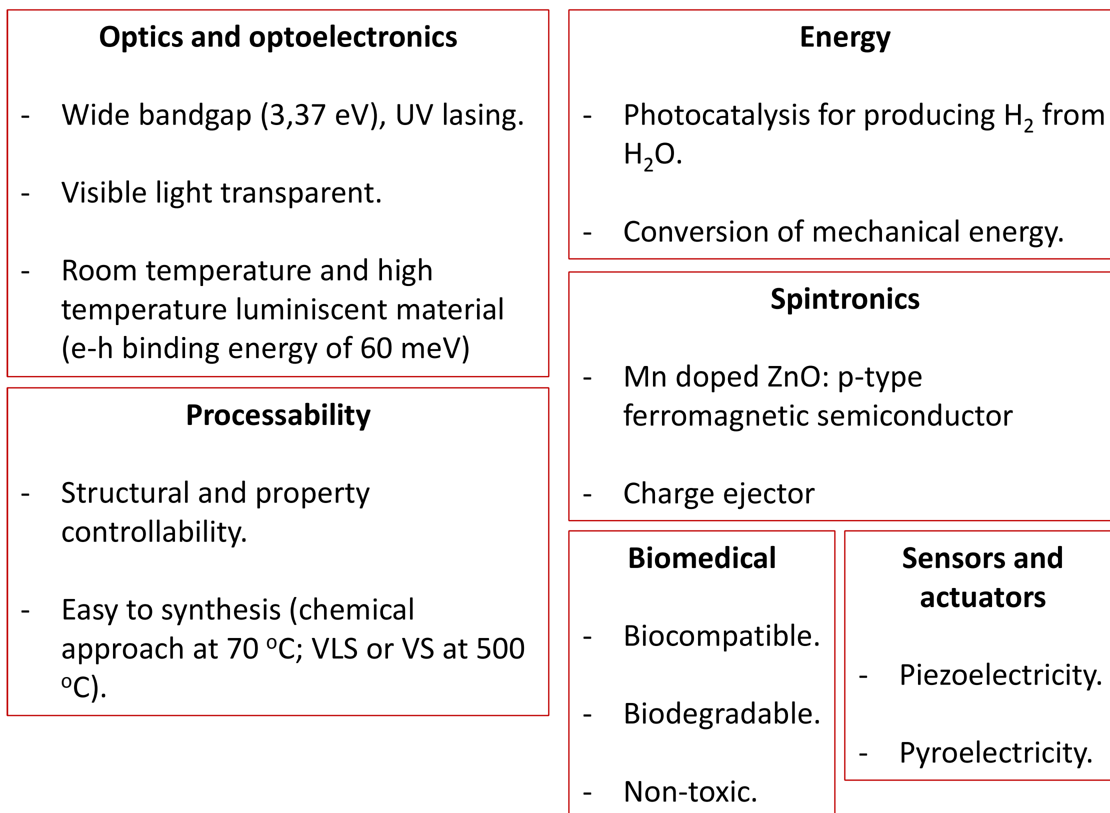

Figure 5.1. Main properties of Zinc Oxide (ZnO)

Under conventional conditions, ZnO has the wurtzite structure, which has a hexagonal unit cell with space group C6mc and lattice parameters a = 0.3296 nm, and c = 0.52065 nm. The oxygen anions and Zn cations form a tetrahedral unit. The entire structure lacks of central symmetry. The structure of ZnO can be simply described as a number of alternating planes composed of tetrahedrally coordinated O^{2-} and Zn^{2+} ions, stacked alternatively along the c-axis (Figure 5.2).

Although the entire unit cell of ZnO is neutral, the distribution of the cations and anions could take specific configuration as determined by crystallography, so that some surfaces can be terminated entirely with cations or anions, resulting in positively or negatively charged

surfaces, called polar surfaces. The polar charge dominated surfaces can give some unique growth phenomena.

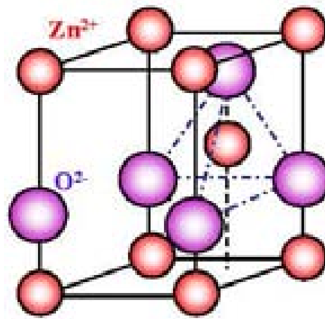

Figure 5.2. Wurtzite structure model of ZnO, which has non-central symmetry and piezoelectric effect.

Due to the semiconductor nature of the ZnO, when a metal is put in contact with ZnO, the metal-semiconductor interface created can behave as a rectifier or a resistor. Depending on the metal work function and the electron affinity of the ZnO, the junction will form an Ohmic or resistive contact instead of a Schottky or rectifier contact. In spite of the fact that high-quality Schottky contacts are critical for ZnO device applications, the chemical reactions between the metal and the semiconductor, the surface states, the contaminants, the defects in the surface layer, and the diffusion of the metal into the semiconductor are well-known problems in the formation of Schottky contacts.

5.3 Nanowire growth methods

There are several ways to grow NWs, some of them will be briefly presented here. A deeper review of the existing methods can be found in [1, 2].

5.3.1 Vapor-solid process

Vapor-solid process is a simple method that allows effectively growing oxide nanostructures without using a catalyst. There are two common approaches for vaporizing the source material: thermal vaporization and laser ablation. The first one is a simple process where the powder source material is vaporized at high temperature. The resultant vapor is condensed under certain conditions (such as temperature, pressure or type of substrate) to obtain the final product (Figure 5.3).

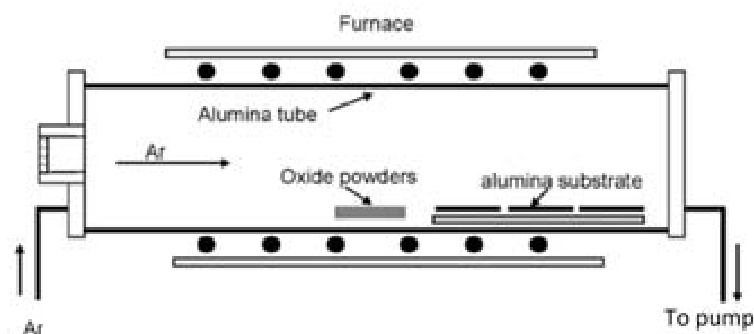

Figure 5.3. Furnace used to grow nanowires by VLS and VSS processes.

5.3.2 Vapor-liquid-solid process

Aligned NWs can be grown with the use of catalyst particles or seed layers. The first demonstration of growth of perfectly aligned ZnO nanowires was on a-plane orientated single-crystal aluminum oxide (sapphire) substrates. The growth was initiated and guided by a catalyst particle of Au and the epitaxial relationship between ZnO and Al_2O_3 leads to the alignment [3]. Unlike the normal vapor-liquid-solid (VLS) process, a moderate growth rate is required for the alignment since the catalyst needs to be molten, form the alloy and precipitate step by step to achieve the epitaxial growth of ZnO on sapphire surface. Thus, a moderate low growth temperature was applied to reduce the vapor concentration. Mixing ZnO with carbon powder (called carbon-thermal evaporation) can reduce the vaporization temperature from 1300ºC to 900ºC.

$$ZnO(s) + C(s) \rightleftarrows Zn(v) + CO(v) \tag{5.1}$$

At a relative lower temperature, the above reaction is reversible. Therefore, when the Zn vapor and CO are transferred to the substrate, they can react and form ZnO again. This ZnO can be absorbed by the gold catalyst and eventually form ZnO NWs.

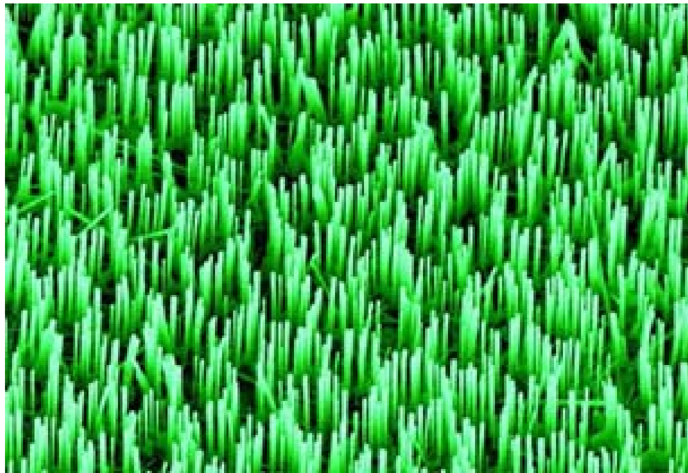

Figure 5.4. SEM image of aligned ZnO nanorods patterned in a honeycomb distribution [3].

The catalyst can be patterned by lithography or self-assembling techniques. Figure 5.4 shows the result of growing ZnO NWs over a hexagonal network of gold layer. This hexagonal distribution was achieved by deposition of a thin layer of gold over a sapphire substrate cover by a monolayer of submicron polystyrene spheres. When the spheres were etched away, the honeycomb-like distribution was obtained [3]. All the NWs are perpendicular to the substrate surface due to the seed layer patterning. When a catalyst is a thin layer of gold, the distribution of the NWs would be random.

The alignment quality is directly related to the epitaxial relationship between the substrate surface and ZnO nanowires. Substrates with small lattice mismatches, such as sapphire and nitride, can get a successful alignment. Aligned ZnO NWs have been successfully grown on sapphire, GaN, AlGaN and AlN substrate [4] through a VLC process, where the crystal structure of the substrate is crucial for the orientation of the NWs. Systematic investigations have been performed to find the influence of the following

parameters with the alignment quality: chamber pressure, oxygen partial pressure [5] and thickness of catalyst layer [6].

5.3.3 Pulse laser deposition

Pulse laser deposition (PLD) is a well-known technique for thin-film deposition that can be used for the deposition of several materials, such as ceramic oxides, nitride films, metallic films and superlattices. The key point for growing vertically aligned NWs is in-situ fabrication of a textured ZnO buffer layer on a silicon substrate before moving to the condition for the NW growth. The topology of the NW array can be controlled by four parameters: substrate temperature, growth pressure, the flow ratio of argon and oxygen and the laser repetition frequency [7].

5.3.4 Chemical approach

One of the main advantages of this growth is the independence with the substrate type as long as a ZnO seed is used, such as a thin-film layer or nanoparticles. Alignment of the ZnO nanocrystals occurs on flat surfaces regardless of their crystallinity or surface chemistry thin film or nanoparticules are used. This approach normally requires an annealing at 150 ºC of the ZnO seed in order to improve the particle adhesion to the substrate. Nanorod vertical alignment is improved by annealing the ZnO seeds at 350 ºC.

Other catalysts such as Au, Ag and Pt can be used to perform ZnO synthesis. These metals can be deposited onto polymeric substrates as thin films to achieve nanowire growth. The surface roughness of the thin film must be carefully controlled to promote nucleation and ensure a vertical alignment of the nanowires.

The most used chemical agents for the hydrothermal synthesis of ZnO NWs are zinc nitrate hexahydrate and hexamethylenetetraine [8, 9]. Zinc nitrate hexahydrate salt provides Zn^{2+} ions required for the ZnO NW growth. The responsible of providing O^{2-} is water. The function of hexamethylenetetraine in the chemical reaction is not completely clear yet. The more accepted hypothesis is that this agent works as a weak base. Therefore, it can slowly hydrolyze in water solution and gradually produce OH^{-}. This fact is critical because a high density of OH ions would translate into a quick precipitation of the ZnO ions in solution due to the high pH value. It would mean a fast consumption of the nutrient and the impossibility of a further growth of ZnO NWs.

The chemistry of the growth is well-known and is controlled by the following five reactions:

$$(CH_2)_6 N_4 + 6H_2O \rightleftarrows 4NH_3 + 6HCHO \quad (5.2)$$

$$NH_3 + H_2O \rightleftarrows NH_3{\cdot}H_2O \quad (5.3)$$

$$NH_3{\cdot}H_2O \rightleftarrows NH_4^+ + OH^- \quad (5.4)$$

$$Zn^{2+} + 2OH^- \rightleftarrows Zn(OH)_2 \quad (5.5)$$

$$Zn(OH)_2 \rightleftarrows ZnO + H_2O \quad (5.6)$$

All of the five reactions are actually in equilibrium that can be controlled by adjusting the reaction parameters, such as precursor concentration, growth temperature and time, in order to push the reaction equilibrium forward and backward. Precursor concentration is usually

responsible for the nanowire density whereas growth time and temperature determine the ZnO NW morphology and aspect ratio.

Grown process description

A silicon wafer (100) is cleaned by a standard cleaning process, which consists of an ultrasonicated bath of acetone, ethanol, IPA (isopropyl alcohol) and de-ionized (DI) water each for 10 minutes. Then, it is dried with nitrogen and baked on hotplate at 200 ºC for 5 minutes to eliminate the absorbed moisture. Afterwards, an intermediate layer of gold, which should assist the NW growth, is deposited by magnetron plasma sputtering. A 20-nm Ti layer is deposited in order to improve the adhesion of the gold layer and to buffer the large lattice mismatch between Si(100) surface with the native oxide and Au(111) surface. An annealing of the substrate is performed after the deposition at 300 ºC for 1 hour. The nutrient solution is composed of 1 to 1 ratio of zinc nitrate and HMTA. The substrate is put floating face down at top of the nutrient solution surface. The nutrient solution with the substrate can be baked in an oven at low temperature for several hours (e.g. 70 ºC for 24 hours to get a length of ~4 µm and a thickness diameter of ~200 nm).

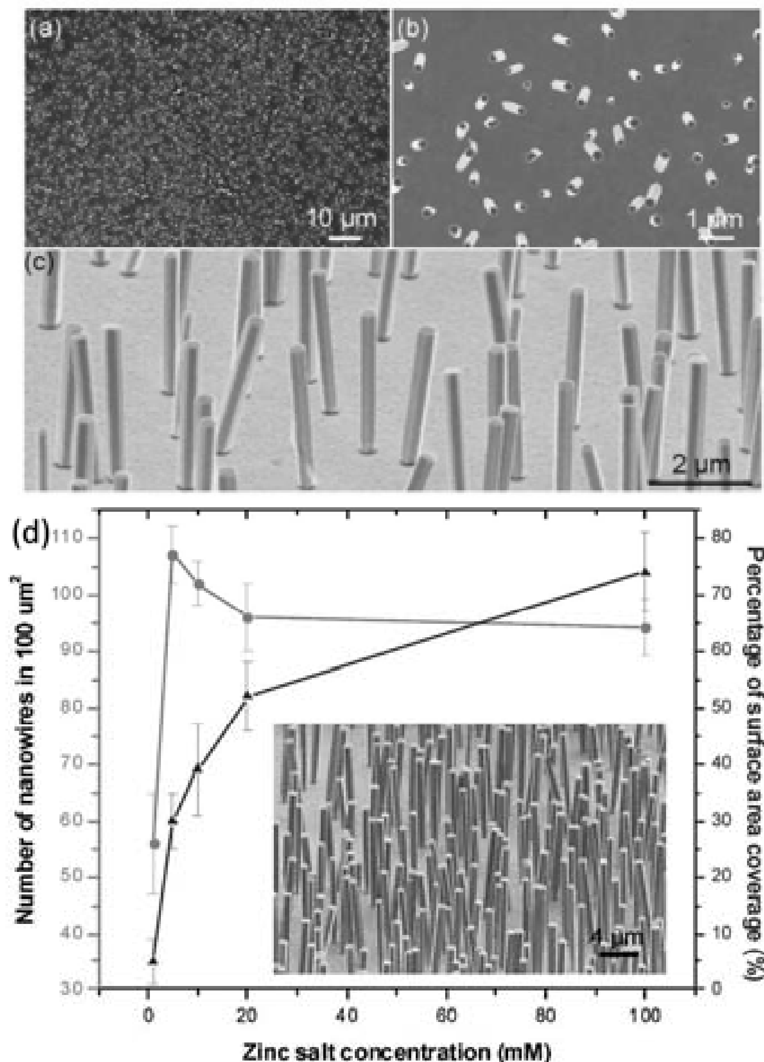

Figure 5.5. Overall view of ZnO NW arrays grown at 5 mM for 24 hours at 70 ºC: (a) top view, (b) enlarged top view, (c) with a 60 º tilt. (d) NW density depending of the zinc salt concentration [1].

The density of ZnO NWs is closely related to the precursor concentrations. Figure 5.5 shows that form 0.1 mM to 5 mM, the ZnO NW density increases dramatically. The more probable reason is that the zinc chemical potential inside the solution increases with zinc concentration. In order to balance the increased zinc chemical potential in solution, more nucleation sites on the substrate surface will be generated with the corresponding increase of the NW density. Above 5 mM, the density remains steady with a certain tendency of decrease. There are two possible reasons to explain this saturation effect: One, considering the critical size required for a nucleus to grow into a crystal, no new nanorods would form if the sizes of the nuclei are smaller than the critical size. Second, due to the existence of the first group of grown nanorods, the newly arrived ions on the substrate have higher probability to reach the existing NWs rather than to the newly formed nuclei, thus, the size of the nuclei may not exceeds the critical size and they will eventually dissolve into the solution body. In such cases, a continuous increase in solution concentration may not increase the density of the NWs when its density is larger than the saturation density.

5.4 Fundamentals of nano-piezogenerators

As a first step of proof of concept, the study of Wang's group was based on aligned ZnO NWs grown on a conductive solid substrate (Figure 5.6(a)). The measurements were performed by AFM using a Si tip coated with Pt film, which has a cone angle of 70º. The rectangular cantilever had a calibrated normal spring constant of 0.76 N/m (see Figure 5.6 (b)). In the AFM contact mode, a constant normal force of 5 nN was maintained between the tip and sample surface. The tip scanned over the top of the ZnO NW, and the tip's height was adjusted according to the surface morphology and local contacting force. The thermal vibration of the NWs at room temperature is negligible. For the electric contact at the bottom of the nanowires, silver paste was applied to connect the (large) ZnO film on the substrate surface with the measurement circuit. The output voltage across an outside load of resistance RL = 500 MΩ was continuously monitored (Figure 5.6 (c)) as the tip scans over the nanowires (note the defined polarity of the voltage signal). No external voltage was applied in any stage of the experiment.

Experimentally, both the topography (Figure 5.6 (d)) (feedback signal from the scanner) and the corresponding output voltage images across the load were recorded simultaneously when the AFM tip was scanned over the aligned NW arrays. In contact mode, as the tip scanned over the vertically aligned NWs, the NWs were bent consecutively.

The bending distance was directly recorded in the topography image, from which the maximum bending deflection distance and the elastic modulus of the NW as well as the density of NWs that have been scanned by the tip are directly derived.

In the corresponding voltage output image for each contact position, many sharp output peaks were observed (Figure 5.6 (c)). Note the output voltage signal was actually negative in reference to the grounded end. By examining the topological profile of a NW and its corresponding output potential, a delay was observed for the voltage output signal ((Figure 5.6 (d))), which means that there was no electric power output when the tip was first in contact with the NW, but a sharp voltage peak was generated at the moment when the tip was about to leave the contact with NW. This delay is a key signature about the power output

process. It is important to note that the voltage V_L presented here was converted from the current flowing through the external load R_L.

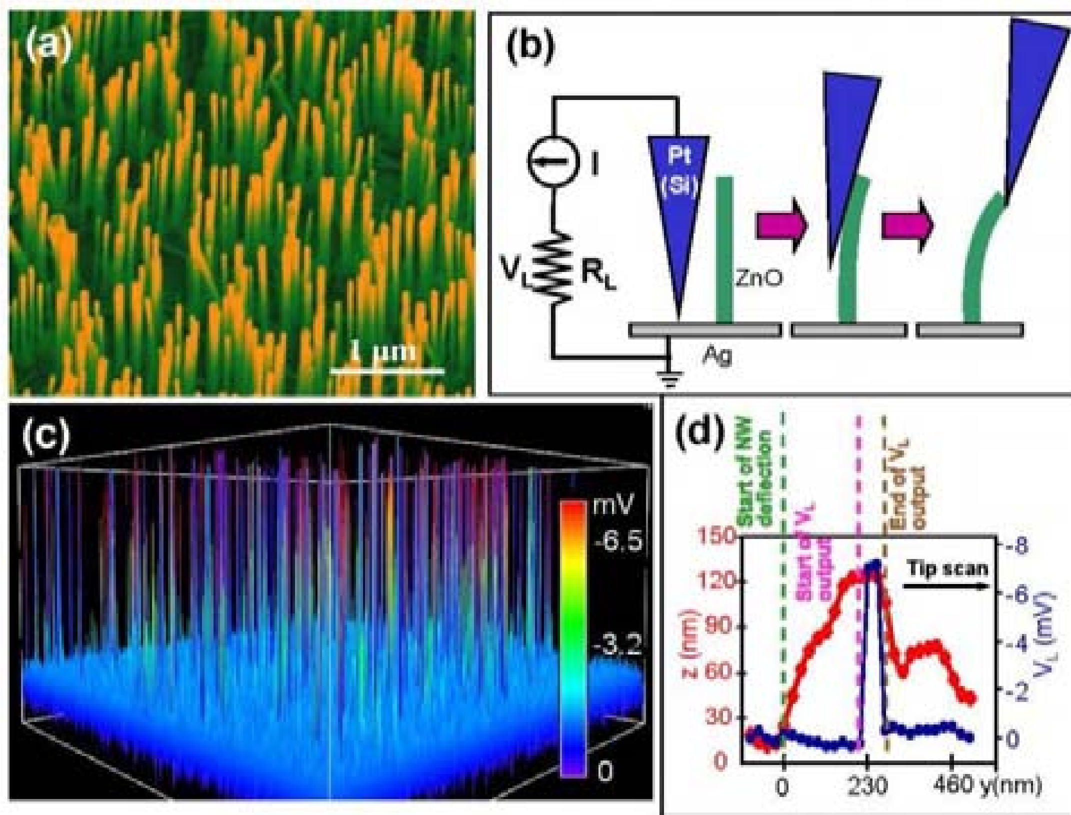

Figure 5.6. (a) Scanning electron microscopy images of aligned ZnO NWs grown on GaN/sapphire substrate. (b) Experimental set up and procedures for generating electricity by deforming a piezoelectric NW using a conductive AFM tip. The AFM scans across the NW arrays in contact mode. (c) Output voltage image of the NW arrays when the AFM tip scans across the NW arrays. (d) An overlap plot of the AFM topological image (red line) and the corresponding generated voltage (blue line) for a single scan of the tip across a NW. A delay in the electricity generation is apparent.

5.5 Vibration-driven energy harvester based on ZnO finewire (FW)

This thesis is focused on the energy generation from vibrations. In order to build a link between this field and ZnO piezotronics, a different approach based on a resonant device that integrates a finewire (FW) has been developed. The first idea was the use of two different poled ZnO NW sets in order to obtain a resonant clamped-free beam. Because both extremes of a NW have to be electrically contacted to get the generated piezopotential, the most nanogenerators are clamped-clamped structures. If one wants to obtain a cantilever, which is the more basic resonant structure, a charge feedback way is needed. The ideal choice is the use of another NW with opposite poling direction, because the piezopotential will be duplicated, and two electrodes will be achieved at the clamped side of the structure.

Figure 5.7(a) shows the diagram of a prototype that was tried to be carried out with two ZnO FWs. The junction between both FWs with a silver paste drop is shown in Figure 5.7(b). Unfortunately, several attempts were performed but the obtained signal was not clear. In order to simplify the experiment, a plastic film was used to form the cantilever and a single

ZnO FW was placed on top. Then, each end of the NW was bonded with silver paste to a fine bonding wire that allows the electrical connection of the FW, without clamping the structure or affecting the dynamic of the cantilever (Figure 5.8).

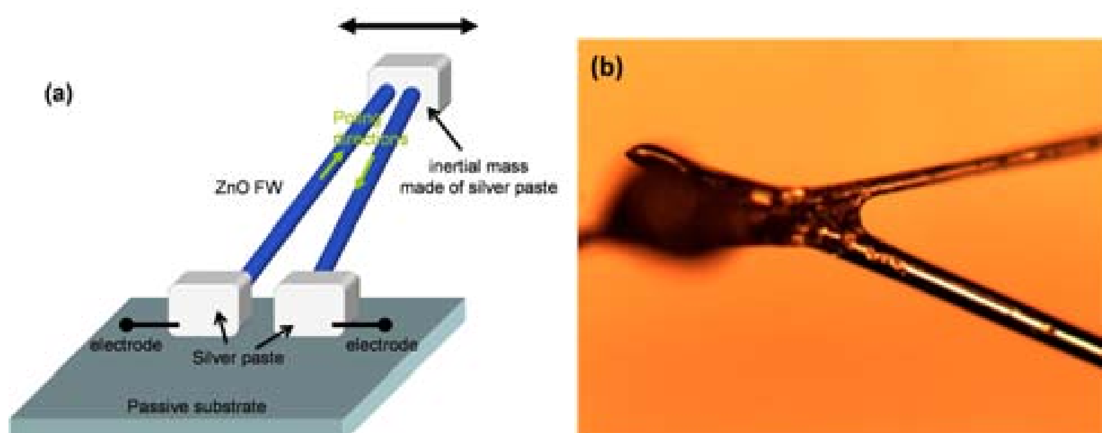

Figure 5.7. Cantilevered generator formed by two ZnO FWs poled in opposite directions (a) and optical image of the junction of the FW made with a silver paste drop.

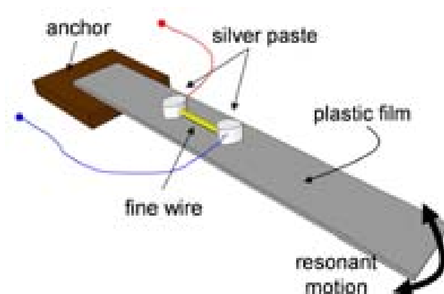

Figure 5.8. Front-side of fabricated final device connected to a load resistor (a) and conceptual diagram of the die back-side showing an integrated autonomous wireless sensor node (b). Inset in (a): Detail of the horizontally grown ZnO NWs.

The whole structure was placed over an electrodynamical shaker that can provide a vibration to drive the cantilever to resonance. Figure 5.9(a) shows a diagram of the whole system, where the vibration direction can be noted. In Figure 5.9(b), the plastic film with the attached ZnO FW can be seen on top of the shaker during a characterization of the system resonance motion.

The system was connected to a digital acquisition card through a low-noise voltage preamplifier (SR560), in order to capture the piezopotential generated by the finewire at the resonance frequency of the cantilever. When the cantilever gets into resonance, the vertical deflection of the plastic film produces an alternated stretch and compression of the clamped FW that means the creation of a piezopotential between its ends. A frequency sweep of the vibration (Figure 5.10) was carried out, and a resonance motion was optically observed in the cantilever at 75 Hz. Moreover, the generated voltage was increased up to a maximum peak-to-peak value of 8 mV over the input resistance of 100 MΩ. That means a RMS power of 8 pW at resonance. Therefore, although this generator is not comparable in terms of power density

to a typical energy harvester with similar dimensions, the concept can be interpolated to a nano-scale device with the use of cantilevered NW arrays.

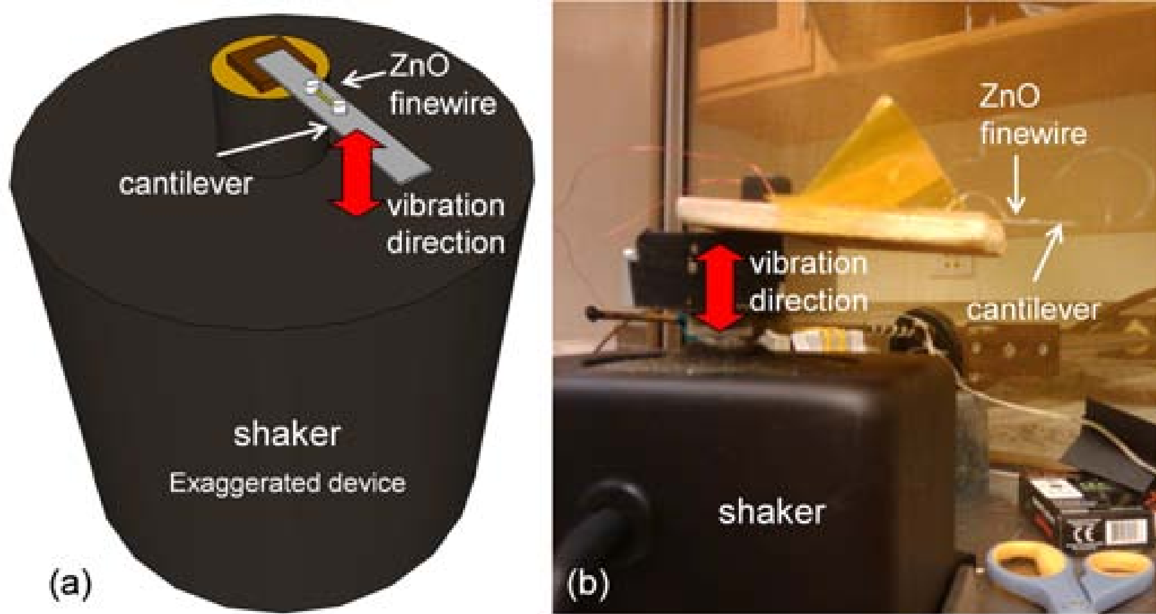

Figure 5.9. Front-side of fabricated final device connected to a load resistor (a) and conceptual diagram of the die back-side showing an integrated autonomous wireless sensor node (b). Inset in (a): Detail of the horizontally grown ZnO NWs.

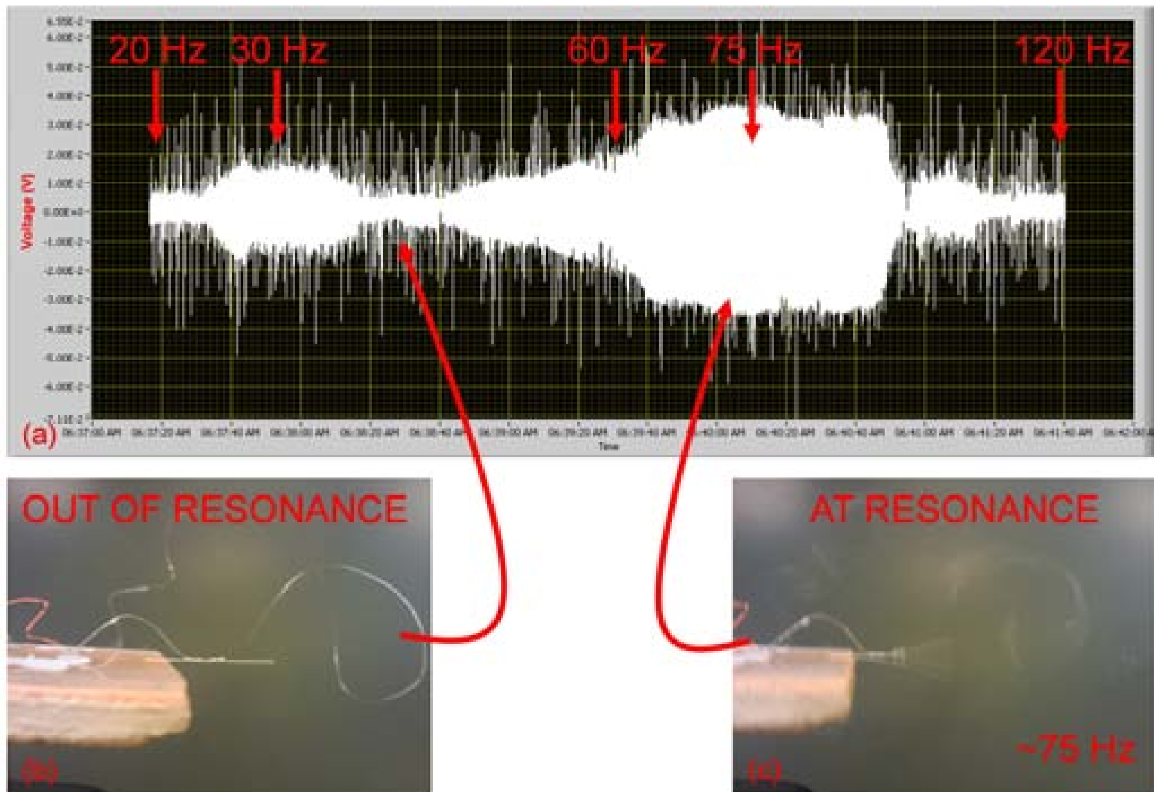

Figure 5.10. Captured output voltage generated by the FW when subjected to a frequency-swept vibration (a), optical images of the cantilever out of resonance (b) and at resonance (~75 Hz and V_{pp} = 8 mV) (c).

5.6 Heterogeneous integration of MEMS energy scavengers based on ZnO-NW

This section introduces a novel concept for energy scavenging from ambient vibrations utilizing ZnO nanowires (NWs). The main idea is the combination into a single device of a resonant element, which consists of an inertial mass and four serpentine suspensions, together with two arrays of NWs that are grown at both sides of the inertial mass from a gold electrode (Figure 5.11(a)). Due to the zigzag-shaped profile of the inertial mass, the NWs can be bent as the resonator is at resonance. This bending generates an electric current between the electrodes. In addition, this generator can be integrated with other elements that can be achieved taking advantage of the ZnO NWs and their unique properties such as chemical sensors, optoelectromechanical systems or logic circuits driven by mechanical or optical signals (Figure 5.11(b)).

Although a single NW strained by a tiny force of 5 nN can only scavenge around 0.05 fJ of energy [10], the integration of thousands or millions of these nanostructures can enhance the power output to fulfill the application requirements [11]. Alternatively, by using a resonant element, the amplitude of motion can be enhanced if the force has a harmonic nature. In this manner, the combination of these two ideas can be a new concept in the field of energy harvesting. The size of the resonator, i.e. inertial mass and suspension dimensions, will determine the operation frequency, and the size and spatial density of NWs, will determine the transduction throughput.

5.6.1 Fundamentals of operation

ZnO has become a hot topic in material science over last few years. It is due to its wonderful properties that are difficult to find in nature in one single material. It was exploited as photonic material because of its direct bandgap of 3.37 eV that can result in the generation/absorption of UV light. It is possible to grow a wide variety of nanostructures utilizing this material, and it has the dual property of being both a semiconductive and piezoelectric material. One of the most useful nanostructures that can be utilized to generate energy is the NW. The ZnO NW can grow from different substrates, even though a crystalline material with a similar lattice constant is the best choice in order to obtain aligned and high-quality NWs. Additionally, in order to catalyze the growth of the NW, a seed material, such as a gold or ZnO layer, has to be used.

As mentioned above, this approach aims to link the NW-based generator invented by Dr. Wang's group and the typical vibration-driven resonant energy harvester. So the mechanical fundamentals of this generator lie in the typical working principle of a damped spring-mass system that can mechanically store part of the energy coming from an external vibration. When an ambient vibration actuates over the resonator at the resonant mode frequencies, the inertial mass will move with enhanced amplitude. This motion can be used to strain an array of NW that will surround the movable mass. Therefore the piezoelectric transduction force, which is generated over the movable mass by means of the sweeping of NWs arrays, converts the friction into electricity by using the same concept used in the zigzag-electrode nanogenerator (NG) [11]. In order to reproduce the same approach a zigzag profile is proposed for the inertial mass as seen in Figure 5.11(a). The same configuration of creating a

Schottky contact with one gold electrode and an Ohmic contact with a second chromium electrode is used here.

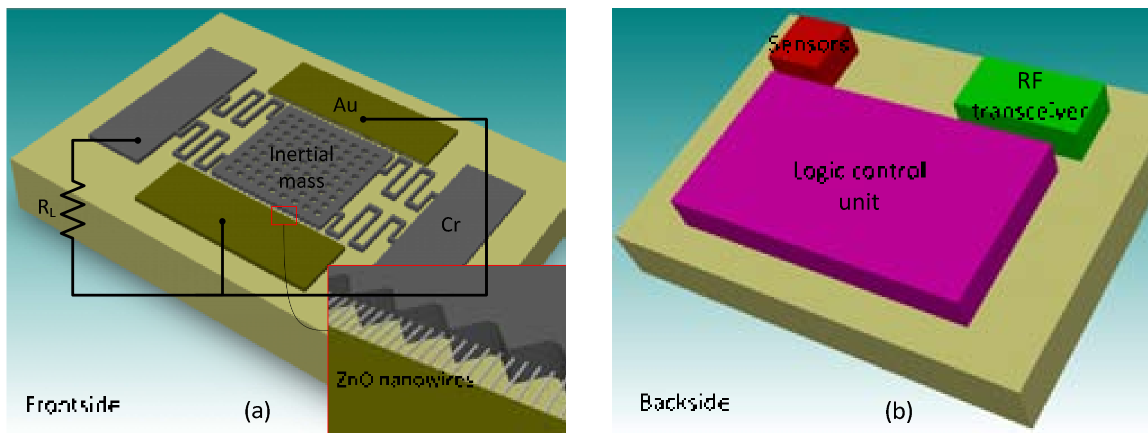

Figure 5.11. Front-side of fabricated final device connected to a load resistor (a) and conceptual diagram of the die back-side showing an integrated autonomous wireless sensor node (b). Inset in (a): Detail of the horizontally grown ZnO NWs.

This generator can be integrated with other elements in order to assemble a WSN node (Figure 5.11(b)). In addition, it can be use ZnO NWs and their unique properties to fabricate the rest of elements (i.e. chemical sensors, optoelectromechanical systems, logic circuits driven by mechanical or optical signal…).

5.6.2 Fabrication of the energy scavenger

NW growth method used for this approach

Among the different approaches for growing NWs, the hydrothermal chemical approach is the most convenient for our purpose. The main reasons are its synthesis simplicity, the low-temperature of this process and the possibility of varying the density and features of the grown NWs by changing the chemical reaction parameters.

Figure 5.12 shows a sample with NWs grown on a piece of a silicon wafer coated by two layers of Ti and Au with thicknesses of 20 nm and 50 nm respectively. It was used the hydrothermal method with a reactive concentration of 5 mM and a temperature of 80 ºC for 24 hours.

Using the same process, laterally aligned NWs can be grown by utilizing different materials to activate or inhibit the growth along different directions [12, 13]. Two materials are used in that case: Au or ZnO seeds for the growth, and Cr layer for preventing the local growth. Any substrates such as inorganic, organic, single crystal, polycrystalline, or amorphous substrates can be used for the lateral growth of ZnO NWs. The first step was to fabricate a ZnO strip pattern covered with Cr at the top over a support silicon wafer.

After a typical wafer cleaning, a photoresist was spin coated on the substrate to get a uniform layer and subsequently patterned by optical lithography. ZnO strips with Cr on top were achieved after lifting-off with acetone. Finally, the substrate was introduced floating upside down on the solution surface for 12 hours at 80 ºC. It is shown in Figure 5.13 that ZnO

NW arrays grew from the lateral sides of the pattern with a good alignment. Moreover, more than 70% NWs were parallel to the substrate. For these reaction parameters, ZnO NWs have a diameter less than 200 nm and a length of about 4 μm. By increasing the growth time and renewing the growth solution, ZnO NWs longer than 13 μm and a diameter of ~300 nm can be synthesized. The hexagonal cross section of NWs implies that c axis of ZnO NW is along its length direction. From this experience, it is clear that a selective horizontally-aligned NW arrays can be growth from the ZnO or gold stripe sidewall.

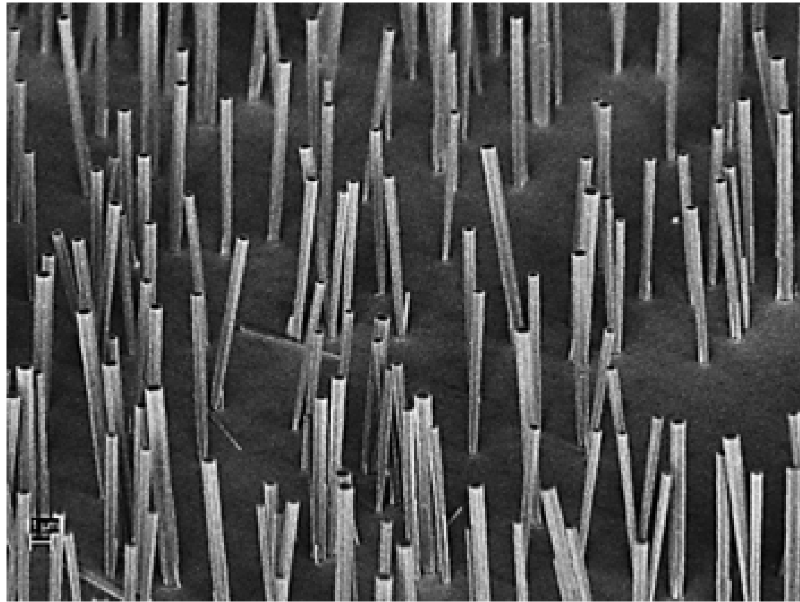

Figure 5.12. SEM image of ZnO NWs grown for 24 hours at 80 ºC with a reactive concentration of 5nM over a silicon substrate coated with a Cr-Au layer.

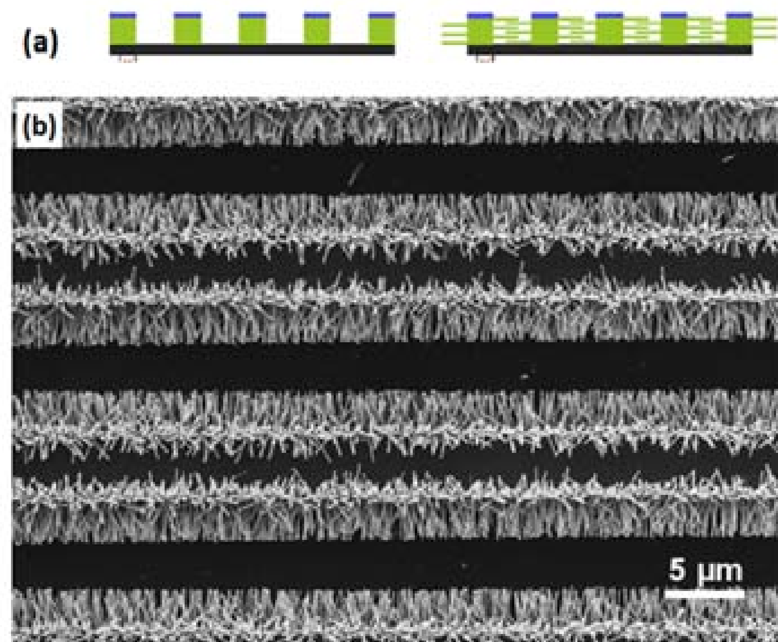

Figure 5.13. (a) Schematic steps for growing patterned and laterally aligned ZnO NW arrays. (b) SEM image of ZnO NW arrays grown laterally on Si substrate. From [12].

In our case, we propose the use of a thick layer of gold as seed block as well as a composite layer with several sheets of gold and chromium in order to reduce the fabrication cost. In addition, a layer of ZnO over an intermediate gold layer can be used as seed for the NW growth. Using a gold layer is a requirement dictated by the necessity of creating a Schottky barrier at this end of the NWs. The other electrode, the zigzag-shaped mass, has to be made of chromium in order to get an Ohmic contact.

5.6.3 Proposed fabrication process

The proposed fabrication process (Figure 5.14) starts with a silicon wafer that only has the function of supporting the metal layer covering it. The first step is the deposition by PECVD of a thick layer of silicon oxide (i.e. 5.65 μm for 100 min at a deposition rate of 56 nm/min) that will play the role of sacrificial layer. Then, in order to perform a lift-off technique, a negative resist (Futurrex NR5-8000) is spin coated at 3500 rpm for 40 s with an acceleration of 1000 rpm/s (step #2). This resist is a negative tone photoresist designed for thick film applications and with UV exposure tools emitting at the 365 nm wavelength. The patterning procedure consist of the following steps: (1) a soft-bake of 60 s at 150 ºC, (2) an UV exposure through the resonator mask (step #3), using the Karl Suss MA-6 Mask Aligner during two consecutive exposure of 10 s for a light intensity of 9 mW/s (i.e. ~21 mJ/cm2 for 1μm and a light source of 365 nm), (3) a post-bake for 60 s in a hot-plate at 100 ºC , (4) a development in RD6 for 20 s following for a rinsing with DI water and a carefully dry with nitrogen gas.

Afterwards, a thick chromium layer is deposited by evaporation (step #5). Then, through an ultrasonic bath in acetone (step #6), the rest of metal can be lifted and removed from the wafer, obtaining the set formed by inertial mass, suspensions and anchors. A similar lift-off process is carried out for the case of the gold electrodes (Note that after the step #7, the cross section line has been moved in the figure to observe the suspensions profile). It is divided into resist spin coating (step #8), patterning with gold electrode mask (steps #9 and #10), deposition of a thick layer (~4 μm) of gold or a gold composite layer (step #11) and remove of the spare metal (step #12). It is important to cover the gold surface with a chromium layer in order to avoid vertical NW growth. In that moment both electrodes for each resonator are created and the NWs can be grown by the hydrothermal method that was described above. When the horizontal NWs have the enough length to reach the corresponding zigzag electrodes, the movable structures can be released.

Then, a buffered HF (BHF) solution is used to remove the silicon dioxide placed under the movable mass (step #14). Previously, it is important to cover the whole wafer surface, except the inertial mass holes (it can be used the same mask to perform it), with resist in order to avoid the completely etch of the ZnO NWs. A critical point drying is necessary to keep away from the sticking of the movable mass to the wafer surface due to the adhesion forces found during a normal drying.

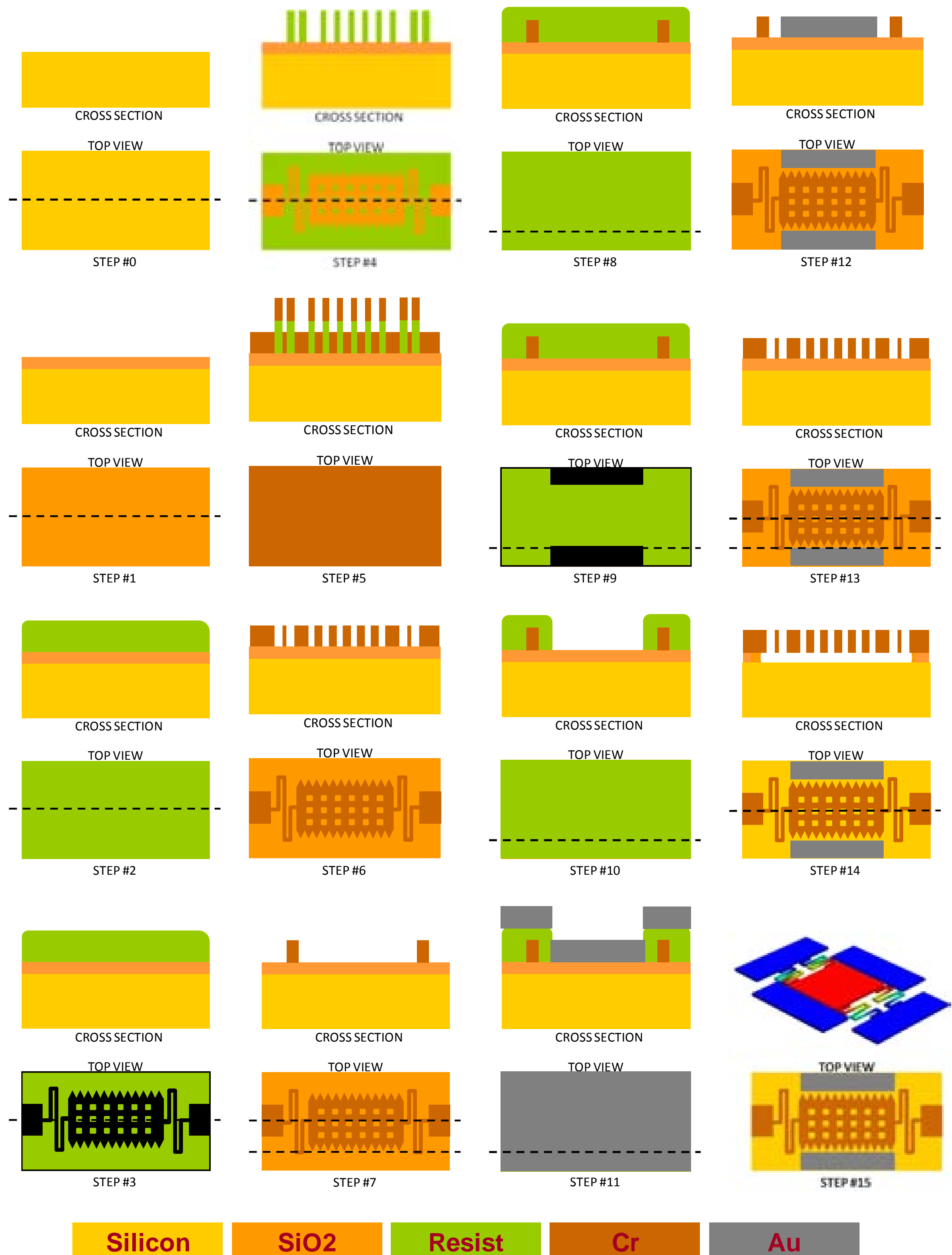

Figure 5.14. Proposed fabrication process and color legend of materials.

5.6.4 Design and simulation of the test devices

The layout of a 100-mm wafer with 120 chips has been carried out. It includes 12 different chip layouts that include a total of 96 resonator designs described in Table 5.1. The spring constant of a serpentine suspension can be found using the following expression [14]:

$$k_{serpentine} = \frac{12EI\left[n(a+b)-b\right]}{b^2(n-1)\left[(3a^2+4ab+b^2)n+3a^2-b^2\right]} \quad (5.7)$$

where E = 140 GPa is the Young's modulus of chromium, a is the pitch between two adjacent beams of the suspension (10 μm), n is the number of meanders of the suspension that can be calculated as the length of the suspension divided by the pitch and b is the width of the suspension (see Figure 5.15(a) for more details)

Finally, I is the moment of inertia that can be calculated as,

$$I = \frac{tw_s^3}{12} \quad (5.8)$$

where t is the thickness of the resonator, and w_s is the width of the suspension's beams.

Every resonator consists of four serpentine-type suspensions that hold the zigzag-shaped inertial mass. The inertial mass surface presents holes to allow the release of the structure by wet etching of the sacrificial oxide layer. The values of the inertial masses, $m_{inertial}$, have been extracted from FEM simulations using COVENTOR® software. With the value of the spring constant of every suspension and multiplying this value by four, it can be found the effective spring constant, k_{total}, of the four suspensions that hold every resonator. Then, the resonance frequency of the first in-plane modes for every device can be estimated as:

$$f_{res} = \frac{1}{2\pi}\sqrt{\frac{k_{total}}{m_{inertial}}} \quad (5.9)$$

From additional FEM modal simulations, it can be found that the resonant frequencies go from 555 kHz to 8.32 kHz corresponding to the smallest and largest resonators respectively (Figure 5.15). This range approximately agrees with the theoretical values calculated and shown in Table 5.1.

In comparison to the commented previous works, this approach achieves several improvements: (i) it is not required an expensive AFM tip to bend the NWs, a zigzag-shaped electrode is used instead. (ii) Due to the use of ultrasonic waves and vibrations in the sound's frequency range, a resonant system is utilized to enhance the relative motion between NWs and zigzag-shaped electrode. This enhancement value is equal to the quality factor of the resonator and it means an amplification of the NW bending and consequently a generated power improvement with respect to the static electrode approach. Therefore this approach meets the advantages of both prototypes, the high voltage output of the single NW generator driven by the AFM tip and the stable and increased generated current of the original zigzag-shaped generator, together with the virtually universal availability of the mechanical excitation (ambient vibrations and sonic or ultrasonic waves).

From [11], it can be supposed that the density of the laterally-grown NWs will be ~10 NW/μm^2 in the sidewall of the gold electrode. The available area for NW growth is 300 μm of length (for the largest device) multiplied by 4 μm (thickness of the chromium layer). Therefore, a total of 24000 NWs can be achieved in a single device. If every NW takes an active part in the charge generation, and from the value of 0.1 pW/NW that is obtained when a NW is bent by an AFM tip [10], it can be estimated a generated power of ~1.2 nW at resonance.

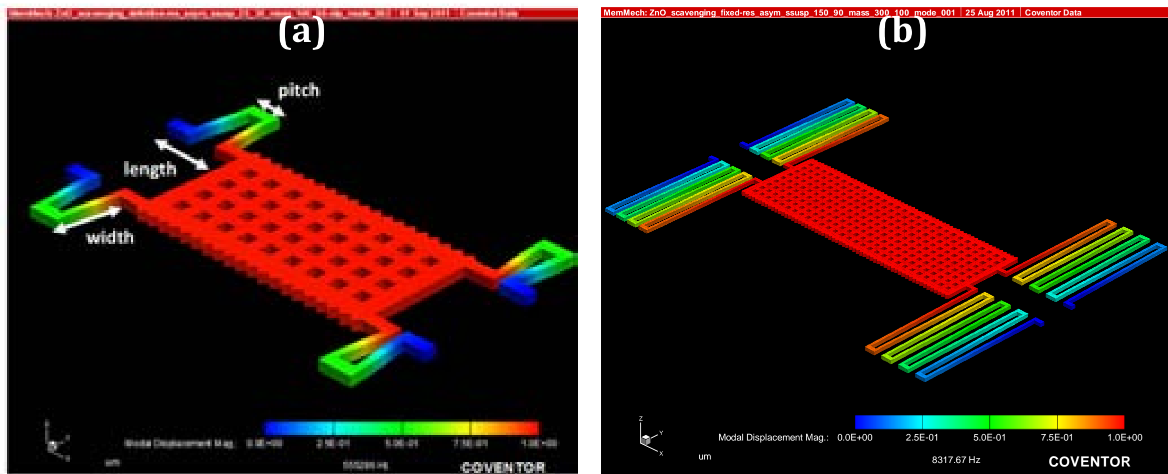

Figure 5.15. FEM simulation of first in-plane resonant modes for the smallest (a) and largest (b) designed resonator with a resonance frequency of 555 kHz and 8.32 kHz respectively.

Table 5.1. Theoretical values of the resonance frequency (in kHz) at the first in-plane mode for every resonator.

	Mass width (μm)		100	200	300	100	200	300
	Mass length (μm)		50	50	50	100	100	100
	Mass value (μg)		0.125	0.247	0.370	0.237	0.467	0.697
25	**30**	177.556	379.21	269.70	220.63	275.78	196.35	160.69
50	**30**	97.548	281.07	199.90	163.54	204.41	145.54	119.11
100	**30**	67.456	233.73	166.23	135.99	169.98	121.02	99.05
150	**30**	51.586	204.40	145.37	118.92	148.65	105.83	86.61
25	**50**	32.223	161.55	114.89	93.99	117.48	83.65	68.46
50	**50**	17.339	118.50	84.28	68.95	86.18	61.36	50.22
100	**50**	11.878	98.08	69.75	57.07	71.33	50.78	41.56
150	**50**	9.035	85.54	60.84	49.77	62.21	44.29	36.25
25	**70**	5.237	65.13	46.32	37.89	47.36	33.72	27.60
50	**70**	2.752	47.21	33.58	27.47	34.34	24.45	20.01
100	**70**	1.868	38.89	27.66	22.63	28.28	20.14	16.48
150	**70**	1.414	33.83	24.06	19.69	24.61	17.52	14.34
25	**90**	1.727	37.40	26.60	21.76	27.20	19.37	15.85
50	**90**	0.897	26.95	19.16	15.68	19.60	13.95	11.42
100	**90**	0.606	22.15	15.75	12.89	16.11	11.47	9.38
150	**90**	0.457	19.24	13.69	11.20	13.99	9.96	8.15
Suspension width (μm)	**Suspension length (μm)**	**Stiffness (N/m)**						

5.7 Conclusions

It has been proposed a novel concept for energy scavenging from vibrations utilizing the hybridization of conventional resonant devices with ZnO NWs. A wafer layout has been designed and the fabrication process has been defined and explored. A huge variety of designs have been included, thus a wide frequency range can be studied. This approach can be used to power wireless sensor nodes at the micro and nanoscale level. In addition, this

generator could be integrated with other elements that can be achieved taking advantage of the ZnO NWs and their unique properties such as chemical sensors, optoelectromechanical systems or logic circuits driven by mechanical or optical signals. FEM simulations also show the feasibility of fabricating this kind of devices to scavenge energy from vibrations in the sonic to ultrasonic frequency range. The fabrication process to develop these devices was started during the stay with Dr. Wang's group, but due to time constrictions and important issues in the cleanroom, it could not be completed there. In the future, this process will be finished in order to demonstrate the concepts presented here.

References

[1] Z. L. Wang, *Nanogenerators for self-powered devices and systems*, 1st ed. Atlanta, GA USA: Georgia Institute of Technology, Atlanta, USA 2011.

[2] U. Ozgur, Y. I. Alivov, C. Liu, A. Teke, M. A. Reshchikov, S. Dogan, A. V, S. J. Cho, and H. Morkoc, "A comprehensive review of ZnO materials and devices," *Journal of Applied Physics,* vol. 98, 2005.

[3] X. D. Wang, C. J. Summers, and Z. L. Wang, "Large-Scale Hexagonal-Patterned Growth of Aligned ZnO Nanorods for Nano-optoelectronics and Nanosensor Arrays," *Nano Letters,* vol. 4, pp. 423-426, 2004.

[4] X. D. Wang, J. H. Song, P. Li, J. H. Ryou, R. D. Dupuis, C. J. Summers, and Z. L. Wang, "Growth of Uniformly Aligned ZnO Nanowire Heterojunction Arrays on GaN, AlN, and Al0.5Ga0.5N Substrates," *Journal of the American Chemical Society,* vol. 127, pp. 7920-7923, 2005.

[5] J. H. Song, X. D. Wang, E. Riedo, and Z. L. Wang, "Systematic Study on Experimental Conditions for Large-Scale Growth of Aligned ZnO Nanwires on Nitrides," *The Journal of Physical Chemistry B,* vol. 109, pp. 9869-9872, 2005.

[6] X. D. Wang, J. Song, C. J. Summers, J. H. Ryou, P. Li, R. D. Dupuis, and Z. L. Wang, "Density-Controlled Growth of Aligned ZnO Nanowires Sharing a Common Contact: A Simple, Low-Cost, and Mask-Free Technique for Large-Scale Applications," *The Journal of Physical Chemistry B,* vol. 110, pp. 7720-7724, 2006.

[7] S. S. Lin, J. I. Hong, J. H. Song, Y. Zhu, H. P. He, Z. Xu, Y. G. Wei, Y. Ding, R. L. Snyder, and Z. L. Wang, "Phosphorus Doped Zn1-xMgxO Nanowire Arrays," *Nano Letters,* vol. 9, pp. 3877-3882, 2009.

[8] L. Vayssieres, "Growth of arrayed nanorods and nanowires of ZnO from aqueous solutions," *Advanced Materials,* vol. 15, pp. 464-466, 2003.

[9] S. Xu, C. Lao, B. Weintraub, and Z. L. Wang, "Density-controlled growth of aligned ZnO nanowire arrays by seedless chemical approach on smooth surfaces," *Journal of Materials Research,* vol. 23, pp. 2072-2077, 2008.

[10] Z. L. Wang and J. H. Song, "Piezoelectric nanogenerators based on zinc oxide nanowire arrays," *Science,* vol. 312, pp. 242-246, 2006.

[11] Z. L. Wang, X. D. Wang, J. H. Song, and J. Liu, "Direct-current nanogenerator driven by ultrasonic waves," *Science,* vol. 316, pp. 102-105, 2007.

[12] Z. L. Wang, Y. Qin, and R. S. Yang, "Growth of Horizonatal ZnO Nanowire Arrays on Any Substrate," *Journal of Physical Chemistry C,* vol. 112, pp. 18734-18736, 2008.

[13] S. Xu, Y. Qin, C. Xu, Y. Wei, R. Yang, and Z. L. Wang, "Self-powered nanowire devices," *Nat Nano,* vol. 5, pp. 366-373, 2010.

[14] G. K. Fedder, "Simulation of Microelectromechanical Systems," University of California, 1994.

CHAPTER 6

CONCLUSIONS AND FUTURE APPLICATIONS

Chapter 1 introduces the global context where this thesis is located. The world crisis related to the energy consumption is presented as a reason for producing new green energies. Saving energy at all levels is being promoted in order to overcome this critical issue. Energy harvesting is a concept that aims to recover residual energy from the environment. Mechanical energy is a source of tiny but endless energy that is virtually always available. This energy can be extracted by N/MEMS devices and used to supply low-power electronics system. These energy scavengers are a key part of the autonomous wireless sensor networks (WSN).

In **Chapter 2**, the fundamental theory about vibration-driven energy scavengers have been described. An overall description of the main blocks that form this system was firstly presented. Detailed model for electrostatic and piezoelectric converters have been developed too. Numerical implementations in several modeling languages have been carried out for both models. The main goal of this chapter is the achievement of expressions to calculate the theoretical power that can be extracted with both transductions.

Chapter 3 reports the detailed theoretical analysis and electromechanical modeling of the concept called energy harvester-on-chip. A complete theoretical study of this type of devices has been developed, and the electromechanical behavior has been simulated by means of FEM tools and a MATLAB® code which solves the complete differential equations system. Using these analyses, a proof of concept prototype was designed and fabricated with a standard CMOS technology. As conclusion of using this type of technology to fabricate this device, we can say that the metallic layers stack thickness is too thin to build a robust enough device. Therefore, the use of a specific MEMS technology with a thicker layer to fabricate the capacitive electrodes and the suspensions would improve the mechanical stability and increase the capacitance values. However, it has been proved the possibility of successfully fabricating large MEMS with a standard CMOS technology by using a stack of its metal layers.

For a 100-cell prototype and from the simulation results, a maximum power about 45.43 nW is expected for a low-level environmental vibration, with a very low-level acceleration of 0.7 m/s^2 and a peak-frequency of 200 Hz. Therefore, for a whole energy harvesting chip, a theoretical power density about 5.78 $\mu W/cm^3$, which is comparable with the state-of-art values. Enhancing the resonant motion amplitude up to its maximum, i.e.

12.3 μm limited by the stoppers, this value could be increased up to a limit value of 110 μW/cm^3. The most relevant conclusion is that comparing these ideal power values with the values calculated for a conventional scavenger designed for a similar resonance frequency and fabricated with the same fabrication technology, the density power is increased in more than one order of magnitude, only by applying the new concept of EHoC. In the future, different CMOS technologies with a thicker metal stack should be explored to develop the same concept.

Chapter 4 has presented two different approaches toward the heterogeneous integration of energy harvester together with the rest of elements that form a WSN node. The use of a heterogeneous integration is presented as a key aspect in the proliferation of this type of devices and toward the development of real autonomous wireless sensors networks. It has been demonstrated that the use of the ideas involved in the concept of EHiP supposes an improvement in the throughput of a vibration energy converter. The design, fabrication and characterization of a fully-dedicated core die of an energy harvester in package (EHiP) with electrostatic transduction are presented in this chapter. A parametric design has been developed by using ARCHITECH® software. A SOI- based MEMS technology, which allows a robustness improvement and better performance, has been used instead of a commercial CMOS technology. An ad-hoc assembling process between the energy-harvesting core die and a test PCB substrate has been successfully developed. Experimental characterizations have been carried out to demonstrate the resonance motion at 289 Hz and the correct operation of the assembled system. An expected maximum generated power of 11 μW has been calculated when the energy harvester operates at charge-constant cycle, for a best-case scenario. That means a power density of ~0.85 mW/cm^3, for an input vibration acceleration of around 1 g, an initial and final voltage of 10 V and 52 V respectively, and an effective quality factor of 50.

In conclusion a manufacture process to build piezoelectric energy scavengers has been proposed, using a well-kwon process compatible with FBAR fabrication. Hence, it is possible use the same run to fabricate energy microgenerators and FBAR devices, such as resonators, mass sensor and others. A deep theoretical study based on numerical method analysis has been performed concerning to the use of the magnetic force generated by a current-carrying cord in a permanent magnet. It has been demonstrated the advantages of using a micro-scale energy harvester to be attached to the power cord. Due to the EHiP concept presented at , it can be obtained a reduced size and a high extracted power density. In order to demonstrate these advantages, two different prototypes are being developed. On one hand, the micro-scale energy harvester presented in this thesis is being adapted with a permanent magnet to achieve a magnetically actuated resonant device tuned to 50 Hz. On the other hand a cm-scale prototype made with commercial piezoelectric beams is being fabricated to be able to compare both devices.

The rest of piezoelectric devices and in particular the EHiP will be characterized and integrated with circuitry to build a whole energy scavenging system. A magnetically-driven EHiP prototype at microscale will be fabricated and characterized.

Finally, **Chapter 5** proposes a novel concept for energy scavenging from vibrations utilizing the hybridization of conventional resonant devices with ZnO NWs. A wafer layout

has been designed and the fabrication process has been defined and explored. A huge variety of designs have been included, thus a wide frequency range can be studied. This approach can be used to power wireless sensor nodes at the micro and nanoscale level. In addition, this generator could be integrated with other elements that can be achieved taking advantage of the ZnO NWs and their unique properties such as chemical sensors, optoelectromechanical systems or logic circuits driven by mechanical or optical signals. FEM simulations also show the feasibility of fabricating this kind of devices to scavenge energy from vibrations in the sonic to ultrasonic frequency range.

There are a huge variety of potential application of ZnO NWs, the mechanical storage of energy with this NWs is being explored. The fabrication process that was started in Georgia Institute of Technology will be continued in the National Center of Microelectronics in Spain to investigate the combination of a resonant microscale device and piezoelectric NWs.

APPENDIX A

MAIN CONTRIBUTIONS OF THE AUTHOR

- **Article in peer-review Journals**

[1] **G. Murillo**, G. Abadal, F. Torres, J.L. Lopez, J. Giner, A. Uranga, N. Barniol, Harvester-on-chip: Design of a proof of concept prototype, Microelectronic Engineering, 86 (2009) 1183-1186.

[2] **G. Murillo**, Z.J. Davis, S. Keller, G. Abadal, J. Agusti, A. Cagliani, N. Noeth, A. Boisen, N. Barniol, Novel SU-8 based vacuum wafer-level packaging for MEMS devices, Microelectronic Engineering, 87 (2010) 1173-1176.

[3] **G. Murillo**, J. Agustí, M. López-Suárez, G. Abadal, Heterogeneous integration of autonomous systems in package for wireless sensor networks, Procedia Engineering, Eurosensors XXV, (2011) *In press*.

[4] **G. Murillo**, M. Lee, C. Xu, G. Abadal, Z.L. Wang, Hybrid resonant energy harvester integrating ZnO NWs with MEMS for enabling zero-power wireless sensor nodes, Nano Communication Networks, 2 (2011) 235-241.

[5] **G. Murillo**, J. Agustí, M. López-Suárez, G. Abadal, Energy harvester in package: a heterogeneous integration of a self-powered wireless sensor node, Sensors and Actuators A: Physical, (2011) *Submitted*.

[6] **G. Murillo**, J. Agusti, G. Abadal, Micropower generation for autonomous wireless sensor nodes in smart-grid cables, Transactions on Industrial Engineering., (2011) *To be submitted*.

[7] **G. Murillo**, J. Agusti, G. Abadal, Study of the monolithic integration of a vibration-based energy harvester in a standard CMOS technology: Part 1. Modeling and prototype design, Smart Materials and Structures, (2011) *To be submitted*.

[8] **G. Murillo**, J. Agusti, G. Abadal, Study of the monolithic integration of a vibration-based energy harvester in a standard CMOS technology: Part 2. Fabrication and characterization, Smart Materials and Structures, (2011) *To be submitted*.

[9] **G. Murillo**, H. Campanella, G. Abadal, J. Esteve, Monolithic integration of piezoelectric energy scavengers within FBAR-compatible technology for enabling self-powered wireless sensor nodes, Journal of Micromechanics and Microengineering, (2011) In preparation.

[10] J.L. Lopez, F. Torres, **G. Murillo**, J. Giner, J. Teva, J. Verd, A. Uranga, G. Abadal, N. Barniol, Research in Microelectronics and Electronics, 2008. PRIME 2008. Ph.D. , vol., no., pp.89-92, June 22 2008-April 25 2008.

[11] J. Lluis Lopez, J. Verd, A. Uranga, J. Giner, **G. Murillo**, F. Torres, G. Abadal, N. Barniol, A CMOS-MEMS RF-Tunable Bandpass Filter Based on Two High-Q 22-MHz Polysilicon Clamped-Clamped Beam Resonators, IEEE Electron Device Letters, 30 (2009) 718-720.

[12] J.L. Lopez, J. Verd, E. Marigo, A. Uranga, **G. Murillo**, J. Giner, F. Torres, G. Abadal, N. Barniol, Monolithically Integrated Double-Ended Tuning Fork- Based Oscillator with Low Bias Voltage in Air Conditions, in: J. Brugger, D. Briand (Eds.) Proceedings of the Eurosensors XXIII Conference, Elsevier Science Bv, Amsterdam, 2009, pp. 614-617.

[13] J.L. Lopez, J. Verd, J. Teva, **G. Murillo**, J. Giner, F. Torres, A. Uranga, G. Abadal, N. Barniol, Integration of RF-MEMS resonators on submicrometric commercial CMOS technologies, Journal of Micromechanics and Microengineering, 19 (2009).

[14] J.L. Lopez, J. Verd, A. Uranga, **G. Murillo**, J. Giner, E. Marigo, F. Torres, G. Abadal, N. Barniol, VHF band-pass filter based on a single CMOS-MEMS double-ended tuning fork resonator, in: J.B.D. Brugger (Ed.) Proceedings of the Eurosensors XXIII Conference, 2009, pp. 1131-1134.

[15] A. Uranga, J. Verd, J. Lluis Lopez, J. Teva, F. Torres, J. Josep Giner, **G. Murillo**, G. Abadal, N. Barniol, Electrically Enhanced Readout System for a High-Frequency CMOS-MEMS Resonator, ETRI Journal, 31 (2009) 478-480.

[16] J. Agusti, I. Pellejero, G. Abadal, **G. Murillo**, M.A. Urbiztondo, J. Sese, M. Villarroya-Gaudo, M. Pina, J. Santamaria, N. Barniol, Optical vibrometer for mechanical properties characterization of silicalite-only cantilever based sensors, Microelectronic Engineering, 87 (2010) 1207-1209.

[17] J.L. Lopez, J. Giner, **G. Murillo**, F. Torres, E. Marigo, A. Uranga, G. Abadal, N. Barniol, Third-mode 48 MHz free-free beam resonator used as a RF balun, Microelectronic Engineering, 87 (2010) 1256-1258.

[18] E. Marigo, J.L. Lopez, **G. Murillo**, F. Torres, J. Giner, A. Uranga, G. Abadal, J. Esteve, N. Barniol, Zero-level packaging of MEMS in standard CMOS technology, Journal of Micromechanics and Microengineering, 20 (2010).

Conferences and Workshops

1. G. Abadal, **G. Murillo**, J. Teva, F. Torres, J.L. Lòpez, A. Uranga, J. Esteve, F. Pérez-Murano, N. Barniol. Micromechanical Hz to MHz frequency up-converter integrated in a standard CMOS-0.35μm technology for energy scavenging applications. 33rd International Conference on Micro- and Nano-Engineering. MNE'07. Copenhagen, Denmark. September 23-26, 2007. Poster.

2. J. Teva, G. Abadal, **G. Murillo**, J. L. Lopez, A. Uranga, J. Verd, F. Torres, J. Esteve, F. Pérez-Murano, N. Barniol. Monolithic integration of MEMS-CMOS RF resonators in the VHF and UHF bands. A comparative study of 0.35-μm and 0.18-μm technologies. 33rd International Conference on Micro- and Nano-Engineering. MNE'07. Copenhagen, Denmark. September 23-26, 2007. Poster.

3. J.L. Lopez, F. Torres, **G. Murillo**, J. Giner, J. Teva, J. Verd, A. Uranga, G. Abadal and N. Barniol. Double-Ended Tuning Fork Resonator in 0.35um CMOS Technology for RF Applications. 2008 PhD Research in Microelectronics and Electronics. Istanbul, Turkey. June 22-25, 2008. Poster.

4. **G. Murillo**, G. Abadal, F. Torres, J. L. Lopez, J. Giner, A. Uranga, N. Barniol. Free-free beam resonator with optimized nodal anchors integrated in a commercial CMOS technology. Eurosensors XXII. Dresden, Germany. September 7-10, 2008. Poster.

5. **G. Murillo**, G. Abadal, F. Torres, J. L. Lopez, J. Giner, A. Uranga, N. Barniol. Harvester-on-Chip: Design of a proof of concept prototype. 34th International Conference on Micro- and Nano-Engineering. MNE'08. Athens, Greece. September 15-18, 2008. Poster.

6. J. L. Lopez, **G. Murillo**, J. Giner, A. Uranga, F. Torres, G. Abadal, J. Esteve, F. Pérez-Murano, N. Barniol. HF and VHF Nanoresonators Fabricated in a 0.18um Commercial CMOS Technology. 34th International Conference on Micro- and Nano-Engineering. MNE'08. Athens, Greece. September 15-18, 2008. Poster.

7. **G. Murillo**, G. Abadal, F. Torres, J. L. Lopez, J. Giner, A. Uranga, N. Barniol. On the monolithic integration of CMOS-MEMS energy scavengers. XXIII Conference on Design of Circuits and Integrated Systems. DCIS-2008. Grenoble, Francia. November 12-14, 2008. Oral.

8. J. Giner, C. Pey, H. Campanella, J. Esteve, A. Uranga, J. L. Lopez, **G. Murillo**, N. Barniol, G. Abadal. 2.25GHz FBAR <2mW Differential Oscillator. XXIII Conference on Design of Circuits and Integrated Systems. DCIS-2008. Grenoble, Francia. November 12-14, 2008. Oral.

9. J. L. Lopez, **G. Murillo**, J. Giner, A. Uranga, G. Abadal, N. Barniol. Fabrication of MEMS Resonators in the HF and VHF Range on a 0.18um CMOS Commercial Technology. XXIII Conference on Design of Circuits and Integrated Systems. DCIS-2008. Grenoble, Francia. November 12-14, 2008. Oral.

10. **G. Murillo**, G. Abadal, F. Torres, J. L. Lopez, J. Giner, H. Campanella, A. Uranga, J. Esteve, N. Barniol. Novel designs of piezoelectric scavengers using FBAR technology. The 8th International Workshop on Micro and Nanotechnology for Power Generation and Energy

Conversion Applications - PowerMEMS+microEMS2008 Workshop. Sendai, Japan. November 10-12, 2008. Poster.

11. **G. Murillo**, G. Abadal, F. Torres, J. L. Lopez, J. Giner, H. Campanella, A. Uranga, J. Esteve, N. Barniol. Harvester-on-Chip: Design and fabrication of a proof of concept prototype. The 8th International Workshop on Micro and Nanotechnology for Power Generation and Energy Conversion Applications - PowerMEMS+microEMS2008 Workshop. Sendai, Japan. November 10-12, 2008. Poster.

12. J. Giner, A. Uranga, J. Verd, **G. Murillo** E. Marigó, G. Abadal, F. Torres, and N. Barniol. Toward VHF Fully Integrated Microelectromechanical Filters. MEMSWave International Symposium. Trento, Italy. July 6-8, 2009. Poster.

13. J. Giner, A. Uranga, F. Torres, E. Marigó, **G. Murillo**, G. Abadal and N. Barniol. A Fully Integrated CMOS-MEMS UHF Ring Resonator. 35th International Conference on Micro- and Nano-Engineering. MNE'09. Ghent, Belgium. September 28 – October 1, 2009. Poster.

14. G. Abadal, J. Agustí, I Pellejero, **G. Murillo**, M.A. Urbiztondo, J Sesé, M Villarroya-Gaudó, M.P. Pina, J. Santamaría, N. Barniol. Mechanical properties characterization of silicalite-only cantilever based sensors for explosives early detection. 35th International Conference on Micro- and Nano-Engineering. MNE'09. Ghent, Belgium. September 28 – October 1, 2009. Poster.

15. E. Marigo, J. L. Lopez, **G. Murillo**, F. Torres, A. Uranga, G. Abadal, J. Esteve, N. Barniol. Zero level package of RF-MEMS in standard CMOS technology. 35th International Conference on Micro- and Nano-Engineering. MNE'09. Ghent, Belgium. September 28 – October 1, 2009. Poster.

16. **G. Murillo**, Z. Davis, S. Keller, G. Abadal, J. Agustí, A. Cagliani, N. Noeth, A. Boisen, N. Barniol. Novel SU-8 based Vacuum Wafer-Level Packaging for MEMS devices. 35th International Conference on Micro- and Nano-Engineering. MNE'09. Ghent, Belgium. September 28 – October 1, 2009. Poster.

17. J. Agustí, I. Pellejero, G. Abadal, **G. Murillo**, M.A. Urbiztondo, J. Sesé, M. Villarroya-Gaudó, M.P. Pina, J. Santamaría, N. Barniol Mechanical properties characterization of silicalite-only cantilever based sensors for explosives early detection. 35th International Conference on Micro- and Nano-Engineering. MNE'09. Ghent, Belgium. September 28 – October 1, 2009. Poster.

18. J.L. Lopez, J. Giner, **G. Murillo**, F. Torres, E. Marigó, A. Uranga, G. Abadal, N. Barniol. Third-Mode 48 MHz Free-Free Beam Resonator used as a RF balun. 35th International Conference on Micro- and Nano-Engineering. MNE'09. Ghent, Belgium. September 28 – October 1, 2009. Poster.

19. **G. Murillo**. Energy harvesting and MEMS: Toward self-powered microsystems. Third STIMESI Workshop on MEMS and Microsystems Research and Teaching. Prague, Czech Republic. November 13, 2009. Oral (INVITED).

20. **G. Murillo**, J. Agusti, G. Abadal, F. Torres, J. Giner, E. Marigó, A. Uranga, N. Barniol. Integration of an improved Harvester-on-Chip core dice on commercial SOI-based MEMS technology. The 9th International Workshop on Micro and Nanotechnology for Power Generation and Energy Conversion Applications - PowerMEMS2009 Workshop. Washington, USA. December 1-4, 2009. Poster.

21. M. López-Suárez, **G. Murillo**, J. Agustí, H. Vocca, L. Gammaitoni and G. Abadal. Efficient non-linear NEMS based energy harvesting from thermomechanical noise. XXII Sitges Conference on Statistical Mechanics. Energy conversion: from nanomachines to renewable sources. Sitges, Spain. June 7-11, 2010.

22. J. Agustí, **G. Murillo**, M. López-Suárez and G. Abadal. RF energy harvester based on MEMS NiPS Workshop: Noise in dynamical systems at the micro and nanoscale. Avigliano Umbro, Italia. June 7-11, 2010.

23. **G. Murillo**, J. Agusti, G. Abadal, F. Torres, J. Giner, E. Marigó, A. Uranga, N. Barniol. Microscale energy harvester driven by a built-in permanent magnet for self-powered nodes in appliance power cables. The 10th International Workshop on Micro and Nanotechnology for Power Generation and Energy Conversion Applications - PowerMEMS2010 Workshop. Leuven, Belgium. November, 30 – December, 3, 2010. Poster.

24. **G. Murillo**. N/MEMS-based energy scavenging for enabling autonomous WSN shrinkage. Third Nanonetworking Summit. Barcelona, Spain. June 22-23, 2011. Oral (INVITED).

25. A. Cuadrado, J. Agustí, M. López-Suárez, **G. Murillo**, G. Abadal, J. Alda. Measurement of the vibration state of an array of micro cantilevers by diffractional methods, OPTOEL. Santander, Spain. June 30 – July 1, 2011. Poster.

26. G. Abadal, **G. Murillo**, J. Agusti, M. López-Suárez, F. Torres, M. Placidi. Zeropower solutions based on integrated vibrational MEMS energy harvesters, Workshop on Energy Efficient Electronic Technologies and Systems. July 18-19, 2011. Oral (INVITED).

27. **G. Murillo**, J. Agusti, M. López-Suárez, G. Abadal. Heterogeneous integration of autonomous systems in package for wireless sensor networks, Eurosensors XXV Conference. Athens, Greece. September, 4-7, 2011. Oral.

28. **G. Murillo**, J. Agusti, M. López-Suárez, G. Abadal. Integration of piezoelectric energy scavengers with FBAR resonators for the miniaturization of autonomous wireless sensor nodes, MEMS 2012. Paris, France. January 29 – February 2, 2012, 4-7, 2011. Poster.

➢ Stays at Foreign Centers

1. Center: **Nanotech (DTU)** City: Lyngby (Denmark)

   Date: September, 2008 Duration (weeks): 12

   Topic: *Novel SU-8 based Vacuum Wafer-Level Packaging for MEMS devices*

   Advisor: Dr. Zachary Davis

2. Center: **MINATEC (CEA/Leti)** City: Grenoble (France)

   Date: October 2009 Duration (weeks): 12

   Topic: *Electrostatic energy scavenger characterization and associated power management circuit design*

   Advisor: Dr. Gishlain Despesse

3. Center: **Georgia Institute of Technology** City: Atlanta, GA (USA)

   Date: August 2010 Duration (weeks): 18

   Topic: *Energy harvesting based on ZnO nanowires*

   Advisor: Prof. Zhong Lin Wang

APPENDIX B

DESIGNED LAYOUTS

B.1. MOS Electrostatic Energy Scavenger

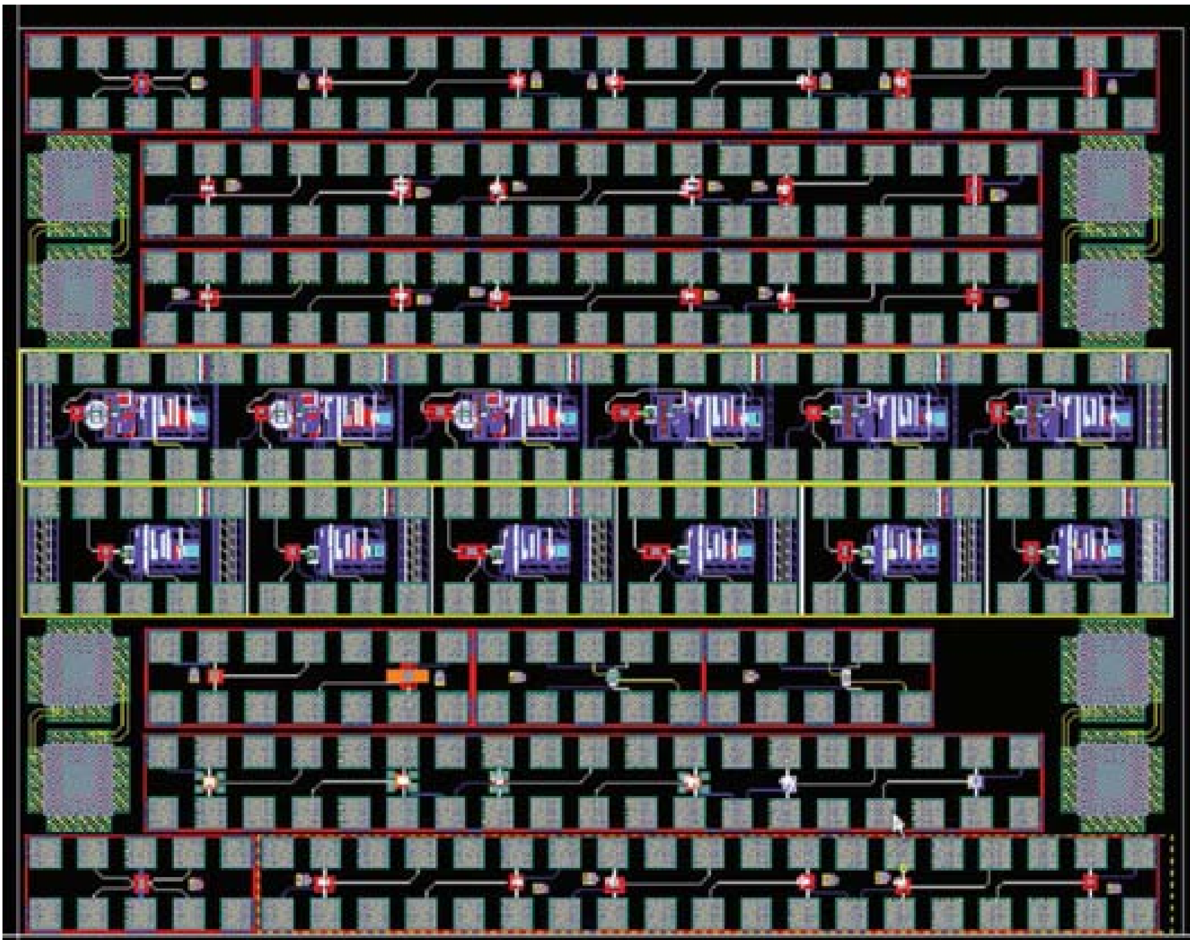

Designers	**Gonzalo Murillo, Joan Lluís Lopez and Jaume Verd.**
Technology	AMS 0.35 CMOS technology 2P4M.
Number of devices	30 chips of 3610 x 2850 μm^2.
Description	RF MEMS fabricated in polysilicon, with and without on-chip amplification. MEMS based oscillators for RF applications. Vacuum encapsulation devices. “Scavenger on-chip” prototype

B.2. MEMS Electrostatic Energy Scavenger

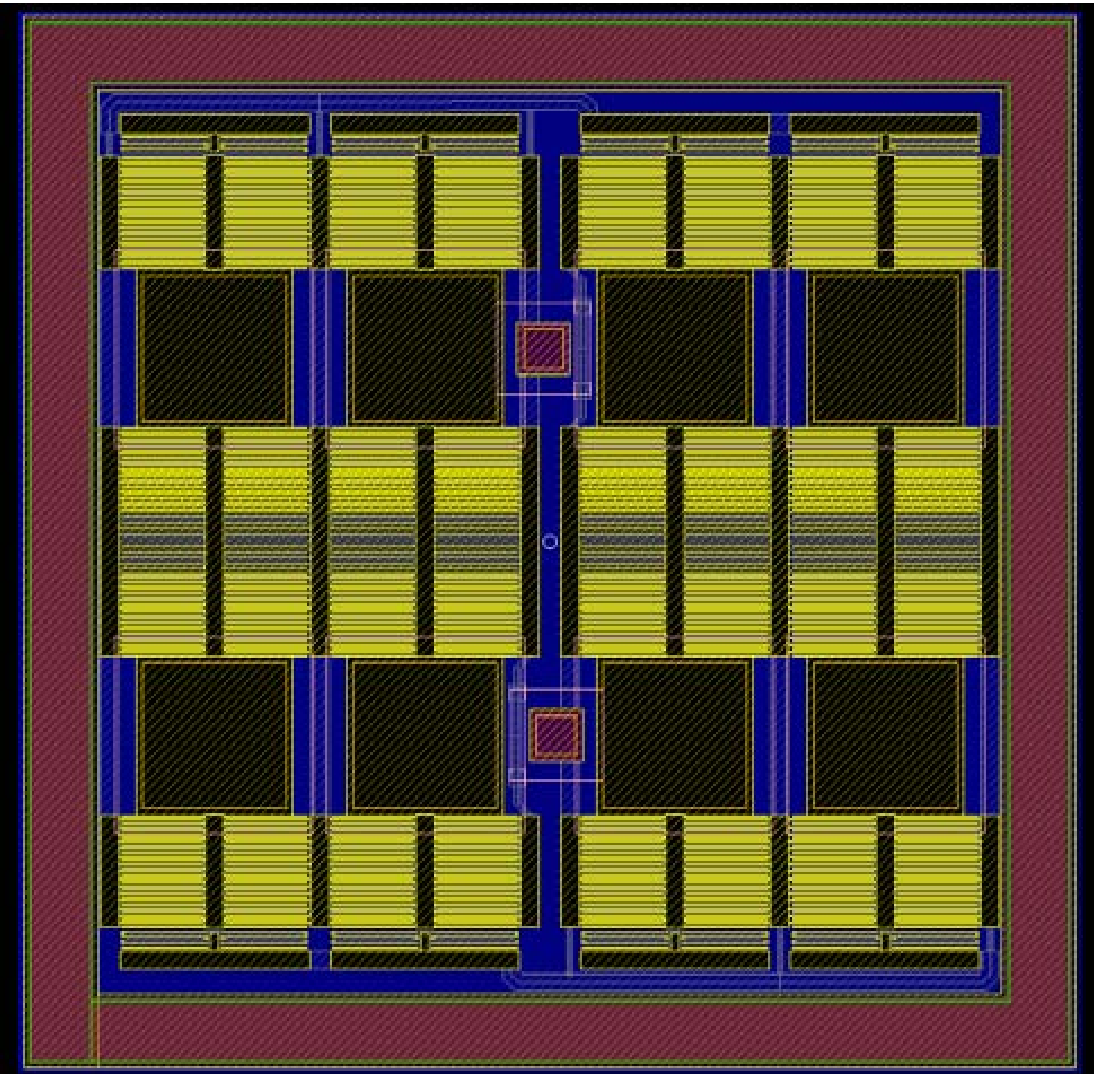

Designers	**Gonzalo Murillo.**
Technology	TRONICS MEMSOI with device silicon of 60 μm thick.
Number of devices	20 chips of 4000 x 4000 μm^2.
Description	Electrostatic vibration-driven energy harvesters integrated in a commercial MEMS technology. The fabrication of the dice was carried out at the foundry Tronics.

B.3. Piezoelectric Energy Scavenger

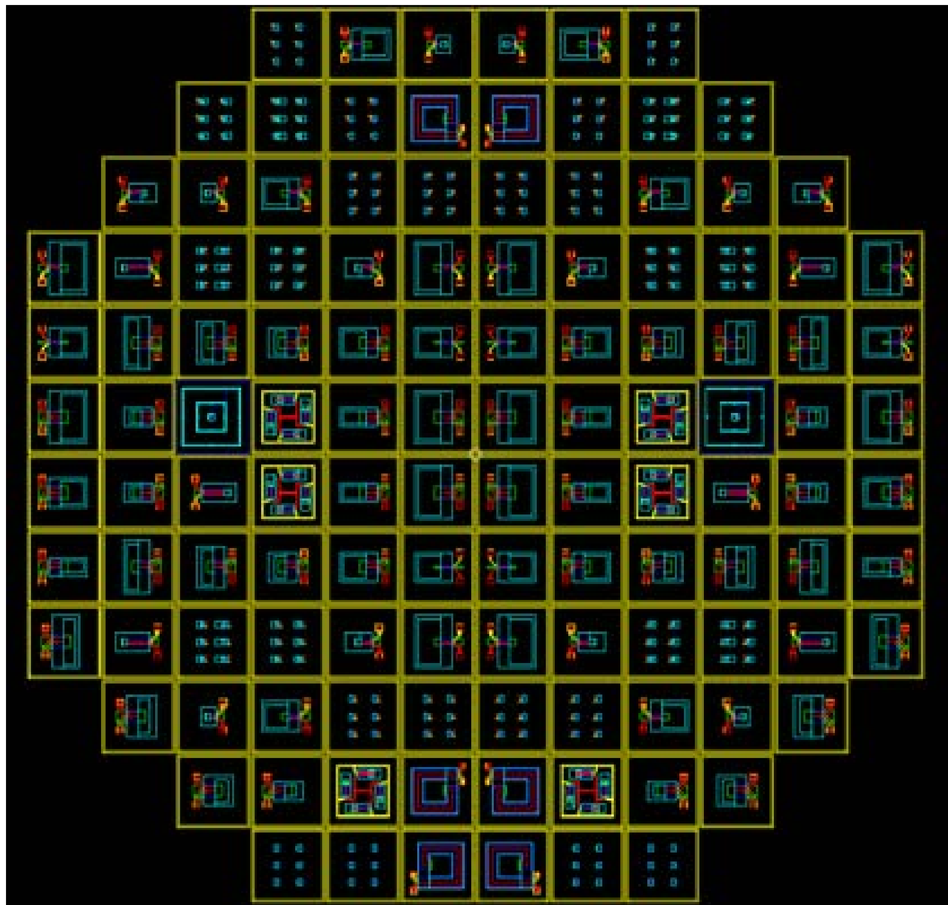

Designer	Gonzalo Murillo.
Technology	AlN-based MEMS technology.
Number of devices	4 wafers of 100 mm with 120 chips.
Description	Piezoelectric vibration-driven energy harvesters integrated in a FBAR-based technology. The fabrication was carried out at the Microelectronics National Center (CNM, Spain).

B.4. Nanopiezotronics approach

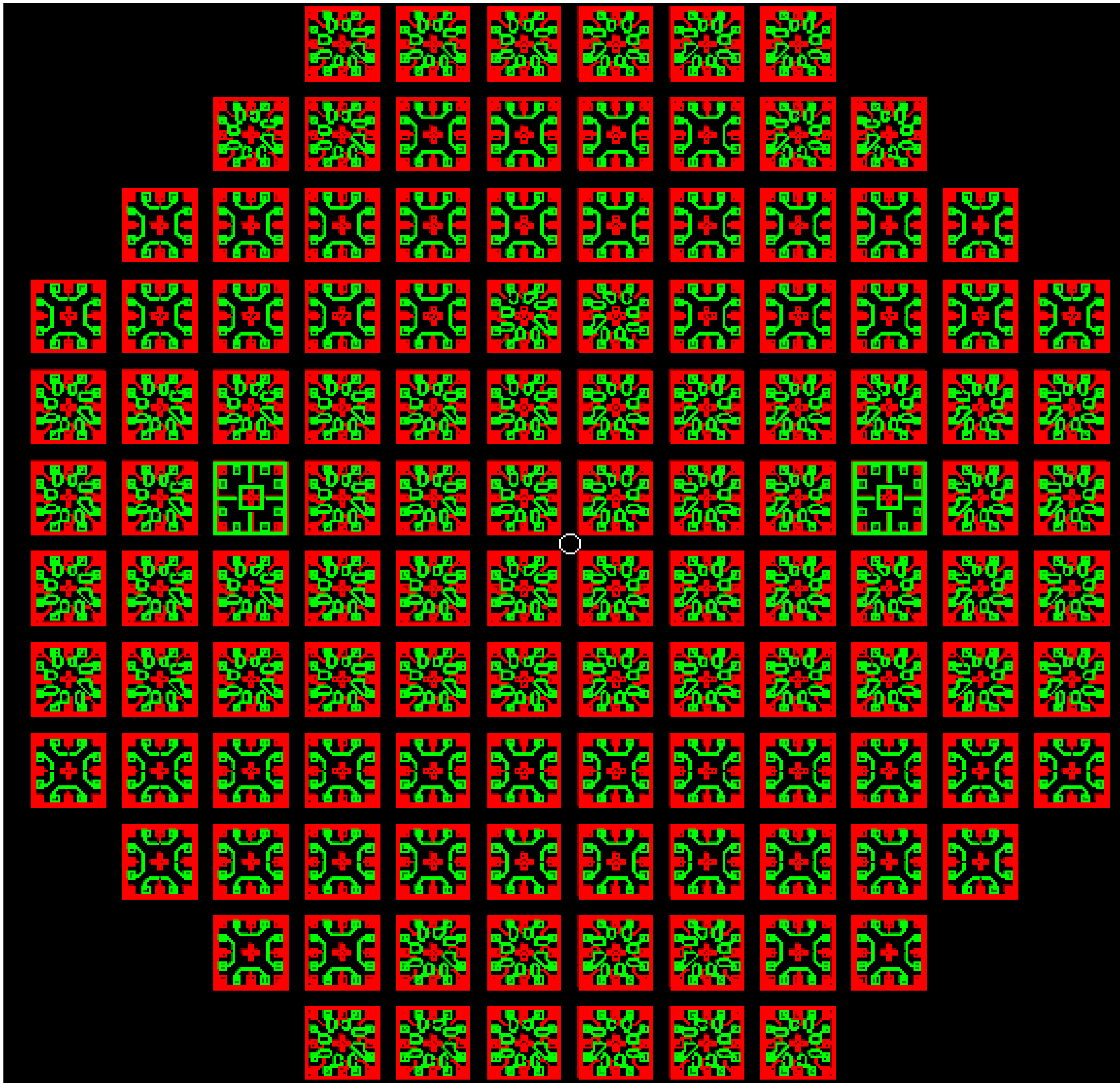

Designers	Gonzalo Murillo.
Technology	Ad-hoc technology with two thick metals (Cr and Au) and final growth of ZnO NWs.
Number of devices	4 wafers of 100 mm with 120 chips.
Description	Electrostatic vibration-driven energy harvesters integrated in a commercial MEMS technology. The fabrication of the dice was carried out at the Georgia Institute of Technology by Gonzalo Murillo.

Abbreviations and Acronyms

AFM	Atomic Force Microscope
BESOI	Bond and Etch-back Silicon Over Insulator
BHF	Buffered Hydrofluoric acid
CNC	Computer Numerical Control
CMOS	Complementary Metal Oxide Semiconductor
DC	Direct Current
DRIE	Deep Reactive-Ion Etching
EHiP	Energy Harvester in Package
EHoC	Energy Harvester on Chip
FEM	Finite Element Method
FoM	Figure of Merit
FW	Finewire
GPIB	General Purpose Interface Bus
IPGC	In-Plane Gap Closing
IPOV	In-Plane Overlap Varying
MEMS	Microelectromechanical Systems
MOEMS	Micro Optical Electro-mechanical Systems
NEMS	Nanoelectromechanical Systems
NW	Nanowire
OPGC	Out-of-Plane Gap Closing
PCB	Printed Circuit Board
RIE	Reactive-Ion Etching

RF	Radio Frequency
RFID	Radio Frequency Identification
SEM	Scanning Electronic Microscope
SiP	System in Package
SMD	Surface Mount Device
SoC	System on Chip
SOI	Silicon Over Insulator
VEH	Vibration-driven Energy Harvester
WSN	Wireless Sensor Network

SUMMARY

Nowadays, the aim of saving energy and finding new renewable sources has become a hot topic. Ambient energy sources are the best solution to obtain free energy in virtually any location. Mechanical energy sources and, in particular, vibrations are a wonderful option to recover a tiny but endless amount of energy from the environment to power low-consumption electronics circuits.

N/MEMS energy harvesting devices are aimed to be the link between these two different domains. An energy scavenger can generate enough electricity to power an autonomous node of a wireless sensor network (WSN) without the need of a dedicated battery.

This thesis is focused on the study, design, fabrication and characterization of different approaches of vibration-driven energy harvesting systems at micro-scale. The transduction methods investigated to convert the mechanical energy into electricity have been the electrostatic and piezoelectric. The first one was used to monolithically integrate an energy scavenger into a commercial CMOS technology. Then, two different MEMS technologies for fabricating an electrostatic and a piezoelectric energy harvesting system were utilized. These systems took advantage of a novel concept, first defined in this thesis, called "Energy Harvesting in Package" that relies on the use of the whole die as inertial mass of the resonator utilized to recover the mechanical energy. The advantage of this concept is the significant increase of the extracted power density in comparison to the conventional approach. As a result of these fabrication processes, several prototypes of the converter part of different energy harvesting systems were developed and characterized showing promising expectations.

In the last part of this thesis, a shift toward nano-scale energy scavenging devices is done. It is focused on the use of piezoelectric ZnO nanowires to generate electricity from motion. This cutting-edge field has been explored and several prototypes were fabricated to prove the combination of microscopic resonant elements with ZnO nanowires.